



UNIVERSIDADE ESTADUAL DE CAMPINAS

Instituto de Física “Gleb Wataghin”

HENRIQUE VIEIRA DE SOUZA

ARAPUCA, LIGHT TRAPPING DEVICE FOR THE  
DUNE EXPERIMENT

ARAPUCA, DISPOSITIVO DE COLETA DE LUZ PARA O  
EXPERIMENTO DUNE

Campinas

2021

HENRIQUE VIEIRA DE SOUZA

# ARAPUCA, LIGHT TRAPPING DEVICE FOR THE DUNE EXPERIMENT

## ARAPUCA, DISPOSITIVO DE COLETA DE LUZ PARA O EXPERIMENTO DUNE

Tese apresentada ao Instituto de Física “Gleb Wataghin” da Universidade Estadual de Campinas como parte dos requisitos exigidos para a obtenção do título de Doutor em Ciências, na área de Física.

Thesis presented to the “Gleb Wataghin” Institute of Physics of the University of Campinas in partial fulfillment of the requirements for the degree of Doctor in Science the area of Physics.

Orientador: Ettore Segreto

Este exemplar corresponde à versão final da tese defendida pelo aluno Henrique Vieira de Souza e orientada pelo Prof. Dr. Ettore Segreto.

Campinas

2021

Ficha catalográfica  
Universidade Estadual de Campinas  
Biblioteca do Instituto de Física Gleb Wataghin  
Lucimeire de Oliveira Silva da Rocha - CRB 8/9174

So89a Souza, Henrique Vieira de, 1990-  
ARAPUCA, light trapping device for the DUNE experiment / Henrique Vieira de Souza. – Campinas, SP : [s.n.], 2021.

Orientador: Ettore Segreto.  
Tese (doutorado) – Universidade Estadual de Campinas, Instituto de Física Gleb Wataghin.

1. Experimento DUNE. 2. Fotodetectores. 3. Argônio líquido. 4. Neutrinos. I. Segreto, Ettore, 1973-. II. Universidade Estadual de Campinas. Instituto de Física Gleb Wataghin. III. Título.

Informações para Biblioteca Digital

**Título em outro idioma:** ARAPUCA, dispositivo de coleta de luz para o experimento DUNE

**Palavras-chave em inglês:**

DUNE experiment

Photon detectors

Liquid argon

Neutrinos

**Área de concentração:** Física

**Titulação:** Doutor em Ciências

**Banca examinadora:**

Ettore Segreto [Orientador]

Anderson Campos Fauth

Orlando Luís Goulart Peres

Hélio da Motta Filho

Filippo Resnati

**Data de defesa:** 23-09-2021

**Programa de Pós-Graduação:** Física

**Identificação e informações acadêmicas do(a) aluno(a)**

- ORCID do autor: <https://orcid.org/0000-0002-2401-6563>

- Currículo Lattes do autor: <http://lattes.cnpq.br/2809205188553745>

MEMBROS DA COMISSÃO JULGADORA DA DISSERTAÇÃO DE DOUTORADO DE **HENRIQUE VIEIRA DE SOUZA – RA: 119549** APRESENTADA E APROVADA AO INSTITUTO DE FÍSICA “GLEB WATAGHIN”, DA UNIVERSIDADE ESTADUAL DE CAMPINAS, EM 23/09/2021.

**COMISSÃO JULGADORA:**

Prof. Dr. Ettore Segreto - Orientador (IFGW/UNICAMP)

Prof. Dr. Anderson Campos Fauth (IFGW/UNICAMP)

Prof. Dr. Orlando Luis Goulart Peres (IFGW/UNICAMP)

Dr. Filippo Resnati (European Organization for Nuclear Research)

Dr. Hélio da Motta Filho (Centro Brasileiro de Pesquisas Físicas)

**OBS.:** Ata da defesa com as respectivas assinaturas dos membros encontra-se no SIGA/Sistema de Fluxo de Tese e na Secretaria do Programa da Unidade.

Campinas

2021

A meus pais, que me incentivaram, apoiaram  
e me ensinaram que se Deus fecha uma porta  
Ele abre uma janela, dedico esta tese, com  
todo meu amor.

# Acknowledgements

First, I would like to thank Ettore Segreto, for the supervision and friendship along this years. It has been a pleasure being his student and I've learned so much and grew a lot professionally thanks to him. I would also like to thank Ana Amelia Machado and all the students and employees of the laboratory who made my days much better and helped me out in my research.

I wish to thank Francesco Terranova and Carla Cattadori for the amazing experience in Italy. Thank you for the guidance and friendship. Thanks also to all students and employees of Milano Bicocca and to everyone from the residence. I cannot express how much I enjoyed my work and staying in Italy, and this is mostly because of you all.

I also thank all the professors who were part of my formation. Special thanks to prof. Anderson C. Fauth, who was my master advisor and has taught me so much, and professors Orlando Peres, Sandro Guedes, Edmilson José, Carola Chinellato, Marcelo Guzzo, Pascoal Pagliuso, Ernesto Kemp, Eduardo Granado, Antonio Riul and Fernando Iikawa. Thanks to the Secretaria de Pós-Graduação for all the help and to all the employees of the Universidade Estadual de Campinas (UNICAMP).

Thanks to Vinicius Pimentel, Laura Paulucci, Franciole Marinho, David Martinez, Roberto Acciarri, Vishvas Pandey, Vincent Basque and everybody else with whom I had the pleasure to collaborate. Thanks also to Hélio da Motta Filho and Filippo Resnati for accepting being part of my Ph.D. committee.

I want to thank specially my parents for all the love and support. You have provided me everything, thank you so much... I am glad the vasectomy failed. I want to thank Aline Souza for being with me for most of this journey giving a lot of support. To all my friends, in particular to João Diniz, Adnei Ercule, Marina Guzzo, Rafaela Ramos, Jully Nascimento, Maria Cecilia, Yago Silva, Marco Ayala, Esteban Cristaldo, Ariel, Bruno Gelli, Greg de Souza and many others that put up with me for so long. To all my friends that I made in Italy, specially to Madalina Munteanu, Antonio Branca, Claudia Brizzolari, Andrea Falcone, Marta Torti, Maura Spanu, Niccolò Gallice, Arenc Tukaj, Danny Giove, Aitesam Tahir, Wenxiang Guo, Hakam Abushanab, Federica Cecuta and many others, thank you for making my stay in Italy so amazing.

Most importantly, I thank God because without Him I am nothing. Even though I do not

deserve, He is always by my side and have put all this amazing people in my life.

Thanks to the “Ministry of Science, Technology and Innovation” and the “National Council for Scientific and Technological Development - CNPq” for the scholarship. This study was financed in part by the Coordenação de Aperfeiçoamento de Pessoal de Nível Superior - Brasil (CAPES) - Finance Code 001.

# Resumo

O Deep Underground Neutrino Experiment (DUNE) será o primeiro mega programa científico em solo americano e irá esclarecer algumas questões em aberto na física de neutrinos. O experimento prevê a realização de um feixe de neutrinos intenso no Fermilab (Chicago - EUA), um detector próximo ao feixe para monitoramento e um detector distante em Sanford Underground Research Facility (SURF) a 1300 km de distância. O detector distante será composto por quatro módulos de câmeras de projeção temporal de argônio líquido (do inglês, LArTPC) de 10 kt de volume ativo cada que realizarão as medidas precisas exigidas para o experimento DUNE. A técnica experimental utiliza sinais de carga e luz de radiações ionizantes em argônio líquido para reconstruir interações de neutrinos com excelente resolução espacial, medidas de calorimetria e identificação de partículas.

A luz de cintilação do argônio líquido é produzida em torno de 127 nm dentro de poucos nanosegundos da passagem da radiação. A sua detecção pode melhorar a calorimetria da LArTPC além de fornecer o registro temporal de eventos não provenientes do feixe, o que é vital para a averiguação de eventos de decaimento de núcleos. O sistema de detecção de luz do DUNE (do inglês, PDS) é responsável por coletar a luz de forma eficiente, a fim de caracterizar o volume ativo do detector com eficiência superior a 99%. O PDS será composto por 1.500 módulos de X-ARAPUCA, um dispositivo de coleta de luz que será o assunto principal dessa tese.

Neste trabalho, a pesquisa e desenvolvimento do dispositivo ARAPUCA será apresentado. A caracterização completa dos protótipos foram realizadas em testes dedicados em argônio líquido no Brasil e na Itália, no qual eficiências comparáveis de  $(2.2 \pm 0.4)\%$  e  $(1.9 \pm 0.1)\%$  foram encontradas, respectivamente. O novo wavelength shifter desenvolvido na Itália em colaboração com a *Università degli Studi di Milano-Bicocca* será apresentado. Componente que permitiu aumentar a eficiência de coleta de luz em cerca de 50% e resultou em uma eficiência de  $(2.9 \pm 0.1)\%$  para o protótipo de X-ARAPUCA.

Os dispositivos de X-ARAPUCAs foram também instalados no protótipo do DUNE (ProtoDUNE) para testes de dopagem de xenônio. Será apresentada nessa tese parte da análise de dados realizada que permitiu a colaboração do DUNE entender e estabelecer a dopagem de xenônio como alternativa para o detector distante.

**Palavras-chave:** Fotodetectores; Argônio líquido; Experimento DUNE; Neutrinos

# Abstract

The Deep Underground Neutrino Experiment (DUNE) will be the first mega-science program on the US soil and will shed light on some of the open questions in neutrino physics. The experiment foresees the realization of an intense neutrino beam at Fermilab (Chicago - USA), of a near detector to monitor the beam and a far detector installed in the Sanford Underground Research Facility (SURF), 1300 km far away. Four 10 kt Liquid Argon Time Projection Chambers (LArTPC) will compose the 40 kt far detector modules to perform the precise measurements required for DUNE. The experimental technique uses charge and light signal from ionizing radiations in liquid argon to fully reconstruct neutrino interactions with excellent spatial resolution, calorimetric measurements and particle identification.

The liquid argon scintillation light is produced around 127 nm within a few nanoseconds from the radiation passage. Its detection may improve the LArTPC calorimetric besides giving the time stamp of non-beam events, which is vital in fiducializing nucleon-decay events. The DUNE Photon Detection System (PDS) is responsible to efficiently collect this light in order to fiducialize the active volume of the detector with  $> 99\%$  efficiency. The PDS will be composed by 1,500 X-ARAPUCA modules, a light trapping device that was the main subject of this thesis.

In this work, the research and development of the ARAPUCA devices will be presented. The full characterization of the prototypes were performed in dedicated liquid argon tests, in Brazil and Italy, where comparable efficiencies of  $(2.2 \pm 0.4)\%$  and  $(1.9 \pm 0.1)\%$  were found. A new wavelength shifter developed in Italy in collaboration with the *Università degli Studi di Milano-Bicocca* will be presented. It allowed to increase the light detection efficiency of about 50% and resulted in an overall efficiency of  $(2.9 \pm 0.1)\%$  of the X-ARAPUCA prototype.

The X-ARAPUCA devices were also deployed in the DUNE prototype (ProtoDUNE) for xenon doping tests. It will be shown in this thesis part of the analysis performed which aided the DUNE Collaboration to understand and establish the xenon doping as an alternative for the far detector modules.

**Keywords:** Photon detectors; Liquid argon; DUNE experiment; Neutrinos

# List of Abbreviations

<b>ADC</b>	Analog-to-Digital Converter
<b>APA</b>	Anode Plane Assemblies
<b>APD</b>	Avalanche Photodiode
<b>BBT</b>	2,5-Bis(5-tert-butyl-benzoxazol-2-yl)thiophene
<b>BisMSB</b>	1,4-Bis(2-methylstyryl)benzol
<b>CC</b>	Charged Current
<b>CERN</b>	European Organisation for Nuclear Research
<b>C.L.</b>	Confidence Level
<b>CP</b>	Charge Parity
<b>CPA</b>	Cnode Plane Assemblies
<b>CPT</b>	Charge Parity Transformation
<b>CT</b>	Charge Time
<b>DAQ</b>	Data Acquisition
<b>DUNE</b>	Deep Underground Neutrino Experiment
<b>DUT</b>	Device Under Test
<b>ES</b>	Elastic Scattering
<b>eV</b>	Electron Volt
<b>FD</b>	Far Detector
<b>Fermilab</b>	Fermi National Accelerator Laboratory
<b>GAr</b>	Gas Argon
<b>HD</b>	Horizontal Drift
<b>ICARUS</b>	Imaging Cosmic And Rare Underground Signals
<b>IO</b>	Inverted Ordering
<b>KamLAND</b>	Kamioka Liquid Scintillator Antineutrino Detector
<b>LAr</b>	Liquid Argon
<b>LArIAT</b>	Liquid Argon In A Test Beam
<b>LArTPC</b>	Liquid Argon Time Projection Chamber
<b>LBNE</b>	Long Baseline Neutrino Experiment
<b>LET</b>	Linear Energy Transfe
<b>MH</b>	Mass Hierarchy
<b>MicroBooNE</b>	Micro Booster Neutrino Experiment

<b>NC</b>	Neutral Current
<b>ND</b>	Near Detector
<b>NO</b>	Normal Ordering
<b>NOvA</b>	NuMI Off-Axis $\nu_e$ Appearance
<b>PD</b>	Photon Detection
<b>PDE</b>	Photon Detection Efficiency
<b>PDS</b>	Photon Detection System
<b>P.E.</b>	Photo-electron
<b>PMMA</b>	Poly(methyl methacrylate)
<b>PMNS</b>	Pontecorvo-Maki-Nakagawa-Sakata
<b>PMT</b>	Photomultiplier tube
<b>POT</b>	Protons On Target
<b>PTP</b>	Para-Terphenyl
<b>PVT</b>	Polivyniltoluene
<b>RMS</b>	Root Mean Square
<b>SBND</b>	Short Baseline Neutrino Detector
<b>SiPM</b>	Silicon Photomultiplier
<b>SNO</b>	Sudbury Neutrino Observatory
<b>SP</b>	Single-Phase
<b>S.P.E.</b>	Single photo-electron
<b>SSM</b>	Standard Solar Model
<b>SURF</b>	Sanford Underground Research Facility
<b>T2K</b>	Tokai-to-Kamioka
<b>TPB</b>	Tetra-phenyl butadiene
<b>TPC</b>	Time Projection Chamber
<b>VD</b>	Vertical Drift
<b>VUV</b>	Vacuum Ultra Violet
<b>WLS</b>	Wavelength shifter

# Contents

<b>Introduction</b>	<b>16</b>
<b>1 DUNE and neutrino physics</b>	<b>18</b>
1.1 Historical context . . . . .	19
1.1.1 Solar neutrino anomaly . . . . .	19
1.1.2 Atmospheric neutrino anomaly . . . . .	20
1.1.3 The neutrino oscillation evidence . . . . .	22
Kamiokande and Super Kamiokande measurements . . . . .	22
SNO measurements . . . . .	23
Oscillation parameters . . . . .	24
1.2 Neutrino oscillation . . . . .	25
1.2.1 Two neutrino mixing . . . . .	28
Averaged probability . . . . .	29
Type of experiments . . . . .	33
1.2.2 Three neutrinos mixing . . . . .	36
CPT, CP and T violations . . . . .	38
Neutrino Mass Hierarchy . . . . .	40
1.3 DUNE Context . . . . .	41
1.3.1 Oscillation in matter . . . . .	44
1.3.2 Parameters measurements . . . . .	47
1.4 Beyond the neutrino beam . . . . .	48
1.4.1 Supernova neutrinos . . . . .	48
1.4.2 Proton decay . . . . .	50
<b>2 Deep Underground Neutrino Experiment</b>	<b>51</b>
2.1 Liquid Argon Time Projection Chamber (LArTPC) . . . . .	51

2.1.1	Principle of operation . . . . .	51
2.1.2	Why using liquid argon . . . . .	54
2.1.3	Neutrino detection in a LArTPC . . . . .	55
2.1.4	LAr purity . . . . .	57
2.2	Experimental details . . . . .	58
2.2.1	Neutrino beam . . . . .	58
2.2.2	Far Detector . . . . .	60
2.2.3	The DUNE specifications for the LArTPC . . . . .	63
<b>3</b>	<b>Light collectors</b>	<b>64</b>
3.1	Scintillation light in LAr . . . . .	64
3.1.1	Process and photons production . . . . .	64
3.1.2	Electron-ion recombination . . . . .	66
3.1.3	Emission spectrum and time profile . . . . .	68
3.1.4	Nitrogen contamination and quenching of light . . . . .	69
3.1.5	Summary . . . . .	70
3.2	The Standard ARAPUCA . . . . .	71
3.3	The X-ARAPUCA . . . . .	72
3.3.1	The device challenges . . . . .	73
3.3.2	The Short Baseline Neutrino Detector (SNBD) . . . . .	75
3.4	Silicon Photomultipliers (SiPMs) . . . . .	76
3.4.1	Principle of working . . . . .	76
3.4.2	Afterpulses and Cross-talk . . . . .	78
3.5	Wavelength shifter . . . . .	79
3.6	Dichroic filter . . . . .	81
<b>4</b>	<b>Research and Development</b>	<b>83</b>
4.1	Dark Box Arapuca prototype . . . . .	83
4.1.1	Calibration . . . . .	84
4.1.2	Trapping effect . . . . .	85
4.1.3	Results . . . . .	85
4.2	Monochromator tests . . . . .	87
4.2.1	Results . . . . .	89

	Fused silica versus B270 . . . . .	89
4.3	Grounding mesh transparency . . . . .	90
4.4	Glass-to-Power Wavelength Shifter . . . . .	93
4.4.1	Warm measurements . . . . .	95
4.4.2	Cryogenic measurements . . . . .	98
<b>5</b>	<b>X-ARAPUCA Efficiency test</b>	<b>101</b>
5.1	X-ARAPUCA single-cell tests . . . . .	101
5.1.1	Experimental setup . . . . .	102
5.1.2	Data Acquisition . . . . .	103
5.1.3	Calibration . . . . .	105
	Single photo-electron (s.p.e.) calibration . . . . .	105
	Matching filter . . . . .	106
	Cross-talk evaluation . . . . .	108
	Liquid Argon purity . . . . .	110
5.1.4	Experimental setup Monte Carlo Simulation . . . . .	112
5.1.5	Efficiency analysis . . . . .	113
5.2	X-ARAPUCA double-cell tests . . . . .	117
5.2.1	Experimental setup and DAQ . . . . .	117
5.2.2	Calibration . . . . .	120
	Single photo-electron (s.p.e.) calibration . . . . .	120
	Cross-talk evaluation . . . . .	120
	Liquid Argon purity . . . . .	122
5.2.3	Monte Carlo “Toy-model” . . . . .	125
5.2.4	Efficiency and enhancement analysis . . . . .	125
<b>6</b>	<b>The ProtoDUNE-SP and Xenon Doping</b>	<b>130</b>
6.1	The ProtoDUNE-SP experiment . . . . .	130
6.2	Xenon Doping tests . . . . .	132
6.2.1	Xe doping effect in LAr . . . . .	133
6.2.2	Experimental setup . . . . .	134
6.2.3	Waveform analysis . . . . .	135
6.2.4	Light yield recovery . . . . .	138

6.2.5 Toy model Monte Carlo . . . . .	140
<b>Conclusion</b>	<b>144</b>
<b>Bibliography</b>	<b>146</b>
<b>Appendix A Deconvolution method</b>	<b>158</b>
<b>Appendix B Total internal reflection</b>	<b>161</b>
<b>Appendix C Photomultiplier tube (PMT)</b>	<b>162</b>
<b>Appendix D Toy Model images</b>	<b>163</b>

# Introduction

In 1914, James Chadwick demonstrated that the electron emitted in  $\beta$ -decays has a continuous spectrum which seemed not to conserve energy. The idea of the neutrino came in 1930, when Wolfgang Pauli proposed the existence of a neutral and low mass particle that would also be emitted during the  $\beta$ -decay to preserve the principle of energy conservation. It was only 26 years later, in 1956, that the neutrino was first directly detected by Cowan and Reines in a nuclear reactor experiment [1].

Neutrinos are classified as neutral fermions, an elementary half-spin particle that interact only via weak interaction and gravity. The Standard Model is a successful theory of elementary particles that has been profoundly probed along the years. It has, however, a few imperfections that still need further theoretical and experimental improvement to a proper understanding of fundamental physics. For example, the predominance of matter over antimatter in the early universe and the observation of Dark Matter and Dark Energy. More recently, the experimental observation of the neutrino oscillation implied that neutrinos have mass, which was not included or predicted by the model, offering the most compelling evidence of physics beyond the standard model.

Although many advances have been made in the field of neutrino physics, there are still open questions such as the origin of neutrino mass, the precise parameters of neutrino mixing, if neutrinos are their own antiparticle or not and if there are more than three flavors of neutrinos. On top of it, the study of neutrinos may contribute to answer some of the open questions in astrophysics and cosmology.

The Deep Underground Neutrino Experiment (DUNE) [2–6] will be a world-class neutrino observatory and nucleon decay detector. The experiment aims to answer the matter and antimatter disparity, the dynamic of supernova neutrino bursts (SNBs) and whether protons eventually decay. The neutrino oscillation mechanism and the key features for experimental measurements in the field are given in Chapter 1, together with the SNB and proton decay signatures in the detector. The DUNE experiment and the technique of detection, the Liquid Argon Time Projection Chamber (LArTPC), are explored in Chapter 2, highlighting the detector proprieties and specifications.

Chapter 3 is dedicated to the DUNE Photon Detection System (PDS), and the ARAPUCA is introduced. The PDS has the role to detect argon scintillation light at a wavelength of 127 nm, a challenging and important task to reach the DUNE ambitious physical goals. An efficient

light collection not only improves DUNE's physics, but is crucial to measure proton decay efficiently. The work developed in this thesis is aimed to study, characterize and improve the ARAPUCA. In Chapter 4, the Research and Development (R&D) of the device is presented, with the main experiments performed and results achieved.

The two main experiments in liquid argon that fully characterized the ARAPUCA device are presented in Chapter 5. The experiments were performed in Brazil and Italy with different prototypes of ARAPUCAs and retrieved comparable results. In Brazil, a dedicated cryogenic setup was built in the "*Laboratório de Léptons*" and three different ionizing radiations were used to retrieve the device photon detection efficiency (PDE). In Italy, an alpha source was used to further investigate the device efficiency and to validate the enhancement in the PDE previously investigated in Chap. 4.

The final chapter (Chapter 6) presents the investigation of xenon doping in the DUNE prototype (namely ProtoDUNE), which resulted to be an excellent alternative for DUNE in case of nitrogen contamination. Data collected with two ARAPUCA devices helped the collaboration to analyze the effects of xenon doping in liquid argon, showing a recovery of light and increased light collection uniformity inside the detector.

As a disclaimer, the figures without reference in the caption were done by the author. The exceptions are the analysis plots for the X-ARAPUCA single-cell and double-cell (Chapters 4 and 5), where the author was responsible for the analysis.

# Chapter 1

## DUNE and neutrino physics

The scientific program of the DUNE experiment is extremely rich and includes: **(1)** measuring the charge-parity symmetry violation phase in the leptonic sector, **(2)** the determination of the octant of  $\theta_{23}$  mixing angle and the determination of the neutrino mass hierarchy, **(3)** search for proton decay modes, providing a portal to Grand Unification of Theory (GUT) which predicts that, if there was an unified physical force at the birth of the universe, protons should decay and **(4)** Detection and measurements of the  $\nu_e$  flux from a core-collapse supernova within our galaxy. This would help to understand the supernova phenomenon and would give fundamental information about the nature of neutrinos [7].

The charge-parity symmetry phase ( $\delta_{CP}$ ) will be measured in DUNE due the fact that neutrinos travel through matter (Sec. 1.3.1), and it may provide insights into the origin of the matter-antimatter asymmetry. The same matter effect makes possible the determination of the neutrino mass hierarchy, due to the sensitivity to the sign of  $\Delta m_{31}^2 \equiv m_3^2 - m_1^2$ . One of the DUNE primary goals is to measure the long-baseline oscillation parameters without constraints [3]. Figure 1.1 shows the allowed region for  $\sin^2(2\theta_{13})$  (Left) (and  $\sin^2(\theta_{23})$  (Right)) and  $\delta_{CP}$  within 90% Confidence Level (C.L.) for 7, 10 and 15 years of operation. The black star represents the hypothetical “true value” assumed to be the central value of the global fit to neutrino oscillation data (NuFIT 4.0).

Furthermore, the intense neutrino beam, the massive 40 kt LArTPC far detector and the high-resolution DUNE near detector makes DUNE an outstanding tool for a rich ancillary science program. Many important researches are included, such as: Beyond Standard Model (BSM) measurements in order to search for sterile neutrinos and Dark Matter, measurements of tau neutrino appearance, measurements of neutrino oscillation phenomena using atmospheric neutrinos, neutrino cross-section and others.

This chapter gives an introduction of the field of neutrino, with an overview of the current challenges and open questions, to provide a context for the subject of this thesis. We give an introduction of neutrino oscillation, with explanation of the usual two-neutrino oscillation mechanism and how this approach is good enough to understand the case of three neutrino mixing. An emphasis will be given to the DUNE experiment, showing why it is important and exploring the basics of DUNE’s physical goals.

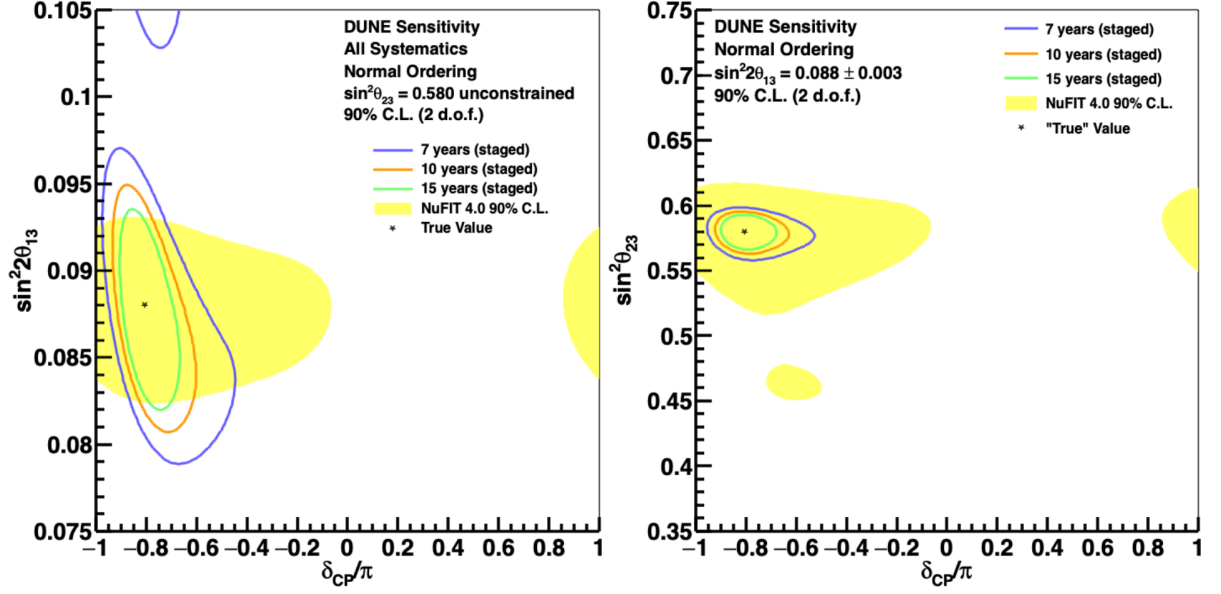


Figure 1.1: (Left) Allowed region within 90% C.L. for  $\sin^2(2\theta_{13})$  and  $\delta_{CP}$  parameters for 7, 10 and 15 years of beam exposure. The global fit to neutrino oscillation data (NuFIT 4.0) 90% C.L. region is represented by the yellow area and the black star is the “true value” assumed to be the central value of the global fit. (Right) Allowed region within 90% C.L. for  $\sin^2(\theta_{23})$  and  $\delta_{CP}$  parameters [3].

## 1.1. Historical context

### 1.1.1. Solar neutrino anomaly

Earth receives a solar neutrino flux of about  $6 \times 10^{10} \text{ } \nu/\text{cm}^2\text{s}$  with energy ranging from 0.1 to 20 MeV. The sun produces energy and neutrinos mostly through  $^4\text{He}$  reaction as:



where 4 protons ( $p$ ) and 2 electrons ( $e^-$ ) will result in an alpha-particle ( $^4\text{He}$ ) and two electron neutrinos ( $\nu_e$ ) with total energy release of 26.7 MeV. The main solar chain is shown in Figure 1.2, where the highlighted reactions  $pp$ ,  $pep$ ,  $hep$ , Be and B always have the release of an alpha-particle ( $\alpha$ ) and two neutrinos  $\nu_e$ , highlighted in blue and red, respectively. Heavier stars will follow the CNO chain, while it gives only a minor additional contribution to the solar neutrino flux [8].

The expected neutrino energy spectrum is shown in Figure 1.3 for both chains ( $pp$  and  $pep$ ) as solid lines and for the CNO cycle as blue dashed lines.

The first experiment to investigate the neutrino flux was led by Ray David in 1968. The experiment, proposed by B. Pontecorvo, used Chlorine to detect neutrinos through inverse

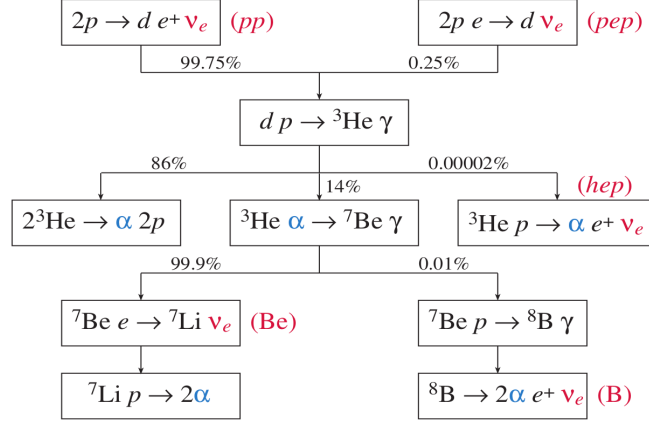


Figure 1.2: Solar chain for electron neutrino production [8].

beta decay ( $\nu + n \rightarrow p + e^-$ ). The Cl reaction has a threshold of  $E_{\nu_e} > 0.814$  MeV, which leaves the experiment mostly sensitive to Boron (B) neutrinos, as can be noticed from Fig. 1.3. The experiment measured, however, a neutrino flux three times lower than the predicted value, giving rise to the so called “solar anomaly”.

Years later the Gallium based experiments, SAGE and GALLEX [9, 10], measured the neutrino flux also through inverse beta decay but now sensitive to the main  $pp$  chain as the  $^{71}\text{Ga}$  target had a lower threshold of 0.233 MeV. Both experiments also reported a disappearance of electron neutrinos, measuring a flux two times lower than the expected, while the predicted flux had an error of only 1% [8]. Therefore, most probably, a new physics was present in the experimental data.

### 1.1.2. Atmospheric neutrino anomaly

Cosmic rays collisions in the upper atmosphere produce pions (mostly) and kaons, the decay of these particles originates the so-called atmospheric neutrinos through the reactions [12, 13]:

$$\pi^- \rightarrow \mu^- + \bar{\nu}_\mu, \quad \mu^- \rightarrow e^- + \bar{\nu}_e + \nu_\mu \quad (1.2a)$$

$$\pi^+ \rightarrow \mu^+ + \nu_\mu, \quad \mu^+ \rightarrow e^+ + \nu_e + \bar{\nu}_\mu \quad (1.2b)$$

where  $\pi^\mp$  are negative and positive pions,  $\mu^\mp$  are negative and positive muons,  $e^\mp$  are electrons and positrons and  $\nu_{\mu,e}$  ( $\bar{\nu}_{\mu,e}$ ) are muon and electron neutrinos (antineutrinos). The atmospheric neutrino flux is about  $1 \text{ } \nu/\text{cm}^2\text{s}$  with an uncertainty of 20% due to, mostly, uncertainties in the cosmic rays flux and hadronic interactions [8].

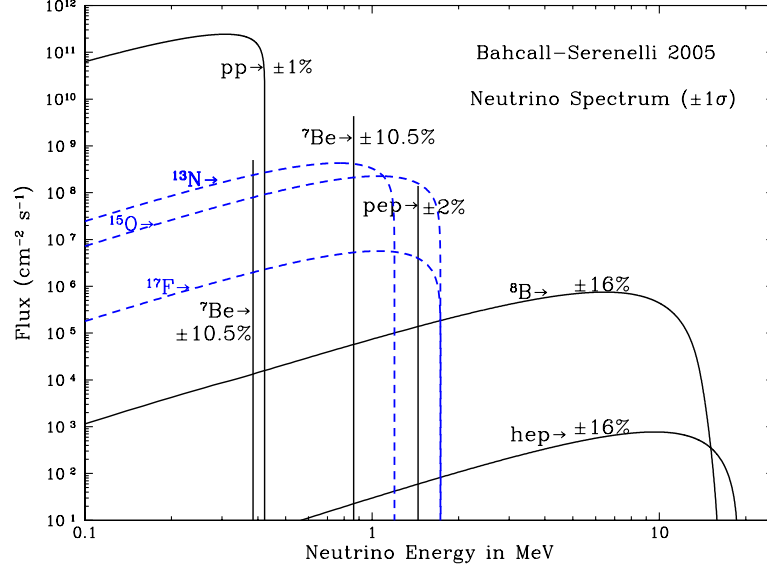


Figure 1.3: Predicted solar neutrino energy spectra. The solid lines represent neutrinos produced by the  $pp$  and  $pep$  chains and the dashed blue lines represent neutrinos from the CNO cycle. The theoretical fractional uncertainties are labeled and are shown for each source [11].

The reactions of Eq. 1.2 imply that the ratio between the flux of muon-flavor and electron-flavor neutrinos is<sup>1</sup> 2 : 1. Taking into account the symmetry of the Earth, the flux should be the same by measuring neutrinos coming from the positive zenith angle (straight from the sky) or negative (down from Earth). Figure 1.4 (Left) shows the expected flux for  $\nu_\mu$  ( $\bar{\nu}_\mu$ ) in solid (dashed) blue lines and for  $\nu_e$  ( $\bar{\nu}_e$ ) in solid (dashed) red lines at the Super Kamiokande (SK) location, while a cartoon (Right) shows that the atmospheric neutrino flux should be the same measured upward-going and or downward-going [8].

The “atmospheric anomaly” was noticed by neutrino experiments and confirmed by the Kamiokande experiment [14] which measured a lower ratio of  $\nu_\mu : \nu_e$  than expected. The (Super)Kamiokande is a Water Cherenkov (WC) detector that detects atmospheric neutrinos through charged current nucleon scattering ( $\nu_\ell + n \rightarrow \ell + p$ ,  $\ell = e, \mu, \tau$ ). The charged particles which travel faster than light in water will emit Cherenkov radiation [15]. This was a hint that the ratio could depend on the distance traveled by the neutrino.

<sup>1</sup>Except for energies above a few GeV, where the muons will reach the earth’s surface before decaying, giving a  $\nu_\mu : \nu_e$  ratio higher than 2.

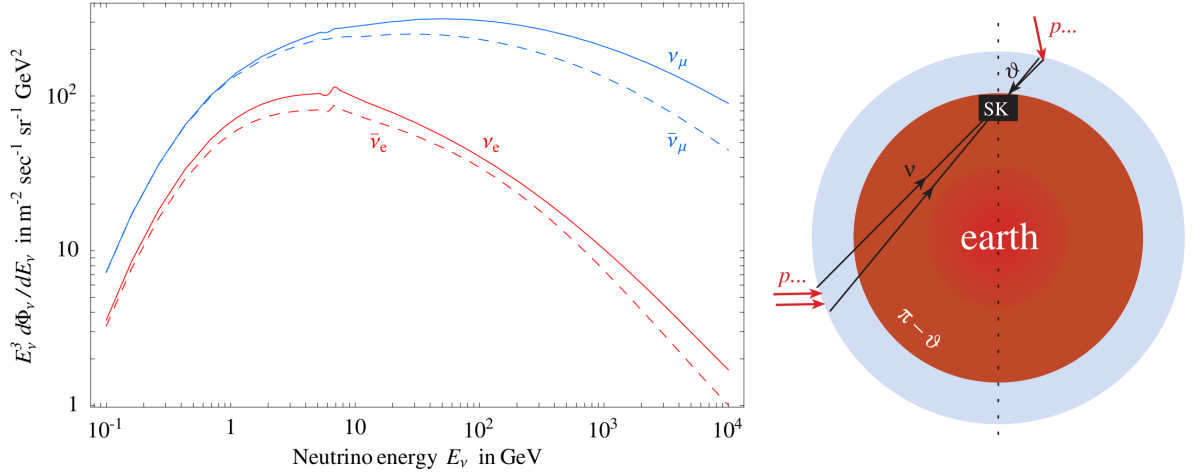


Figure 1.4: (Left) Predicted atmospheric neutrinos flux in absence of oscillation, average over the zenith angle was taken. (Right) Cartoon of the up and down symmetry on the neutrino flux [8]. Without considering oscillations, the flux of atmospheric neutrinos would be symmetric following the flux in the left panel.

### 1.1.3. The neutrino oscillation evidence

In the late 1990s, the Kamiokande and Super Kamiokande experiments in Japan [14, 16] and the SNO experiment in Canada [17] produced unquestionable evidences of the neutrino oscillation together with explanations for the discrepancies observed. The SNO experiment found evidence of  $\nu_{\mu,\tau}$  appearance with confirmation of the KamLAND experiment [18] discovering disappearance of  $\bar{\nu}_e$  from reactors [8]. The (Super)Kamiokande measured disappearance of atmospheric  $\nu_\mu$  and  $\bar{\nu}_\mu$  with confirmation of K2K [19] experiment with  $\nu_\mu$  beam.

#### Kamiokande and Super Kamiokande measurements

The analysis of atmospheric neutrinos in (Super)Kamiokande was originally regarded as background for proton decay searches. The SK is an underground (1000 m) experiment consisting of a 50 kton cylindrical water tank surrounded by 13,142 photomultipliers (PMT). The experiment detected the rings of light produced by scattered leptons in the water. The detector can distinguish between  $\nu_\mu$  and  $\nu_e$  due to the topology of the rings [8, 20], however, it could not differentiate particles from antiparticles.

Figure 1.5 shows the famous result from Super Kamiokande for the neutrino oscillation, where the zenith angle distribution is shown for muon-like and electron-like (bottom and top panels, respectively) events in two different set of data, sub-GeV and multi-GeV event. The  $\mu$ -like events with multi-GeV are separated in fully contained and partially

contained<sup>2</sup>, while the others have the momentum threshold displayed. Upward-going and downward-going particles<sup>3</sup> have  $\cos\Theta < 0$  and  $\cos\Theta > 0$ , respectively. The dashed regions are Monte Carlo expectation for no oscillations, the bold line is the best-fit expectation assuming  $\nu_\mu \rightarrow \nu_\tau$  oscillation.

It is noticeable that the  $\mu$ -like events show a disappearance of  $\nu_\mu$  when comparing between upward-going ( $\cos\Theta = -1$ ) and downward-going ( $\cos\Theta = 1$ ) muons, specially for the multi-GeV events. This means that muons crossing the Earth are missing and the data suggest that the oscillation  $\nu_\mu \rightarrow \nu_\tau$  is maximum. Looking at the data, the oscillation begins for horizontal neutrinos ( $\cos\Theta \sim 0$ ), traveling a distance  $L \sim 1000$  km. Multi-GeV neutrinos have energy of  $E_\nu \sim 3$  GeV, this means that the relation  $E_\nu/L \sim \Delta m_{atm}^2 \sim 3 \times 10^{-3} \text{ eV}^2$  (see Sec. 1.2.1, Eq. 1.42) is well satisfied<sup>4</sup>. While the zenith-angle distribution of  $\mu$ -like events is clearly asymmetric,  $e$ -like events show no asymmetry.

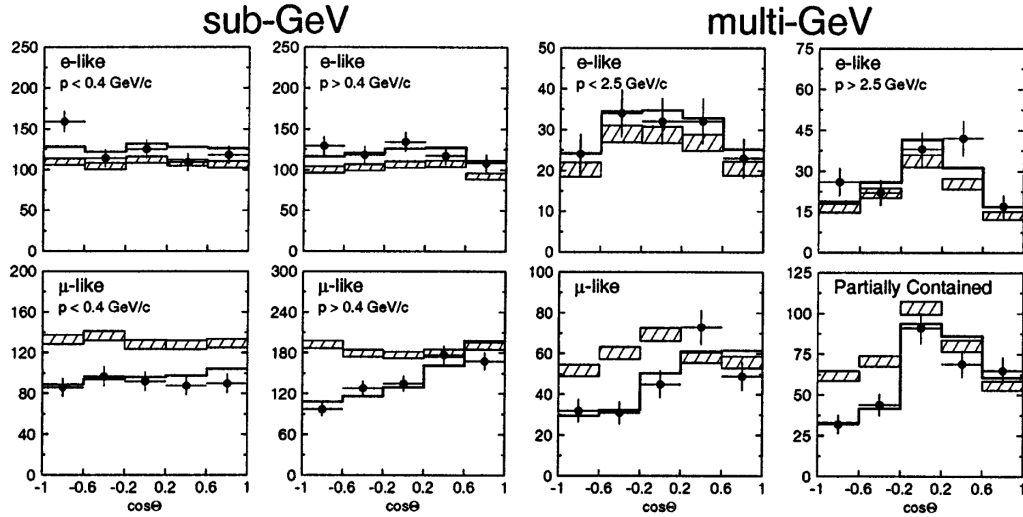


Figure 1.5: Zenith angle distribution of  $\mu$ -like (bottom panels) and  $e$ -like (top panels) events for sub-GeV and multi-GeV events in the Super Kamiokande. Upward-going and downward-going particles have  $\cos\Theta < 0$  and  $\cos\Theta > 0$ , respectively. The dashed regions are Monte Carlo expectation for no oscillations and the bold line is the best-fit expectation for  $\nu_\mu \rightarrow \nu_\tau$  oscillations [16].

## SNO measurements

The SNO solar experiment [17] is a Water Cherenkov detector with a major improvement: SNO employs 1 kton of salt heavy water ( $D_2O$ ) rather than water, allowing to measure sepa-

<sup>2</sup>High energy muons will travel too further, escaping the detector.

<sup>3</sup>Vertically downward-going particles traveled 15 km in the atmosphere, while vertically upward-going particles have traveled about 13,000 km before interacting with the detector.

<sup>4</sup>The current value is  $2.6 \times 10^{-3} \text{ eV}^2$ .

rately the  $\nu_e$  and  $\nu_{\mu,\tau}$  fluxes by different neutrino interactions. SNO is the first solar neutrino appearance experiment. The experiment used 12 m radius acrylic spheres shell at a depth of 6010 m of water equivalent with 9,456 PMTs to readout the signals.

The SNO was sensitive to charged-current (CC) and neutral-current, (NC) interactions and electron elastic scattering (ES), they can be written respectively as:

$$\nu_e + d \rightarrow p + p + e^- \quad (\text{CC}) \quad (1.3)$$

$$\nu_\ell + d \rightarrow p + n + \nu_\ell \quad (\text{NC}) \quad (1.4)$$

$$\nu_\ell + e^- \rightarrow \nu_\ell + e^- \quad (\text{ES}). \quad (1.5)$$

The CC interaction (Eq 1.3) is sensitive only to  $\nu_e$  flux, while the NC and ES are sensitive to all flavors but cannot distinguish between them. The fragmentation of deuterons in the NC interaction (Eq. 1.4) has a threshold of  $E_\nu > 2.2$  MeV and it is detected by 6.25 MeV  $\gamma$ -ray emission after the neutron capture [8].

Figure 1.6 shows the famous SNO experiment plot that gives a  $5\sigma$  evidence for  $\nu_e \rightarrow \nu_{\mu,\tau}$  appearance, proving that the Solar Standard Model (SSM) correctly predicted the neutrino flux and that electron neutrinos were not disappearing but rather changing flavor to  $\mu$ ,  $\tau$  neutrinos. The plot is made to show the flux of  $\nu_{\mu,\tau}$  as function of the  $\nu_e$  solar flux from the  $^8\text{B}$  process (see Fig. 1.2 and 1.3). The red area represents the neutrino flux measured with the CC interactions ( $\phi_{CC}^{SNO}$ ), where the  $\nu_{\mu,\tau}$  flux is unknown. The NC and ES measured neutrino flux in blue and green ( $\phi_{NC}^{SNO}$  and  $\phi_{ES}^{SNO}$ ) are composed by  $\nu_e$  and/or  $\nu_{\mu,\tau}$  fluxes, therefore they are represented as function of  $\nu_e$  flux. The intersection of the three bands gives the best estimate of  $\phi_e$  and  $\phi_{\mu,\tau}$  with  $1\sigma$ ,  $2\sigma$  and  $3\sigma$  confidence level. The data clearly agrees with the SSM predicted flux ( $\phi_{SSM}$ ) [17].

### Oscillation parameters

The neutrino oscillation has been extensively studied and many experiments contributed to retrieve its parameters. A summary of the squared-mass difference and mixing angles, as the region where the confidence level (C.L.) is 99%, is given in the table in Figure 1.7 by [8].

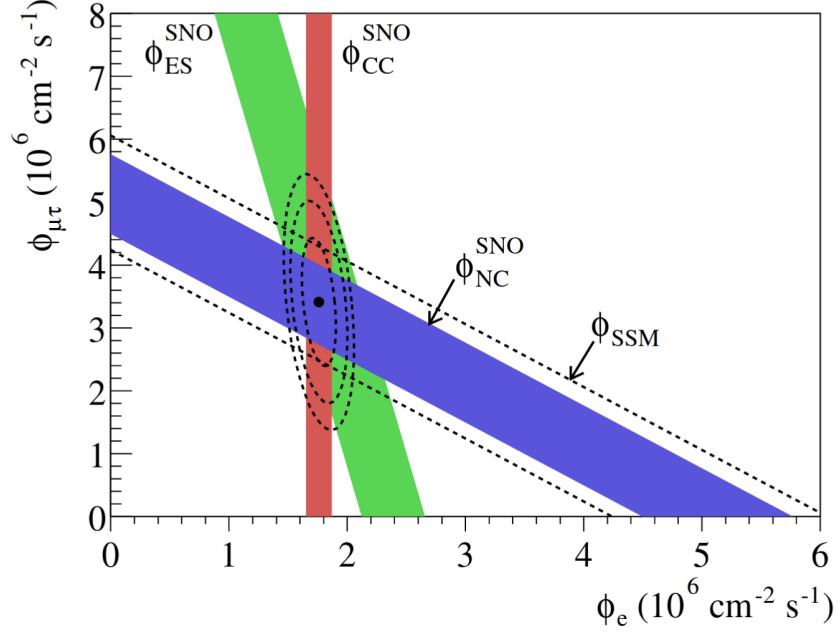


Figure 1.6: Flux of  $^8\text{B}$  solar neutrino for the SNO experiment measured via CC, NC and ES interactions ( $\phi_{CC}^{SNO}$ ,  $\phi_{NC}^{SNO}$  and  $\phi_{ES}^{SNO}$ ). The axes are the inferred fluxes of  $\nu_\mu + \nu_\tau$  versus  $\nu_e$ . The sensitive of NC and ES interactions give the slope of the fluxes bands. The CC measurement is sensitive only to  $\nu_e$ , so the slope is infinity. The intersection of three bands give the best estimation of  $\phi_{\mu,\tau}$  and  $\phi_e$ , with the  $1\sigma$ ,  $2\sigma$  and  $3\sigma$  confidence level expressed as dashed ellipses. The solar neutrino flux predicted by the SSM is indicated as  $\phi_{SSM}$  [17].

Oscillation parameter	central value	99% CL range
solar mass splitting	$\Delta m_{12}^2 = (7.58 \pm 0.21) 10^{-5} \text{ eV}^2$	$(7.1 \div 8.1) 10^{-5} \text{ eV}^2$
atmospheric mass splitting	$ \Delta m_{23}^2  = (2.40 \pm 0.15) 10^{-3} \text{ eV}^2$	$(2.1 \div 2.8) 10^{-3} \text{ eV}^2$
solar mixing angle	$\tan^2 \theta_{12} = 0.484 \pm 0.048$	$31^\circ < \theta_{12} < 39^\circ$
atmospheric mixing angle	$\sin^2 2\theta_{23} = 1.02 \pm 0.04$	$37^\circ < \theta_{23} < 53^\circ$
‘CHOOZ’ mixing angle	$\sin^2 2\theta_{13} = 0.07 \pm 0.04$	$0^\circ < \theta_{13} < 13^\circ$

Figure 1.7: Summary of neutrino masses and mixing from oscillation data [8].

## 1.2. Neutrino oscillation

Neutrino oscillation was considered already in 1967 by Pontecorvo [21], only 9 years after the first direct observation of neutrinos in 1956 by Cowan and Reines. However, only in the years 2000 the anomalies in different neutrino flavors were confirmed by the experiments KamLAND, (Super)Kamiokande and K2K [18, 19, 22]. To understand the results from this experiments and the physical goal of DUNE, it is important to understand the process of oscillation and explore its characteristics.

It happens that, the evidence of neutrino oscillation implies massive neutrinos and flavor-mixing in the leptonic charged current (CC). This means that muon, electron and

tau neutrinos ( $\nu_e$ ,  $\nu_\mu$  and  $\nu_\tau$ , respectively), which are the CC interaction eigenstates, can be expressed as a linear combination of the mass eigenstates  $\nu_1$ ,  $\nu_2$  and  $\nu_3$  (with masses  $m_1$ ,  $m_2$  and  $m_3$  respectively) in the form:

$$\begin{pmatrix} \nu_e \\ \nu_\mu \\ \nu_\tau \end{pmatrix} = \begin{pmatrix} U_{e,1} & U_{e,2} & U_{e,3} \\ U_{\mu,1} & U_{\mu,2} & U_{\mu,3} \\ U_{\tau,1} & U_{\tau,2} & U_{\tau,3} \end{pmatrix} \begin{pmatrix} \nu_1 \\ \nu_2 \\ \nu_3 \end{pmatrix}, \quad (1.6)$$

or in a more compact way:

$$|\nu_\alpha\rangle = \sum_{k=1}^3 U_{\alpha k}^* |\nu_k\rangle \quad (\alpha = e, \mu, \tau), \quad (1.7)$$

Where  $U_{\alpha k}$  is the Pontecorvo-Maki-Nakagawa-Sakata (PMNS) matrix.

Reminding that  $U$  must be unitary:

$$U^\dagger U = 1 \quad \Longleftrightarrow \quad \sum_{\alpha} U_{\alpha k}^* U_{\alpha j} = \delta_{kj}. \quad (1.8)$$

In this way, the massive neutrino states  $|\nu_k\rangle$  are eigenstates of the Hamiltonian  $\mathcal{H}$  in the form  $\mathcal{H}|\nu_k\rangle = E_k|\nu_k\rangle$  where  $E_k = \sqrt{p^2 + m_k^2}$  is the energy. With this, the Schrödinger equation will have the solution as:

$$i \frac{d}{dt} |\nu_k(t)\rangle = \mathcal{H} |\nu_k(t)\rangle \quad (1.9)$$

$$|\nu_k(t)\rangle = e^{-iE_k t} |\nu_k\rangle. \quad (1.10)$$

Which describes the time evolution of the massive states. By using Eq. 1.7 one can retrieve the time evolution of a neutrino with flavor state  $\alpha$  created at  $t = 0$  as:

$$|\nu_\alpha(t)\rangle = \sum_k U_{\alpha k}^* e^{-iE_k t} |\nu_k\rangle. \quad (1.11)$$

Equation 1.11 already gives the principle of neutrino oscillation, it described how the linear combination of the mass eigenstates changes in time for a flavor  $\alpha$  neutrino. One can calculate the transition probability of an  $\alpha$  neutrino to a  $\beta$  neutrino, that is, what is the probability of finding the original  $\nu_\alpha$  as  $\nu_\beta$  at any given time. This can be achieved by writing the state  $\nu_\alpha$  as function of  $\nu_\beta$ . We can invert Eq. 1.7 performing:

$$\left[ \sum_{\alpha} U_{\alpha j} \right] |\nu_\alpha\rangle = \sum_{\alpha} \sum_k U_{\alpha j} U_{\alpha k}^* |\nu_k\rangle \quad \Rightarrow \quad \sum_{\alpha} U_{\alpha j} |\nu_\alpha\rangle = \sum_k \left( \sum_{\alpha} U_{\alpha j}^* U_{\alpha k} \right)^* |\nu_k\rangle,$$

where, using Eq. 1.8 and inverting the sides of the equality, leads to:

$$|\nu_k\rangle = \sum_{\alpha=e,\mu,\tau} U_{\alpha k} |\nu_\alpha\rangle,$$

or, as we are going to use,

$$|\nu_k\rangle = \sum_{\beta=e,\mu,\tau} U_{\beta k} |\nu_\beta\rangle. \quad (1.12)$$

Substituting Eq. 1.12 back to Eq. 1.11 we have:

$$|\nu_\alpha(t)\rangle = \sum_{\beta=e,\mu,\tau} \left( \sum_k U_{\alpha k}^* e^{-iE_k t} U_{\beta k} \right) |\nu_\beta\rangle. \quad (1.13)$$

One can notice that at  $t = 0$  the sum inside the parenthesis becomes simply the unitary property of Eq. 1.8. For  $t > 0$ , the neutrino becomes a superposition of all the three different flavors, but only if the mixing matrix is not diagonal<sup>5</sup>.

Therefore, the amplitude of the transition between  $\nu_\alpha$  to  $\nu_\beta$  as function of time ( $A_{\nu_\alpha \rightarrow \nu_\beta}(t)$ ) is defined as

$$A_{\nu_\alpha \rightarrow \nu_\beta}(t) \equiv \langle \nu_\beta | \nu_\alpha(t) \rangle = \sum_k U_{\alpha k}^* U_{\beta k} e^{-iE_k t}. \quad (1.14)$$

And the transition probability is defined as:

$$P_{\nu_\alpha \rightarrow \nu_\beta}(t) \equiv |A_{\nu_\alpha \rightarrow \nu_\beta}(t)|^2 = \sum_{k,j} U_{\alpha k}^* U_{\beta k} U_{\alpha j} U_{\beta j}^* e^{-i(E_k - E_j)t}. \quad (1.15)$$

To move further in any analysis, one should take here the assumption that the neutrinos are ultra-relativistic. Giving that the masses are expected to be lighter than about 0.2 eV [8], this is a good approximation from an experimental point of view. In this case, the limit can be taken as:

$$E_k = \sqrt{p^2 + m_k^2} = p \left( 1 + \frac{m_k^2}{p^2} \right)^{1/2} \xrightarrow{p \gg m} E \left( 1 + \frac{m_k^2}{2E^2} \right), \quad (1.16)$$

which allow us to use,

$$E_k - E_j \simeq \frac{\Delta m_{kj}^2}{2E}, \quad (1.17)$$

where

$$\Delta m_{kj}^2 = m_k^2 - m_j^2 \quad (1.18)$$

is the squared-mass difference.

One can notice that  $p = p_k = p_j$  was assumed to retrieve Eq. 1.17. As a matter of fact, the proper treatment would consist in considering the neutrinos as wave-packets, allowing massive neutrinos to have different velocities and, therefore, being able to reach an observer with different times. This effect has interesting implications from the theoretical point of

---

<sup>5</sup>To see this, one can choose the electronic flavor and open the terms of the sum, for instance. The only term that will not vanish is  $U_{e1}^* e^{-iE_1 t} U_{e1}$ , which no longer mixes the flavors.

view which will not be explored in this thesis. However the result of Eq. 1.17 still holds when using the wave-packet treatment [20, 23].

Finally, we take into account that neutrino oscillation experiments do not measure the time of flight but rather the distance  $L$  traveled by the neutrino. For ultra-relativistic neutrinos we have  $L \approx t$  ( $c = 1$ , natural units) and the probability of transition as function of distance and energy becomes:

$$P_{\nu_\alpha \rightarrow \nu_\beta}(L, E) = \sum_{k,j} U_{\alpha k}^* U_{\beta k} U_{\alpha j} U_{\beta j}^* \exp\left(-i \frac{\Delta m_{kj}^2 L}{2E}\right). \quad (1.19)$$

We will come back to this equation later, let's first introduce the two-neutrinos mixing and understand better the processes in this specific case. Since in the end it will be shown that the experiments are usually sensitive to the oscillation between two of the three neutrinos flavor, this approach results to be pretty realistic. This simplification of the problem makes the experimental results and discussions much easier to be understood.

### 1.2.1. Two neutrino mixing

Assume only 2 massive neutrinos are coupled with the flavor eigenstates. In this case we can only have two flavor neutrinos oscillating from one to another. Let's consider  $\alpha$  and  $\beta$  as the flavors of the neutrinos which are a linear superposition of the mass eigenstates  $\nu_1$  and  $\nu_2$ :

$$\begin{pmatrix} \nu_\alpha \\ \nu_\beta \end{pmatrix} = \begin{pmatrix} \cos\theta & \sin\theta \\ -\sin\theta & \cos\theta \end{pmatrix} \begin{pmatrix} \nu_1 \\ \nu_2 \end{pmatrix}, \quad (1.20)$$

where  $0 \leq \theta \leq \pi/2$  is the mixing angle.  $U^\dagger U = 1$  is satisfied. Let's assume that  $\nu_1$  is the lightest massive neutrino and the squared-mass difference will be positive as:

$$\Delta m^2 \equiv \Delta m_{21}^2 \equiv m_2^2 - m_1^2. \quad (1.21)$$

Now, from Eq. 1.19, follows that

$$\begin{aligned} P_{\nu_\alpha \rightarrow \nu_\beta}(L, E) = & U_{\alpha 1}^* U_{\beta 1} U_{\alpha 1} U_{\beta 1}^* \exp\left(-i \frac{\Delta m_{11}^2 L}{2E}\right) + U_{\alpha 2}^* U_{\beta 2} U_{\alpha 1} U_{\beta 1}^* \exp\left(-i \frac{\Delta m_{21}^2 L}{2E}\right) \\ & + U_{\alpha 1}^* U_{\beta 1} U_{\alpha 2} U_{\beta 2}^* \exp\left(+i \frac{\Delta m_{21}^2 L}{2E}\right) + U_{\alpha 2}^* U_{\beta 2} U_{\alpha 2} U_{\beta 2}^* \exp\left(+i \frac{\Delta m_{22}^2 L}{2E}\right). \end{aligned} \quad (1.22)$$

Which, using the fact that  $U_{ij} = U_{ij}^*$  and the fact that  $e^{i\phi} + e^{-i\phi} = 2\cos\phi$ , can be compressed as:

$$P_{\nu_\alpha \rightarrow \nu_\beta}(L, E) = |U_{\alpha 1}|^2 |U_{\beta 1}|^2 |U_{\alpha 2}|^2 |U_{\beta 2}|^2 + 2U_{\alpha 1} U_{\alpha 2} U_{\beta 1} U_{\beta 2} \cos\left(\frac{\Delta m^2 L}{2E}\right). \quad (1.23)$$

From here, we can explore the transition ( $\nu_\alpha \rightarrow \nu_\beta$ ) or the survival probability ( $\nu_\alpha \rightarrow \nu_\alpha$ ). Using the matrix from Eq. 1.20 the equation above becomes

$$P_{\nu_\alpha \rightarrow \nu_\beta}(L, E) = 2\cos^2\theta \sin^2\theta \left(1 - \cos\left(\frac{\Delta m^2 L}{2E}\right)\right), \quad (1.24)$$

which, using the trigonometrical properties  $\sin 2\phi = 2\cos\phi \sin\phi$  and  $\cos 2\phi = 1 - \sin^2\phi$ , gives the transition probability:

$$P_{\nu_\alpha \rightarrow \nu_\beta}(L, E) = \sin^2 2\theta \sin^2\left(\frac{\Delta m^2 L}{4E}\right) \quad (1.25)$$

or, in another common form,

$$P_{\nu_\alpha \rightarrow \nu_\beta}(L, E) = \frac{1}{2} \sin^2 2\theta \left[1 - \cos\left(\frac{\Delta m^2 L}{2E}\right)\right]. \quad (1.26)$$

The easiest way to retrieve the survival probabilities is using the fact that one of the two cases,  $\nu_\alpha \rightarrow \nu_\beta$  or  $\nu_\alpha \rightarrow \nu_\alpha$  should always occur, resulting in:

$$P_{\nu_\alpha \rightarrow \nu_\alpha}(L, E) = 1 - P_{\nu_\alpha \rightarrow \nu_\beta}(L, E) = 1 - \sin^2 2\theta \sin^2\left(\frac{\Delta m^2 L}{4E}\right), \quad (1.27)$$

which is the survival probability.

### Averaged probability

Experiments that evaluate the transition probability (Eq. 1.25) between different neutrinos flavors are called *Appearance experiments*. For this experiments, if the final neutrino state is not present in the source, the background is reduced. Differently, the ones that measure the survival probability given by Eq. 1.27 are called *Disappearance experiments*. The choice between the two type of experiments is given by the sensitivity of the detector (threshold of interactions, flavor distinguishing, uncertainties, etc.) and the values of mixing angles.

There are two factors that must be taken into consideration: experiments have different ranges of energy and distance and measurements have uncertainties in energy and distance. As a consequence of this, neutrino experiments measure an average oscillation probability.

As a starting point, it is more convenient to write Equations 1.25 and 1.27 with units in agreement with the experiment ranges of energy and distance. Experiments such as nuclear reactors will usually operate in the MeV and meters range, while Long baselines experiments (LBL) such as DUNE will operate in the GeV and kilometers range, for instance. Lets take the case of DUNE, with  $\Delta m^2$  in  $\text{eV}^2$ ,  $E$  in GeV and  $L$  in km, we can rewrite the term inside the sine of Eq. 1.25 as:

$$\begin{aligned} \frac{\Delta m^2 L}{4E} &= \left(\frac{1}{4}\right) \frac{(\Delta m^2/\text{eV}^2)(L/\text{km})}{E/\text{GeV}} \left\{ \frac{\text{eV}^2 \text{ km}}{\text{GeV}} \right\} = \frac{1}{4} \frac{\Delta m^2[\text{eV}^2] L[\text{km}]}{E[\text{GeV}]} \left\{ \frac{10^3}{10^9} \cdot \text{eV m} \right\} \\ &= \frac{1}{4} \frac{\Delta m^2[\text{eV}^2] L[\text{km}]}{E[\text{GeV}]} \left\{ 10^{-6} \cdot \frac{1}{1.97327 \times 10^{-7}} \right\} \approx 1.27 \frac{\Delta m^2[\text{eV}^2] L[\text{km}]}{E[\text{GeV}]}, \end{aligned} \quad (1.28)$$

where  $E[\text{GeV}]$  means that the energy is expressed in GeV and natural units were used. Exactly the same procedure can be used for  $L[\text{m}]$  and  $E[\text{eV}]$ , which gives a more convenient way to write Eq. 1.25 as:

$$P_{\nu_\alpha \rightarrow \nu_\beta}(L, E) = \sin^2 2\theta \sin^2 \left( 1.27 \frac{\Delta m^2[\text{eV}^2] L[\text{m}]}{E[\text{eV}]} \right) \quad (1.29)$$

$$= \sin^2 2\theta \sin^2 \left( 1.27 \frac{\Delta m^2[\text{eV}^2] L[\text{km}]}{E[\text{GeV}]} \right). \quad (1.30)$$

For the averaged probability, the simplest case is to consider that the measurement  $L/E$  follows a Gaussian distribution, with average value  $\langle L/E \rangle$  and standard deviation  $\sigma_{L/E}$  as

$$\phi\left(\frac{L}{E}\right) = \frac{1}{\sqrt{2\pi\sigma_{L/E}^2}} \exp\left[-\frac{(L/E - \langle L/E \rangle)^2}{2\sigma_{L/E}^2}\right]. \quad (1.31)$$

In this case, the transition probability must be averaged in terms of the cosine for Eq. 1.26 (or sine for Eq. 1.25) as

$$\left\langle P_{\nu_\alpha \rightarrow \nu_\beta}(L, E) \right\rangle = \frac{1}{2} \sin^2 2\theta \left[ 1 - \left\langle \cos\left(\frac{\Delta m^2 L}{2E}\right) \right\rangle \right], \quad (1.32)$$

where

$$\left\langle \cos\left(\frac{\Delta m^2 L}{2E}\right) \right\rangle = I = \int \cos\left(\frac{\Delta m^2 L}{2E}\right) \phi\left(\frac{L}{E}\right) d\frac{L}{E}. \quad (1.33)$$

To solve the integral  $I$  of Eq. 1.33, one can rewrite the cosine as sum of exponentials and use Eq. 1.31 as the probability density. After simplifications, we obtain:

$$I = \frac{1}{\sqrt{2\pi\sigma^2}} \int \cos(\alpha x) e^{-\frac{(x-\mu)^2}{2\sigma^2}} dx = \frac{1}{2\sqrt{2\pi\sigma^2}} \left( \int e^{i\alpha x} e^{-\frac{(x-\mu)^2}{2\sigma^2}} dx + \int e^{-i\alpha x} e^{-\frac{(x-\mu)^2}{2\sigma^2}} dx \right), \quad (1.34)$$

which using the substitution  $x - \mu = \sigma\sqrt{2}u$  becomes

$$I = \frac{\sqrt{2}\sigma}{2\sqrt{2\pi\sigma^2}} \left[ e^{i\alpha\mu} \int e^{i\alpha\sigma\sqrt{2}u} e^{-u^2} du + e^{-i\alpha\mu} \int e^{-i\alpha\sigma\sqrt{2}u} e^{-u^2} du \right]. \quad (1.35)$$

Noticing that

$$-(u^2 - i\alpha\sigma\sqrt{2}u) = -\left(u - i\alpha\frac{\sqrt{2}\sigma}{2}\right)^2 - \frac{\alpha^2\sigma^2}{2}$$

we can rewrite the integral as:

$$I = \frac{1}{2\sqrt{\pi}} e^{-\frac{\alpha^2\sigma^2}{2}} \left[ e^{i\alpha\mu} \int_{-\infty}^{\infty} e^{-(u - i\alpha\sqrt{2}\sigma/2)^2} du + e^{-i\alpha\mu} \int_{-\infty}^{\infty} e^{-(u + i\alpha\sqrt{2}\sigma/2)^2} du \right]. \quad (1.36)$$

Using the result

$$I' = \int_{-\infty}^{\infty} e^{-(x \pm ib)^2} dx = \sqrt{\pi} \quad (1.37)$$

it follows that

$$I = \frac{1}{2} e^{-\frac{\alpha^2\sigma^2}{2}} \left[ e^{i\alpha\mu} + e^{-i\alpha\mu} \right] = e^{-\frac{1}{2}(\alpha\sigma)^2} \cos(\alpha\mu) \quad (1.38)$$

and we finally obtain the average over the cosine function of Eq. 1.33:

$$\left\langle \cos\left(\frac{\Delta m^2 L}{2E}\right) \right\rangle = \exp\left(-\frac{1}{2}\left(\frac{\Delta m^2}{2}\sigma_{L/E}\right)^2\right) \cos\left(\frac{\Delta m^2}{2}\left\langle\frac{L}{E}\right\rangle\right). \quad (1.39)$$

We then have the averaged transition probability as:

$$\left\langle P_{\nu_\alpha \rightarrow \nu_\beta}(L, E) \right\rangle = \frac{1}{2} \sin^2 2\theta \left[ 1 - \exp\left(-\frac{1}{2}\left(\frac{\Delta m^2}{2}\sigma_{L/E}\right)^2\right) \cos\left(\frac{\Delta m^2}{2}\left\langle\frac{L}{E}\right\rangle\right) \right]. \quad (1.40)$$

It is reasonable to assume an uncertainty  $\sigma_{L/E}$  proportional to  $\langle L/E \rangle$  [23], and since the uncertainties of L and E are independent, the uncertainty of the ratio is:

$$\left(\frac{\sigma_{L/E}}{\langle L/E \rangle}\right)^2 = \left(\frac{\sigma_L}{\langle L \rangle}\right)^2 + \left(\frac{\sigma_E}{\langle E \rangle}\right)^2, \quad (1.41)$$

where  $\langle L \rangle$  and  $\sigma_L$  are the average distance and the distance uncertainty and  $\langle E \rangle$  and  $\sigma_E$  are the average energy and energy uncertainty, respectively.

There are, of course, different uncertainties for different ranges of energies and distances. In particular, minimum ionizing particles will have a better defined energy, while low or high energy particles will be more tricky to have their energy reconstructed. However, as a first order approximation, one can assume that both, energy and distances, have uncertainties proportional to their values. It is worth considering the case of  $\sigma_{L/E} = 0.2 \langle L/E \rangle$  [23], as an illustrative one.

Figure 1.8 shows the averaged and unaveraged (solid and dashed lines) transition probability from  $\nu_\alpha$  to  $\nu_\beta$  as function of  $\langle L/E \rangle [\text{km/GeV}] \Delta m^2 [\text{eV}^2]$  with  $\sin^2 2\theta = 1$  and  $\sigma_{L/E} = 0.2 \langle L/E \rangle$ , using Eq. 1.40 and 1.26 respectively.

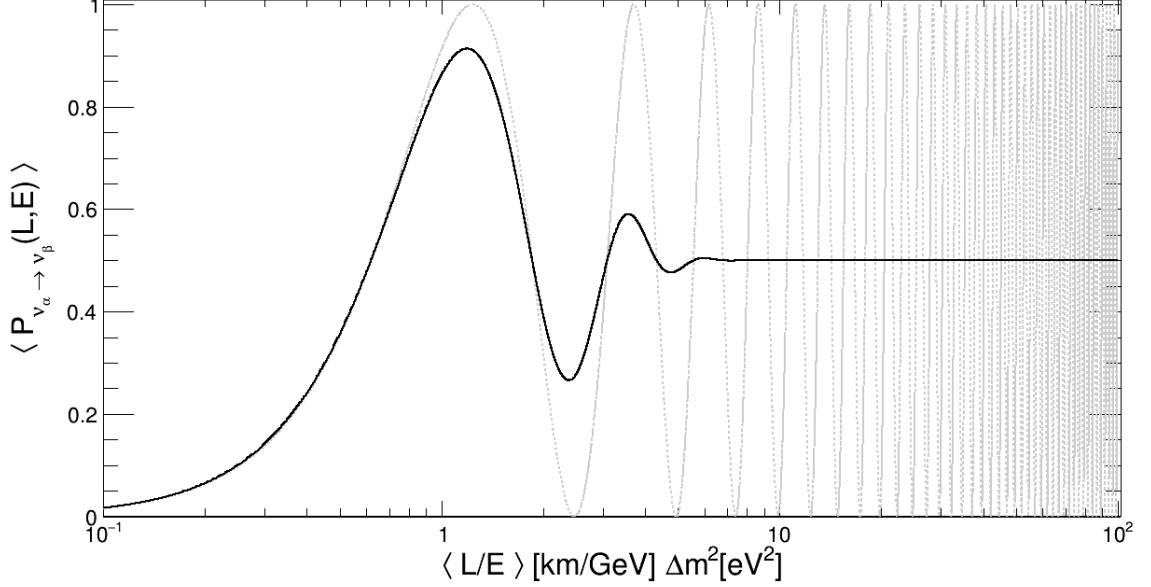


Figure 1.8: Transition probability of  $\nu_\alpha \rightarrow \nu_\beta$  for  $\sin^2 2\theta = 1$  as function of  $\langle L/E \rangle [\text{km/GeV}] \Delta m^2 [\text{eV}^2]$ . The solid line is the averaged transition from Eq. 1.40 with  $\sigma_{L/E} = 0.2 \langle L/E \rangle$  and the dashed line comes from Eq. 1.26 without any averaging.

This result implies that experiments will have a range of sensitivity to neutrino oscillation, making it necessary to match the distance and energy to the squared-mass difference. Experiments will usually have a fixed energy with variable distance or vice-versa. Matching the ratio  $L/E$  of the experiment is the so called *sensitivity* to  $\Delta m^2$  of an experiment [23]. The result from Fig. 1.8 indicates the best matching will happen when

$$\frac{\Delta m^2 L}{E} \sim 1 \quad (1.42)$$

is satisfied. If  $\frac{\Delta m^2 L}{E} \ll 1$  the oscillation probability is very small and the transition between flavors cannot be easily measured, if  $\frac{\Delta m^2 L}{E} \gg 1$ , only information about  $\sin^2 2\theta$  can be retrieved.

The reason why the two-flavor mixing formalism is a good-enough approximation for the three-flavor one relies on the fact that the square mass-differences are very distant from each other, making the frequency of oscillation too apart. As consequence, if an experiment satisfies the condition 1.42 for a given  $\Delta m^2$ , it will not satisfy for the other and the oscillation is either negligible or have average equal to zero. In the next section, this result will be shown for the DUNE, emphasizing the similarity of the two methods hoping to convince the reader.

## Type of experiments

Regarding the sensitivity condition of Eq. 1.42 one can check the sensitivity of few experiments in order to understand better the implications of these results. A summary of the different types of experiments and sensitivities is given in [13, 23]. A **Short baseline experiment (SBL)** has a nuclear reactors or accelerators as source of neutrinos. The reactor experiments will be constrained by the energy  $E \sim 1$  MeV of antineutrinos from beta decays and need to have a distance  $L \sim 10$  m, to be sensitive to  $\Delta m^2 \sim 0.1$  eV<sup>2</sup>. In this case, the antineutrino's energy is too low to produce muons or taus, making it only possible to measure the survival probability of  $\bar{\nu}_e$ . Accelerator experiments, on the other hand, have different energy ranges depending on the type of neutrino production and must be built to match the distance. The sensitivity here goes from 1 to 100 eV<sup>2</sup> [23].

For instance, The PROSPECT detector is placed 7 - 9 meters from the reactor, with a sensitivity of  $\Delta m^2 \sim 1$  eV<sup>2</sup> [13]. The SBND [24] experiment will use a beam with energy around 1 GeV and a baseline 0.1 km, which gives a sensitivity around  $\Delta m^2 \sim 0.1$  eV<sup>2</sup>. This experiments search for oscillations evidence with models beyond 3 neutrinos oscillation, such as sterile neutrinos.

The **Long baseline experiments (LBL)** operate with much greater distance from the source, about 1 km away in the case of reactors and 100 to 1000 km away for beam experiments. LBL reactor and beam experiments are sensitive to  $\Delta m^2 \gtrsim 10^{-3}$  eV<sup>2</sup>, because of their range of energy ( $L/E \lesssim 10^3$  m/MeV for reactors and  $L/E \lesssim 10^3$  km/GeV for beam experiments). Examples of reactor and beam experiments are Double CHOOZ and ICARUS [23, 25], respectively. The experiments are sensitive to the so-called atmospheric mass splitting (see Fig. 1.7).

Experiments with a source-detector distance larger by one or two orders of magnitude than LBL are called **Very Long-Baseline experiments (VLB)**. Here the mass difference sensitivity will be around  $\Delta m^2 \gtrsim 10^{-5}$  eV<sup>2</sup> for reactors, which have a distance on the order of 100 km from the source. Neutrino beam experiments, on the other hand, will have a sensitivity of  $\Delta m^2 \gtrsim 10^{-4}$  eV<sup>2</sup> and a distance of several thousands of km. At this same range, **Atmospheric neutrino experiments (ATM)** are able to take measurements. They measure the flux of atmospheric neutrinos<sup>6</sup>, which have a wide range of energy (from 500 MeV to

---

<sup>6</sup>Cosmic rays interaction in the upper atmosphere generate pions and kaons that will decay into muons. This negative (or positive) muons may decay in flight into electron (positron), muon neutrino (antineutrino) and electron antineutrino (neutrino). These neutrinos are called atmospheric neutrinos.

100 GeV), in two different ranges: around 20 km for neutrinos coming from above and about  $1.3 \times 10^4$  km for neutrinos crossing the Earth.

The KamLAND experiment [18], for instance, has the detector  $\sim 180$  km away from the reactor and energy between 1 to 10 eV. This gives a sensitivity from  $\sim 2 \times 10^{-5}$  to  $2 \times 10^{-4}$  eV<sup>2</sup>. The DUNE experiment have its optimum energy around 0.5 to 4 GeV and it the far detector is 1300 km away from the near detector [2, 7], giving a sensitivity of  $\Delta m^2 \sim 10^{-4}$  eV<sup>2</sup>. The Super Kamiokande [22] is one example of ATM experiment.

Finally, there are the **Solar neutrino experiments (Sol)**, where the distance of  $1.5 \times 10^{11}$  m between the Sun and the Earth is used. The thermonuclear reactions in the core of the Sun can only produce neutrinos with energy between 0.5 to 14 MeV [26], giving a sensitivity around  $\Delta m^2 \sim 10^{-12}$  eV<sup>2</sup>. The so-called solar mass splitting come to the fact that experiments had measured a deficit in the electronic neutrinos flux coming from the Sun, which was later confirmed by SNO experiment [17] detecting solar neutrinos and also by KamLAND with reactor ones.

A summary of the different neutrino oscillation experiments is given in Table 1.1, with their respective distance, energy and  $\Delta m^2$  sensitivity.

Table 1.1: Summary of experiments types and sensitivities.

Type of experiment	L	E	$\Delta m^2$ sensitivity	Example
Reactor SBL	$\sim 10$ m	$\sim 1$ MeV	$\sim 0.1$ eV <sup>2</sup>	PROSPECT
Accelerator SBL	$\sim 10$ m to 1 km	$\sim 0.01$ to $10^2$ GeV	$\sim 1$ to $10^2$ eV <sup>2</sup>	SBND
Reactor LBL	$\sim 1$ km	$\sim 1$ MeV	$\sim 10^{-3}$ eV <sup>2</sup>	Double CHOOZ
Accelerator LBL	$\sim 10^3$ km	$\gtrsim 1$ GeV	$\gtrsim 10^{-3}$ eV <sup>2</sup>	ICARUS
Reactor VLB	$\sim 10^2$ km	$\sim 1$ MeV	$\gtrsim 10^{-5}$ eV <sup>2</sup>	KamLAND
Accelerator VLB	$\sim 10^4$ km	$\gtrsim 1$ GeV	$\gtrsim 10^4$ eV <sup>2</sup>	DUNE
ATM	20 to $10^4$ km	0.5 to $10^2$ GeV	$\sim 10^{-4}$ eV <sup>2</sup>	(Super)Kamiokande
Sol	$\sim 10^{11}$ km	0.2 to $15^2$ MeV	$\sim 10^{-12}$ eV <sup>2</sup>	SNO

Although this is the two flavors approach, the measurements in the three flavors formalism will be driven by massive neutrinos combination that matches the requirement of Eq. 1.42. Therefore, the mixing angle in the matrix of Eq. 1.20 represents one the three mixing angles  $\theta_{12}$ ,  $\theta_{13}$  or  $\theta_{23}$  that will be described at Sec. 1.2.2.

It is worth to present how experiments usually show their sensitivities. If an experiment does not measure any oscillation, the data suggest that the transition between flavors might be too small to be detected. In this case, the averaged transition probability must be below

an upper limit determined by the experiment  $(P_{\nu_\alpha \rightarrow \nu_\beta}^{\max})$ . This means that [23]:

$$\langle P_{\nu_\alpha \rightarrow \nu_\beta}(L, E) \rangle \leq P_{\nu_\alpha \rightarrow \nu_\beta}^{\max}, \quad (1.43)$$

which, using Eq. 1.32, leads to a limitation in  $\sin^2(2\theta)$  and  $\Delta m^2$  as

$$\sin^2(2\theta) \leq \frac{2P_{\nu_\alpha \rightarrow \nu_\beta}^{\max}}{1 - \langle \cos\left(\frac{\Delta m^2 L}{2E}\right) \rangle}. \quad (1.44)$$

Figure 1.9a shows the allowed region from Eq. 1.44 not averaged (gray dashed lines) and averaged (black solid line) cosine term. The maximum probability was set to 0.1 and uncertainty used was  $\sigma_{L/E} = 0.2 \langle L/E \rangle$ . If the experiment did not detect any oscillation, it means that  $\sin^2(2\theta)$  and  $\Delta m^2$  lie in below the curve. Therefore the left region above the curve is then called excluded area. In the other hand, when the experiment actually detects oscillation, the same graph can be generated, but the excluded region will be on the opposite side of the curve, constraining the possible values of  $\sin^2(2\theta)$  and  $\Delta m^2$ .

Data results will be usually presented by inverting the axis as shown in Fig. 1.9b, only as a matter of preference. In the results from KamLAND [18] or K2K [19], for instance, a graph similar to Fig. 1.9b can be found but with a fixed  $\langle L/E \rangle$  value, giving limits to the square mass-difference value instead.

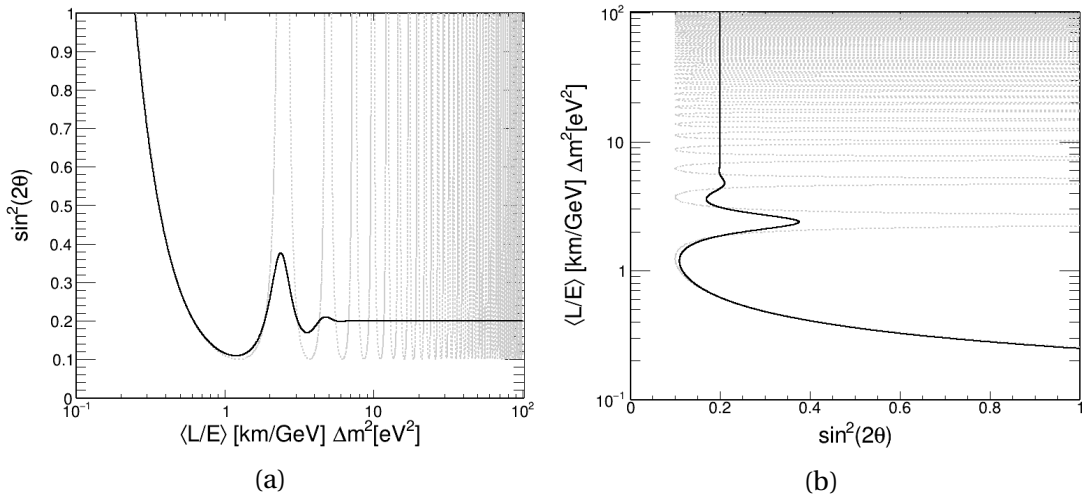


Figure 1.9: **(a)** Limit between  $\sin^2(2\theta)$  and  $\langle L/E \rangle [\text{GeV/km}] \Delta m^2 [\text{eV}^2]$  given by Eq. 1.44 with  $P_{\nu_\alpha \rightarrow \nu_\beta}^{\max} = 0.1$ . The black solid line is the evaluation with average given by Eq. 1.39 with  $\sigma_{L/E} = 0.2 \langle L/E \rangle$  and the gray dashed line is without any average. **(b)** Inverting the axis as experiments will usually present their data.

The results presented in this section give the overview of oscillation experiments. Using this approximations one can understand where is the sensitivity and what are the results of

the experiment. We can now come back to three flavors formalism and understand a little better the oscillations.

### 1.2.2. Three neutrinos mixing

One can represent the Pontecorvo-Maki-Nakagawa-Sakata (PMNS) matrix of Eq. 1.6 by the mixing angles in the same way done for Eq. 1.20. The PMNS mixing matrix  $U$  is a 3 by 3 complex matrix that has 18 degrees of freedom. However, the unitary condition (Eq. 1.8) decreases it to 9, which can be expressed by 3 real angles and 6 complex phases<sup>7</sup>. One global phase can be absorbed and other 4 can be absorbed due to the invariance over global phases between the leptons and massive neutrinos (two for muons and taus and other two for  $\nu_2$  and  $\nu_3$ , for example) [20]. In this case, the PMNS matrix can be parameterized as:

$$U = \begin{pmatrix} 1 & 0 & 0 \\ 0 & \cos\theta_{23} & \sin\theta_{23} \\ 0 & -\sin\theta_{23} & \cos\theta_{23} \end{pmatrix} \begin{pmatrix} \cos\theta_{13} & 0 & \sin\theta_{13}e^{-i\delta} \\ 0 & 1 & 0 \\ -\sin\theta_{13}e^{i\delta} & 0 & \cos\theta_{13} \end{pmatrix} \begin{pmatrix} \cos\theta_{12} & \sin\theta_{12} & 0 \\ -\sin\theta_{12} & \cos\theta_{12} & 0 \\ 0 & 0 & 1 \end{pmatrix}. \quad (1.45)$$

In order to be able to retrieve the individual elements, the expression can be rewritten using the definition  $c_{ij} \equiv \cos\theta_{ij}$  and  $s_{ij} \equiv \sin\theta_{ij}$ :

$$U_{PMNS} = \begin{pmatrix} U_{e,1} & U_{e,2} & U_{e,3} \\ U_{\mu,1} & U_{\mu,2} & U_{\mu,3} \\ U_{\tau,1} & U_{\tau,2} & U_{\tau,3} \end{pmatrix} = \begin{pmatrix} c_{12}c_{13} & s_{12}c_{13} & s_{13}e^{-i\delta} \\ -s_{12}c_{23} - c_{12}s_{23}s_{13}e^{i\delta} & c_{12}c_{23} - s_{12}s_{23}s_{13}e^{i\delta} & s_{23}c_{13} \\ s_{12}s_{23} - c_{12}c_{23}s_{13}e^{i\delta} & -c_{12}s_{23} - s_{12}c_{23}s_{13}e^{i\delta} & c_{23}c_{13} \end{pmatrix}. \quad (1.46)$$

All the results and plots for experiments will be in terms of sines and cosines of the mixing angles. However, it is healthier to keep developing the probabilities in terms of the generic form of Eq. 1.19 than with the (very) complex form presented above. Getting back to Eq. 1.19, one can separate the sum into three parts, when  $k = j$ ,  $k > j$  and  $k < j$ :

$$P_{\nu_\alpha \rightarrow \nu_\beta}(L, E) = \sum_k |U_{\alpha k}|^2 |U_{\beta k}|^2 + \sum_{k>j,j} U_{\alpha k}^* U_{\beta k} U_{\alpha j} U_{\beta j}^* \exp\left(-i \frac{\Delta m_{kj}^2 L}{2E}\right) + \sum_{k<j,j} U_{\alpha k}^* U_{\beta k} U_{\alpha j} U_{\beta j}^* \exp\left(-i \frac{\Delta m_{kj}^2 L}{2E}\right). \quad (1.47)$$

One should notice that for any of the two cases ( $k>j$  or  $k<j$ ) it is true that  $\Delta m_{kj}^2 = -\Delta m_{jk}^2$  (Eq. 1.18) and that  $U_{\alpha k}^* U_{\beta k} U_{\alpha j} U_{\beta j}^* = [U_{\alpha j}^* U_{\beta j} U_{\alpha k} U_{\beta k}^*]^*$ . This makes clear that one can switch

<sup>7</sup>This is easily understood if you assume the matrix is real, in which case it can be parameterized by the rotating matrix of Eq. 1.45 (without the phase)

the indexes  $j$  and  $k$  in the last term, summing up for  $j > k$ , in Eq. 1.47 and use the properties just mentioned to obtain:

$$P_{\nu_\alpha \rightarrow \nu_\beta}(L, E) = \sum_k |U_{\alpha k}|^2 |U_{\beta k}|^2 + \sum_{k > j, j} U_{\alpha k}^* U_{\beta k} U_{\alpha j} U_{\beta j}^* \exp\left(-i \frac{\Delta m_{kj}^2 L}{2E}\right) + \sum_{k > j, j} \left[ U_{\alpha k}^* U_{\beta k} U_{\alpha j} U_{\beta j}^* \exp\left(-i \frac{\Delta m_{kj}^2 L}{2E}\right) \right]^*,$$

which, using the definition of  $\text{Re}\{Z\} = (Z + Z^*)/2$ , can be rewritten as

$$P_{\nu_\alpha \rightarrow \nu_\beta}(L, E) = \sum_k |U_{\alpha k}|^2 |U_{\beta k}|^2 + 2 \text{Re} \sum_{k > j, j} U_{\alpha k}^* U_{\beta k} U_{\alpha j} U_{\beta j}^* \exp\left(-i \frac{\Delta m_{kj}^2 L}{2E}\right). \quad (1.48)$$

Now, using  $P_{\nu_\alpha \rightarrow \nu_\beta}(L = 0, E) = \delta_{\alpha\beta}$ , which means that there is no oscillation at the source, the first term in the right-hand side of Eq. 1.48 can be written as:

$$\sum_k |U_{\alpha k}|^2 |U_{\beta k}|^2 = \delta_{\alpha\beta} - 2 \text{Re} \sum_{k > j, j} U_{\alpha k}^* U_{\beta k} U_{\alpha j} U_{\beta j}^*. \quad (1.49)$$

Substituting back in Eq. 1.48 we have<sup>8</sup>:

$$P_{\nu_\alpha \rightarrow \nu_\beta}(L, E) = \delta_{\alpha\beta} - 2 \sum_{k > j, j} \text{Re}\{U_{\alpha k}^* U_{\beta k} U_{\alpha j} U_{\beta j}^*\} \left[ 1 - \cos\left(\frac{\Delta m_{kj}^2 L}{2E}\right) \right] + 2 \sum_{k > j, j} \text{Im}\{U_{\alpha k}^* U_{\beta k} U_{\alpha j} U_{\beta j}^*\} \sin\left(\frac{\Delta m_{kj}^2 L}{2E}\right), \quad (1.50)$$

or in the form

$$P_{\nu_\alpha \rightarrow \nu_\beta}(L, E) = \delta_{\alpha\beta} - 4 \sum_{k > j, j} \text{Re}\{U_{\alpha k}^* U_{\beta k} U_{\alpha j} U_{\beta j}^*\} \sin^2\left(\frac{\Delta m_{kj}^2 L}{4E}\right) + 2 \sum_{k > j, j} \text{Im}\{U_{\alpha k}^* U_{\beta k} U_{\alpha j} U_{\beta j}^*\} \sin\left(\frac{\Delta m_{kj}^2 L}{2E}\right). \quad (1.51)$$

The transition probability, where  $\beta \neq \alpha$ , is straightforward in Eq. 1.50 with only the Kronecker delta vanishing. The survival probability, on the other hand, can be taken noticing that the product between the mixing matrix elements inside the real and imaginary parts is real in the case where  $\beta = \alpha$ , giving the form

$$P_{\nu_\alpha \rightarrow \nu_\alpha}(L, E) = 1 - 4 \sum_{k > j, j} |U_{\alpha k}|^2 |U_{\alpha j}|^2 \sin^2\left(\frac{\Delta m_{kj}^2 L}{4E}\right). \quad (1.52)$$

It is straightforward to retrieve the survival probability of Eq. 1.27 using the two mixing matrix (Eq. 1.20) in the equation above.

<sup>8</sup>Here we use the fact that  $e^{-ix} = \cos x - i \sin x$  and that  $\text{Re}\{iZ\} = -\text{Im}\{Z\}$ , because if  $Z = a + ib$ , then  $\text{Re}\{iZ\} = \text{Re}\{ia - b\} = -b$ . This means that  $\text{Re}\{Ze^{-ix}\} = \text{Re}\{Z\} \cos(x) + \text{Im}\{Z\} \sin(x)$ .

### CPT, CP and T violations

The oscillation for antineutrinos can be taken in the same way as for neutrinos, noticing that instead of the mixing from Eq. 1.7 we need to start from

$$|\bar{\nu}_\alpha\rangle = \sum_k U_{\alpha k} |\bar{\nu}_k\rangle \quad (\alpha = e, \mu, \tau). \quad (1.53)$$

for the antineutrinos. Without much effort, the transition probability can be found as

$$P_{\bar{\nu}_\alpha \rightarrow \bar{\nu}_\beta}(L, E) = \sum_{k,j} U_{\alpha k} U_{\beta k}^* U_{\alpha j}^* U_{\beta j} \exp\left(-i \frac{\Delta m_{kj}^2 L}{2E}\right). \quad (1.54)$$

Which is very similar to equation 1.19. Doing the same computations as for the neutrinos, the antineutrinos transition probability can be written as:

$$\begin{aligned} P_{\bar{\nu}_\alpha \rightarrow \bar{\nu}_\beta}(L, E) = & \delta_{\alpha\beta} - 4 \sum_{k>j,j} \text{Re}\{U_{\alpha k}^* U_{\beta k} U_{\alpha j} U_{\beta j}^*\} \sin^2\left(\frac{\Delta m_{kj}^2 L}{4E}\right) \\ & - 2 \sum_{k>j,j} \text{Im}\{U_{\alpha k}^* U_{\beta k} U_{\alpha j} U_{\beta j}^*\} \sin\left(\frac{\Delta m_{kj}^2 L}{2E}\right). \end{aligned} \quad (1.55)$$

One can immediately notice the similarity between Eq. 1.51 and 1.55 and the fact that they only differ by a negative sign in the imaginary part. This means that, if the mixing matrix from Eq. 1.6 have complex elements, the transition probability of neutrinos have a different amplitude than the antineutrinos one, i. e., neutrino oscillation violates charge and parity transformation (CP) by it self. The phase present in Eq. 1.45, if different than 0,  $\pi$  or  $2\pi$ , will be responsible for the CP violation, because of that it is usually named CP phase ( $\delta_{CP}$ ).

Particles and antiparticles are related by a Charge and Parity<sup>9</sup> (CP) transformation, the example in Figure 1.10 by Thomson [20] illustrates this relation very well. In (a) it shows a negative pion decaying into a right-handed (RH) muon and right-handed antineutrino. Performing a parity transformation the situation expressed in (b) is achieved with a left-handed (LH) antineutrino and muon. In this case, the weak-charged current matrix element is zero<sup>10</sup>. The same can be said of (c), where from (a) we performed only a charge transformation. The result is that the antiparticles will have helicity changed and the right-handed neutrino will cancel the weak current. In the end, transforming parity and charge (or charge and parity) the situation on (d) will give a non-zero current, as we have a left-handed neutrino and a left-handed anti-muon.

<sup>9</sup>The parity transformation is the spatial inversion only, this means  $x \rightarrow -x$ ,  $y \rightarrow -y$ ,  $z \rightarrow -z$  and  $t \rightarrow t$ .

<sup>10</sup>As described in [20] Chapter 6.4.2, ultra-relativistic particles, such as neutrinos, will have Chirality equivalent to Helicity. In this case, only left-handed particles and right-handed antiparticles will have a non-zero contribution in the weak-charged current.

This is called the CP symmetry and, in principle, the same transition amplitude for the process in situation (a) and (d) should be found. The CP violation in the neutrino sector could contribute to explain better the baryon-antibaryon asymmetry of the universe [2, 20]. The CP transformation can be represented by  $\nu_\alpha \xleftrightarrow{\hat{C}P} \bar{\nu}_\alpha$ .

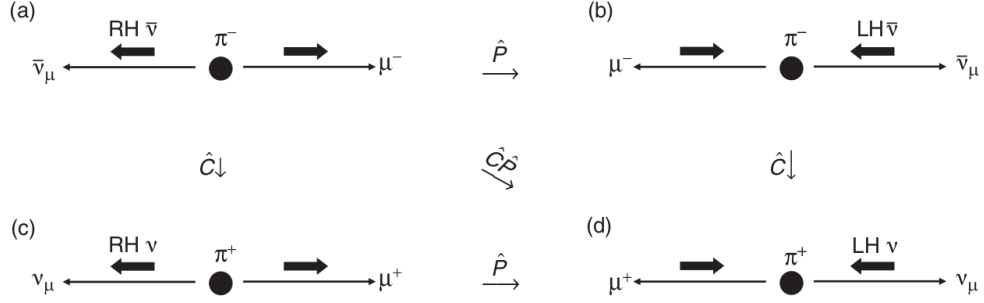


Figure 1.10: Pion decay (a), with the parity (b), charge (c) and CP (d) transformations, from [20].

The time transformation consists in looking the same event backwards, in this case a certain  $\nu_\alpha \rightarrow \nu_\beta$  transition will change through a time transformation as  $\nu_\alpha \rightarrow \nu_\beta \xleftrightarrow{\hat{T}} \nu_\beta \rightarrow \nu_\alpha$ . And finally, if you combine CP and T transformation you have the CPT transformation that can be written as  $\nu_\alpha \rightarrow \nu_\beta \xleftrightarrow{\hat{C}P\hat{T}} \bar{\nu}_\beta \rightarrow \bar{\nu}_\alpha$ . Figure 1.11 shows a simple scheme for all the three transformations for the transitions between two different neutrino's flavor.

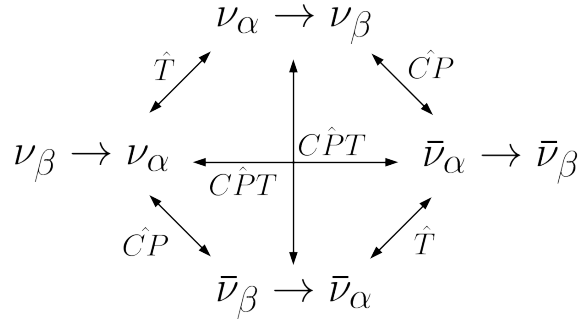


Figure 1.11: Schematic of CPT, CP and T transformations for neutrinos flavors transitions [23].

The asymmetry of any transformation can be evaluated by the difference in the transitions probabilities of the same event before and after transformations. Taking CPT as example, we have:

$$A_{\alpha\beta}^{\hat{C}P\hat{T}} = P_{\nu_\alpha \rightarrow \nu_\beta} - P_{\bar{\nu}_\beta \rightarrow \bar{\nu}_\alpha}. \quad (1.56)$$

And the same can be done for CP and T transformations following the schematic of Fig. 1.11.

We can now easily evaluate the transition probability of  $\bar{\nu}_\alpha \rightarrow \bar{\nu}_\beta$ , by simply changing the index of flavors in Eq. 1.54. This leads to

$$P_{\bar{\nu}_\beta \rightarrow \bar{\nu}_\beta}(L, E) = \sum_{k,j} U_{\beta k} U_{\alpha k}^* U_{\beta j}^* U_{\alpha j} \exp\left(-i \frac{\Delta m_{kj}^2 L}{2E}\right), \quad (1.57)$$

which is precisely the same as Eq. 1.19. This means that, in principle, there is no CPT violation in neutrinos oscillation.

The CP asymmetry, on the other hand, can be obtained by comparing Eq. 1.51 and Eq. 1.55. More precisely

$$A_{\alpha\beta}^{\hat{C}P} = P_{\nu_\alpha \rightarrow \nu_\beta} - P_{\bar{\nu}_\alpha \rightarrow \bar{\nu}_\beta}, \quad (1.58)$$

which can be evaluated as:

$$A_{\alpha\beta}^{\hat{C}P} = 4 \sum_{k>j,j} \text{Im}\{U_{\alpha k}^* U_{\beta k} U_{\alpha j} U_{\beta j}^*\} \sin\left(\frac{\Delta m_{kj}^2 L}{2E}\right). \quad (1.59)$$

If CPT is symmetric and the mixing matrix is complex, then the CP violation previously discussed implies T violation. The CPT symmetry implies, through Eq. 1.56, that  $P_{\nu_\alpha \rightarrow \nu_\beta} = P_{\bar{\nu}_\beta \rightarrow \bar{\nu}_\alpha}$ , which causes the time asymmetry to be equal to the charge-parity asymmetry, because:

$$A_{\alpha\beta}^{\hat{T}} = P_{\nu_\alpha \rightarrow \nu_\beta} - P_{\nu_\beta \rightarrow \nu_\alpha} = P_{\nu_\alpha \rightarrow \nu_\beta} - P_{\bar{\nu}_\alpha \rightarrow \bar{\nu}_\beta} = A_{\alpha\beta}^{\hat{C}P}, \quad (1.60)$$

where we used a simply change of index in the equality given by the CPT symmetry of the example.

In such a case, one could measure the asymmetry in neutrinos oscillation by the T or CP transformed channels. That is, if the experiment measures the probability  $P_{\nu_\alpha \rightarrow \nu_\beta}$ , it can measure either  $P_{\nu_\beta \rightarrow \nu_\alpha}$  or  $P_{\bar{\nu}_\alpha \rightarrow \bar{\nu}_\beta}$  to fully measure the asymmetry. This however is not a simple task because of the averaging effect described in the two flavor mixing, which is also present here.

The CPT symmetry is not a coincidence. In fact, CPT transformation is a symmetry of any local quantum field theory [23] such as the one used for neutrino oscillations. However, Quantum Field Theory describes neutrino oscillations approximately, which can led to small violations of CPT.

## Neutrino Mass Hierarchy

Current data allow to understand the modulus of the squared-mass difference, but not the sign. Because of this, it is not known in which order the massive neutrinos are distributed

and what is the mass of the lightest neutrino. Figure 1.12 shows the two possible mass hierarchies for the neutrinos choosing  $m_2 > m_1$ . The left side is the so-called Normal Mass Hierarchy and the right side is the Inverted Mass Hierarchy.

The DUNE experiment will be able to determine the mass ordering with a significance of  $5\sigma$  level in 2-3 years for all possible values of  $\delta_{CP}$  and, basically, regardless of all the other parameters constrains [2].

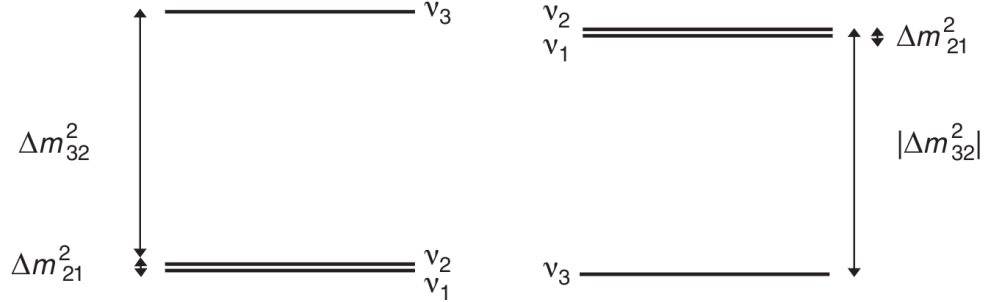


Figure 1.12: (Left) Normal neutrino mass hierarchy representation ( $m_3 > m_2$ ) and (Right) inverted mass hierarchy ( $m_1 > m_3$ ) [20].

### 1.3. DUNE Context

The main goal of this section is to give an introduction and background for neutrinos oscillations in the framework of the DUNE experiment. We will use one of the main channels of detection  $\nu_\mu \rightarrow \nu_e$  instead of a generic one. The distance from the near to far detector is defined as  $L = 1300$  km and will operate within 0.1 to 10 GeV, with the optimum energy around 0.5 to 5 GeV [2]. With this, we already know that DUNE will be sensitive to squared-mass difference around  $10^{-3}$  eV<sup>2</sup>.

Figure 1.13 shows the transition probability  $P_{\nu_\mu \rightarrow \nu_e}$  as function of energy from Eq. 1.26 (dashed line) and Eq. 1.40 (solid line). The squared-mass difference  $\Delta m_{32}^2 = 2.4 \cdot 10^{-3}$  eV<sup>2</sup> and  $\sin^2(2\theta) = 1$  were chosen and the uncertainty selected is  $\sigma_{L/E} = 0.13 \langle L/E \rangle$  [3]. The green area represents the optimum energy region. One can see that, in this ideal case, DUNE can measure three oscillations peaks and this explains why this distance and energy were chosen.

Lets make a comparison between the two and three neutrinos formalism. The transition probability  $P_{\nu_\mu \rightarrow \nu_e}$  can be extracted from Eq. 1.51 using the PMNS matrix 1.46, it follows that [27, 28]:

$$P_{\nu_\mu \rightarrow \nu_e} \approx P_{atm} + 2\sqrt{P_{atm}}\sqrt{P_{sol}}\cos\left(\frac{\Delta m_{32}^2 L}{4E} + \delta\right) + P_{sol}, \quad (1.61)$$

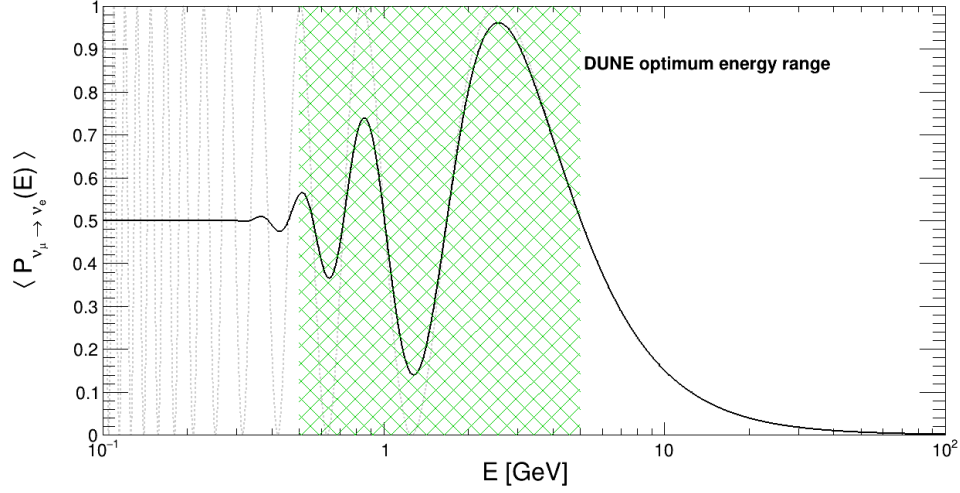


Figure 1.13: Averaged transition probability for  $\nu_\mu$  to  $\nu_e$  as function of energy from Eq. 1.40 (solid line). The unaveraged transition probability from Eq. 1.26 (dashed line) is also displayed. The green crosshatched region represents the DUNE optimum energy range.

where

$$\begin{aligned}\sqrt{P_{atm}} &\equiv \sin\theta_{23} \sin 2\theta_{13} \sin\left(\frac{\Delta m_{31}^2 L}{4E}\right) \\ \sqrt{P_{sol}} &\equiv \cos\theta_{23} \cos\theta_{13} \sin 2\theta_{12} \sin\left(\frac{\Delta m_{21}^2 L}{4E}\right).\end{aligned}\quad (1.62)$$

The reference  $P_{atm}$  and  $P_{sol}$  are due to the fact that the only squared-mass difference contributions are  $\Delta m_{31}^2$  and  $\Delta m_{21}^2$ , respectively.

Figure 1.14 shows the two different results of transitions probabilities (without averaging) for two neutrinos flavor (black, Eq. 1.25) and for three flavors (blue, Eq. 1.61). All the parameters were set using the table of Figure 1.7 and the phase was chosen  $\delta = 0$ . It is very clear that, although the two flavors approximation fails to fully describe the oscillation pattern, it can predict quite well the oscillation peaks giving a hint of how well will the experiment perform in the energy (or mass) region.

By comparing Fig. 1.13 and Fig. 1.14 one can notice that the oscillation due to the  $\Delta m_{21}^2$  (solar) contribution only grows for lower energy, where the initial first peak (right to left) starts to increase as the oscillation due to  $\Delta m_{31}^2$  (atmospheric) is already too fast. This is why the two flavors formalism manages to give a reasonable approach.

Now, one should notice from Fig. 1.14 that the transition probability for muon neutrinos to electron neutrinos is quite small. This small chance of transition between the two flavors causes the flux of electron neutrinos to be much smaller decreasing the statistics and making this channel not the ideal to measure  $\nu_\mu$  oscillation. There are still two channels: the survival

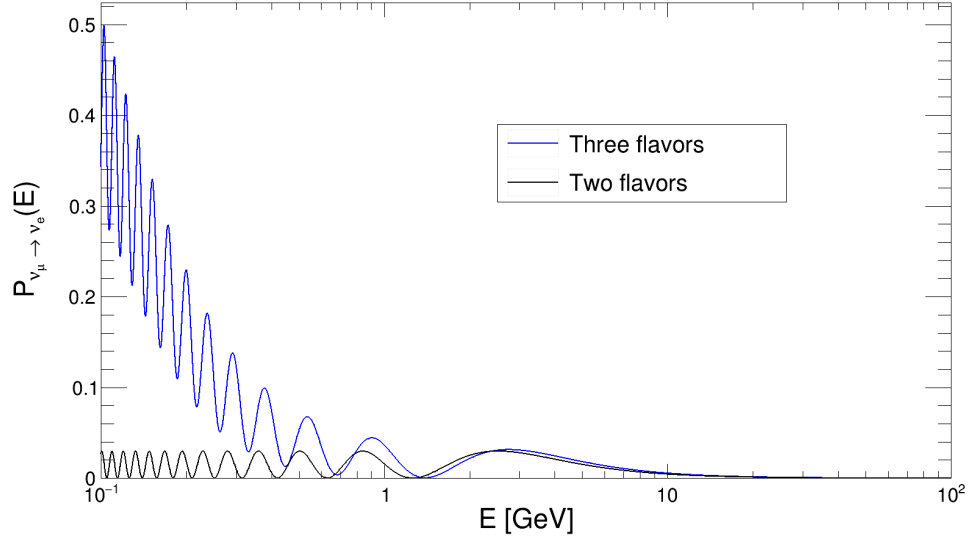


Figure 1.14: Three flavor (blue) and two flavor transition probability  $P_{\nu_\mu \rightarrow \nu_e}$  as function of energy.

probability  $\nu_\mu \rightarrow \nu_\mu$  or the transition to tau neutrino  $\nu_\mu \rightarrow \nu_\tau$ .

To make it simple, but still with a realistic approach, we can use Eq. 1.51 for all the channels and then use the approximation  $\Delta m_{32}^2 \cong \Delta m_{31}^2 \cong \Delta m_{atm}^2$  and  $\Delta m_{21}^2 \cong \Delta m_{sol}^2 \cong 0$ . This is nicely done by [28] (with  $\delta = 0$ ) which results<sup>11</sup> in:

$$P_{\nu_\mu \rightarrow \nu_e}(L, E) = \sin^2(2\theta_{13}) \sin^2(\theta_{23}) \sin\left(\frac{\Delta m_{atm}^2 L}{4E}\right) \quad (1.63)$$

$$P_{\nu_\mu \rightarrow \nu_\tau}(L, E) = \sin^2(2\theta_{23}) \cos^4(\theta_{13}) \sin\left(\frac{\Delta m_{atm}^2 L}{4E}\right) \quad (1.64)$$

$$P_{\nu_\mu \rightarrow \nu_\mu}(L, E) = 1 - [\sin^2(2\theta_{13}) \sin^2(\theta_{23}) + \sin^2(2\theta_{23}) \cos^4(\theta_{13})] \sin\left(\frac{\Delta m_{atm}^2 L}{4E}\right) \quad (1.65)$$

Figure 1.15 is the averaged transitions probabilities for equations 1.63 to 1.65 with  $\sigma_{L/E} = 0.13L/E$  and the constants from the table of Fig. 1.7. It can be easily seen that the transition probability to tau neutrinos or the survival probability are much higher than the transition probability to electron neutrinos. So the DUNE experiment should measure the oscillation in one of these two channels. To understand better this choice, one can notice that the first peak of oscillation (right to left) happens with an energy around 3 GeV, but the energy threshold to produce a  $\tau$  lepton is  $E_{\nu_\tau} > 3.5$  GeV [20] (see Sec 2.1.3). This makes impossible to use this channel for the DUNE range of energy.

<sup>11</sup>Note that this is the same approach as the two-mixing neutrinos, however now the amplitudes do not need to be guessed.

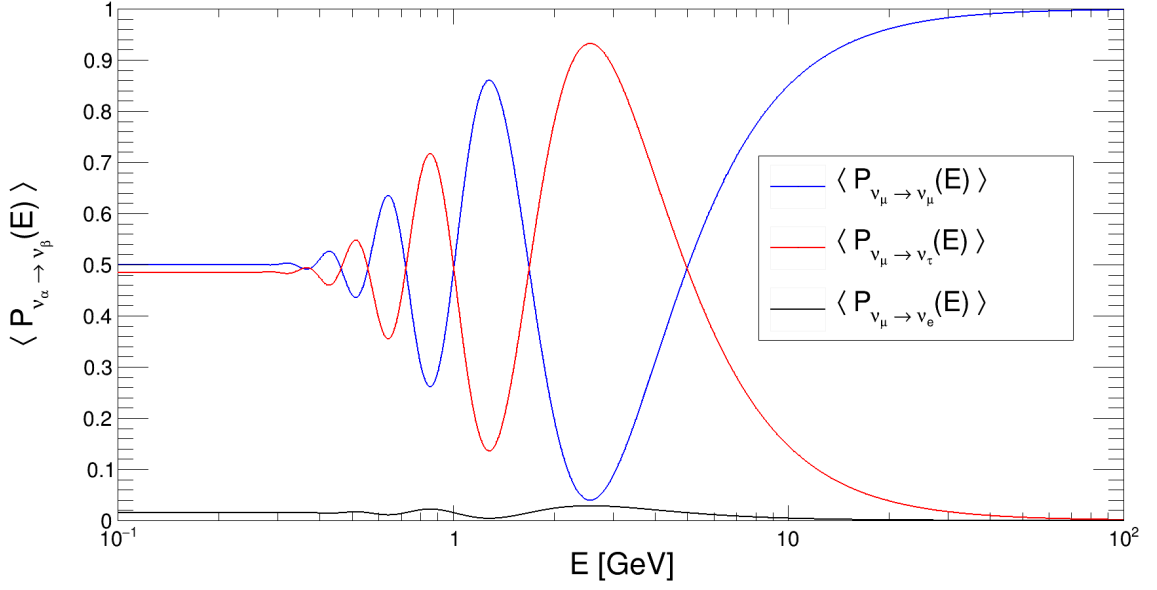


Figure 1.15: Averaged survival probability for  $\nu_\mu$  (blue) and averaged transition probability  $\nu_\mu \rightarrow \nu_\tau$  (red) and  $\nu_\mu \rightarrow \nu_e$  (black) as function of energy at the DUNE baseline  $L = 1300$  km.

### 1.3.1. Oscillation in matter

Before moving forward to DUNE scientific program, we need to go through neutrinos oscillation in matter. Up to here all the expressions were found for vacuum oscillations. However, the fact that the neutrinos cross matter instead of vacuum must be taken into account as it can induce a fake CP violation effect and allows the DUNE experiment to measure the mass ordering (Sec. 1.2.2) [2, 27].

When traveling through matter, neutrinos can interact with it as incoherent inelastic scattering or coherent scattering. The first one is the usual process that causes the detection of the neutrinos in DUNE and have a very small cross section and, therefore, a small probability to happen. The latter is defined as an interaction that does not change the initial conditions of the medium after the interaction but interferes with the neutrino propagation. This sort of interaction will not affect the beam intensity, but the phase velocity of the neutrinos [13]. A good analogy to this effect is how the refraction index of mediums affects the phase velocity of light without absorbing it [8].

Since Earth is composed by electrons instead of muons and taus, the interaction of  $\nu_e$  will be different than  $\nu_\mu$  and  $\nu_\tau$ . All the three flavors will interact in the same way with electrons, protons and neutrons through neutral-current (NC), but only  $\nu_e$  will interact with electrons mediated by  $W$  boson in a charged-current (CC) [8, 13] (see Sec. 2.1.3). Besides, a matter asymmetry can be expected due to the presence of electrons and absence of positrons in the

Earth [2].

In this scenario, the transition probability  $\nu_\mu \rightarrow \nu_e$  through a constant density matter will be given by [27]:

$$\begin{aligned}
 P(\nu_\mu \rightarrow \nu_e) \cong & \sin^2(\theta_{23}) \sin^2(2\theta_{13}) \frac{\sin^2(\Delta_{31} - aL)}{(\Delta_{31} - aL)^2} \Delta_{31}^2 \\
 & + \sin(2\theta_{23}) \sin(2\theta_{13}) \sin(2\theta_{12}) \frac{\sin(\Delta_{31} - aL)}{(\Delta_{31} - aL)} \Delta_{31} \frac{\sin(aL)}{aL} \Delta_{21} \cos(\Delta_{31} + \delta_{CP}) \\
 & + \cos^2(\theta_{23}) \sin^2(2\theta_{12}) \frac{\sin^2(aL)}{(aL)^2} \Delta_{21}^2,
 \end{aligned} \tag{1.66}$$

where  $\Delta_{ij} = \Delta m_{ij}^2 L / 4E$ ,  $a = G_F N_e / \sqrt{2}$ ,  $G_F$  is the Fermi constant,  $N_e$  is the number density of electrons in the Earth. For the anti-neutrino transition  $\bar{\nu}_\mu \rightarrow \bar{\nu}_e$ , both the  $\delta_{CP}$  and  $a$  change sign giving rise to the neutrino-antineutrino asymmetry due to CPV and matter effect [2].

Figure 1.16 shows the probabilities for neutrinos (left) and anti-neutrinos (right) for three values of  $\delta_{CP}$  at the baseline distance  $L = 1300$  km. The black line represents the oscillation only due to the solar term (making  $\theta_{13} = 0$ ) and “Normal MH” means Normal Mass Hierarchy. Present data corroborate with negative values of  $\sin \delta_{CP}$ , but poorly constrained, so all the values of  $\delta_{CP}$  from  $\pi$  to  $2\pi$ , including the CP-conservation values 0 and  $\pi$ , are consistent with neutrino data [2].

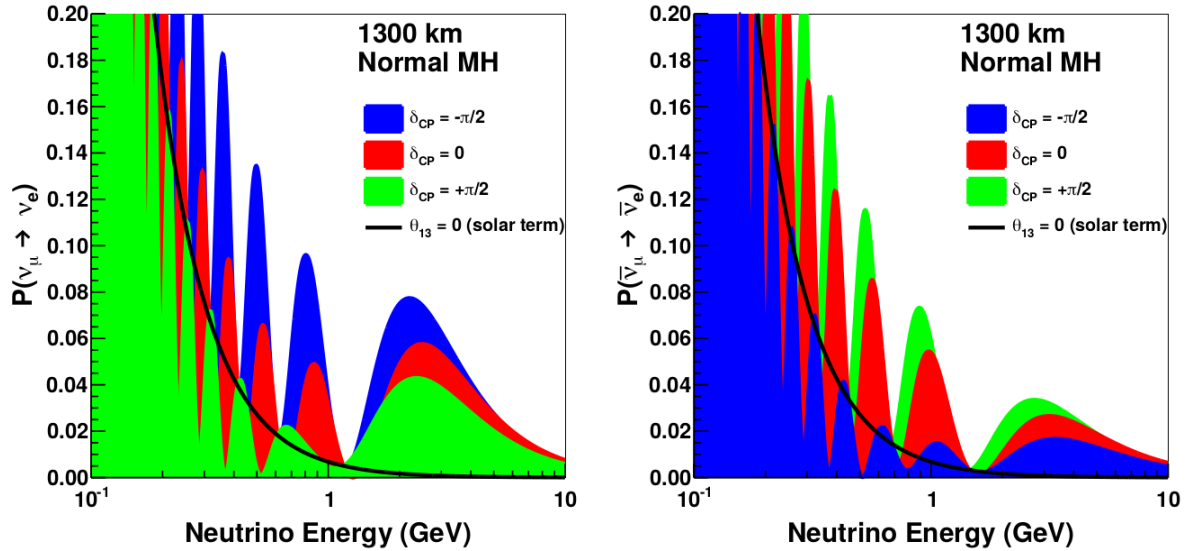


Figure 1.16: Electron neutrino appearance probability at the DUNE baseline  $L = 1300$  km as function of neutrino energy. Three different values of CP phase are used,  $\delta_{CP} = -\pi/2$  (blue), 0 (red) and  $\pi/2$  (green) for neutrinos (Left) and antineutrinos (right). Normal hierarchy is used and the black line indicates the oscillation probability if  $\theta_{13}$  were equal to zero [3].

Another new feature appears from Eq. 1.66: the transition is now sensitive to the sign of  $\Delta m_{31}^2$ . Comparing to equations 1.61 or 1.63, for instance, the sign of the squared-mass

difference is suppressed by the sine square, allowing to retrieve only the modulus of  $\Delta m_{ij}^2$ . This new dependence on the signal is crucial to determine the neutrinos Mass Hierarchy (MH). One of the reasons why DUNE have a baseline of 1300 km is because the ability of distinguishing the CP asymmetry from matter effects starts around  $\sim 1200$  km and increases with the baseline [2, 29].

Recent results from T2K [30] and NOvA [31] showed a preference for maximum CP violation  $\delta_{CP} = 3\pi/2$  when inverted neutrino mass ordering (see Sec. 1.2.2) is assumed. However, the results are in tension when considering normal ordering, with  $\delta_{CP}$  preferred as  $3\pi/2$  for T2K and  $\pi/2$  for NOvA. The combined result is shown by the  $\delta_{CP}$  and  $\sin^2(\theta_{23})$  two-dimensional plane in Figure 1.17 [32], where the allowed regions inside  $1\sigma$  and  $2\sigma$  are represented for NOvA (blue shading), T2K (red shading) and their combined result (black curves). The left panel represents the preferred inverted ordering (IO) while the right panel the normal ordering (NO).

Currently global fit analyses prefer the normal ordering, however, it went from  $1.6\sigma$  level to  $2.7\sigma$  due to the IO preferred data Super-Kamiokande [22] presented in 2020 [32]. Nevertheless, there is still statistical agreement between the two experiment data and a joint analysis of the experiments will further improve the results. Both experiment have a moderated preference for the upper octant of  $\theta_{23}$  ( $\sin^2(\theta_{23}) > 0.5$ ).

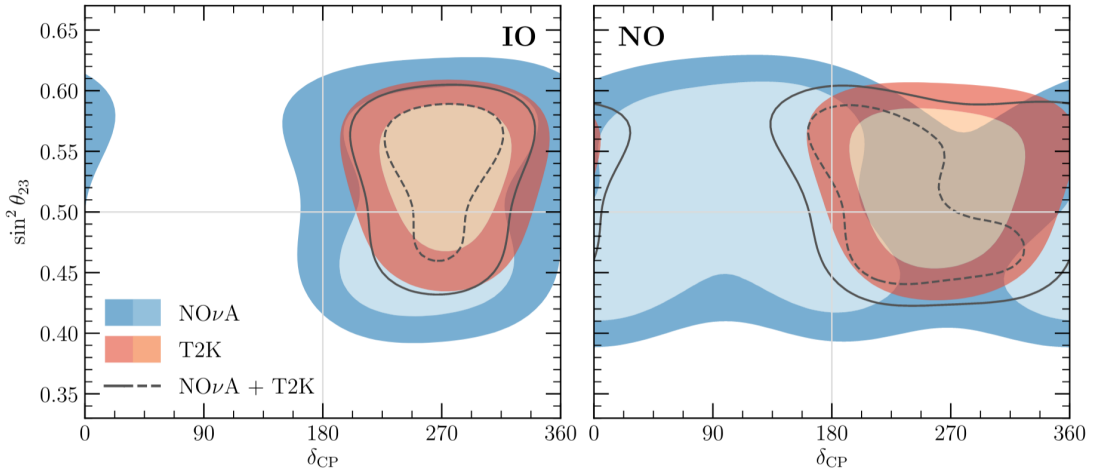


Figure 1.17: Allowed region inside  $1\sigma$  and  $2\sigma$  level (lighter and darker shading) for NOvA (blue shading), T2K (red shading) and their combination (black curves). Inverted ordering (IO) and normal ordering (NO) are taken into account (left and right panels, respectively) [32].

### 1.3.2. Parameters measurements

The oscillation patterns of  $\nu_\mu$  and  $\bar{\nu}_\mu$  are going to be exhaustively studied by reconstruction of the energy spectra of  $\nu_\mu$ ,  $\bar{\nu}_\mu$ ,  $\nu_e$  and  $\bar{\nu}_e$  as described above. To collect enough statistics the DUNE will have a beam of 1.2 MW minimum (upgradable to 2.4 MW after 6 years [3]) and corresponding proton-on-target per year assumed as  $1.1 \times 10^{21}$  POT [2]. This will result in an increase on  $\nu_e$  and  $\bar{\nu}_e$  event yield of one order-of-magnitude with respect to the current NOvA [31] and T2K [30] data sample and even a bigger increase in the survival probabilities channels.

As result, besides being able to measure the mass hierarchy ordering and the CP violation (as described in Sections 1.3.1 and 1.2.2), DUNE will provide more precise measurements of some of the key parameters of neutrinos oscillations, like  $\delta_{CP}$ ,  $\sin^2(2\theta_{13})$ ,  $\Delta m_{31}^2$  and  $\sin^2(\theta_{23})$ . Moreover, the experiment will be able to determine the octant of  $\theta_{23}$ , as it is known with the present data that  $\theta_{23}$  is close to the maximal-mixing value of  $\pi/4$  (see Fig. 1.7), but it is not known in which octant it lies, that is, if  $\theta_{23} > \pi/4$  or  $\theta_{23} < \pi/4$ .

Figures 1.18a and 1.18b show the DUNE sensitivity for the mass hierarchy and CP violation, respectively, over the years of operation [3]. The colored areas represent different assumptions for  $\delta_{CP}$ , as a fixed value of  $-\pi/4$  (red) and for every possible value (dark blue) for mass hierarchy for instance. The same is done for CP violation but for a fixed value, 50% and 75% of the values. The solid line delimits the region with nominal values reported in the figures and the dashed line is the limit for unconstrained  $\theta_{13}$ .

It can be seen that DUNE will be able to determine the mass ordering between 2-3 years of operation with a  $5\sigma$  confidence level as previously cited. The CP violation, on the other hand, can take up to 14 years operation to have a  $3\sigma$  sensitivity or about 6 years for  $5\sigma$  if  $\delta_{CP} = -\pi/2$ . It is also reported in [2] the resolution of each parameter as function of the time of exposure<sup>12</sup>, which can change depending on its own values and on others parameters. For instance,  $\delta_{CP}$  after 15 years of operation can have a resolution of 17 degrees (for  $\delta_{CP} = \pm\pi/2$ ) or up to 7 degrees (for  $\delta_{CP} = -\pi, 0, \pi$ ).

<sup>12</sup>The exposure is given by kt·MW·year, this means a detector of 1 kt exposed to 1 MW beam for one year. To get the correct amount of years exposed one should remember that DUNE will have 4 phases of operation as described previously.

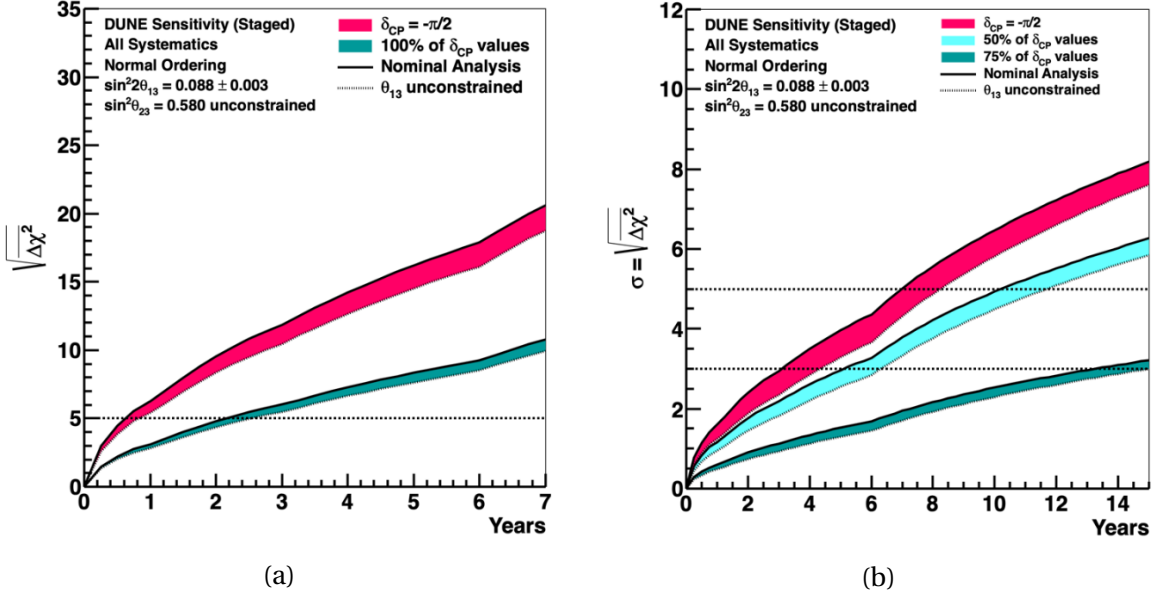


Figure 1.18: **(a)** Confidence level of the DUNE determination of the neutrino mass ordering in the case where  $\delta_{CP} = -\pi/2$  (red area) and for all possible values of  $\delta_{CP}$  (green area) as a function of years of operation. Normal ordering is assumed [2]. **(b)** Confidence level for the determination of CP-violation (if any) for the case where  $\delta_{CP} = -\pi/2$  (red area) and for 50% (light green) and 75% (green) of the possible values in normal ordering situation, as function of years of operation [2].

## 1.4. Beyond the neutrino beam

Besides the measurements with the neutrino beam from the Long Baseline Neutrino Facility (LBNF), DUNE will be able to perform measurements with non-beam neutrinos. The photon detection (PD) system is crucial to measure the events not related to the neutrino beam, being responsible for the trigger system of supernova neutrinos and proton decay (if any). The PD will also enable the precise measurement of the  $t_o$  for every event, time resolution for neutrinos bursts and reconstruction of events energy and topology in the drift coordinate.

### 1.4.1. Supernova neutrinos

In 1987, the supernova SN 1987A [33] occurred in the Large Magellanic Cloud, about 50 kpc from Earth, and opened a new era of extragalactic neutrino astronomy. During this event, the 25 antineutrino events detected along three detectors have confirmed the basic physical picture of core collapse supernovas and gave new inputs for a wide range of new physics [3].

It is expected that a core collapse supernova will occur in the Milk Way (within about 20 kpc) once every 10 to 50 years and also about the same rate for Andromeda Galaxy (the closest galaxy to Earth) about 780 kpc away [34]. Although these events are rare, there is a reasonable chance of a supernova occurring in the few-decade long lifetime of a large neutrino detector. Because of that, it is important that at least one module of the DUNE far detector be online at all time to observe this unpredictable event, if and when it occurs [2].

The Supernova burst (SNB) signature from the core collapse is expected to last few tens of seconds and produce from a few hundreds to several thousands interactions<sup>13</sup>. The neutrino spectrum retrieved from these interactions will provide information about the progenitor, the collapse, the explosion and the remnant of the supernova [3]. The neutrinos energy spectrum from SNB peaks around 10 MeV with appreciable flux to about 30 MeV. Such low energies are below the charged-current threshold for  $\nu_\mu$ ,  $\nu_\tau$ ,  $\bar{\nu}_\mu$  and  $\bar{\nu}_\tau$  causing, together with the fact that neutral-current interactions have low cross sections and does not carry flavor information, the  $\nu_e$  and  $\bar{\nu}_e$  flux measurements the most rich in information [2, 3].

Getting back to the importance of the photon detection system, it is expected that during the first 50 ms of a SNB 10 kpc away the mean interval between successive neutrino interactions is 0.5 - 1.7 ms depending on the model. Moreover, events closer to Earth can have a rate tens or hundreds of times higher [3]. The TPC provides a resolution of 0.6 ms at 500 V/cm which is not enough for theses events. The PD system provides a resolution smaller than 10  $\mu$ s which allows DUNE to measure the flux without a time resolution constrain [3].

Specially in the case of SN neutrinos, the PD system allows to improve the resolution of the reconstructed energy. By associating events on the TPC and the light output, one can determine where the event happened along the drift direction. This allows to define the detector fiducial volume and to correct the data for electron quenching. Figure 1.19 shows the energy residuals for the supernova neutrinos events without (black) and with (colored) drift correction to the reconstructed energy. Blue, green and pink are effective areas (light collector area  $\times$  efficiency) of light collection and the red histogram assumes that event vertex is perfectly known. It can be easily noticed the improvement in resolution when the drift correction is applied. However, one should know that the effective area of 23 cm<sup>2</sup> is the minimum specification for DUNE.

---

<sup>13</sup>This number depends on the distance of the supernova and the number of operating modules.

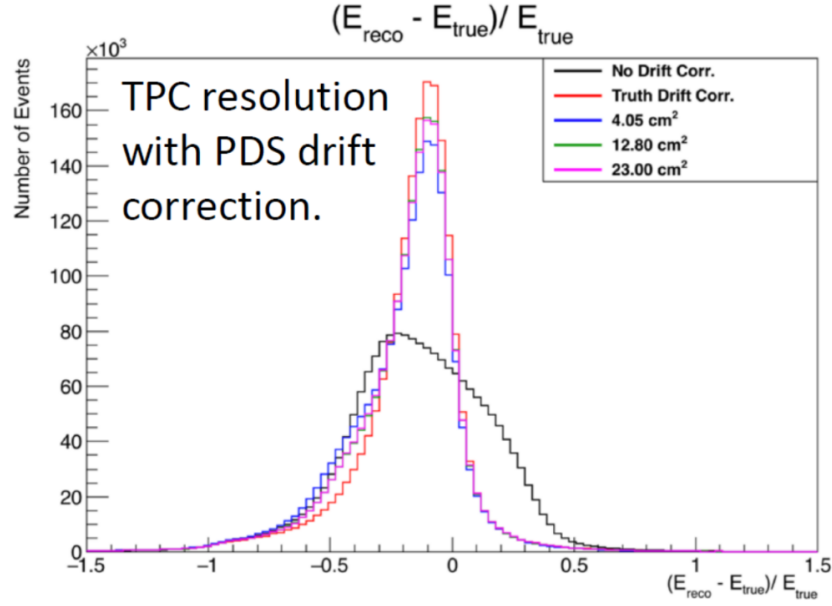


Figure 1.19: Residual between reconstructed and true energy for supernova neutrino events without (black) and with (color) a drift time correction with the photon detection system to the reconstructed energy. The red histogram assumed the event vertex is known perfectly, while the others corresponds to effective area of the light collection. The 23 cm<sup>2</sup> histogram correspond roughly to the 0.5 p.e./MeV requirement [3].

#### 1.4.2. Proton decay

Due to the DUNE large fiducial mass, low background (because of its deep underground location), excellent event imaging, particle identification and calorimetry, proton and neutron decays signatures can be searched to probe baryon-number violation (BNV) [35]. It is unknown up to now if protons are stable particles and, therefore, if baryon-number is conserved or not. In the current Standard Model framework, baryon-number is defined as conserved, although no symmetry requires so and grand unified theories foresee nucleon decay. Because of that, nucleon decays would be a clear evidence of physics beyond Standard Model [3].

DUNE will be sensitive to many possible proton decay channels but, in general, the favored channels are  $p \rightarrow K^+ \bar{\nu}$  or  $p \rightarrow e^+ \pi^0$ . In both cases, the detector needs to have a good particle identification capability, being able to distinguish all the particles in this kind of events, and of rejecting the background induced by atmospheric muons. Preliminary results from ProtoDUNE demonstrate a good particle identification capability for DUNE [2]. The fiducialization of the detector volume is crucial for the background removal and will be performed with the assistance of the PD system.

## Deep Underground Neutrino Experiment

The Deep Underground Neutrino Experiment (DUNE) [2–5] will be a 40 kt modular liquid argon time-projection chamber (LArTPC) placed 1.5 km underground exposed to the world’s most intense neutrino beam, and will answer some of the open questions in elementary particle physics. The experiment will take place in the Long-Baseline Neutrino Facility (LBNF) hosted by Fermilab, which will provide the infrastructure for DUNE, the deep-underground site and the neutrino beam.

The far detector (FD) will be installed in the Sanford Underground Research Facility (SURF) in South Dakota, 1,300 km away from Fermilab. The final configuration of the detector foresees the construction of four liquid argon time-projection chambers (LArTPC) with an active mass of 10 kt each. The total active mass will be of 40 kt.

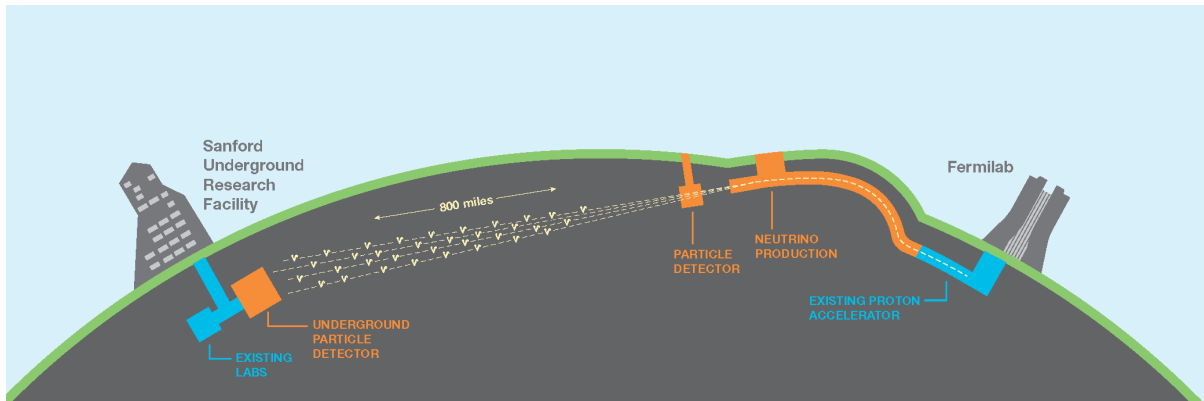


Figure 2.1: Schematic concept of neutrinos beam directed from Fermilab to SURF [2].

In this chapter, the DUNE experiment will be discussed starting with the description of the LArTPC technology, highlighting the features of this detector and the motivations of its use. There will be than an overview of the experiment, pointing out the sensitivities and requirements for potential discoveries.

### 2.1. Liquid Argon Time Projection Chamber (LArTPC)

#### 2.1.1. Principle of operation

The Liquid Argon Time Projection Chamber (LArTPC) follows the idea of a bubble chamber, with the concept of a readable trail left by the particle in a high quality three-dimensional

image. It was first proposed by Carlo Rubbia in 1977 [36], who pointed out that with simple techniques a desirable argon purity could be reached and “*In this case a multi-hundred-ton neutrino detector with good vertex detection capabilities could be realized*”.

The basic concept is that charged particles cross the active liquid argon (LAr) volume of the TPC leaving a track of ionized atoms and electrons. A strong and very uniform electric field is applied to the LAr volume, which allows to separate the electrons and Ar ions. A typical ionizing particle through the LAr produces around 60 thousand ionization electrons per centimeter. Electrons are drifted toward the anode grid, which is made by three parallel wire planes. Reading-out the signal induced by the drifting electrons on the wires allows to obtain a 2-dim representation of the ionizing event for each wire plane. Combining the three different 2-dim view of the same events allows to perform a complete 3-dim reconstruction of the same event.

Two different designs of LArTPC will be implemented for the DUNE experiment, the single-phase (SP) horizontal drift (HD) and vertical drift<sup>1</sup> (VD). In the SP-HD design, electrons are drifted horizontally in the liquid argon volume (whenever only “SP” is mentioned, it is understood to refer to the HD). In the vertical drift the electrons are drifted vertically in the LArTPC. The main subject of this chapter will be the SP design, but in order to contextualize the reader: the vertical drift has a simplified field cage design, which permits the LArTPC to be divided in two volumes while there are four volumes in the SP. The photon detection system can be placed behind the field cage and inside the cathode plane, but not behind the anode plane as in the HD design, since it is not transparent. This technology is still under development and a full description will be published soon.

Figure 2.2 represents the interaction of a neutrino resulting in two charged particles in a single-phase LArTPC module. An electric field of 500 V/cm is applied between the cathode and the three anode wire grids to drift the electrons. The relative voltage between the layers is chosen to ensure all but the final layer are transparent to the drifting electrons, and these first layers (U and V) produce bipolar induction signals (right side of the figure) as the electrons pass through them. The final layer (X) collects the drifting electrons, resulting in a monopolar signal [5].

Besides the charge signals from the ionized drifting electrons, liquid argon is also an ex-

---

<sup>1</sup>The original option was the dual-phase (DP) technology, which employs a layer of GAr above the liquid, through which the drift electrons are extracted. This grants a signal amplification due to electron avalanches in the gas phase with the electric field, decreasing the detection threshold allowing for a larger fiducial volume.

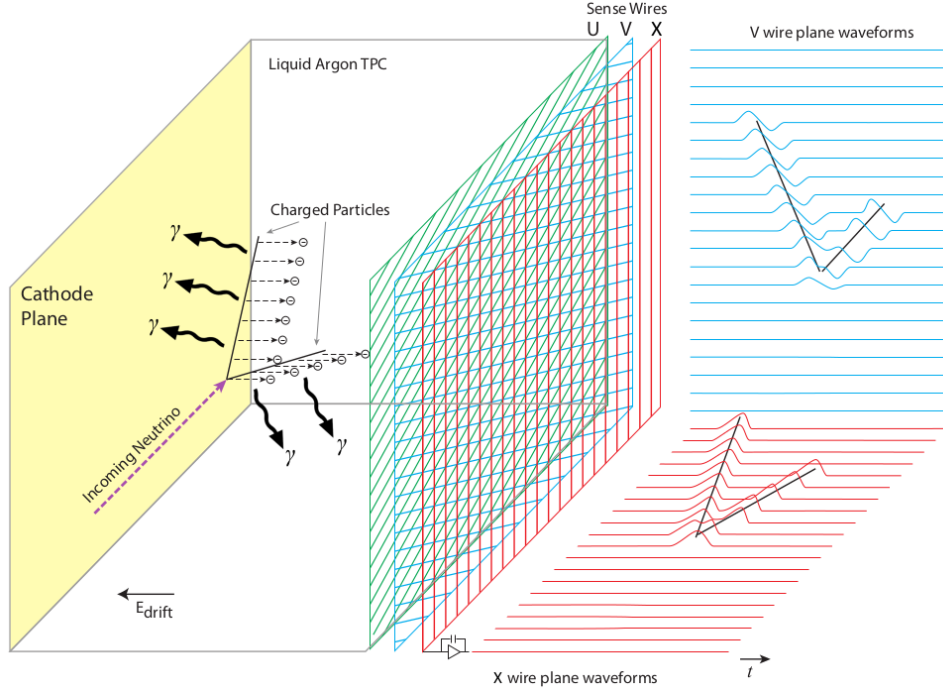
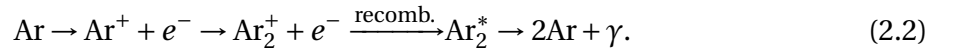
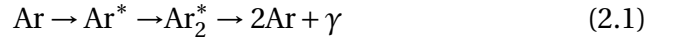


Figure 2.2: Diagram of the single-phase LArTPC basic operation [5].

cellent scintillator, emitting VUV light at a wavelength of 127 nm after de-excitation of argon molecules [5, 37]. Scintillation light in LAr is produced when ionizing radiation produces excitation and ionization of the argon atoms. The mechanism can be described by:



In Eq. 2.1, argon was excited to a higher energy state and in Eq. 2.2 ionized. In the latter case, the electron can recombine with the argon ionized molecule formed. The recombination will result in the same argon excited molecule of Eq. 2.1, which can lose energy by emitting scintillation photons. The TPC signal is accompanied by a flash of scintillation light which may be detected and provide the time  $T_0$  at which the ionization electrons start drifting toward the anode.

The ionizing electron has a certain probability of recombining with the argon ion or being drifted by the electric field. The electric field of 500 V/cm is chosen to balance between the charge from ionization and scintillation light which are competing processes (see Sec. 3.1).

A higher E field results in: a higher electron drift velocity, which reduces drift time and minimizes the losses due to impurities (see Sec. 2.1.4); a decrease in the recombination probability and a lower free electron diffusion (proportional to the square root of the drift time).

Therefore, improving the signal-to-noise, the calorimetry capabilities of the detector and spacial resolution [5].

However, without scintillation light, it is impossible to place an absolute time scale on the event detected, not allowing to solve the coordinate along the drift direction. The E field should not be raised beyond certain limits to not affect the electron recombination to a point where there is not enough scintillation photons to be detected and to avoid electric discharges in the LArTPC.

It was experimentally established [38] that a 500 V/cm field is an appropriate trade-off between charge and light signal. At this level, about 60% of the electrons can recombine and a drift velocity of  $\sim 1.6 \text{ mm}/\mu\text{s}$  [39] is achieved, taking around 2.2 ms to travel from the cathode to anode. Furthermore, the design and construction has already been tested to be cost-effective for a large scale experiment.

### 2.1.2. Why using liquid argon

The use of a noble liquid rather than gas is necessary in neutrino experiments to provide a high enough target mass for increased neutrino interactions probability. Noble liquids have a high electron mobility for being electropositive; they are dielectrics, which allows high voltages; and they have high radiation length<sup>2</sup>. Besides, LAr also has a high density, which makes it a good target for neutrino interactions, and abundantly produces scintillation light. Table 2.1 summarizes some of the properties of noble gases for a possible use in a TPC with water only for reference. Stopping power ( $dE/dx$ ) is defined as the average energy lost by ionizing radiation in a medium per unit path length traveled.

Table 2.1: Properties of noble liquids [40–44].

	Water	He	Ne	Ar	Kr	Xe
Boiling point [K] @ 1 atm	373	4.2	27.1	87.3	120	165
Density [ $\text{g}/\text{cm}^3$ ]	1	0.125	1.2	1.4	2.4	3.0
Radiation length [cm]	36.1	755.2	24	14	4.9	2.8
Scintillation Yield [ $\gamma/\text{keV}$ ]	-	19	30	40	25	42
Scintillation $\lambda$ [nm]	-	80	78	127	150	175
$dE/dx$ [MeV/cm]	1.9	0.24	1.4	2.1	3.0	3.8
Abundance (Earth atm) [ppm]	$25 \times 10^3$	5.2	18.2	9300	1.1	0.09
Electron mobility [ $\text{cm}^2/\text{V}\cdot\text{s}$ ]	-	$< 0.3$	$< 0.01$	$\sim 500$	$\sim 1800$	$\sim 2200$

<sup>2</sup>Radiation length is defined as the mean distance in which a high energy electron loses all but  $1/e$  of its energy by bremsstrahlung and the  $7/9$  of the mean free path for pair production by high energy photons.

Helium and Neon can be discarded because of the very low electron mobility, making it impossible to build a large TPC (they also have a very low boiling temperature, making very challenging to keep them at liquid state). Besides that, their scintillation light is very energetic, being easily absorbed and very challenging to be detected. Krypton, on the other hand, has a good electron mobility, density and stopping power ( $dE/dx$ ). However, the low scintillation yield summed-up with its low abundance in nature makes challenging its use in a large TPC.

Even though liquid xenon (LXe) has better features, besides the short radiation length, its low abundance makes quite impossible to build a 10 kt LXeTPC. Liquid argon satisfies all the requirements for a high quality TPC with the additional advantage of a low ionization threshold of  $W_l = 23.6 \pm 0.3$  eV [45, 46] which is the average energy expected per ion pair. This makes LAr the preferred choice for a massive detector such as the DUNE experiment.

### 2.1.3. Neutrino detection in a LArTPC

Neutrinos of one of the three flavors ( $\nu_\ell$ ) will interact in matter through charged current (CC) and neutral current (NC) following the Feynman diagrams [20]:

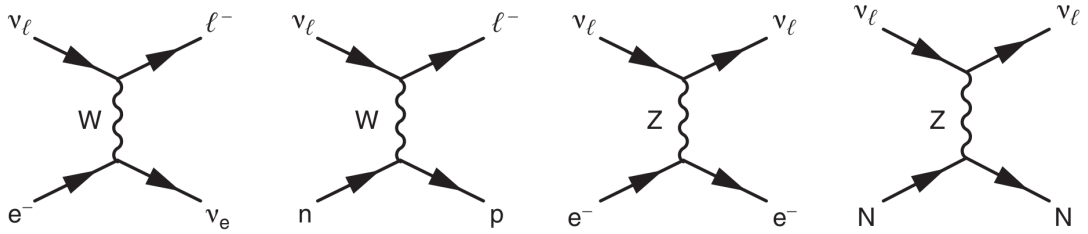


Figure 2.3: Feynman diagrams for CC and NC neutrino interactions in matter [20]. For  $\bar{\nu}_e$  there is an extra  $\bar{\nu}_e + e^- \rightarrow \bar{\nu}_e + e^-$  CC and NC scattering.

The two first diagrams are CC interactions and the last two are NC. In Sec. 1.3.1 the difference between  $\nu_e$  interactions and  $\nu_{\mu,\tau}$  was mentioned, notice that in the first diagram the only neutrino flavor that can interact without changing flavor is  $\nu_e$ , this charged current scattering channel is not accessible to  $\nu_{\mu,\tau}$  (without changing flavor). The neutral current scattering (third diagram) is accessible to all flavors. The fourth diagram is mostly not detectable in a LArTPC.

While NC interactions happen for any neutrino energy, CC interactions need to have sufficient centre-of-mass energy to produce a charged lepton and the final stage hadronic system or  $\nu_e$  (second and first diagrams, respectively) [20]. Therefore, the CC absorption

$\nu_\ell + n \rightarrow \ell^- + p$  will have the centre-of-mass energy squared<sup>3</sup> in the laboratory frame as:

$$s = (p_\nu + p_n)^2 = (E_\nu + E_n)^2 - (\vec{p}_\nu + \vec{p}_n)^2, \quad (2.3)$$

where  $p$  here is the four vector  $(\vec{p}, E)$  of momentum and energy. The neutrino is considered massless here and the neutron without motion, so, considering the momentum in the x-axis:

$$p_\nu = (E_\nu, 0, 0, E_\nu) \quad (2.4)$$

$$p_n = (m_n, 0, 0, 0), \quad (2.5)$$

which makes Eq. 2.3 to become:

$$s = (E_\nu + m_n)^2 - E_\nu^2 = 2E_\nu m_n + m_n^2. \quad (2.6)$$

The interaction  $\nu_\ell + n \rightarrow \ell^- + p$  is only kinematically allowed if the lepton and proton are created in rest, that is  $s > (m_\ell + m_p)^2$ . Therefore, a threshold can be established [20]:

$$E_\nu > \frac{(m_p^2 - m_n^2) + m_\ell^2 + 2m_p m_\ell}{2m_n}. \quad (2.7)$$

The resulting neutrino energy threshold for charged current interactions with a nucleon is:

$$E_{\nu_e} > 0, \quad E_{\nu_\mu} > 110 \text{ MeV} \quad \text{and} \quad E_{\nu_\tau} > 3.5 \text{ GeV}. \quad (2.8)$$

The threshold here is to produce the primary particles; nevertheless, the secondary particles need to be detected. Although there is no precise threshold for the detection of electrons, a few MeV particle is needed to produce signal well above the electrical signal in the wire. Supernova muon and, evidently, tau neutrinos (see Sec. 1.4.1) are above the threshold to produce signals in a LArTPC. The charged current absorption for supernova neutrinos in the LArTPC has the form:

$$\nu_e + {}^{40}\text{Ar} \rightarrow e^- + {}^{40}\text{K}^*, \quad (2.9)$$

which are likely to also give gamma rays signals from the de-excitation of  $\text{K}^*$  [3].

For CC interactions with atomic electron  $\nu_\ell + e^- \rightarrow \nu_\ell + \ell^-$  (first diagram), the same approach can be done with the condition that the centre-of-mass energy must be high enough to produce a lepton at rest, that is,  $s > m_\ell^2$  in the laboratory frame. Therefore:

$$s = (p_\nu + p_e)^2 = (E_\nu + m_e)^2 - E_\nu^2 = 2E_\nu m_e + m_e^2, \quad (2.10)$$

---

<sup>3</sup>Centre-of-mass energy squared is a Lorentz invariant, formed by the total energy and momentum of the initial or final-state particles. For further explanation Ref. [20] is exceptional.

resulting in the condition:

$$E_\nu > \frac{m_\ell^2 - m_e^2}{2m_e}. \quad (2.11)$$

Therefore the neutrino electron charged current scattering has the thresholds:

$$E_{\nu_e} > 0, \quad E_{\nu_\mu} > 11 \text{ GeV} \quad \text{and} \quad E_{\nu_\tau} > 3090 \text{ GeV}. \quad (2.12)$$

Considering the threshold energy for muon neutrino interaction through electron scattering, it is evident that this channel does not contain any peak of oscillation (by comparing with Fig. 1.15).

In DUNE, even though the electron neutrino appearance is quite low compared to muon neutrino survival or tau neutrino appearance (see Fig. 1.15), the matching sensibility of the detector for  $\nu_e$  interactions, the fact that  $\nu_{\mu,\tau}$  are background majorly in the NC interactions, in which the flavor cannot be distinguished, and the matter effect in  $\nu_e$  make the measurement of electron neutrino appearance an obvious choice.

For supernova neutrinos, only three channels will be accessible: the CC nucleon absorption for electron neutrino, the CC absorption for antineutrino and the neutrino electron scattering for all flavors [3]:

$$\nu_e + {}^{40}\text{Ar} \rightarrow e^- + {}^{40}\text{K}^* \quad (2.13)$$

$$\bar{\nu}_e + {}^{40}\text{Ar} \rightarrow e^+ + {}^{40}\text{Cl}^* \quad (2.14)$$

$$\nu_\ell + e^- \rightarrow \nu_\ell + e^-. \quad (2.15)$$

#### 2.1.4. LAr purity

The purity of the LAr is of great concern for the DUNE experiment. As discussed in Sec. 2.1.2, LAr has a high electron mobility, for being electropositive; however, electronegative contaminants such as oxygen or water will absorb ionized electrons in the drift. Moreover, nitrogen contaminants quench the scintillation of LAr and decreases the quality of light signals.

The DUNE FD has a requirement of electronegative contaminants in LAr lower than 100 ppt (part per trillion)  $\text{O}_2$ -equivalent, which is enough to ensure a lifetime greater than 3 ms for the ionized electron [5]. One can assume that the rate of electrons absorbed is proportional to the number of electrons, that is:

$$\frac{dQ}{dt} = -\lambda_e Q. \quad (2.16)$$

where  $\lambda_e$  is the absorption constant and  $Q$  is the total charge. Defining  $\tau_e = 1/\lambda_e$  as the electron lifetime and solving the differential equation, it results that:

$$Q(t) = Q_0 e^{-t/\tau_e}, \quad (2.17)$$

where  $Q(t)$  is the charge as function of the drift time  $t$  and  $Q_0$  is the initial charge. For the DUNE SP module the maximum drift length will be 3.5 m (full distance from the cathode to anode planes) and, at nominal 500 V/cm drift voltage, this correspond to a drift time of  $t_{\max} = 2.2$  ms. In the target electron lifetime of 3 ms, an attenuation of about 48% is expected for ionizing radiation near the cathode plane, ensuring a S/N ratio greater than 5 in the induction planes and  $S/N > 10$  for the collection planes, which are necessary to perform pattern recognition and two-track separation [5].

In ProtoDUNE-SP run I, dedicated measurements were performed to determinate the electron lifetime. At the end of the Run, it reached approximately  $89 \pm 22$  ms, which corresponds<sup>4</sup> to a concentration in liquid argon of  $3.4 \pm 0.7$  ppt O<sub>2</sub>-equivalent, much lower than the DUNE requirement of <100 ppm O<sub>2</sub> equivalent [39]. During the run I, electron lifetime was stable above 20 ms.

## 2.2. Experimental details

The DUNE experiment has been carefully designed to reach its ambitious physics goals. In this section we highlight some of the key features of the experiment. A complete description can be found in Refs. [2–4]. The near detector (ND) conceptual design report can be found at Ref. [6], but will not be explored in this thesis.

### 2.2.1. Neutrino beam

As described in Sec. 1.3, the DUNE aims to study the two oscillation maximum for neutrinos around 1 GeV at 1300 km. A proton beam, from the Long Baseline Neutrino Facility (LBNF) is generated at Fermilab with an energy ranging from 60 to 120 GeV and bent downwards towards the far detector as shown in Fig. 2.4 [2].

The beam will hit a target and produce secondary mesons, that will be focused in a decay pipe by magnetic horns and will successively decay into muons and neutrinos. Neutrino

---

<sup>4</sup>Assuming a that the concentration is given by  $N_{O_2} = (k_a \tau)^{-1}$ , where  $k_a = (300 \text{ ppt ms})^{-1}$  being the attachment constant for oxygen [39].

or antineutrino beam is chosen by switching the horn polarity. Muons produced and any residual hadron are stopped, producing the neutrino beam with tuned energy between 0.5 and 5 GeV [2]. Figure 2.5 shows the predicted neutrinos and antineutrinos fluxes at the Far Detector (FD) at 1300 km when operating as neutrino (left) and antineutrino mode (right). The flux is given as neutrinos per GeV per ( $1 \times 10^{21}$ ) proton-on-target (POT) per  $\text{m}^2$ . It is assumed  $1.1 \times 10^{21}$  POT per year for the 1.2 MW neutrino beam [2]. This numbers are given by the assumption that the uptime and efficiency of the Fermilab accelerator complex and the LBNF beamline are 56% combined. An upgrade to 2.4 MW of beam power is foreseen by 2030.

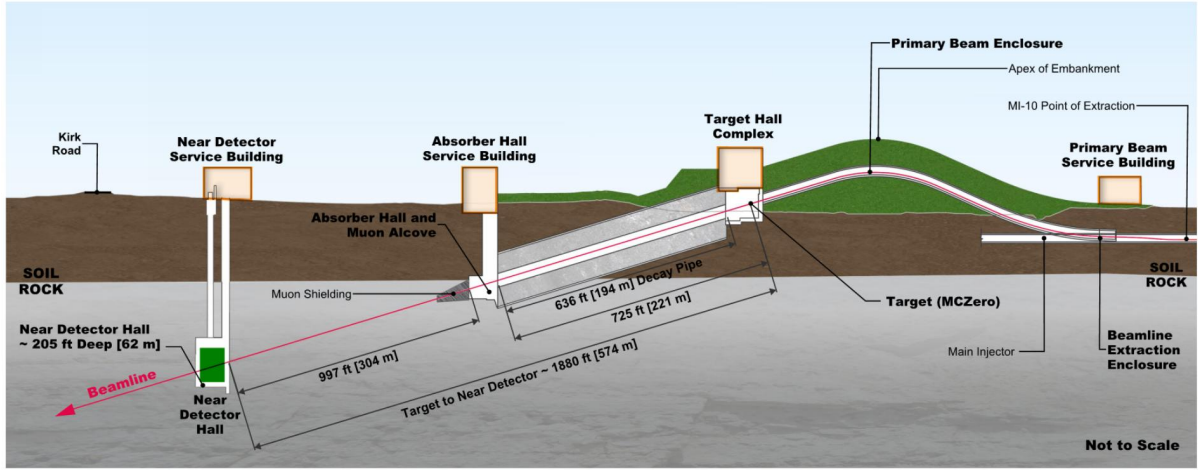


Figure 2.4: Longitudinal section of the Long Baseline Neutrino Facility beamline at Fermilab [2].

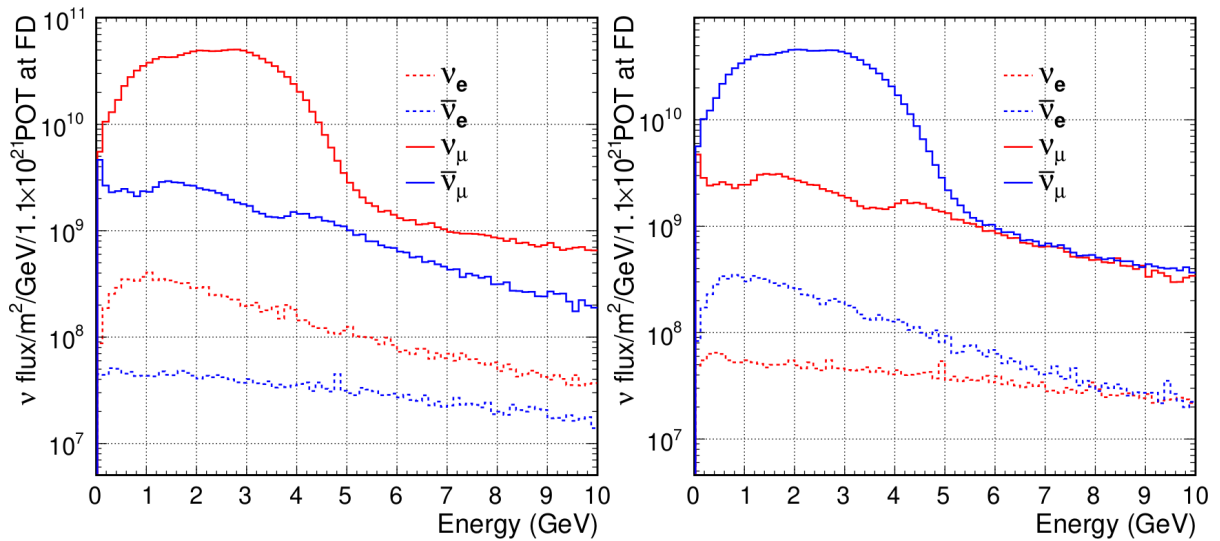


Figure 2.5: Predicted neutrino fluxes at the far detector (FD) when operating as neutrino mode (left) and antineutrino mode (right) [3].

### 2.2.2. Far Detector

The DUNE Far Detector Single-Phase will consist of four modules of 10 kt LArTPCs. Figure 2.6 shows the 10 kt module (17.5 kt of total liquid argon mass). The LArTPC is composed by four drift volumes of 3.5 m between anode and cathode walls, with dimensions of 58 m  $\times$  12 m with the beam arriving into the 58 m dimension direction.

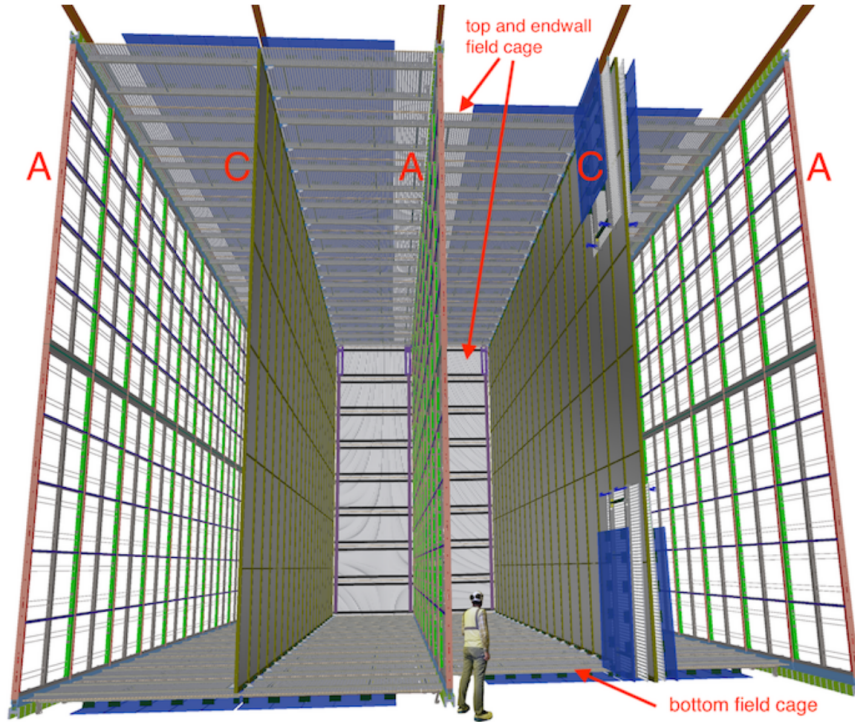


Figure 2.6: Basic design of the DUNE Far Detector (FD) SP module of 10 kt. The Anode (A) and Cathode (C) are separated by 3.5 m and are 12 m high [5].

The two cathode walls are composed of cathode plane assembly (CPA) panels. The CPA is a 1.2 m  $\times$  4 m panel that form the CPA arrays of Fig 2.6. Each CPA array contains 150 CPAs (300 in total). The CPA arrays are set to  $-180$  kV, which results in a uniform electric field of 500 V/cm across the drift volume to the grounded anode planes. The anodes are each composed by 50 anode plane assemblies (APA) units (150 in total) with 6 m  $\times$  2.3 m dimension placed vertically.

The APAs are two-sided, with three wire layers and an additional grid layer for shielding<sup>5</sup> wrapped around them. Figure 2.7 shows the APA schematic, the wire spacing on the layers is 4.75 mm. The collection layer X and the grid G are placed horizontally (in the figure), with wires spaced (pitch) 4.790 mm from each other. The induction U- and V-layers are wrapped

<sup>5</sup>The grid improves the signal shapes on the U induction channels.

around the APA at  $\pm 35.7^\circ$  from the vertical and pitch of 4.669 mm. A grounding mesh is mounted on both sides of the APA frame. The blue boxes in Fig. 2.7 represent the read-out electronic of the TPC.

The  $\pm 35.7^\circ$  angle is chosen to ensure that each induction wire only crosses a given collection wire once<sup>6</sup>, reducing the ambiguities on reconstruction, while keeping a performance close to the optimum  $45^\circ$  wire angle configuration [5].

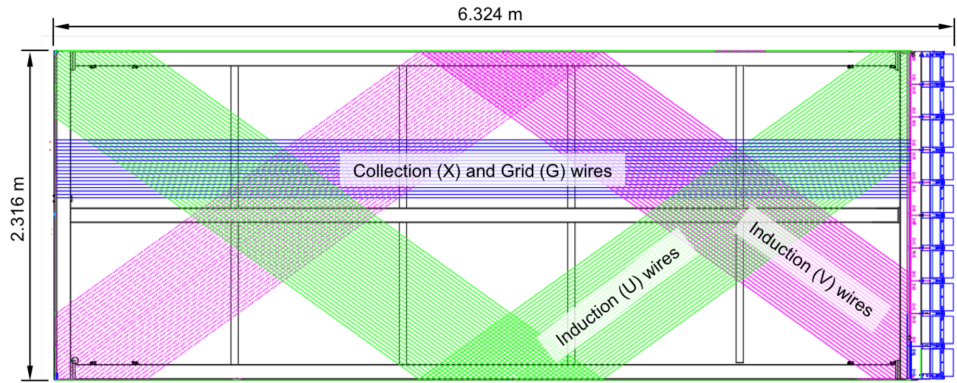


Figure 2.7: Illustration of the DUNE APA scheme showing small portions of the wires from the three signal planes (U, V, X) and fourth wire plane (G) present to improve the pulse shape on the U plane signals. The TPC electronics boxes, shown in blue on the right, mount directly to the frame and process signals from both the collection and induction channels [5].

The wires pitch is chosen so the volume can be fiducialize to a precision of 1%, in which the vertex position resolution is of 1.5 cm along each coordinate. Besides, the radiation length for photons in LAr is of 14 cm, the spacial resolution given by the pitch of  $\sim 0.47$  cm allows the gap between a neutrino interaction vertex and a photon conversion point to be easily visible. The tolerance of the wire pitch is  $\pm 0.5$  mm to maintain the reconstruction precision required [5].

Each wire will collect about 20k to 30k electrons from a minimum ionizing particle traveling parallel to the wire plane and perpendicular to the wire orientation. Therefore, a noise below  $1k e^-$  is required.

The ProtoDUNE-SP experiment (see Chap. 6) has set a bias voltage for the grids of -370 V, 0 V and +820 V for U, V and X planes respectively, and it has reported a signal-to-noise (S/N) of at least 12.1 for the U plane and up to 48.7 for the X plane [39]. Results that safely satisfy the DUNE specifications of  $S/N > 5$  for the U and V and  $S/N > 10$  for the X plane [5].

Each APA will host 10 Photon Detection (PD) modules shown in Figure 2.8 (Left). The X-ARAPUCA modules are  $209 \text{ cm} \times 12 \text{ cm} \times 2 \text{ cm}$  bars placed between the wire layers of the

<sup>6</sup>This condition is achieved if an angle  $\theta < 36.2^\circ$  is set.

APA (Right). Each module is composed by 24 X-ARAPUCA cells assembled in groups of six to form four X-ARAPUCA supercell. In total, 1,500 X-ARAPUCA modules will be installed in one DUNE FD module, which gives a total of 6,000 supercells installed in the 10 kt LArTPC.

The X-ARAPUCA device is described in Sec. 3.3.

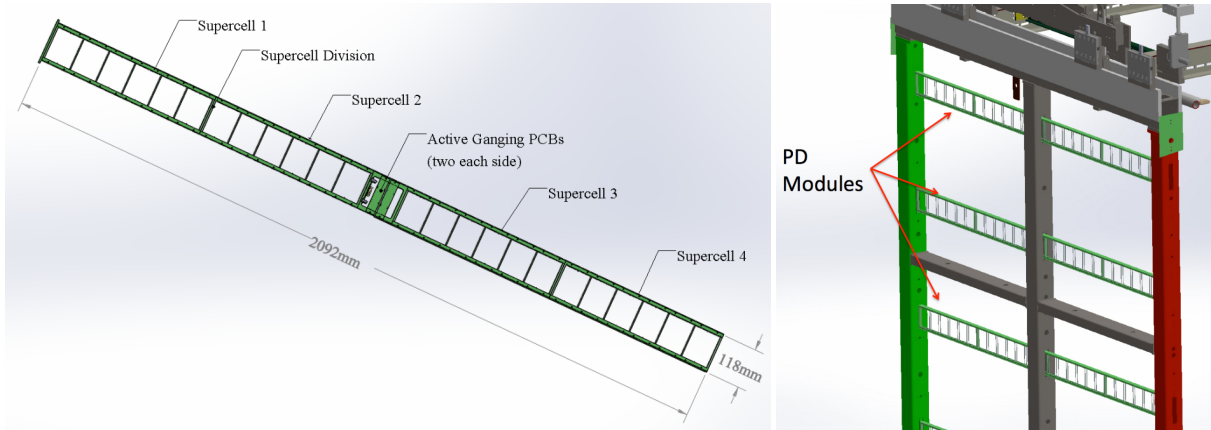


Figure 2.8: (Left) The X-ARAPUCA module schematic, composed by 24 X-ARAPUCA cells grouped into a set of four supercells. The active ganging PCBs, which read-out the signals, is displayed at the center [5]. (Right) 3D model of the X-ARAPUCA module assembled horizontally in the APA.

The 10 kt LArTPC will be hosted inside the cryostat of Figure 2.9, with outer dimensions of  $65.8 \text{ m} \times 17.8 \text{ m} \times 18.9 \text{ m}$ .

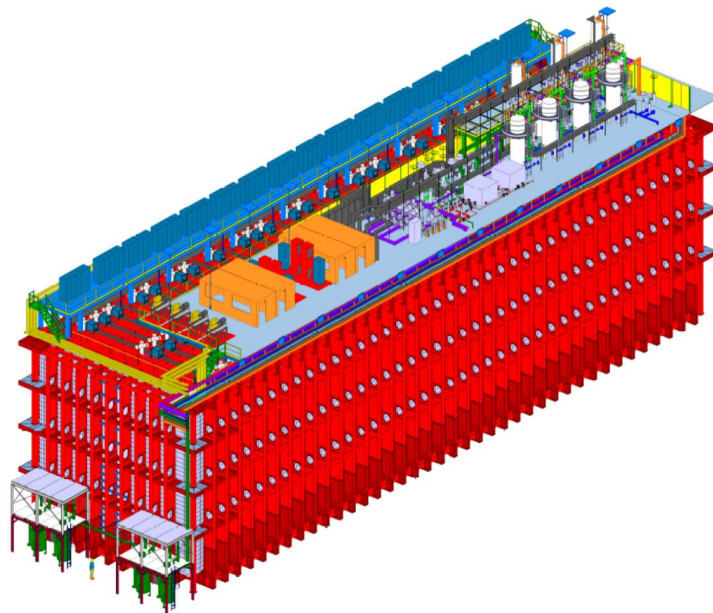


Figure 2.9: The cryostat that houses a 10 kt FD module. A mezzanine (light blue) installed 2.3 m above the cryostat supports both detector and cryogenics instrumentation. At lower left, between the LAr recirculation pumps (green) installed on the cavern floor, the figure of a person indicates the scale [5].

### 2.2.3. The DUNE specifications for the LArTPC

Here we report the high level specification of the far SP detector. The specifications shown in Table 2.2 concern the TPC and Table 2.3 concern the Photon Detection System.

Table 2.2: TPC specifications [5].

Description	Specification (Goal)	Justification
APA wire angles	$0^\circ$ for the collection wires; $\pm 35.7^\circ$ for induction wires	Minimize inter-APA dead space.
APA wire spacing	4.669 mm for U, V; 4.790 mm for X, G	Enable 100% efficiency MIP detection and a 1.5 cm yz vertex resolution. Spatial resolution lower than the radiation length for photons allow a visible gap between the neutrino interaction vertex and photon conversion point.
Minimum drift field	$> 250$ V/cm ( $> 500$ V/cm)	Reduces recombination, reduces impact of $e^-$ lifetime and diffusion, and space charge.
System noise	$< 1000 e^-$	Ensures $S/N > 5$ on induction planes for pattern recognition and two-tracks separation.
Front-end peaking time (readout)	$1 \mu\text{s}$	Ensures vertex resolution; optimized for 5 mm wire spacing.

Table 2.3: PDS specifications [5].

Description	Specification (Goal)	Justification
Light Yield	$> 20$ p.e./MeV (average); $> 0.5$ p.e./MeV (minimum)	PDS energy resolution comparable with TPC for 5 to 7 neutrinos from Supernova. Allows tagging of $> 99\%$ of nucleon decay backgrounds with light at all points of the detector.
Time resolution	$< 1 \mu\text{s}$ ( $< 100$ ns)	Position resolution of 1 mm for 10 MeV SNB candidate events in a rate lower than $1 \text{ event m}^{-3} \text{ms}^{-1}$ .
LAr nitrogen contaminant	$< 25$ ppm	Necessary to reach the 0.5 p.e./MeV PDS sensitivity for triggering proton decay near the cathode.
Signal-to-noise	$> 4$	Keep data rate within electronic bandwidth limit.
Dark noise rate.	$< 1$ kHz	Keep data rate within electronic bandwidth limit.

# Chapter 3

## Light collectors

In DUNE, the Photon Detection System (PDS) is based on the ARAPUCA<sup>1</sup> technology (Sec. 2.2.2). The ARAPUCA device needs to efficiently detect liquid argon (LAr) scintillation light with a wavelength of 127 nm as it improves the determination of the neutrino interaction vertex for beam events and will be crucial to determinate the vertex for non-beam events. It will also help to trigger SNBs and to perform calorimetric measurements. A review of the LAr scintillation is given in the first section. In the following sections the ARAPUCA light trapping device is introduced with the description of the two main prototypes, the Standard ARAPUCA (S-ARAPUCA) and the X-ARAPUCA. The device components are described with more details in the succeeding sections.

### 3.1. Scintillation light in LAr

#### 3.1.1. Process and photons production

The passage of ionizing radiation in LAr produces excitation and ionization of the argon atoms that will ultimately produce an excited dimer state ( $\text{Ar}_2^*$ ), as shown in the diagram of Fig. 3.1. In the case of ionization (bottom part of the diagram), argon ions will gather together and form an ionized molecule ( $\text{Ar}_2^+$ ) and, if the electric field is not high enough to completely separate the electron, the recombination process will generate an excited molecule ( $\text{Ar}_2^*$ ). The excitation of argon atom (top part of the diagram) will result in the same excited molecule, this molecule will lose energy through the emission of a scintillation photon decaying to the fundamental state remaining with two separate argon atoms [37].

One can estimate the maximum number of photons  $N_{ph}$  produced in the scintillation. The number of photons originated from ionized atoms will be proportional to the energy deposited divided by the average energy expected per ion pair, that is  $N_i = E_0/W_l$  [47]. The ratio of the number of excited atoms to the number of ionized ones ( $N_{ex}/N_i$ ) produced by the passage of an ionizing particle is assumed to be independent of the particle type and energy and is given by [45, 48, 49]:

$$\frac{N_{ex}}{N_i} = 0.21 \quad (3.1)$$

---

<sup>1</sup>*Arapuca*, from the original *ara'puka*, comes from tupi-guarani and refers to a handcraft bird trap.

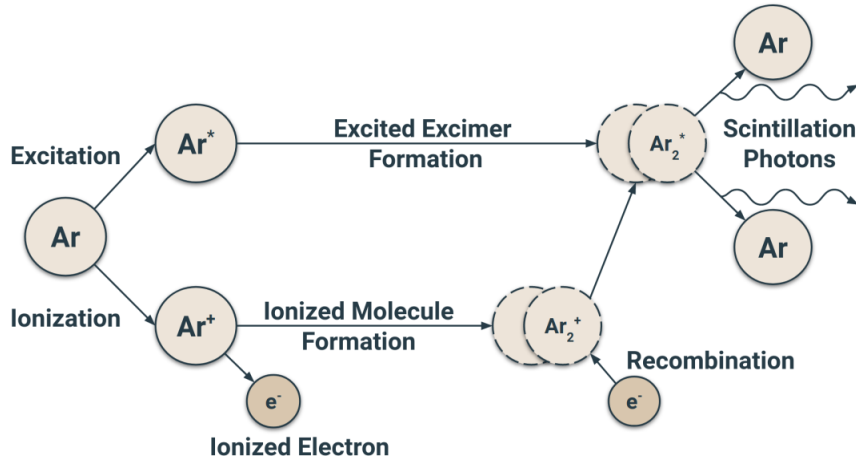


Figure 3.1: Schematic of scintillation light production in argon [5].

Therefore, we can consider that:

$$N_{ph} = N_i + N_{ex} = N_i \cdot (1 + N_{ex}/N_i) = E_0/W_l \cdot (1 + N_{ex}/N_i), \quad (3.2)$$

which can assume the form:

$$N_{ph} = \frac{E_0}{W_{ph}^{\min}} \quad (3.3)$$

with

$$W_{ph}^{\min} = \frac{W_l}{1 + N_{ex}/N_i} = 19.5 \pm 1.0 \text{ eV} \quad (3.4)$$

as the minimum (or average) energy<sup>2</sup> to produce one scintillation photon (at maximum yield) [45, 48]. Therefore, the maximum number of photons emitted per MeV deposited is taken by assuming  $E_0 = 1 \text{ MeV}$ :

$$Y_{ph}^{\text{ideal}} \sim 51.3 \times 10^3 \text{ photons/MeV}. \quad (3.5)$$

The light yield of Eq. 3.5 assumes that all the ionized or excited atoms produce scintillation light, thus neglecting quenching processes (see Sec. 2.1.4) and electrons escaping recombination (see Fig. 3.3). In Chapters 5 and 6 a maximum light yield of 51,000 photons/MeV was assumed as input of Monte Carlo simulations.

However, the light yield of LAr is affected by the type of particle and the Linear Energy Transfer<sup>3</sup> (LET). Light particles, such as electrons and muons, will have a decreased light yield due to escaping electrons from recombination because of the low density of ionized

<sup>2</sup>In Ref. [48]  $W_{ph}^{\min}$  is reported as  $W_{ph}(\text{max})$  to emphasize that this is the maximum absolute scintillation.

<sup>3</sup>The main difference between LET and stopping power is the fact that LET does not take into account the production of high energetic electrons production [50], being a locally energy loss described as restricted stopping power. If there is no production of large energy electrons, LET becomes the unrestricted linear energy transfer which equals to the stopping power

atoms. Non-relativistic heavy particles, such as protons, alpha particles and fission fragments, will cause a high density of excited states, that can diffuse and suffer a quenching process due to biexcitonic interactions [49].

Figure 3.2 shows the relative light yield with respect to the maximum yield (Eq. 3.5) as function of LET for different particles [48]. Therefore, it can be expected from a minimum ionizing particle (mip), which LET in LAr is about  $1.5 \text{ MeV}/(\text{g}/\text{cm}^2)$ , a relative light yield of  $Y_{ph}^{\text{mip}} = 0.8 \cdot Y_{ph}^{\text{ideal}}$ . Alpha particles, on the other hand, will have a relative light yield of 0.71. These values are used for the Monte Carlo simulation of Chapters 5 and 6.

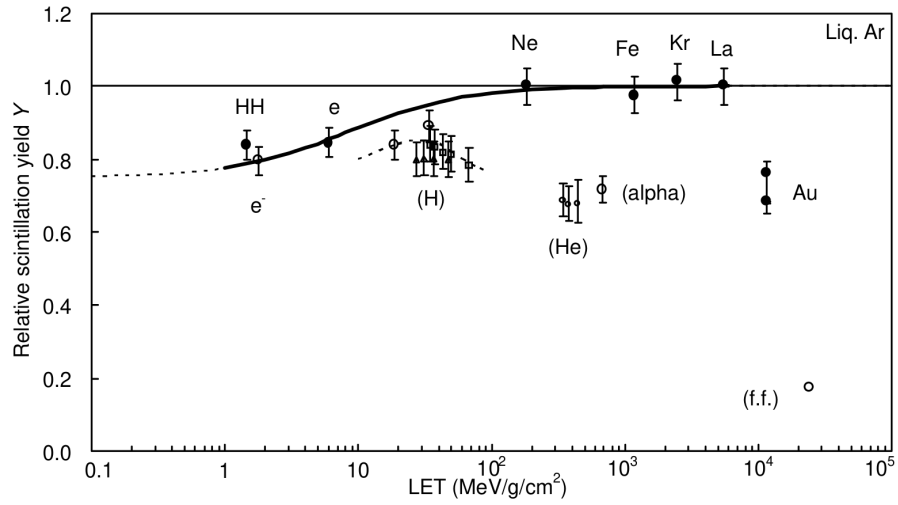


Figure 3.2: Relative light yield as function of LET for different particles in liquid argon. Solid circles are measurements for relativistic particles, while open circles are non-relativistic. Squares and small circles represent non-relativistic protons and helium, respectively [48].

### 3.1.2. Electron-ion recombination

The light yield is also affected by the electric field applied. Figure 3.3a shows the charge recombination probability versus the applied electric field, where the ICARUS experiment [38] has measured a recombination of the electron ion pair of 60% [51, 52] for a minimum ionizing particle and an electric field of 500 V/cm. The charge recombination factor  $R_C$  can be modeled as [52]:

$$R_C = \frac{Q}{Q_0} = \frac{A}{1 + (k/\epsilon)dE/dx}, \quad (3.6)$$

where  $Q_0$  and  $Q$  are the initial and collected charge, respectively.  $\epsilon$  is the electric field in kV/cm,  $dE/dx$  is the particle stopping power,  $A = 0.800 \pm 0.003$  is a normalization parameter and  $k = 0.0486 \pm 0.0006 \text{ (kV/cm)(g/cm}^2\text{)/MeV}$  is a Birks parameter [52]. By assuming

that only light from self excitation is produced when the charge collection is maximum, it was measured [51] that about 67% of the light of the LAr scintillation is produced by ionization process and only 33% is caused by the self excitation process<sup>4</sup>. The light recombination factor  $R_L$  will be the complementary of  $R_C$  as:

$$R_L = 1 - \alpha R_C, \quad (3.7)$$

where  $\alpha$  is an attachment factor [53]. Figure 3.3b shows the charge and light recombination factors as function of the electric field [51, 52, 54]. The electric field of 500 V/cm is a good compromise between light production and charge collection.

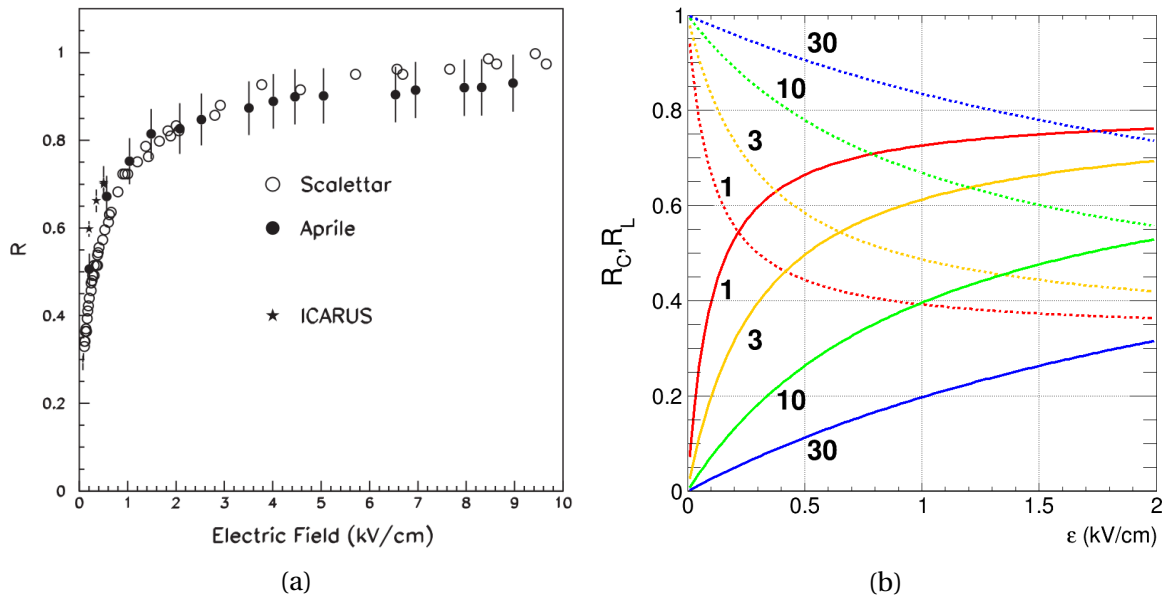


Figure 3.3: **(a)** Charge recombination of the electron-ion pairs with ICARUS [52], Scalettar et al. experiment [55] and Aprile et al. [56] versus electric field applied. **(b)** Recombination factors versus the electric field applied. The solid lines represent the charge recombination ( $R_C$ ) and the dashed lines represent the light recombination ( $R_L$ ) for different values of energy loss ( $dE/dx$ ) in units of minimum ionizing particles [51, 52, 54]. This plot is based on the image created by Craig Thorn in the LBNE DocDB 4482-v1.

The DUNE FD expects about 24,000 photons/MeV [5], because the light yield of 41,000 photons/MeV for minimum ionizing particles will have 60% reduction in the recombination due to the 500 V/cm electric field.

<sup>4</sup>The light yield (luminosity) and charge collected were measured as function of an electric field up to 10 kV/cm. At the highest field, the collected charge reached a maximum of 95% of the produced and the luminosity decreased 67%. At this electric field, only the self excitation process contributes with the light yield.

### 3.1.3. Emission spectrum and time profile

The scintillation light is emitted in the Vacuum Ultra Violet (VUV) in a ten nm band centered around 127 nm [57] as shown in Figure 3.4 [58] for liquid and gaseous argon, black and red lines respectively.

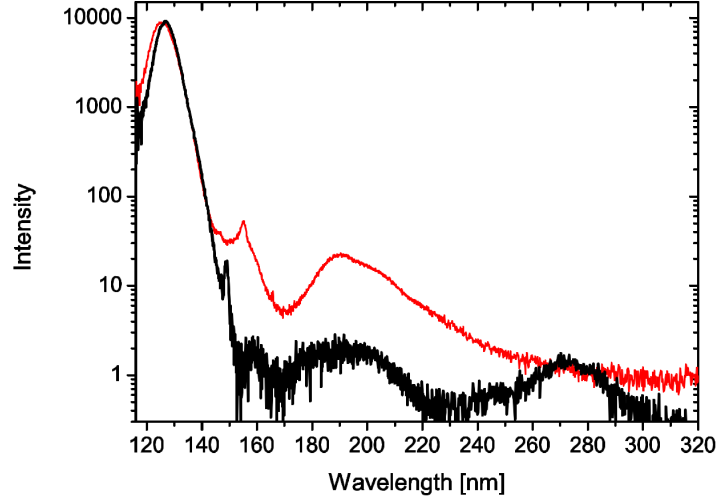


Figure 3.4: Scintillation light emission spectrum for LAr (Black line) and GAr (red line) [58].

Excited argon molecules have two possible excimer states, singlet and triplet ( $^1\Sigma_u$  and  $^3\Sigma_u$ ). The de-excitation of the  $^1\Sigma_u$  state is very fast with a characteristic time of  $\sim 6$  ns, while the  $^3\Sigma_u$  state, for been a forbidden transition, de-excites with a characteristic time of  $\sim 1600$  ns [37, 57].

The prompt light response of the LAr to the passage of ionizing radiation is the key to point the  $T_0$ , the time when the electrons started drifting, for non-beam events such as proton decays or supernovas since for beam events the  $T_0$  is calculated on the basis of the protons spill time at Fermilab. The drift time is taken by the difference between  $T_0$  and the arrival of the ionized electrons on the anode wires and it is used to reconstruct the coordinate along the drift direction with a resolution better than 1 mm. The coordinate along the drift direction is important to correct for the ionized charge absorption along the drift and to fiducialize the active volume of the detector [5].

The time evolution of the LAr scintillation signal  $I(t)$  can be described as the sum of two exponentially decaying distributions [37, 59]:

$$I(t) = A_S \exp\left(-\frac{t}{\tau_S}\right) + A_T \exp\left(-\frac{t}{\tau_T}\right), \quad (3.8)$$

where  $A_S$  and  $A_T$  are the relative amplitudes and  $\tau_S$  and  $\tau_T$  are the time constants of the singlet and of the triplet dimer states<sup>5</sup>, respectively, and the normalization  $A_S + A_T = 1$  is typically applied. The relative intensity of the singlet and triplet components ( $A_S/A_T$ ) is related to the ionization density of LAr and depends on the ionizing particle: 0.3 for electrons, 1.3 for alpha particles and 3 for neutrons [37, 59, 60].

The dependence of singlet and triplet (fast and slow) contribution with the type of particle is useful feature for particle identification (PID). In Chapter 5, a Pulse-shape Discrimination (PSD) method is applied to separate  $\alpha$ -particle signals from cosmic muons. For the DUNE experiment, the PID is mainly done by the TPC signal, because in such a large detector, the chance of having single particle events is pretty small [5].

### 3.1.4. Nitrogen contamination and quenching of light

The inelastic collisions of Ar excimers with Nitrogen molecules can cause the non-radiative de-excitation of the excimer, with consequent loss of the scintillation photons. The process can be summarized as follows:



In this situation, the quenching process decreases the excimer concentration  $[\text{Ar}_2^*]$ , while keeping constant the contaminant concentration  $[\text{N}_2]$ . As a first approximation, the first-order rate can be assumed as [59]:

$$\frac{d[\text{Ar}_2^*]}{dt} = -k_Q[\text{N}_2][\text{Ar}_2^*] \quad \longrightarrow \quad [\text{Ar}_2^*](t) = [\text{Ar}_2^*](t=0)e^{-k_Q[\text{N}_2]t}, \quad (3.10)$$

where  $k_Q = 0.11 \mu\text{s}^{-1}\text{ppm}^{-1}$  is the quenching rate constant. The  $\text{N}_2$  quenching process affects mainly the triplet component, due to its longer lifetime. The effective decay time constant can be written as:

$$\frac{1}{\tau_j^{\text{eff}}} = \frac{1}{\tau_j} + k_Q[\text{N}_2], \quad (3.11)$$

where  $j = [S, T]$  for singlet and triplet. Also the amplitude of each component is affected. Figure 3.5a shows the signal shapes of the LAr scintillation light for three different concentration of  $\text{N}_2$  [59]. One can see the two pure exponential components (Eq. 3.8) for 0 ppm concentration and the triplet time constant decreases with increasing  $\text{N}_2$  contaminant. To

---

<sup>5</sup>The components are often labeled as fast and slow to emphasize the time profile of each emission.

better illustrate this effect, Figure 3.5b brings the fitted values of singlet, triplet and intermediate<sup>6</sup> components. The singlet lifetime is affected only with high contaminant concentrations, otherwise, the triplet lifetime is the most affected.

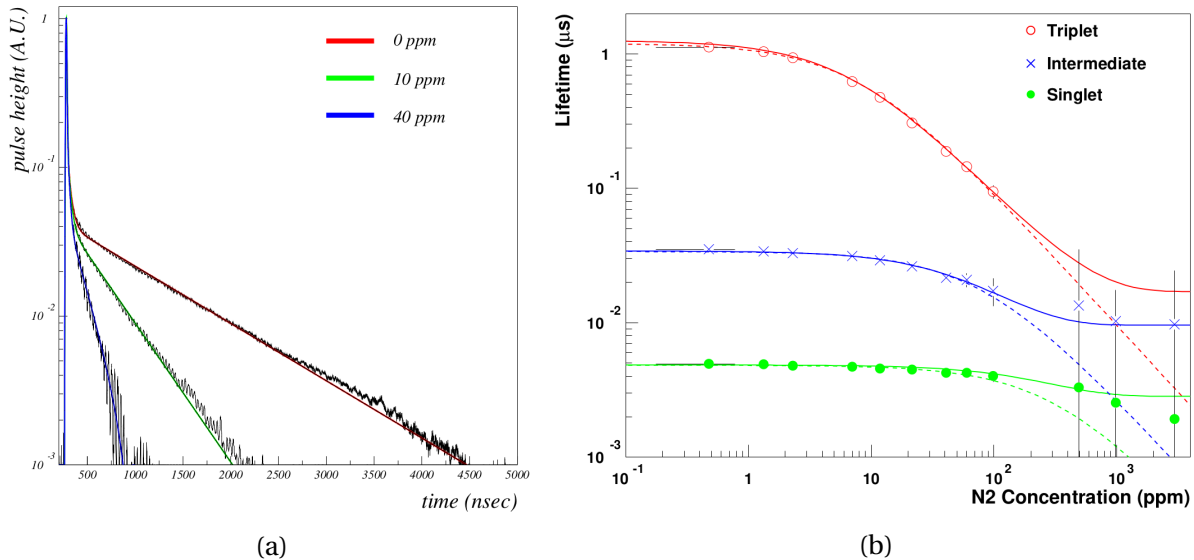


Figure 3.5: **(a)** LAr scintillation signal shape for 0 ppm, 10 ppm and 40 ppm of  $N_2$  contamination [59]. The fits are performed with an intermediate component to better adjust the data. **(b)** Lifetime of singlet, triplet and intermediate components versus  $N_2$  contaminant in ppm [59]. The dashed lines are fits considering Eq. 3.9, while the solid line is the fit considering a possible saturation at increasing concentration.

The DUNE experiment requires that Nitrogen contamination must be below 10 ppm [5].

### 3.1.5. Summary

Table 3.1 summarizes the LAr characteristics that are relevant for this work. The three first rows are parameters relevant for the TPC and scintillation, while the others concern only the light emission properties of LAr.

Rayleigh scattering is the elastic scattering of light by argon atoms. The Rayleigh scattering length of a photon strongly depends on its wavelength ( $\propto \lambda^{-4}$ ) and on the optical properties of the medium. Recent measurements<sup>7</sup> point to a Rayleigh scattering length of  $99.1 \pm 2.3$  cm for  $\lambda = 127$  nm [64]. The absorption length is related to the absorption of LAr scintillation light from impurities such as dissolved nitrogen.

<sup>6</sup>The intermediate component was introduced to better fit the data and, as reported at Ref [59] it is not well understood.

<sup>7</sup>The Rayleigh scattering length was previously calculated to be about 90 cm which was in disagreement with the measured value of  $66 \pm 3$  cm [61, 62]. Recently calculations [63] have pointed to a length of  $55 \pm 5$  cm, but with a higher refraction index.





dichroic filter or on the Vikuiti foils.

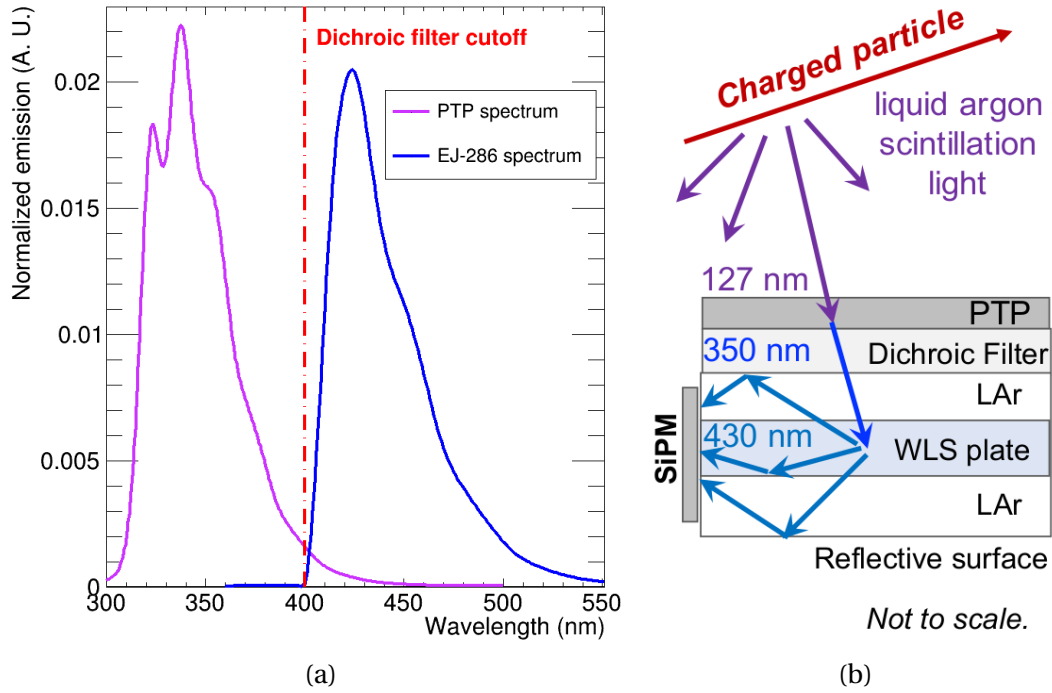


Figure 3.7: **(a)** The dichroic filter cutoff (red dashed line), the PTP (purple) and the EJ-286 emission spectra. **(b)** X-ARAPUCA principle of work, with total internal reflection and the reflective cavity trapping the photons [5].

Besides the fact that the internal WLS is no longer coated onto Vikuiti foil, the X-ARAPUCA can be deployed as either single-sided or double-sided by using either an opaque reflector plate (single) or a second dichroic filter window (double) on the second face (bottom part of Fig. 3.7b). This is an interesting feature of the device, allowing to place the double-sided X-ARAPUCAs in the central APA of DUNE (see Fig. 2.6), collecting light from both sides. The schematic of a double-sided X-ARAPUCA is displayed in Fig. 3.8, the two yellow transparent plates are the dichroic filters and the blue one is the wavelength shifter.

The structure of the X-ARAPUCA is made of FR-4 G-10 (Garolite<sup>®</sup>), a material with good adhesion to Vikuiti foils, cryogenic resistant, low thermal contraction, isolating and with a low cost and easy to manufacture.

### 3.3.1. The device challenges

Different factors can impact the X-ARAPUCA efficiency: the matching of spectrums and dichroic filter cutoff, the transmittance and reflectance of the dichroic filter, the thickness of the WLS slab, the thickness of the PTP deposition, the quality of the deposition, the efficiency of both WLS deployed, the amount of SiPMs to detect the light, the gap between the WLS

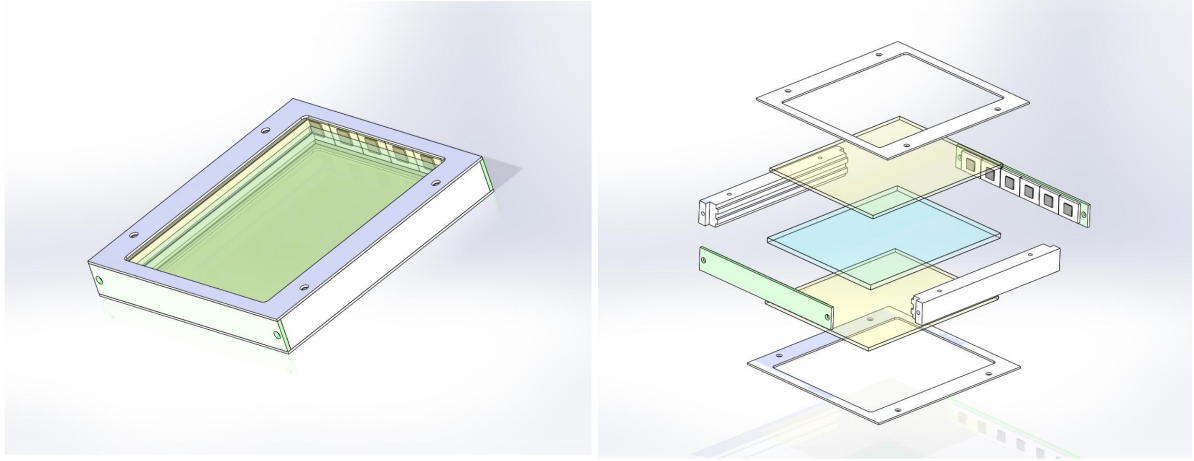


Figure 3.8: Simplified schematic of a double-sided X-ARAPUCA [5] assembled (left) and exploded view (right). The yellow plates are dichroic filters coated with PTP externally to the X-ARAPUCA and the blue plate is the WLS slab.

and the SiPMs, the SiPMs quantum efficiency. Some of these characteristics are quite easy to control and do not play a major role in the efficiency, while others can be more difficult to investigate and may significantly contribute to the light collection efficiency.

The gap between the WLS and the SiPMs is caused due to the higher thermal contraction coefficient of the WLS slab compared to the FR-4, in which the SiPMs are attached. The Shrinkage Factor for a 206 °C temperature drop was measured<sup>9</sup> to be  $1.4 \times 10^{-2}$  m/m for Polystyrene (WLS Bars) and  $2.1 \times 10^{-3}$  m/m for the FR-4 G10 [5]. Simulations performed for the X-ARAPUCA prototype [74] showed a drop of  $\sim 30\%$  in the total efficiency of the device for a separation of 0.5 mm, while keeping almost constant up to 1.5 mm. New designs are under investigation to achieve a better optical coupling between the SiPMs and the WLS bars.

The minimum value of the PTP layer must be between 100 to 200  $\mu\text{g}/\text{cm}^2$  to ensure the VUV is fully absorbed. For the DUNE FD module a thickness of 400  $\mu\text{g}/\text{cm}^2$  was chosen, to ensure that the minimum thickness is reached everywhere on the filter, even in the case of exceptional fluctuations [5]. The WLS slab thickness was chosen as 3.5 mm to allow almost complete absorption of the photons emitted by the PTP to ensure the nominal conversion efficiency and to keep a 2 mm gap in which LAr can enter in both sides preventing physical contact with the surface.

<sup>9</sup>The units given is a shrink of one meter for each one meter of material.

### 3.3.2. The Short Baseline Neutrino Detector (SNBD)

The X-ARAPUCA with two dichroic filters deployed, namely X-ARAPUCA double-cell, will also be part of the Short Baseline Neutrino Detector (SBND) light detection system. The Short Baseline Neutrino (SBN) program at Fermilab [24, 75, 76] consists of three LArTPCs: the SBND, the ICARUS T600 [38] and MicroBooNE [77], and aims to resolve the short baseline  $\nu_e$  and  $\bar{\nu}_e$  appearance measured by MiniBooNE and LSND experiments. The SBND will be a 112 t single phase LArTPC 110 meters away from a neutrino beam with energy up to 3 GeV. Besides the primary scientific goal of measuring the  $\nu_e$  appearance and  $\nu_\mu$  disappearance at the same time, the experiment will also perform high-precision neutrino-argon cross section measurements.

The SBND will count with 200 X-ARAPUCA double-cell and 120 PMTs of 8 inches. The light detection system in SBND will allow a more precise vertex localization and will help to handle the background induced by cosmic rays (as it is a ground level experiment). To improve the light collection, the SBND cathode plane has reflective foils coated with TPB. This effect is shown in Figure 3.9 [78], where the average number of detected photons per MeV for different distances to photocathode plane (equivalent to distance to the PDS) is displayed. Direct scintillation light is displayed in blue and decreases the farther the light

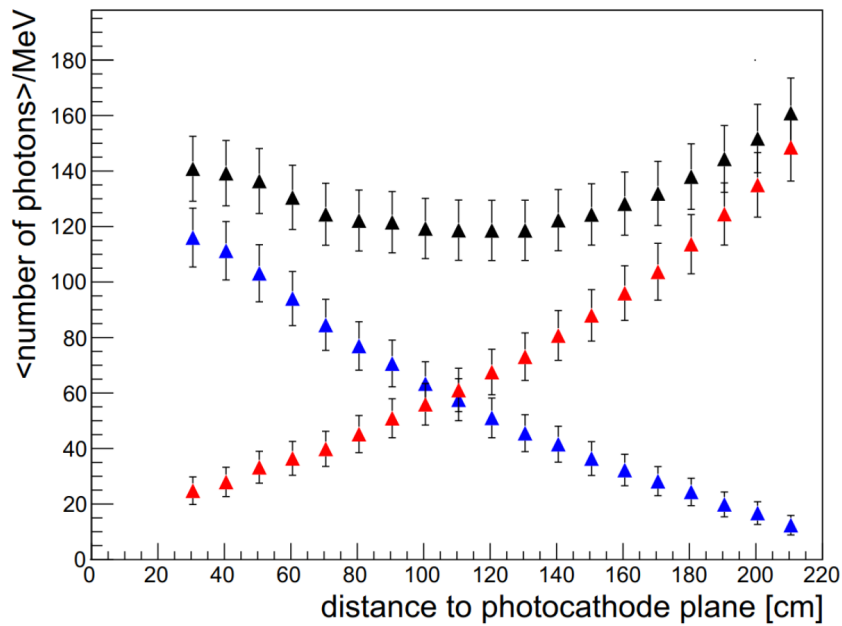


Figure 3.9: Average number of detected photons per MeV as a function of the distance to the photocathode plane (PDS at 0). The direct UV light detection (in blue) decreases with the distance of the source, while the reflected light (in red) increases. The total light (black) is more uniform along the source distance from the PDS system [78].

source is from the PDS. On the other hand, the reflected light, in red, will increase. The total light is displayed in black and shows a good uniformity along the drift direction.

In order to detect the 430 nm light, 20% of the PMTs are sensitive to visible light while the other 80% are coated with TPB to detect UV light. Besides, 100 X-ARAPUCAs will be sensitive to UV light and 100 X-ARAPUCAs will be sensitive to visible light.

## 3.4. Silicon Photomultipliers (SiPMs)

### 3.4.1. Principle of working

The ARAPUCA device will use Silicon Photomultipliers (SiPMs) or Multi-Pixel Photon Counters (MPPCs) as active photon sensors. Silicon (Si) has an intrinsic high resistance, however, doping with atoms of 5 or 3 electrons in the outermost electron shell (such as Phosphorus or Aluminium) can turn the doped Si into an electron or hole (positive) donor, respectively. An electron donor region is named N region and the hole donor is named P region. The N region is formed by the donation of 4 electrons from the electron donor to complete the Si valence band and an extra free electron in the conduction band, this free electron becomes the charge carrier. In a similar way, the P region is formed by donation of 3 electrons from the donor to the Si valence band, leaving a free empty space (hole) for an electron, this hole can pass from atom to atom in the crystal lattice and becomes the positive charge carrier.

A PN junction is formed by the contact of the two regions: electrons from the N region will drift towards the P junction and occupy empty holes, while holes in the P region will drift towards the N junction for free electrons. The accumulation of negative charges and positive charges in the P and N region will produce an electric field that opposes to the transition of charge carries to other regions. The junction enters in equilibrium, where the electron does not have enough energy to cross the junction layer, called *depletion layer*. This is the standard configuration of a diode, where the P layer is the Anode and the N layer is the Cathode as shown in bottom of Figure 3.10a [79]. Just above, a diagram shows the positive and negative charge accumulation forming the electric field.

The energy gap between the valence and conduction bands from the layer is kept the same (typically of 1.14 eV for Si [79]), however, P layer bands will increase energy while N

layers will decrease<sup>10</sup>, creating a potential barrier that the electrons cannot surpass. One can break this balance by introducing an opposite electric field, which will lower the potential and let the electrons freely drift back. This is namely forward bias, where positive voltage is applied to the anode (P layer) and negative to the cathode (N layer). In the case of SiPM, a reverse bias is used, increasing the intensity of the electric field and the gap between the conduction bands of P and N layers.

The SiPMs light detection will happen when photoelectric effect happens in the P layer or N layer passing an electron from the valence band to the conduction band, forming an electron-hole pair. The electron drifts towards the cathode N (positively biased) and holes towards the anode. The electric field gives enough energy to the charge carriers to produce new ionization while traveling, creating an avalanche effect.

Thermal agitation can cause a surplus of charge carriers resulting in the same process, this is defined as “Dark Current”. In SiPMs at room temperature the Dark Current dominates, typically making unfeasible to see single photo-electrons.

The diagram of Fig 3.10b shows one microcell or pixel, for a P-to-N pixel<sup>11</sup>. A resistor

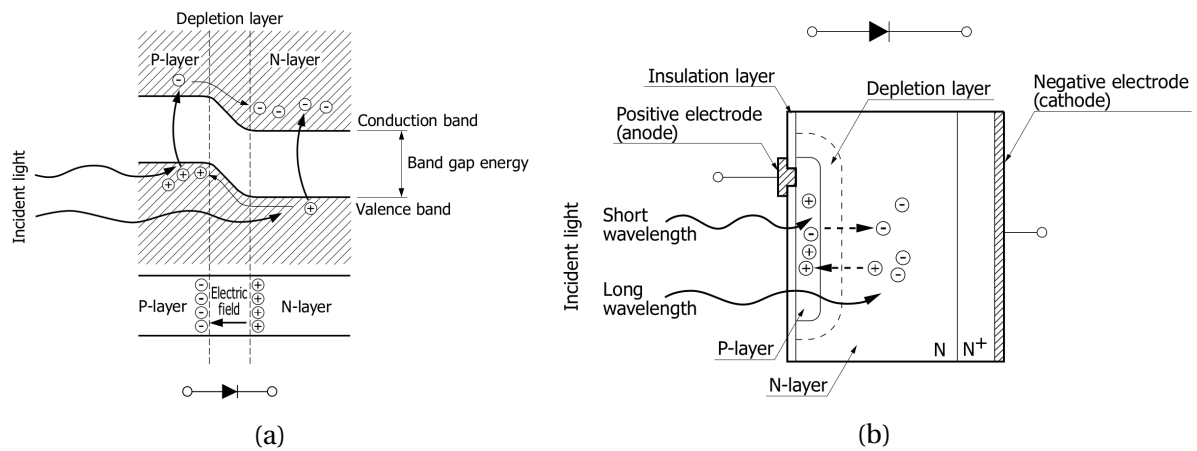


Figure 3.10: **(a)** Doped silicon energy gap between the valence and conduction bands [79]. **(b)** Absorption of light by a Silicon PN photodiode [79].

(namely quenching resistor) is introduced in the anode to quench the current driven by the avalanche. The quenching resistor allows to operate the photodiode in Geiger-mode, that is above the breakdown voltage where the gain stops to be linear and increases exponentially (in theory, infinity gain). The microcells are ganged together in parallel as shown in

<sup>10</sup>The energy bands of P layers is naturally higher than N layers, because the impurities in the P layer can exert lower force in the electrons, resulting in a slightly later orbit with higher energy.

<sup>11</sup>P-to-N are more sensitive to Ultra-Violet/blue, because shorter wavelength photons have a low penetration depth, being more easily absorbed in the P-layer. N-to-P pixels are, therefore, more sensitive to red/Near-infrared wavelengths.

Figure 3.11 forming the SiPM matrix, biased positively in the cathode (top connector) and signal read on the anode<sup>12</sup> (bottom connector). The center-to-center distance between the microcells, defined as pitch, can change for different SiPMs. The S13360-6050VE MPPC used in the liquid argon tests in Brazil (Chapter 5) has a pixel pitch of  $50\ \mu\text{m}$  and a  $6\times 6\ \text{mm}^2$  unity is composed by 14336 pixels.

A SiPM will have a gain around  $10^5$  to  $10^6$  operating in the Geiger-mode. The Avalanche Photodiode (APD), utilized in the Monochromator tests (Sec. 4.2), consist of a single pixel operated in the linear region gain of the reverse bias, having a lower gain from one to a few hundreds. The APD high sensitivity compensate the low gain, being suitable to detect higher flux of photons with respect to a SiPM.

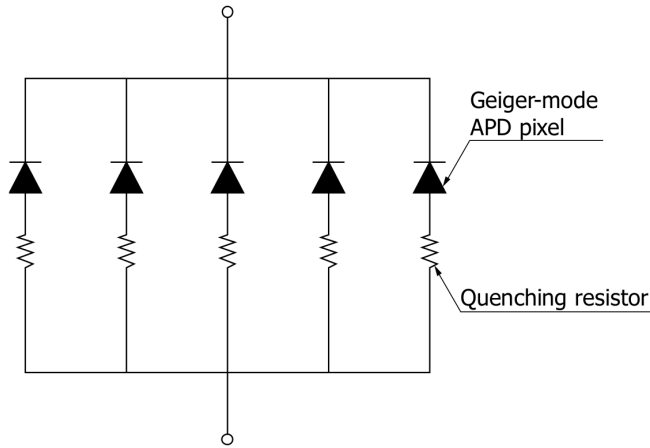


Figure 3.11: Concept of the MPPC matrix of Geiger-mode Avalanche Photodiode (GAPD) pixels connected in parallel [79].

### 3.4.2. Afterpulses and Cross-talk

Afterpulses are caused by impurities that trap a portion of the avalanche carriers for a short time during the avalanche. A new avalanche will start in their release causing a secondary late signal. If the afterpulse is released during the SiPM recovery time (the characteristic discharge time), its amplitude will be shorter than of a regular pulse of one photoelectron (p.e.) as shown in Figure 3.12a. If the release is done after the recovery time of the SiPM, the afterpulse will have a full 1 p.e..

Cross-talk, or optical crosstalk, is caused due to energy loss of the avalanche carriers into emission of photons with Near-infrared (NIR) wavelength [80]. These secondary photons

<sup>12</sup>The read-out at the negatively biased anode make the SiPM signal positive.

can reach a neighboring pixel and initiate avalanches in them. The output is a signal with amplitude and charge higher than the original signal as shown in Figure 3.12, where the number of events with amplitude greater than 1 p.e. has increased due to cross-talk.

Both effects, afterpulses and cross-talk, can be triggered by photons or thermal carriers (Dark Current).

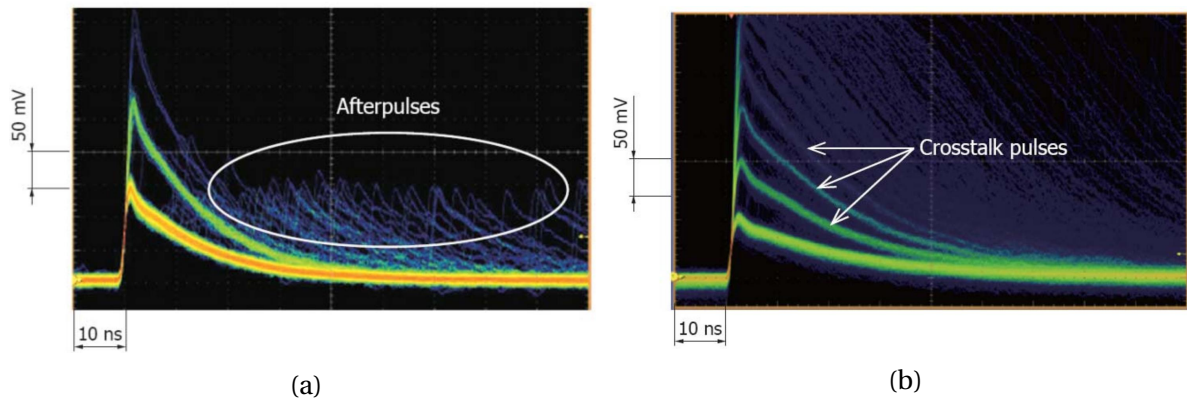


Figure 3.12: Waveforms showing the occurrence of afterpulses **(a)** and cross-talk **(b)** [79]. One can notice that afterpulses have amplitude lower than 1 p.e., while the cross-talk increases the events with more than 1 p.e..

The DUNE FD module will have 48 SiPMs ganged together with the requirement to operate with a  $S/N > 4$  and a dark noise rate, or Dark Count Rate (DCR), lower than 1 kHz.

### 3.5. Wavelength shifter

The outer Wavelength shifter (WLS) of the S-ARAPUCA and the X-ARAPUCA is the para-Terphenyl (PTP) [67]. For the S-ARAPUCA tetra-phenyl butadiene (TPB) [68] was used as the inner wavelength shifter. Organic WLS, such as PTP and TPB are aromatic hydrocarbons compounds that contain linked benzene-ring structures, as shown in Figure 3.13.

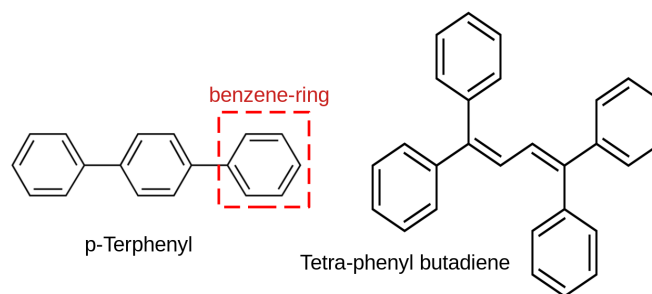


Figure 3.13: Organic wavelength shifters para-Terphenyl (PTP) and tetra-phenyl butadiene (TPB).

The wave shifting is a process where higher energy photons transfer their energy to the WLS which re-emits photons with a lower energy. Free valence electrons (occupying the so called  $\pi$ -molecular orbital [81]) absorb the photons and make a transition from the singlet ground state  $S_0$  to an excited singlet states ( $S_1, S_2, S_3$ , etc.) as shown in Figure 3.14a (thinner lines are vibrational states).

After excitation, electrons can immediately decay ( $\leq 10$  ps) to the  $S_1$  state without radiation emission, a process named internal degradation. Molecules also go through vibration relaxation to lose any excess vibrational energy, transferring the electrons from the vibrational states to the lowest excited state (tick lines). There is now a high probability of a de-excitation from  $S_1$  state to one of the ground singlet vibrational states within a few nanoseconds. This process is called fluorescence, with a prompt light emission. The fact that  $S_1$  states can decay to  $S_0$  vibrational states with emission of photons with energy lower than that required for the transition  $S_0 \rightarrow S_1$  also explains why the material is typically transparent to its own light [81].

Alternatively, electrons can also jump to triplet states ( $T_1, T_2$ , etc.) by inter-system crossing<sup>13</sup>. The decay from triplet states to ground state is a highly forbidden transition by selection rule, therefore, this process (called phosphorescence) takes place with a “long time” emission, it can take from milliseconds to several minutes or even hours. The contribution of light from phosphorescence is negligible for most organic crystals.

Figure 3.14b shows the PTP absorption and emission spectra [82]. It is very common to have the absorption and emission spectrum intercepting each other as seen around 300 nm. A good WLS needs to have a high shifting efficiency, emit mostly prompt light and needs to be transparent to its own light.

For the WLS slab, the principle of scintillation is the same. The main difference is that they are a solution of organic scintillators in a solid plastic solvent. For instance, the EJ-286 slab uses polivyniltoluene (PVT) as plastic solvent (the organic scintillator is a company secret). The WLS developed by the G2P co. and tested at Milano Bicocca (see Sec. 4.4) uses Poly(methyl methacrylate) (PMMA) doped with 2,5-Bis(5-tert-butyl-benzoxazol-2-yl)thiophene (BBT).

---

<sup>13</sup>Photons will, ideally, not transfer to the triplet states from the ground singlet state because it is a forbidden transition.

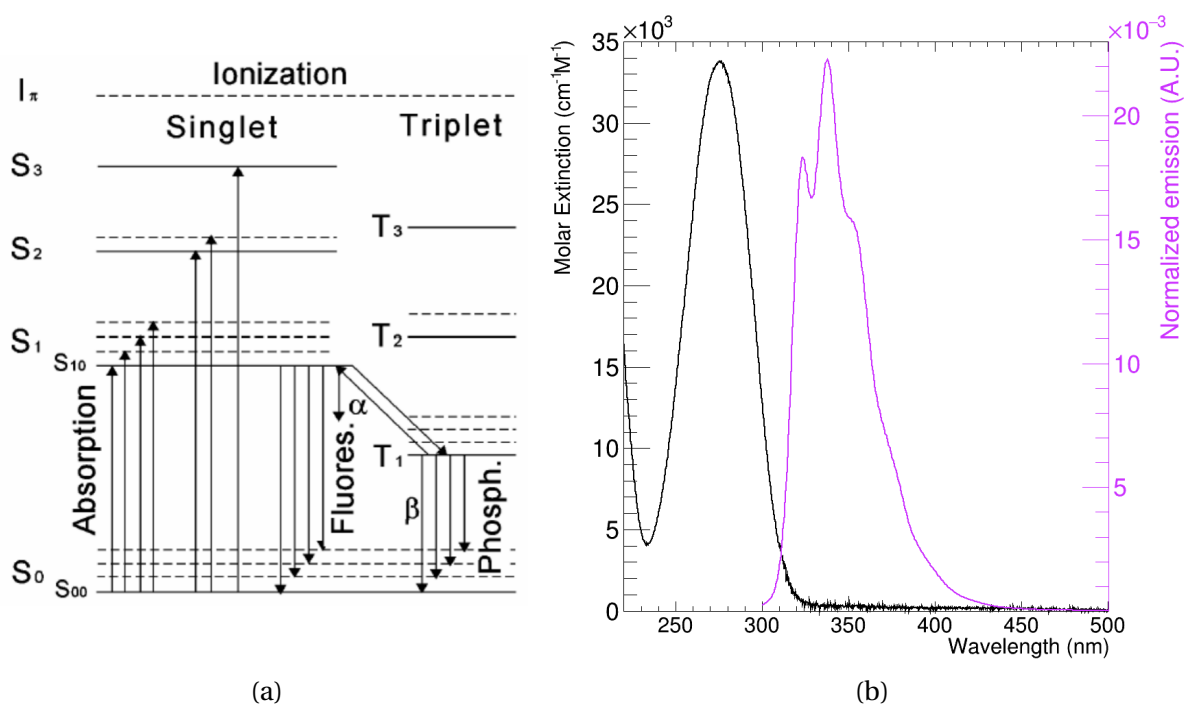


Figure 3.14: (a) Jablonski diagram showing the energy levels of an organic wavelength shifter [83]. (b) Absorption and emission spectra of PTP(taken from Ref. [82]). The absorption is giving in  $\text{cm}^{-1} \text{M}^{-1}$  where  $M = \text{mol}/\text{m}^3$  is the molar concentration.

### 3.6. Dichroic filter

The dichroic filter plays a major role in the trapping effect of the ARAPUCA. The dichroic filter is a thin interference film, like tantalum or silicon oxides, that selectively let a specific band of light pass through the filter while being highly reflective to other colors. The principle of work is the same as thin oil film in water: a thin layer of oil will reflect an incident light on its surface and in the contact face with water. Depending on the wavelength and length traveled by the reflected light with water surface it can create a constructive or destructive interference with the incident reflected light. Dichroic filters use this property by coating layers of thin materials over an optical surface.

Figures 3.15a and 3.15b show the transmittance and reflectance of the (Edmund optics [84]) dichroic filter. Transmittance and reflectance of the filter will also depend on the angle and polarization of incident light, therefore an average is given. If compared with Fig. 3.7a with the PTP and EJ-286 emission spectrum, one can notice that PTP light is transmitted through the filter with  $\sim 90\%$  efficiency and the EJ-286 re-emitted light will be reflected (and therefore trapped) with a  $\sim 98\%$  efficiency.

As the PTP is coated onto the surface of the dichroic filter, it is of great importance that

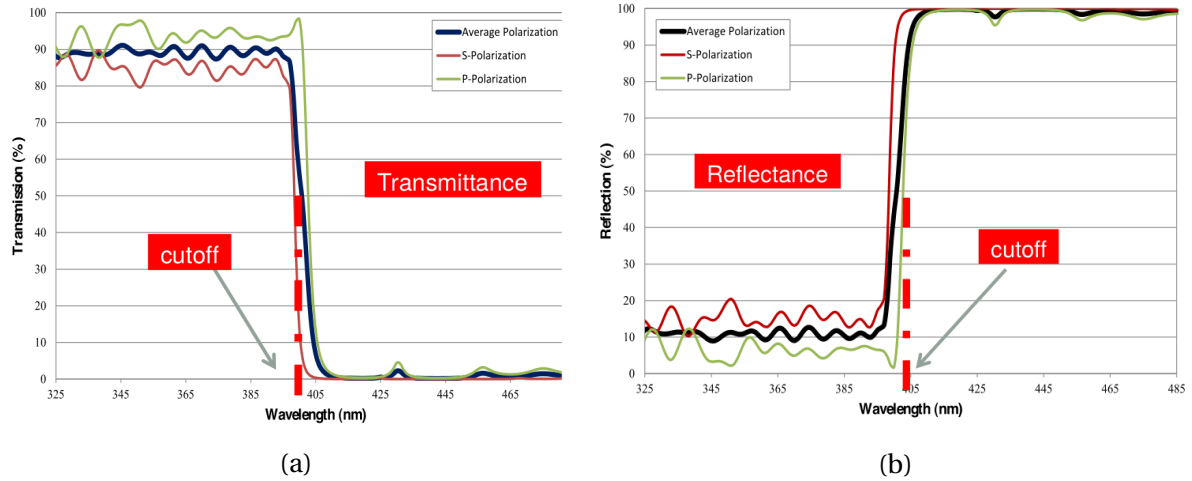


Figure 3.15: Dichroic filter transmittance **(a)** and reflectance **(b)** measured for two different light polarities and the average [66].

it has good adhesion to the PTP and is able to survive to several cryogenic cycles without losing the quality of the coated film or filter. In total, 48,000 dichroic filters will be deployed in the DUNE FD module. Dichroic filters from four different companies were investigated, Edmunds optics [84], Opto Electronica S.A. [85], Ashai [86] and Omega Optical Inc. [87]. Edmunds dichroic filters did not present a good performance for the S-ARAPUCA tests. The high cost of the Omega filters is impractical for the usage in DUNE. Opto filters were chosen as the baseline option by the Collaboration, since they showed performances competitive with the other filters and are much cheaper.

# Chapter 4

## Research and Development

In this chapter the research and development (R&D) of the S-ARAPUCA and X-ARAPUCA carried out during the period of this Ph.D thesis will be discussed. In the first section, the Dark Box set-up is presented, in which the trapping effect of the ARAPUCA could be tested. In Section 4.2 and 4.3 the measurements with Monochromator are presented. Section 4.4 show the room and cryogenic temperature tests performed in Italy for a new wavelength shifter to enhance the X-ARAPUCA light collection efficiency.

### 4.1. Dark Box Arapuca prototype

The liquid argon tests performed for the X-ARAPUCA and presented in Chapter 5 are not easy to be performed. The prototyping of the device involves the coating of PTP on a dichroic filter and, for the S-ARAPUCA, the coating of TPB on Vikuiti. After assembled, the ARAPUCA needs to go under liquid argon, a complex procedure that needs time and investment. In order to speed up the optimization process, several tests of ARAPUCA prototypes were performed in a specifically designed Dark Box.

The Dark Box set-up consists in an 3D printed S-ARAPUCA coupled with a Photomultiplier tube (PMT) as shown in Figure 4.1. The S-ARAPUCA was a  $5 \times 5 \text{ cm}^2$  area and 1 cm height cavity with Vikuiti [69] on the internal surfaces. A drawer-like compartment holds the internal wavelength shifter coated on Vikuiti. The PTP was coated on optical glass and could be placed over the dichroic filter as seen in Fig. 4.1a. A natural Uranium alpha source (see Sec. 5.1) is placed over the PTP which will scintillate, producing light around 350 nm. The light detection is then performed by a Photomultiplier ETL D750 (see Appendix C) in the open cavity of the device, with a 3D mask to cover any external light (Fig 4.1b). Assembling the S-ARAPUCA as described makes it much easier to change between different components of the device, enabling the study of different WLS molecules type and thicknesses and dichroic filters.

The setup was read-out by a CAEN Digitizer DT5720B with 12 bit resolution and 250 MSamples/s.

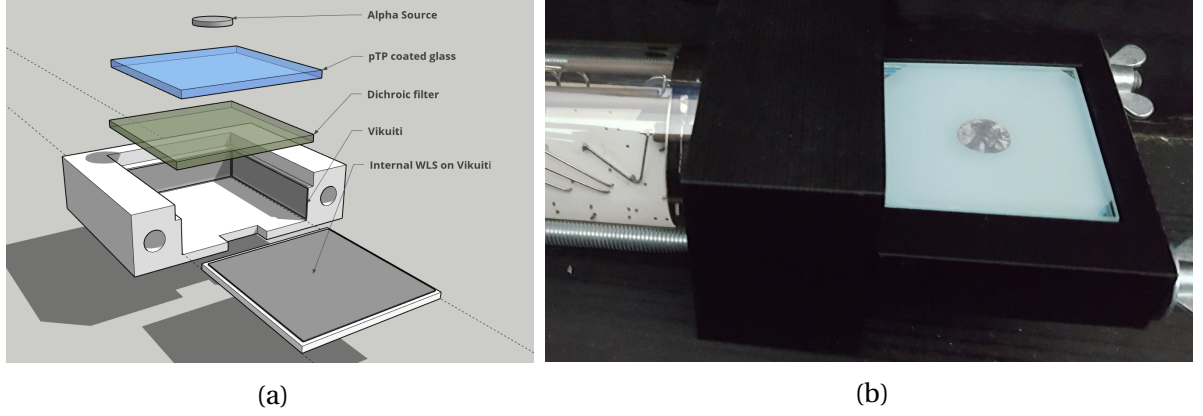


Figure 4.1: **(a)** S-ARAPUCA 3D model used in the Dark Box test. **(b)** Photo of the experimental setup showing the PMT ETL D750 attached to the ARAPUCA.

#### 4.1.1. Calibration

The system was calibrated by searching for single photo-electrons in the tail of the signal as shown in Figure 4.2, a method similar to the one described at Sec. 5.2.2. Peaks of photo-electrons produced by thermionic emission are searched between  $5\sigma$  and  $20\sigma$  from the baseline and integrated for 36 ns. In this illustrative waveform, three signals from the scintillation of  $\alpha$  particles into PTP can be seen, six other signals are integrated.

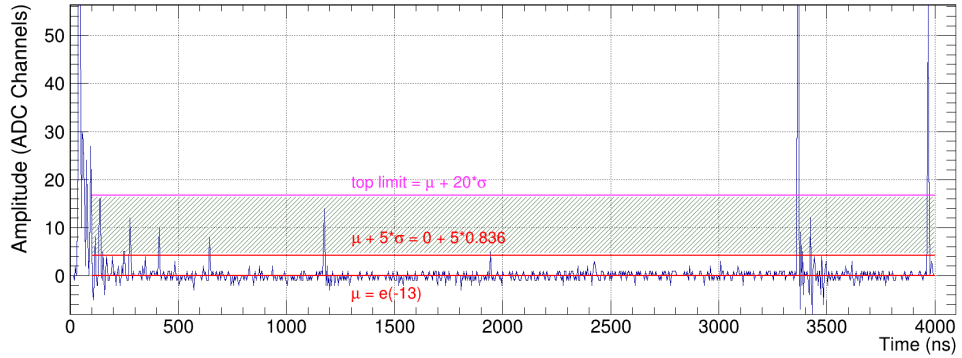


Figure 4.2: Single photo-electron selection, events inside 5 and  $20\sigma$  from the baseline are integrated for 36 ns.

Figure 4.3 shows the single photo-electron (s.p.e.) charge spectrum obtained. The fit is performed with  $N + 1$  Gaussian distributions, where the first one corresponds to the baseline noise and the others correspond to one or more photo-electrons response. The noise and s.p.e. Gaussian distributions have 3 free parameters each (mean value, standard deviation and normalization constant). The other Gaussians have mean and standard deviation constrained to be  $N \times \mu_1$  and  $\sqrt{N} \times \sigma_1$ , where  $\mu_1$  and  $\sigma_1$  are the mean and standard deviation of the s.p.e..

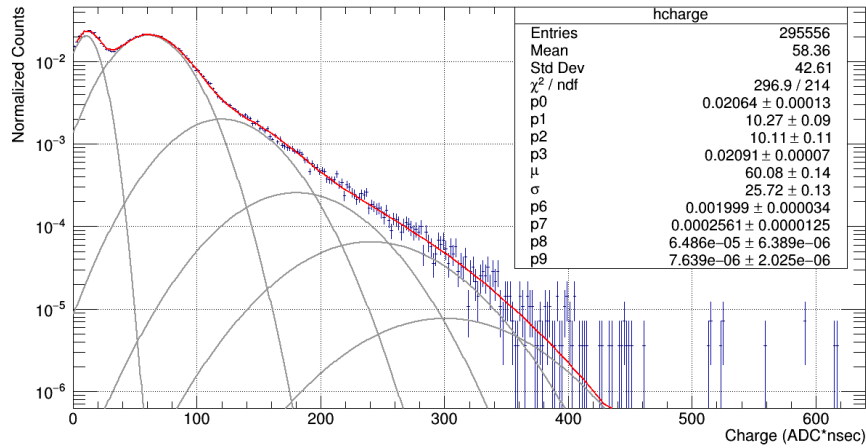


Figure 4.3: Single photo-electron charge spectrum obtained, fit described in the text.

The charge of alpha signals was always divided by value of the s.p.e. charge (fitted as  $60.1 \pm 0.1$  ADC-ns in Fig. 4.3) found for each run to give the resulting photo-electrons detected.

#### 4.1.2. Trapping effect

To verify the consistence of the Dark Box tests, the trapping effect of the ARAPUCA was tested. First, the alpha spectrum was measured with the S-ARAPUCA. Later, the dichroic filter was replaced by a normal optical glass and the measure was repeated. The waveforms are acquired for  $4 \mu\text{s}$ , for the baseline and s.p.e. calibration, and integrated for 100 ns.

Figure 4.4a shows the resulting spectra found for each configuration. It is noticeable that the trapping effect of the ARAPUCA device significantly increases the amount of light detected.

To quantify the increase in light collection, a  $\chi^2$  minimization was performed between the two histograms using the TMinuit tool from Root CERN [88]. Figure 4.4b shows the result, two free parameters are used: a normalization constant and a scaling factor that is directly related to the collection efficiency. A scaling factor of  $\sim 2.16$  was found, meaning that the trapping effect of the ARAPUCA increases the efficiency by  $\sim 116\%$ .

#### 4.1.3. Results

The S-ARAPUCA has a lower efficiency than the X-ARAPUCA [57, 89], therefore only preliminary results are given here as no further investigation was taken. Two interesting results point to two alternatives to TPB: (1) BisMSB (1,4-Bis(2-methylstyryl)benzol), where prelim-

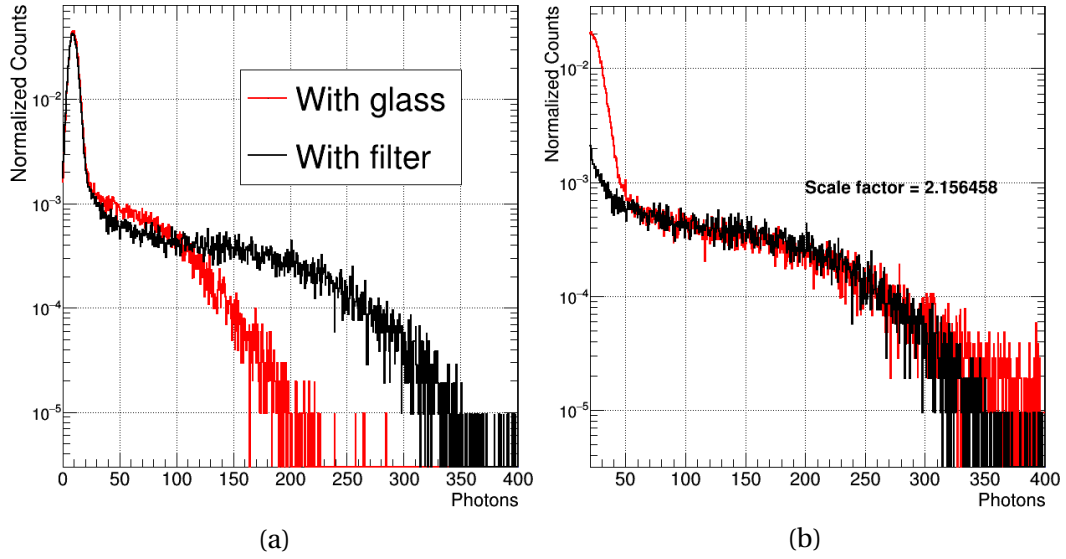


Figure 4.4: **(a)** Alpha source spectrum measured with the dichroic filter (black) and with the optical glass replacing it (red). **(b)** Factor of  $\sim 2.16$  found between the two histograms through  $\chi^2$  minimization.

inary results (Fig. 4.5a) show an efficiency  $\sim 5\%$  greater for BisMSB and (2) liquid WLS, that, as shown in Fig. 4.5b has almost the same performance as the BisMSB.

However, BisMSB may degrade when exposed to UV light and it has not been widely tested and the liquid wavelength shifters deposition did not surpass a liquid nitrogen test, making necessary to develop a better deposition technique.

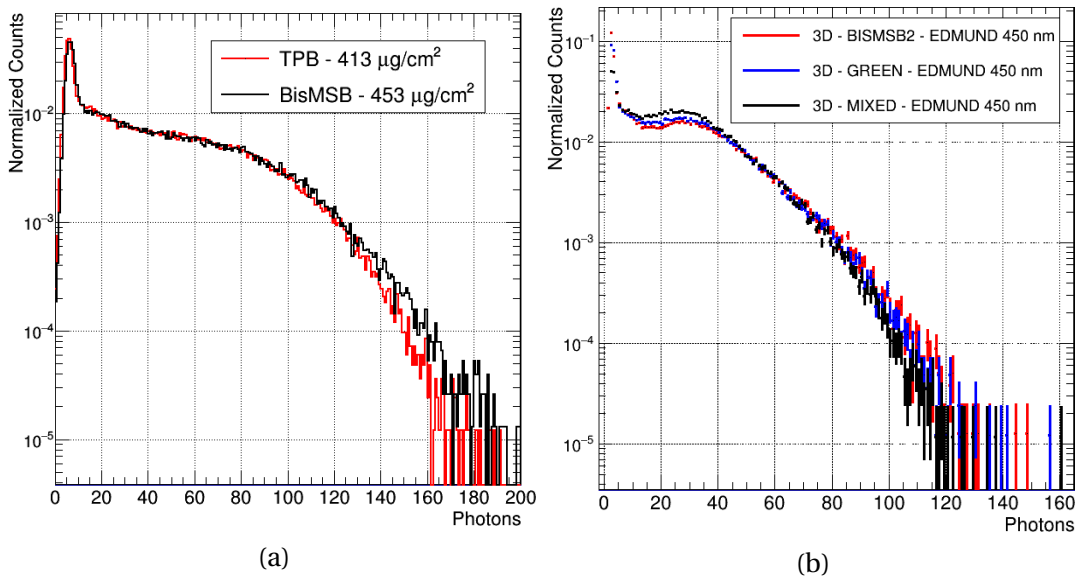


Figure 4.5: **(a)** Comparison between TPB and BisMSB as internal WLS for the S-ARAPUCA an increase of  $\sim 5\%$  was noticed for BisMSB. **(b)** Liquid WLS compared with BisMSB giving comparable spectra. GREEN and MIXED refer to emission in green and mixture of green/blue.

## 4.2. Monochromator tests

Prototypes and components were also exposed to monochromatic light from a H20-UVL Horiba [90] Monochromator installed at the “*Laboratório de Léptons*” in Campinas. The Monochromator uses a grating diffracted light from a Deuterium light source (150 W). Figure 4.6 shows the emission spectra of the Monochromator that goes from 120 to 400 nm ( $\pm 0.1$  nm). The Monochromator must be operated in vacuum, specially below 185 nm due to air (O<sub>2</sub>) absorption of the light [91]. Therefore, it was a more “complicate” system than the Dark Box but with the same idea of speeding up the optimization process, limiting the use of liquid argon.

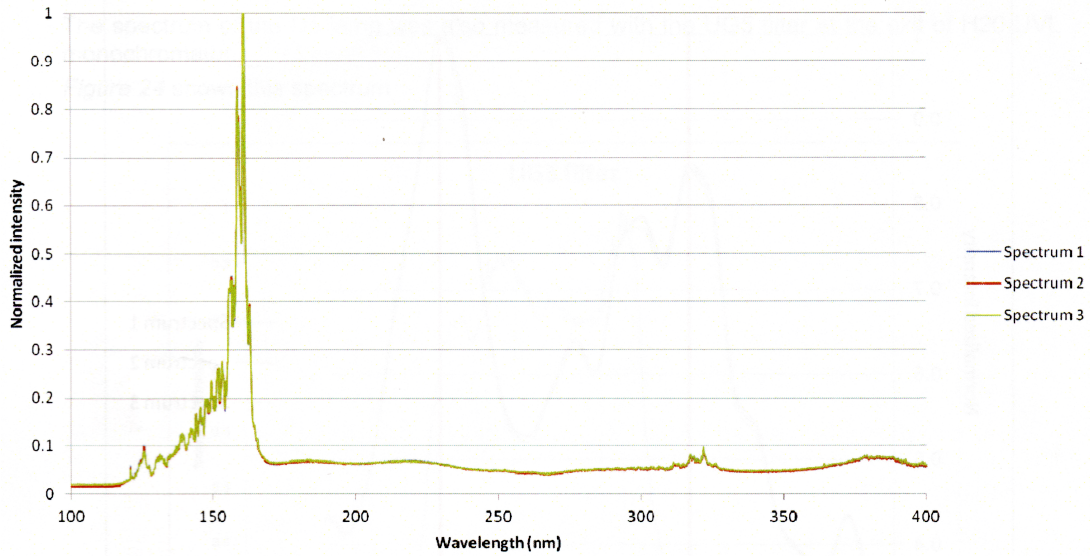


Figure 4.6: Monochromator emission spectrum ranging from 120 to 400 nm.

Figure 4.7 shows the experimental setup: the Monochromator kept in high vacuum  $P \sim 10^{-5}$  mbar isolated by the gate valve in the middle. The test chamber can be operated separately and the gate valve is opened when the pressure is below  $10^{-3}$  mbar. With this, one measure can be done in about 1 hour and half, including vacuum breaking and pumping.

The light detection was done with an APD (see Sec 3.4) S8664-1010 from Hamamatsu [92] placed behind the sample as shown in Figure 4.8a. The APD has a breakdown voltage of 400 V and it was operated at 350 V with a gain  $G = 50$  and quantum efficiency of about 70% for 400 nm. The producer gives a spectral response ranging from 320 to 1000 nm, however, detection of light was possible in all the spectral range of the Monochromator.

Figure 4.8b shows the circuit to readout the APD [79], the RC circuit close to the Bias

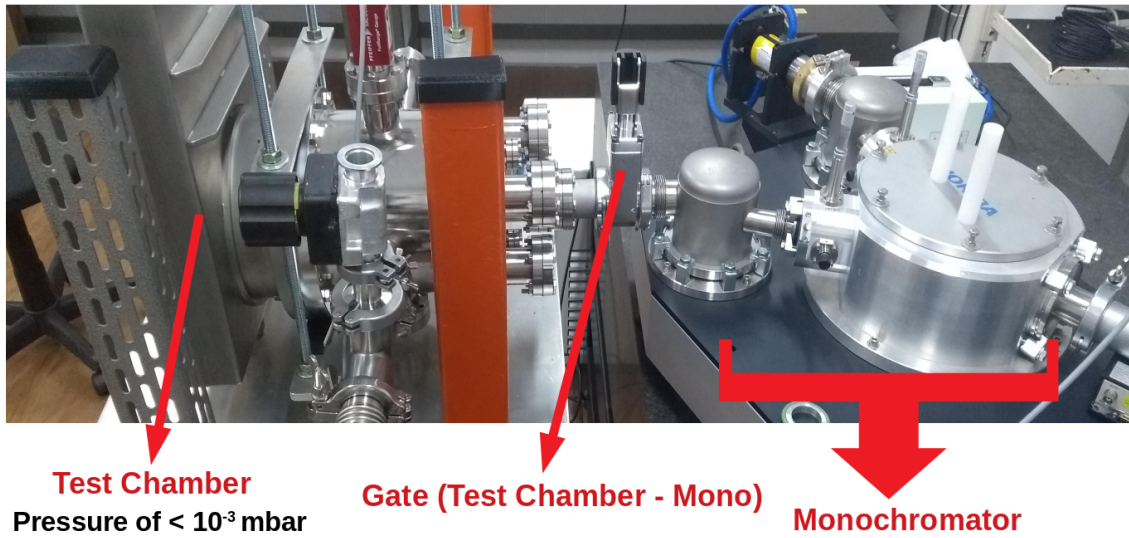
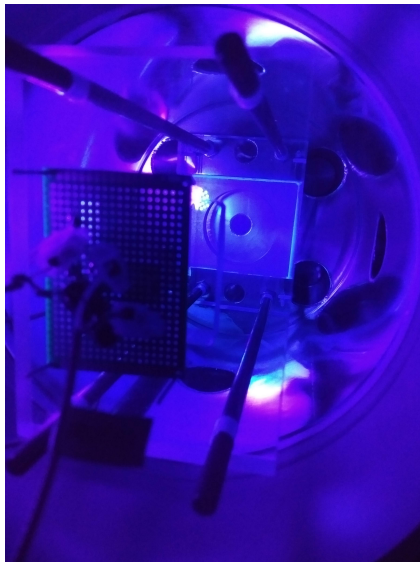
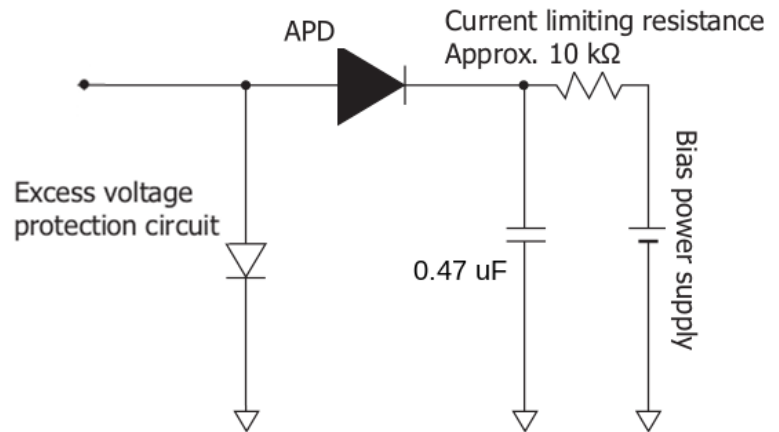


Figure 4.7: Experimental setup, the test chamber is vacuum isolated from the Monochromator through the Gate.

power supply serves as a low pass filter and current limiting. The resistance and capacitance were chosen to efficiently cut frequencies above the  $f_C \approx 33$  Hz, significantly reducing fast oscillation noise and the 60~70 Hz from the electric wires. A diode is placed on the APD anode exit as an excess voltage protection. The voltage amplitude was read-out with an oscilloscope, always retrieving the baseline by measuring in dark. The Deuterium light bulb requires approximately ten minutes to stabilize after turning on.



(a)



(b)

Figure 4.8: **(a)** Photo inside the testing chamber, a wavelength shifter exposed to UV light and in the back of it (at the left side of the photo) the APD to detect the light. **(b)** Diagram of the APD readout [79].

In order to make a relative comparison between two different samples, for instance two types of WLS, there is no need to correct for the emission spectrum of Fig 4.6. However, for absolute measurements this characterization is essential. In this case, a reference measurement was taken but, ideally, the reference measurement of the beam must be taken online, using a beam splitter with another light detector. These new feature are being implemented.

### 4.2.1. Results

#### Fused silica versus B270

Fused silica is typically used as dichroic filter substrate due to its optical properties [93], with excellent light transmittance to wavelengths of 195 nm up to  $2.1 \mu\text{m}$ . Due to the high cost of fused silica, other alternatives of dichroic filter substrates were investigated, seeking good transparency, good PTP adhesion and low cost. Among the candidates, the optical glass B270 showed to have good PTP adhesion and a higher robustness of the film at liquid nitrogen temperatures, in addition to being easier to cut and cheaper than fused silica.

A comparison between B270 and fused silica was then performed. Figure 4.9 shows the transmittance for two dichroic filters produced by Opto Co., one with thin film deposition on B270 and another one on fused silica. The spectra are simply normalized by the direct light of the Monochromator. It was noticed that both substrates have similar performance around the PTP emission and, therefore, B270 was chosen due its adhesion, lower cost and because it is easier to cut.

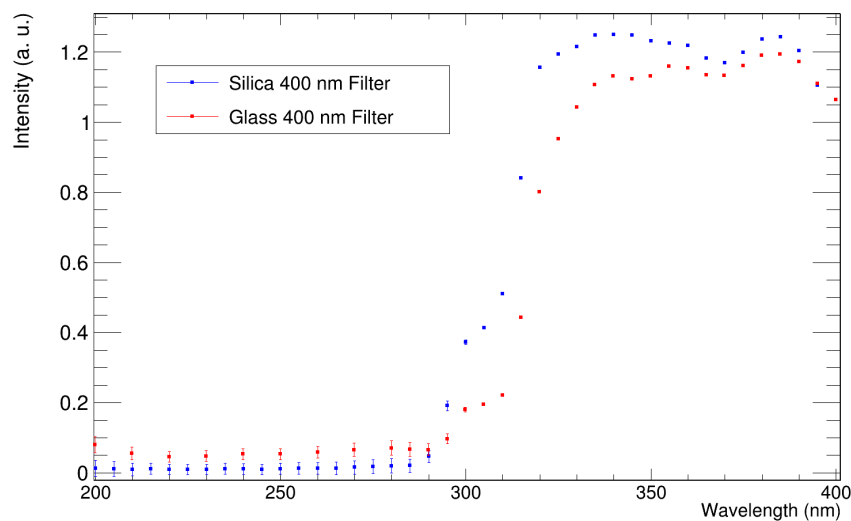


Figure 4.9: Transmission from Opto dichroic filter with thin film deposition in Fused Silica and optical glass (B270).

The fused silica substrate, without the thin layers that characterize the dichroic filter (Sec. 3.6), was tested. Figure 4.10 shows the normalized transmittance found, the Opto fused silica sample data (blue) was normalized to match the given transmittance [93] of fused silica (thick black line).

This test was originally performed to better understand the transparency of the materials. However, it came in hand later to define the fused silica as the ideal material to block LAr scintillation light without significantly attenuate Xenon light (175 nm) for the Xenon Doping tests performed at ProtoDUNE-SP (see Sec. 6.2).

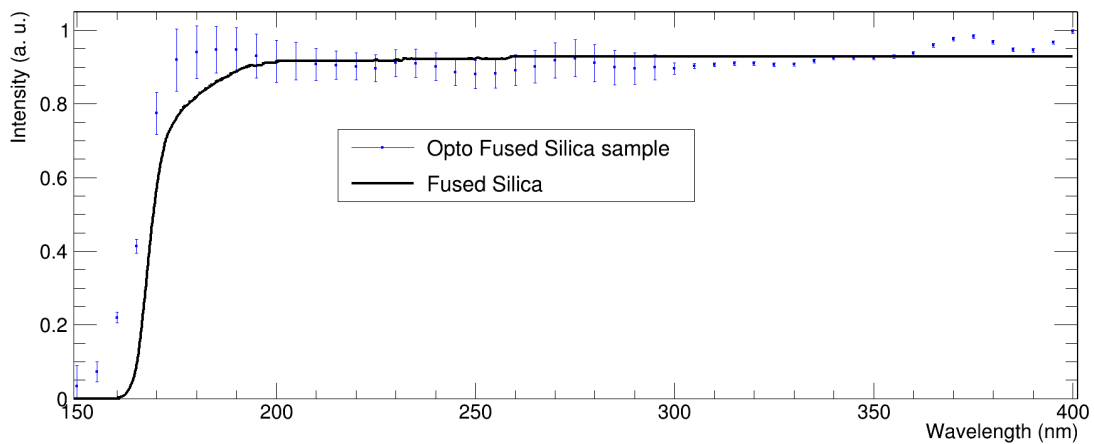


Figure 4.10: Transmission measurements (data points) for sample of the Opto Co. fused silica. The fused silica data was normalized to match the given transmittance [93] of the fused silica (thick black line).

### 4.3. Grounding mesh transparency

Transparency measurements of the grounding mesh that surrounds the APA, so ionizing radiation inside the APA does not produce signals, were performed in the Monochromator. This is an important feature to be implemented in light simulations to correctly perform the energy reconstruction, for example. Figure 4.11a shows the 3D model of the experimental setup while Figure 4.11b shows a photo of the 3D-printed model in front of the Monochromator.

The APD is placed in the back of the setup. The grounding mesh to be tested is installed in the front of the beam and, in between the mesh and the APD, there is a indium tin oxide<sup>1</sup>

<sup>1</sup>Indium tin oxide is widely used in research and industry. It is a transparent conducting oxide, which is electrical conductor and optical transparent. It was chosen due to its transparency to PTP emission light and thickness (another set of measurements were planned with electric field applied to the ITO).

(ITO) thin film coated with PTP. Figure 4.12a shows the grounding mesh and the ITO coated with PTP (top and bottom, respectively).

A step motor controlled by an Arduino rotates the upper part (orange in the Fig. 4.11b) over the mesh vertical axis to study the angular dependence of the transparency. The setup is built so the grounding mesh will fall down when it reaches  $80^\circ$  (Fig. 4.12b). In this way, it is possible to measure the direct light, as a reference for the transparency, without changing anything in the system (such as vacuum level, setup position, light intensity, etc.).

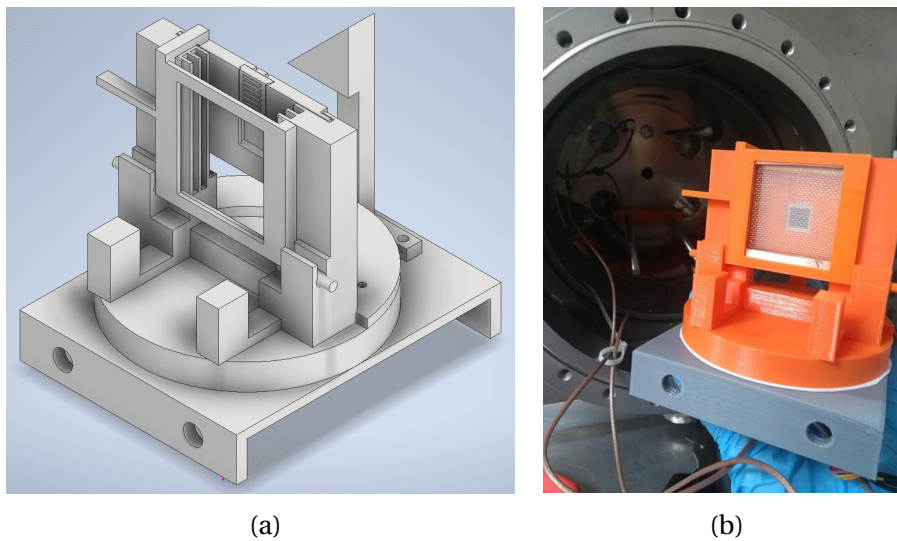


Figure 4.11: **(a)** 3D model of the experimental setup. **(b)** Photo of the 3D printed setup. In the background the testing chamber can be seen with the hole in which the beam comes from. The system is designed so the mesh falls down when it reached  $80^\circ$ .

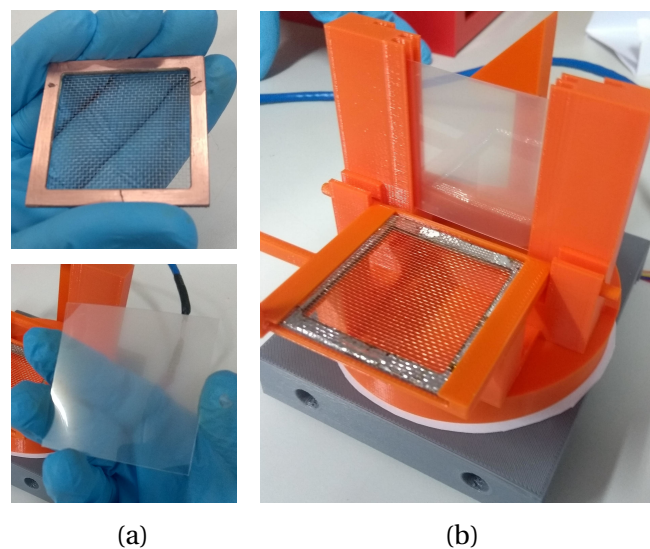


Figure 4.12: **(a)** (top) Photo of the grounding mesh (bottom) Indium tin oxide (ITO) thin layer coated with PTP. **(b)** Photo of the experimental setup with the grounding mesh down, for direct light data taking.

A simplified model can be used to predict and interpret the data. In Figure 4.13a a representation of the incident light (in blue) is made arriving at the grounding mesh with angle  $\theta$ . A section of the mesh is displayed (the other one is rotated by  $90^\circ$  and not displayed for simplicity), the wires with diameter  $d$  and pitch  $L$  will produce a projected shadow (ps). By using the angle relations:

$$\cos(\theta) = \frac{d}{ps}. \quad (4.1)$$

Therefore, for a light strip with width  $L$ , the proportional shadow ( $S_P$ ) created by the two wires can be written as:

$$S_P = \frac{ps}{L} = \frac{d}{L \cos(\theta)}, \quad (4.2)$$

and, the transparency  $T = 1 - S_P$  is:

$$T = 1 - \frac{d}{L \cos(\theta)}. \quad (4.3)$$

Figure 4.13b shows the transparency of the mesh as function of the incidence angle  $\theta$ . The transparency is defined as the ratio between the voltage of the APD with the mesh in front by the voltage with direct incidence. An average was made among the three different wavelengths<sup>2</sup> used: 165, 170 and 175 nm.

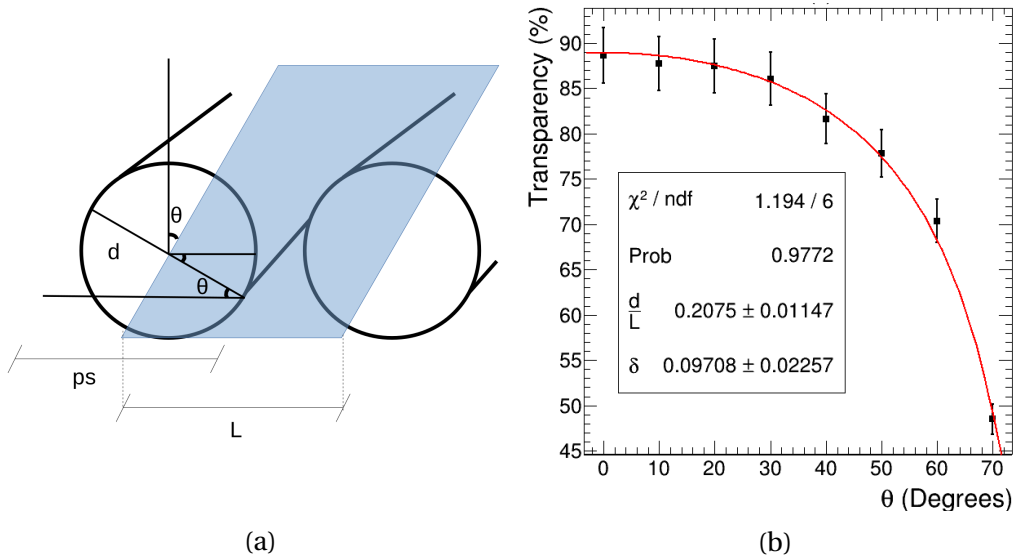


Figure 4.13: **(a)** Illustrative light (blue) with width  $L$  arriving with an angle  $\theta$  at the mesh wires of diameter  $d$  and pitch  $L$ . **(b)** Grounding mesh transparency as function of the light incident angle  $\theta$ . The maximum angle is  $70^\circ$  due to the mechanical constraints of the project.

The data were fitted with Eq. 4.3 plus a constant factor  $\delta$ , as the model does not take into account the second section of wires that, most probably, has a constant relation with the

<sup>2</sup>The choice of the wavelength is due to the emission amplitude of the Monochromator (see Fig. 4.6) and to have a good reference in the Xenon emission wavelength (see Chap. 6).

incidence angle. Therefore, the transparency as a function of  $\theta$  can be written as:

$$T(\theta) = 1 - \frac{0.2075}{\cos(\theta)} + 0.09708 \quad (4.4)$$

and the total average transparency ( $T_U$ ) for an isotropic light source can be estimated by integrating over the solid angle:

$$T_U = \frac{1}{2\pi} \int_0^\phi d\phi \int_0^{\theta'} T(\theta) \sin(\theta) d\theta \cong 54.4\%, \quad (4.5)$$

where  $\theta' \approx 79.1^\circ$  was set so  $T(\theta') = 0$  to avoid negative values.

This is not a realistic approach as the light does not arrive uniformly. Muons will have a long track along the TPC, while electrons will produce showers with length of 1~2 meters long. As informed in a private communication with professor Franciole Marino, the angular distribution of the photons coming from a punctual light source 1 meter away from the detector can be described by the polynomial:

$$D(\theta) = 0.0111797 + 0.000675671 \cdot \theta - 1.84617 \cdot 10^{-5} \cdot \theta^2 + 1.06234 \cdot 10^{-7} \cdot \theta^3, \quad (4.6)$$

that gives:

$$T_L = \int_0^{\theta'} T(\theta) D(\theta) d\theta = 80.9\%. \quad (4.7)$$

Therefore, a transparency of 80.9% can be expected from the grounding mesh, close to the value of 85% given by Ref. [5].

The study of the grounding mesh transparency was very useful to understand the data from the Xenon doping tests in ProtoDUNE-SP, as will be described in Chapter 6. Equations 4.3 and 4.4 were used to better simulate photons arriving in the X-ARAPUCA deployed for the tests.

## 4.4. Glass-to-Power Wavelength Shifter

A new wavelength shifter was designed and developed by the team of University of Milano Bicocca in collaboration with Glass-to-Power (G2P) company [94] a spin-off from Milano-Bicocca. The WLS slab is produced with Poly(methyl methacrylate) (PMMA), acrylic glass, doped with 2,5-Bis(5-tert-butyl-benzoxazol-2-yl)thiophene (BBT) [95]. The prototype of this WLS are named here as FB118. In this section the preliminary results that led to the evaluation of the X-ARAPUCA double-cell efficiency in LAr will be discussed. The final result is shown in Chapter 5.

The PMMA, without doping, has a good transparency for the PTP emission spectrum as shown in Figure 4.14 where the absorption edge of PMMA is around 300 nm. However, the absorption spectra peaks around 370 nm when doped with BBT, as can be seen in the red line. Two BBT concentrations are displayed, 104 mg and 35 mg, so its possible to see that increasing the BBT concentration in the 800 ml of PMMA the absorbance also increases<sup>3</sup>. During the tests performed at Milano-Bicocca three different concentrations were used. The initial WLS slab tested at warm had good results, therefore, double and half concentrations were tested. For the cryogenic tests and liquid argon tests (Sec. 4.4.2 and Sec. 5.2) the double concentration one was used.

The emission spectra is also shown in Fig. 4.14 with the label on the right side. The peak emission around 430 nm and the spectrum starting edge around 400 nm allow the use of the same dichroic filters with cutoff of 400 nm.

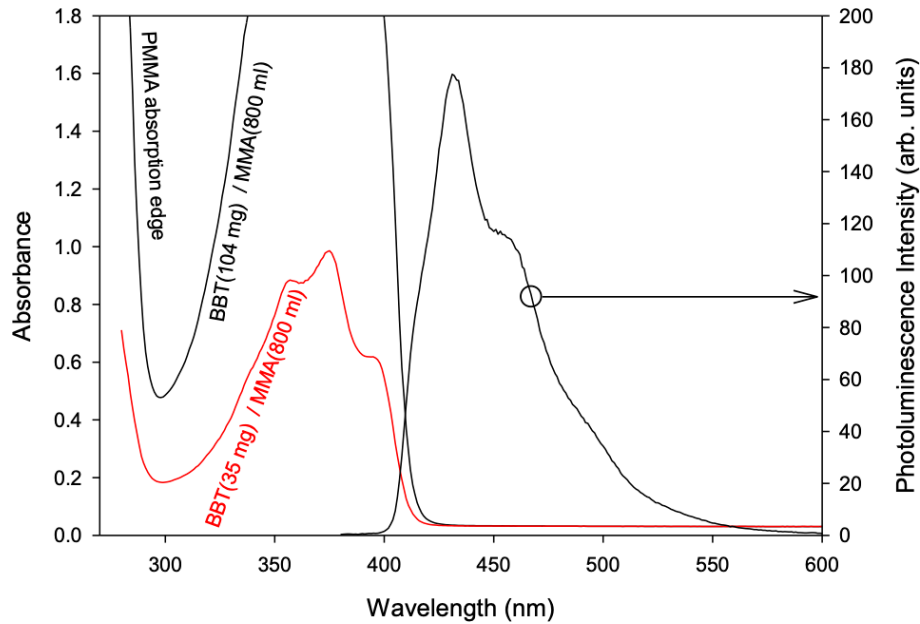


Figure 4.14: The secondary wavelength shifter absorption and emission spectra together with the PMMA absorption [95].

A set of measurements in warm and cold were done in order to measure the enhancement in efficiency with respect to EJ-286 slab from Eljen [73]. It was also possible to measure the increase in collection efficiency by placing Vikuiti reflector foils on the WLS slab edges, leaving gaps for the SiPM devices.

<sup>3</sup>Note that absorbance here is defined as  $A = -\log_{10}(T)$ , giving the corresponding transmittance. Therefore, an absorbance of  $A = 1$  means a transmittance of 10%, while  $A = 1.8$  means  $T \approx 1.6\%$ .

#### 4.4.1. Warm measurements

Tests at room temperature were initially performed to search for hints of the photon detection efficiency (PDE) and to understand the photon detection uniformity (PDU) of each WLS. For these measurements, a CAEN SP5601 LED with peak emission  $\sim 405$  nm was used and the dichroic filter was replaced by a plastic mask with equally spaced points where the optical fiber could be connected, as shown in Fig 4.15. Four channels, each with an array of four Hamamatsu S14160-6050HS SiPMs, read out the LED pulses.

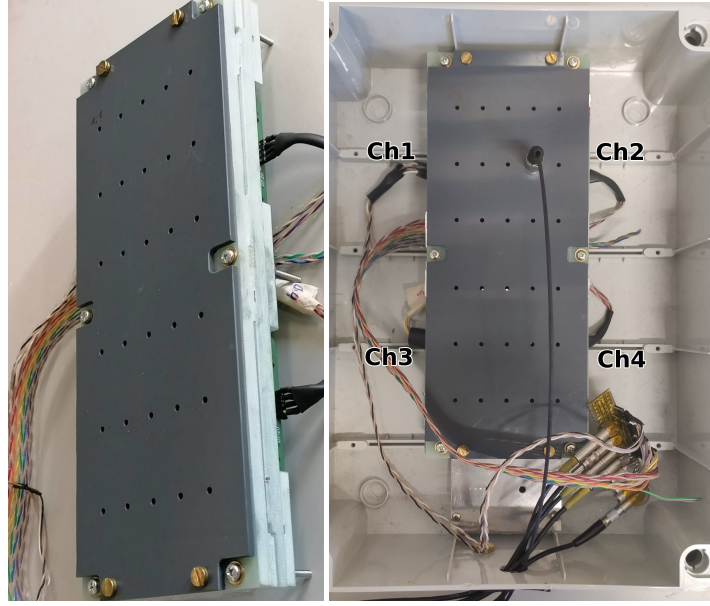


Figure 4.15: The X-ARAPUCA with the plastic mask and the optical fiber plugged, a total of 30 deployment points could be used to scan the WLS uniformity [95].

As these are room temperature measurements, single photo-electron calibration to evaluate the absolute number of photo-electrons could not be performed due to the high dark current. Therefore, LED pulses signals were measured in area and amplitude, always discounting the baseline area with the LED turned off three times during the measurement, to check the stability. To be able to compare the two WLS response, the LED intensity should be the same in between the tests, as much as dark current, SiPM bias voltage, etc.

For both, amplitude and area, the PDU matrix of each WLS slab is determined by the measurement  $V_{ij}$  at each position coordinate  $i$  and  $j$  as:

$$V_{ij} = \frac{V_{ij}^{\text{ch1}} + V_{ij}^{\text{ch2}} + V_{ij}^{\text{ch3}} + V_{ij}^{\text{ch4}}}{\text{Average}(V^{\text{ch1}} + V^{\text{ch2}} + V^{\text{ch3}} + V^{\text{ch4}})}, \quad (4.8)$$

where  $V_{ij}^{\text{ch1}}$  corresponds to the readout of channel 1 (see Fig. 4.15) at position  $ij$  and  $V$  denotes the readout area or amplitude. This was done for both slabs with and without applying Vikuiti on the edges. To evaluate the dispersion, the RMS of the PDU matrix is computed.

Figure 4.16 shows the PDU matrix in terms of amplitude for the EJ-286 slab, without (Left) and with (Right) the Vikuiti applied. One can see that applying Vikuiti reflector directly on the WLS slab edges the RMS decreases from 15% to 9%, that is, the uniformity response of the device increases. For the FB118 slab the RMS decreased from 17% to 9%. It is noticeable that the second and fifth rows have a higher value, this is caused by the fact that the SiPM array is positioned directly in front of the optical fiber.

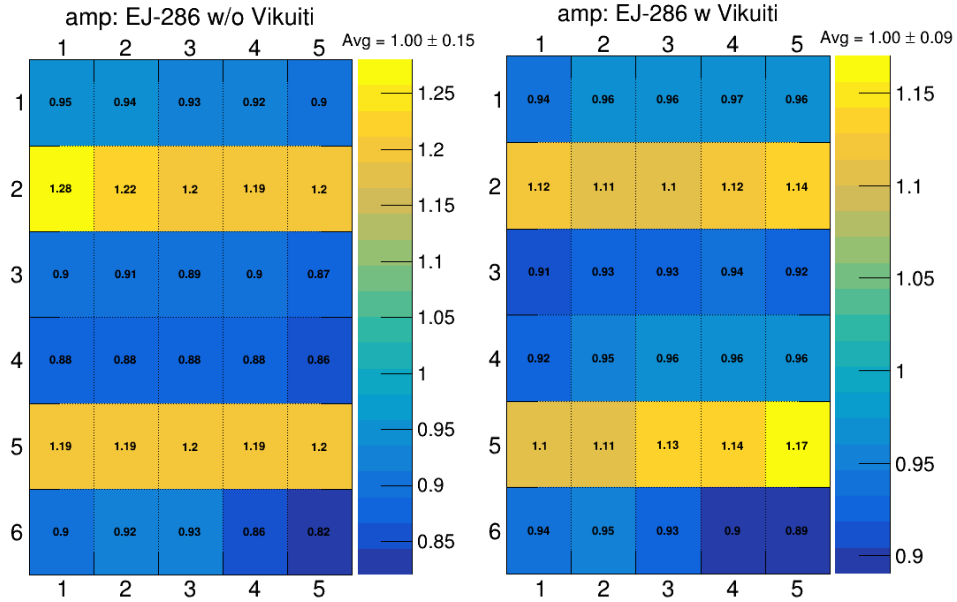


Figure 4.16: The PDU matrix of the EJ-286 slab, without (left) and with (right) Vikuiti.

Another relevant measurement is the comparison between two samples  $A$  versus  $B$ . The relative photon detection efficiency (PDE) variation between the two samples can be computed by the ratio matrix  $R_{ij}$ :

$$R_{ij} = \frac{A_{ij}^{\text{ch1}} + A_{ij}^{\text{ch2}} + A_{ij}^{\text{ch3}} + A_{ij}^{\text{ch4}}}{B_{ij}^{\text{ch1}} + B_{ij}^{\text{ch2}} + B_{ij}^{\text{ch3}} + B_{ij}^{\text{ch4}}}, \quad (4.9)$$

where  $A_{ij}^{\text{ch1}}$  is the signal collected in the  $ij$ -th position by channel 1 for sample A. Figure 4.17 (Left) shows the relative measurement between the EJ-286 slab with versus without Vikuiti applied. An increase of ~22% is noticeable, while the FB118 had an increase of ~33%. On the other hand, Figure 4.17 (Right) shows the relative measurement in terms of amplitude between the FB118 versus the EJ-286 slabs (both with Vikuiti). By computing the average,

the relative gain of FB118 over EJ-286 was found to be ( $\sim 50\%$ )  $\sim 65\%$  when (not) applying the Vikuiti.

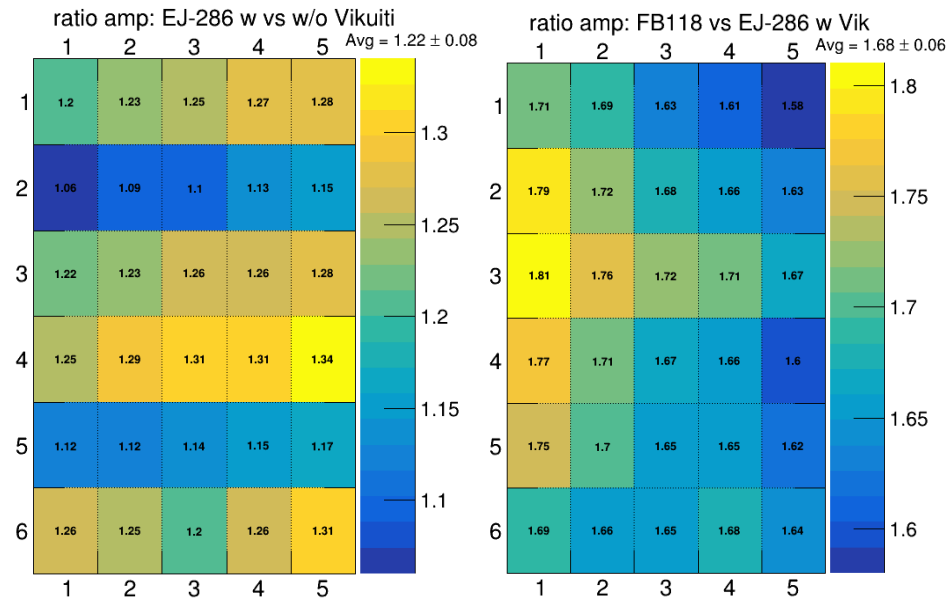


Figure 4.17: The PDE ratio matrix for the slab with versus without Vikuiti (Left) and the comparison of FB118 versus EJ-286, both with Vikuiti (Right) [95].

The measurements with signal amplitude and integrals were consistent among them. The gain in PDE found at room temperature gave a great hint about the relative measurements of the two slabs; however, there are some drawbacks: (1) The detection is performed without s.p.e. calibration, (2) the trapping effect of the X-ARAPUCA is not taking place and (3) the wavelength of the LED peaks at 405 nm, where the absorbance of the slabs are different, as can be seen in Figure 4.18 where EJ-286 have an absorption of  $\sim 80.2\%$  and the FB118 slab  $\sim 72.9\%$ .

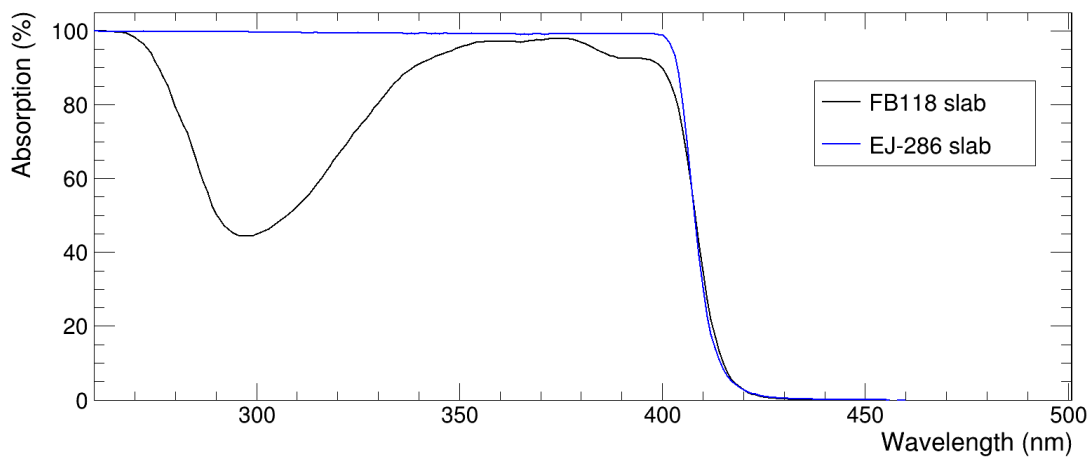


Figure 4.18: Absorption in percentage for different wavelengths for EJ-286 and FB118 slab. Data taken from Eljen data-sheet [73] and provided by G2P Co. [94].

#### 4.4.2. Cryogenic measurements

Prior to moving to the tests of the X-ARAPUCA in liquid argon (Chapter 5), similar tests were performed at cryogenic temperature.

In these tests, the cryogenic stainless steel chamber sizing 250 mm in diameter by 310 mm in height (see Sec. 5.2.1) was pumped down to a pressure of about  $10^{-3}$  mbar. Inside the chamber the X-ARAPUCA was mounted (with the dichroic filter deployed) and an americium alpha source ( $^{241}\text{Am}$ ) was placed a few millimeters from the PTP coated in the dichroic filter as can be seen in Figure 4.19. This configuration was inspired by the Dark Box tests (Sec. 4.1):  $\alpha$ -particles can travel through the vacuum and stimulate the PTP scintillation.

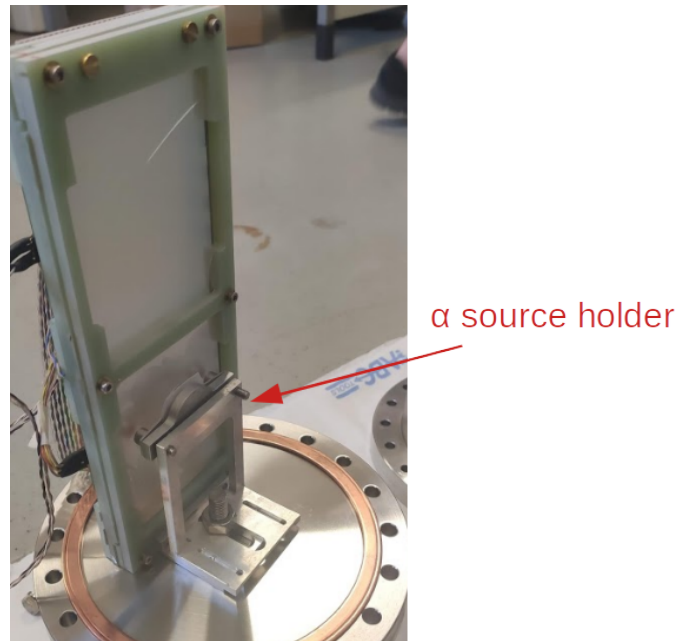


Figure 4.19: Photo of the X-ARAPUCA with the  $\alpha$  source holder a few millimeters away from the dichroic filter.

The testing chamber was submerged in a thermal bath of liquid nitrogen ( $\text{LN}_2$ ) and a temperature sensor PT100 was placed in contact with the X-ARAPUCA so the measurements could be performed at a known temperature<sup>4</sup>. Performing a cryogenic test in such way allows a better measurement of the wavelength downshifting properties of the slabs, as the PTP emitted light follows the normal emission spectrum (Fig. 3.14b).

<sup>4</sup>As the chamber is in vacuum, the thermal contact between the X-ARAPUCA and the external is through the bottom flange to which the device is attached. Therefore,  $\text{LN}_2$  baths were done overnight.

The waveforms were acquired for  $20\ \mu\text{s}$  with a CAEN Digitizer DT5725 and signals were monitored during the cooling down. Figure 4.20 shows the averaged waveforms for one of the channels. It is noticeable that the decay constant time of the waveforms increases with the drop of temperature. This is mostly probably related to the PTP intrinsic scintillation. Unfortunately, the cold trans-impedance amplifier was not available at the time, so measurements had low signal-to-noise due to warm amplification and the s.p.e. calibration was rudimentary and no deconvolution of the signal was possible (see Sec. 5.2.2)

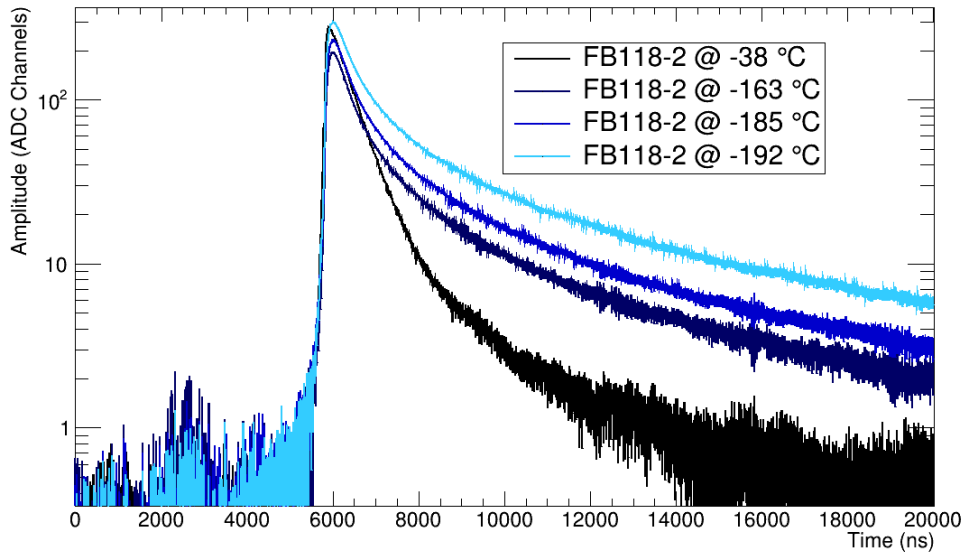


Figure 4.20: Averaged waveforms for four different temperatures.

As there was a different output depending on the temperature, the comparison between EJ-286 and FB118 slabs was performed with the closest temperature possible. Figure 4.21 shows the  $\alpha$  spectrum in terms of photo-electrons detected for the X-ARAPUCA deployed with EJ-286 (black dashed) or FB118 (blue solid) WLS slabs. An empirical fit was performed with two Gaussians, with the intention of modeling and also taking into account the fraction of light from PTP that is emitted back towards the vacuum and reflected back by the  $\alpha$  source holder. Figure 4.21 reports the set of parameters from two Gaussian functions as:

$$f(x) = p_0 \cdot \exp\left(-\frac{1}{2} \left(\frac{x - p_1}{p_2}\right)^2\right) + p_3 \cdot \exp\left(-\frac{1}{2} \left(\frac{x - p_4}{p_5}\right)^2\right), \quad (4.10)$$

where  $p_0$  and  $p_3$  correspond to the amplitudes,  $p_1$  and  $p_4$  to the means and  $p_2$  and  $p_5$  to the standard deviations of the two Gaussians respectively [95].

By comparing the peak positions of the two spectra, a light collection increase of  $(42 \pm 13)\%$  can be estimated. The large uncertainty is mainly due to the s.p.e. calibration and to the weighted average of the two Gaussian peaks.

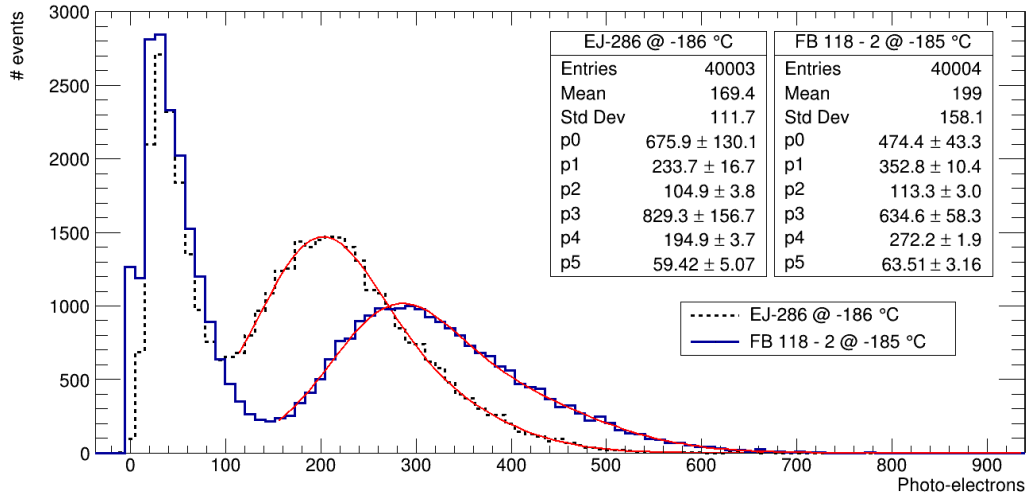


Figure 4.21: Alpha spectrum in photo-electrons detected by the X-ARAPUCA with EJ-286 (black dashed) and FB118 (blue solid) slabs. The fit was performed with the sum of two Gaussians [95].

Besides this measurement, the intrinsic scintillation of the secondary wavelength shifters was studied. To do so, the alpha source was removed so the X-ARAPUCA was exposed only to cosmic muons. In this case, muons crossing the EJ-286 slab generated scintillation light signals well above 100 p.e.. It happens that, EJ-286 slab is based on polivyniltoluene (PVT), that is known to be a scintillator [96] with light yield of  $\mathcal{O}(10^3)$  photons/MeV [95]. the Eljen producer, in the EJ-286 data sheet [73], mentions the attempt to reduce the direct scintillation component. There was no noticeable scintillation in the FB118 slab tested in vacuum, as PMMA is not known to scintillate.

The results achieved at room and cryogenic temperature motivated the comparison of the two wavelength shifters in liquid argon.

## X-ARAPUCA Efficiency test

Two different sets of experiments were performed in Brazil and Italy to evaluate the light collection efficiency of the X-ARAPUCA device. The experiments in Brazil were performed from October 2019 to March 2020 and consisted in exposing the device to  $\alpha$  and  $\gamma$  sources and to cosmic muons [89]. A GEANT4 dedicated simulation was performed to retrieve the device efficiency with the three different ionizing radiations. In Italy, experiments to retrieve the efficiency and enhancement of the light collection were done in 2020/2021 by exposing the device to an  $^{241}\text{Am}$  source. Different positions along the longitudinal axis of the cell were tested and a Monte Carlo toy-model evaluated the number of expected photons arriving on the X-ARAPUCA acceptance window [95]. In this chapter, these two experiments are presented.

### 5.1. X-ARAPUCA single-cell tests

The *device under test* (DUT) was a X-ARAPUCA prototype with external dimensions of 9.6 cm  $\times$  12.5 cm hosting one single dichroic filter with an area of 8 cm  $\times$  10 cm as shown in Fig. 5.1a. The dichroic filter, from OPTO [85] (see Sec. 4.2), is designed to have a cut-off wavelength of 400 nm, a transmittance band which goes from 300 nm to 400 nm (transmissivity  $\simeq 90\%$ ) and a reflective band ranging from 400 nm to 500 nm (reflectivity  $\simeq 98\%$ ). The internal wavelength shifter (WLS) selected was a 3.5 mm thick Eljen EJ-286 [73]. The absorption band spectrum of the WLS plate is well matched with the emission spectrum of the PTP with maximum absorbance around 350 nm, while its emission is centered around 430 nm, inside the reflective band of the filter. The filter was coated with  $\sim 400 \mu\text{g}/\text{cm}^2$  of PTP (see Sec. 3.5). Two arrays of 4 SiPM each are installed on the 10 cm long lateral sides of the cavity. The SiPMs are Hamamatsu S13360-6050VE with active area of  $6 \times 6 \text{ mm}^2$  [92]. The internal surfaces of the cavity are lined with 3M ESR Vikuiti reflective foils, as well as the lateral sides of the WLS plate, with the exception of the regions where the SiPMs are installed.

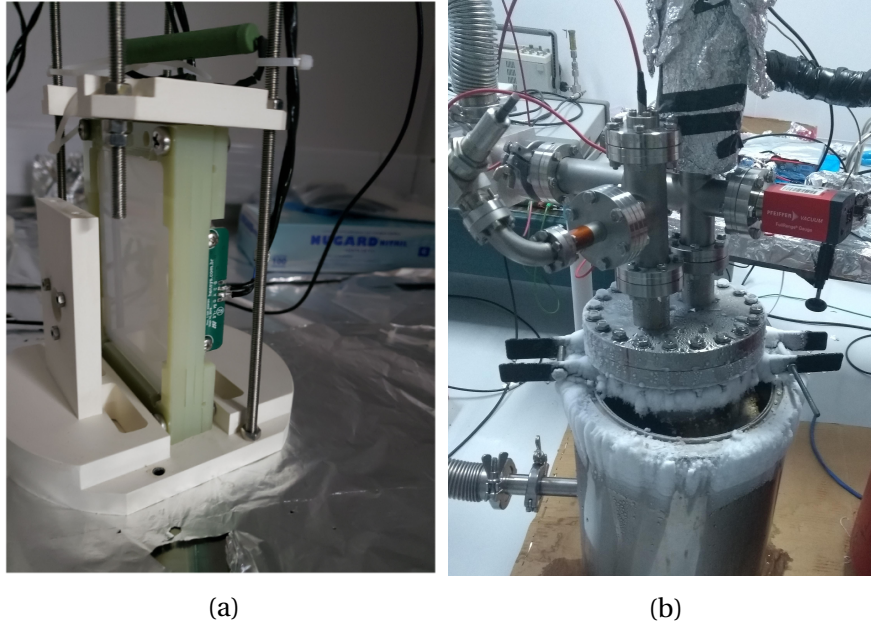


Figure 5.1: **(a)** the prototype when installed in its sustaining mechanical structure together with the holder of the  $\alpha$ -source. Level sensor can be seen above the prototype with a green color. **(b)** Picture of the cryogenic setup during  $\alpha$ -source run [89].

### 5.1.1. Experimental setup

The cryogenic setup of Figure 5.1b was assembled to carry out the X-ARAPUCA photon collection efficiency tests. The schematic diagram of the set-up is shown in Fig. 5.2. The inner stainless-steel cylinder (green) is pumped down to a pressure  $\sim 10^{-4}$  mbar at room temperature. Then, a cryogenic pump down to a pressure of  $\sim 10^{-6}$  mbar is performed by filling the external open thermal bath (yellow) with liquid argon (LAr)<sup>1</sup>. The pump's gate valve is closed and Gas Argon 6.0<sup>2</sup> is injected in the cylinder, keeping the inner pressure  $1 < P_{\text{work}} < 1.4$  bar. Argon gas (GAR) is liquefied thanks to the heat exchange with the thermal bath and a level sensor<sup>3</sup> installed inside the stainless-steel cylinder ensures that the X-ARAPUCA is completely submerged in LAr (the level sensor can be seen in Figure 5.1a, as a green resistor over the DUT). A vacuum tight optical feed-through was installed inside the stainless-steel cylinder to generate pulsed LED flashes in order to properly calibrate the system (see Sec. 5.1.3).

The X-ARAPUCA is installed facing an  $\alpha$ -source 3 cm away from the center of the dichroic

<sup>1</sup>In Italy, we discovered that a more successful method is to not make a cryogenic pump down. Instead, slowing filling with argon gas and stopping the pumps before starting the thermal bath will reduce the chance of contamination.

<sup>2</sup>Gas Argon 6.0 refers to a contaminants level equal or below 1 ppm.

<sup>3</sup>The level sensor consists of a resistor sensitive to temperature variation. By monitoring the increase of the current going through the circuit one can determine when the resistor is fully covered by LAr.

filter, as shown in the diagram of Figure 5.2 (Right) and the picture of Figure 5.1a. The DUT is held vertically by the Polyvinyl chloride (PVC) support that hosts the  $\alpha$  source. For the  $\gamma$ -rays and cosmic- $\mu$  tests, the  $\alpha$ -source was removed but the holder was kept in place to maintain the same geometrical configuration and not to bias the measurements with different amount of environmental reflected light. The signals from the two SiPM arrays are amplified with a gain of 32 dB by a custom made, low-noise, two channels, pre-amplifier produced by the Brazilian Company Hensys and read-out with a 14 bit CAEN DT5730 digitizer with sampling frequency of 500 MHz.

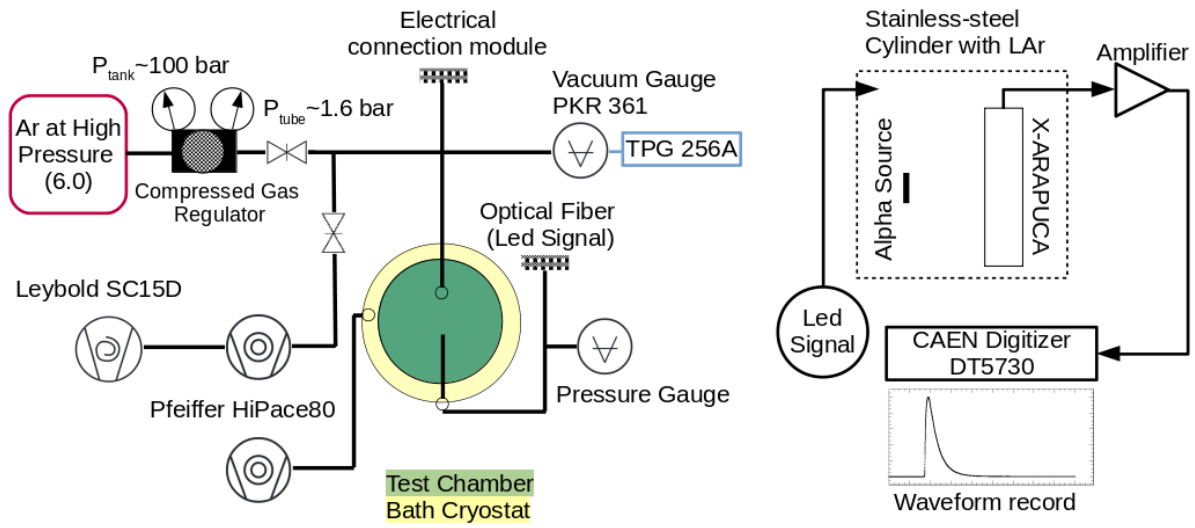


Figure 5.2: (Left) Schematic diagram of the cryogenic setup. (Right) Schematic diagram of the DAQ [89].

The  $\alpha$ -source is made of an alloy of aluminium and natural uranium in the form of a thin disk with thickness of 0.14 mm and diameter of 1 cm. An aluminium cover was placed in front of the alloy to reduce the count rate of the device, this is important to retrieve a clear spectrum. This source was previously studied by the Chronology group of University of Campinas [57]. The energy, relative abundance and parent nucleus of the  $\alpha$  source are shown in Table 5.1 [97]. For the  $\gamma$ -rays test, the  $\alpha$ -source was removed and a  $^{60}\text{Co}$  source was placed outside the cryostat in a position where the emission of the source faces the X-ARAPUCA acceptance window.

### 5.1.2. Data Acquisition

The data acquisition (DAQ) was performed with a customized version of the *wavedump* software from CAEN. The ADC read-out was performed every time that one of the two ar-

Table 5.1: Energy, relative intensity and parent nucleus of the  $\alpha$  particles emitted by the natural uranium [97].

$\alpha$ energy (MeV)	relative intensity	parent nucleus
4.187	48.9%	$^{238}\text{U}$
4.464	2.2%	$^{235}\text{U}$
4.759	48.9%	$^{234}\text{U}$

rays exceeded a fixed threshold, which corresponded to approximately 5 photo-electrons. However, a fine tuning of the threshold was done manually for each run searching for a good balance between trigger rate and spectrum resolution. For each triggered event a waveform with 18  $\mu\text{s}$  record length, which corresponds to 6,000 samples, with 3.6  $\mu\text{s}$  of pre-trigger was saved for both channels. A total of 40,000 trigger events were acquire for  $\alpha$  and  $\mu$  runs. The  $^{60}\text{Co}$   $\gamma$ -source has a low activity being necessary to subtract the background. For that, the data were taken during a fixed period of time of about 30 minutes with and without the source with a fixed trigger.

Dedicated calibration runs were performed each time the SiPMs overvoltage was changed. A blue LED was flashed using pulses of approximately 50 ns, frequency of 1 kHz and amplitude set in order to produce signals of few photo-electrons. The acquisition of the signals was performed with the external trigger of the Pulse Generator *Agilent* with the same record length of 18  $\mu\text{s}$  used for source signals.

A graphical user interface (GUI) was build in C++ with QtCreator software tool to automatically save the data. Figure 5.3 shows the two taps of the GUI. The data were saved in folders with the specific name given by the user, for example, “20220101\_my\_new\_test”. The run and sub-run<sup>4</sup> numbers are changed automatically by the GUI, while the bias voltage, threshold, trigger channel and extra information are inserted by the user. The pulse width and voltage amplitude of the LED flashes can be set for the calibration runs. In the example of Fig. 5.3, the run file for channel 0 would be named as “0\_wave0\_48V0\_450ADC\_Ch0.dat” in a folder named “run0\_48V0\_450ADC\_Ch0”. Calibration runs are saved in an internal folder “Calibration” as “wave0\_48V00\_3V00\_100ns.dat”. The data was collected initially as ASCII format and later changed to binary format due to its better compression.

The collected waveforms are pre-processed and stored in root files. Each channel has a class associated with stored information such as: event ID, maximum amplitude value and position, charge,  $F_{\text{prompt}}$  (see Sec 5.2.2) and selection cuts. The root files have the waveforms

<sup>4</sup>Sub-runs were necessary because data were saved in packs of 10,000 events.

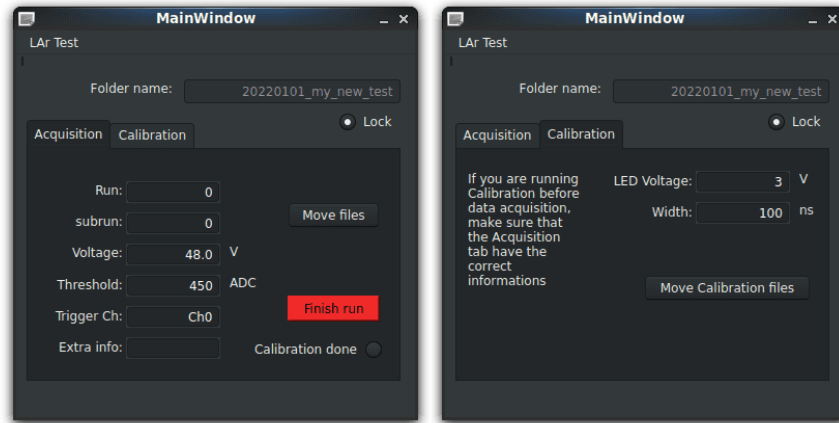


Figure 5.3: (Left) Tab for the main acquisition. (Right) Tab for calibration runs.

stored with the baseline already calculated and filtered with the denoise algorithm for 1-D signals [98]. The filter preserves the signal rise-time and integral [39] and the C code is available on the authors website. The baseline is calculated in the first  $3.6 \mu\text{s}$ , the pre-trigger region.

### 5.1.3. Calibration

#### Single photo-electron (s.p.e.) calibration

The SiPMs were operated in reverse bias with a few volts over the breakdown voltage of  $43.0 \pm 0.2 \text{ V}$ . Starting from  $+3.5 \text{ V}$  overvoltage (O.V.) to  $+5.5 \text{ V}$  with steps of  $0.5 \text{ V}$ . Between the different overvoltages (O.V.) used, the values of  $+5.0$  and  $+5.5 \text{ V}$  ( $\pm 0.2 \text{ V}$ ) O.V. were selected due to the quality of the calibration and spectrum.

In order to properly evaluate the amount of photo-electrons (p.e.) detected by the device, the calibration data were used to retrieve the single photo-electron (s.p.e.) response. The waveforms, acquired with the LED as external trigger, are integrated for  $900 \text{ ns}$  (decay time of s.p.e. signal  $\sim 300 \text{ ns}$ ) starting from the trigger point ( $3.6 \mu\text{s}$ ) [99].

A spectrum obtained with a bias voltage of  $48.0 \text{ V}$  ( $+ 5.0 \pm 0.2 \text{ O.V.}$ ) is shown in Figure 5.4. The fit is performed with  $N + 1$  Gaussian distributions, where the first one corresponds to the electronic noise and the others correspond to first, second and  $N$ -th photo-electron responses. The noise and s.p.e. Gaussian distributions have 3 free parameters each (mean value, standard deviation and normalization constant). The mean values and standard deviations of the other peaks are constrained by the following conditions:

- the mean value of the  $N$ -th peak is given by  $N \times \mu_1$ , where  $\mu_1$  is the mean value of the single photo-electron peak;
- the standard deviation of the  $N$ -th peak is given by  $\sqrt{N} \times \sigma_1$ , where  $\sigma_1$  is the standard deviation of the single photo-electron peak;

The gain was considered to be the distance between the first and second photo-electron. The result for different bias voltages is shown in Figure 5.4 for the two channels of the X-ARAPUCA. A linear fit is shown together with the data.

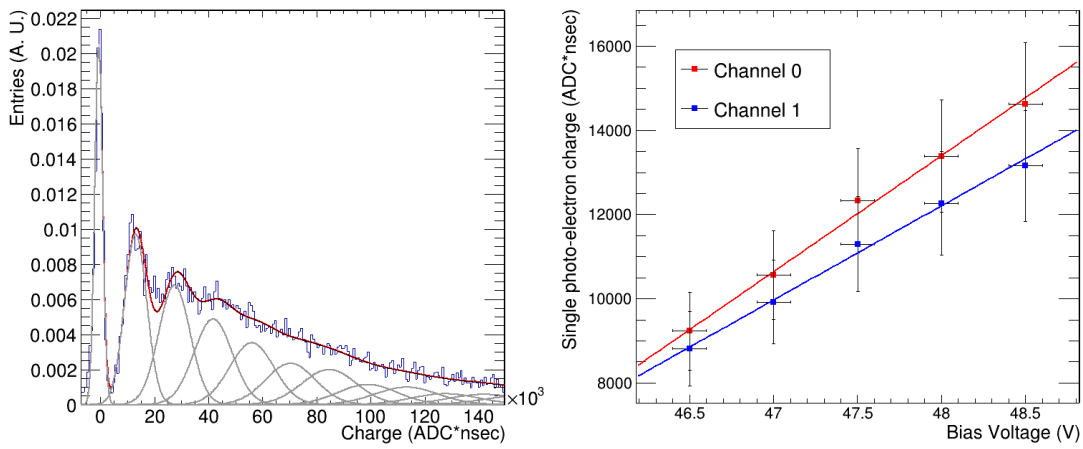


Figure 5.4: (Left) Single photo-electron response obtained during calibration. The distance between the first and second peaks after the noise gives the gain of the SiPM. (Right) Gain versus bias voltage for the two channels of the X-ARAPUCA. Red and blue lines represent linear fits of the experimental points. The breakdown voltage was found to be  $43.0 \pm 0.2$  V [89].

### Matching filter

Unfortunately, during the run with cosmic muons and  $\gamma$ -rays there was the appearance of a periodic external noise that prevented a proper calibration for low voltages. For +5.0 and +5.5 O.V. a noise suppression algorithm was made with a *Matching filter* or *Optimum filter*.

The filter consists of a convolution between the reference signal  $r(t)$  and the waveform signal  $s(t)$ . The conventional convolution inverts, for instance, the reference signal during the integration. However, in the *Matching filter* the signal is unchanged, that is:

$$\text{matching}(s, r)[n] = \sum_{i=0}^{k-1} s[n+i] \times r[i], \quad (5.1)$$

where  $n$  is the number of points in the complete event  $s$  and  $k$  is the number of points in the reference  $r$ . Once the convolution results in the area under the two curves, it is necessary to

normalize the signals to compensate the difference in amplitude. In this way, it is necessary to perform the following operation:

$$\text{matching}_{\text{norm}}(s, r)[n] = \frac{\sum_{i=0}^{k-1} s[n+i] \times r[i]}{\sqrt{\sum_{i=0}^{k-1} s[n+i]^2 \times \sum_{i=0}^{k-1} r[i]^2}}. \quad (5.2)$$

Lets take, for example, the signal  $r$  extracted from  $s$  as in the Figure 5.5 (top), where the red line (moving average) represents the signal  $s$ . Taking  $r$  as the signal between 6000 ns and 8100 ns, which corresponds to the periodic noise (the blue line is the normal signal, without any processing). In this way, one can imagine that in a certain point  $n'$ , one has  $s[n' + k] = r[k]$  for all  $k$  in the sum (precisely between 6000 and 8100 ns). It is clear, from Eq. 5.2 that the result is equal to 1. For every other point, where the matching is not 100%, the factor  $\text{matching}_{\text{norm}}$  will be always lower than 1 ( $\text{matching}_{\text{norm}} \leq 1$ ). In the bottom part of Fig. 5.5 the matching for the red signal from the top part using  $r$  as described above is presented. One can notice that the maximum matching is achieved around 7,000 ns.

Therefore, in the calibration analysis of  $\gamma$  and  $\mu$  runs any pulse with a matching  $> 0.55$  was discarded. This value was chosen manually trying to minimize the amount of false positive events lost. As lower voltages decrease the amplitude of the SiPMs signals but does not affect the amplitude of the noise, the matching filter was not enough to discard noisy signals and the calibration was not successfully performed.

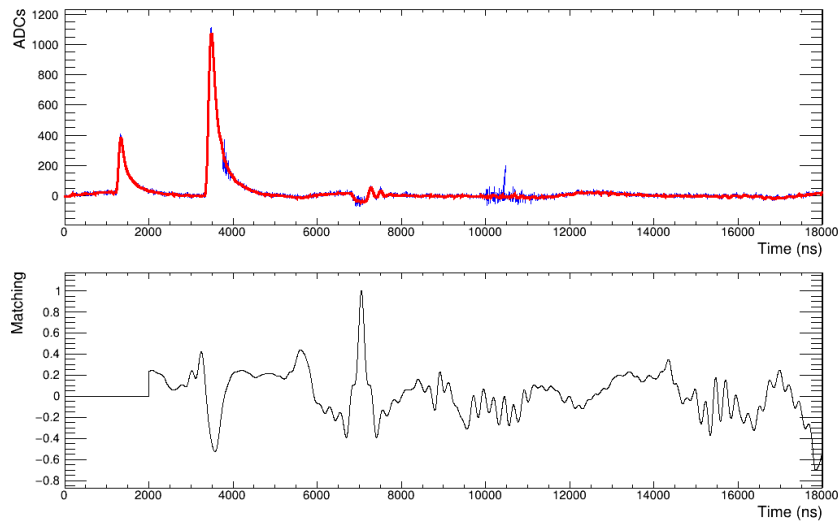


Figure 5.5: (Top) Example of a waveform in blue with a moving average of 35 points in red. (Bottom) Result obtained by applying the *Matching filter* of Eq. 5.2, using as reference the points between 6000 and 8100 ns. A Matching value equal to 1.0 means a perfect match. The filter was applied only for  $t > 2000$  ns.

This filter can also be used to search s.p.e. peaks instead of noise. This, however, was not necessary due to the dedicated calibration procedure.

### Cross-talk evaluation

The cross-talk probability strongly depends on the temperature of the sensor. Operating them at LAr temperature, makes the cross-talk probability quoted by the vendor not usable, since it is referred to room temperature. To estimate the cross-talk probability and find a correction factor to better estimate the number of photo-electrons the method described in [100] was applied. The method assumes that:

- (i) The number of “primary” pulses has the Poisson distribution with  $\lambda = L$ .
- (ii) Each “primary” pulse can generate one or several duplicated pulses independently of preceding events.

In this case, the number of duplicated pulses for each primary pulse has the geometrical distribution:

- (a) The first additional pulse is generated with probability  $p$ .
  - (b) In the presence of the first additional pulse, the second additional pulse is generated with the same probability  $p$ , and so on;
  - (c) The chain of duplicated pulses is unlimited.
- (iii) Primary pulses and all the chains of secondary pulses generated by them are detected.

The recursive function to calculate the compound Poisson distribution for  $k$  photo-electrons was found to be:

$$P_k(L, p) = \exp(-L) \sum_{i=0}^k B_{i,k} \cdot [L(1-p)]^i \cdot p^{k-i}$$

where,

$$B_{i,k} = \begin{cases} 1 & \text{if } i = 0 \text{ and } k = 0 \\ 0 & \text{if } i = 0 \text{ and } k > 0 \\ \frac{(k-1)!}{i!(i-1)!(k-i)!} & \text{otherwise} \end{cases} \quad (5.3)$$

where  $L$  is the mean value of the Poisson distribution and  $p$  is the cross-talk probability [100].

To apply this method into the calibration data, we considered that the probability of detecting  $k$  photo-electron is given by the total number of events containing  $k$  photo-electrons, divided by the total number of events. The integration of the  $k$ -th Gaussian distribution from Figure 5.4 gives the number of events with  $k$  p.e..

Equation 5.3 was used to minimize the normalized calibration spectra, where  $L$  and  $p$  were considered as free parameters together with a normalization constant. One of the results of the fitting procedures is shown in Figure 5.6a. The plot of the number of SiPM avalanches per photon ( $1 + p$ ) vs. the bias voltage is shown in Figure 5.6b for each channel. These values are used as correction factors when we convert the number of detected avalanches into photo-electrons. It ranges between 1.32 and 1.58 avalanches per photon and is consistent with what was found in the first run of the protoDUNE detector [39]. The calibration to convert the charge read-out as  $\text{ADC} \times \text{ns}$  to single photo-electrons is performed by dividing the charge of the signal by the gain of the *s.p.e.* times the number of avalanches per photon.

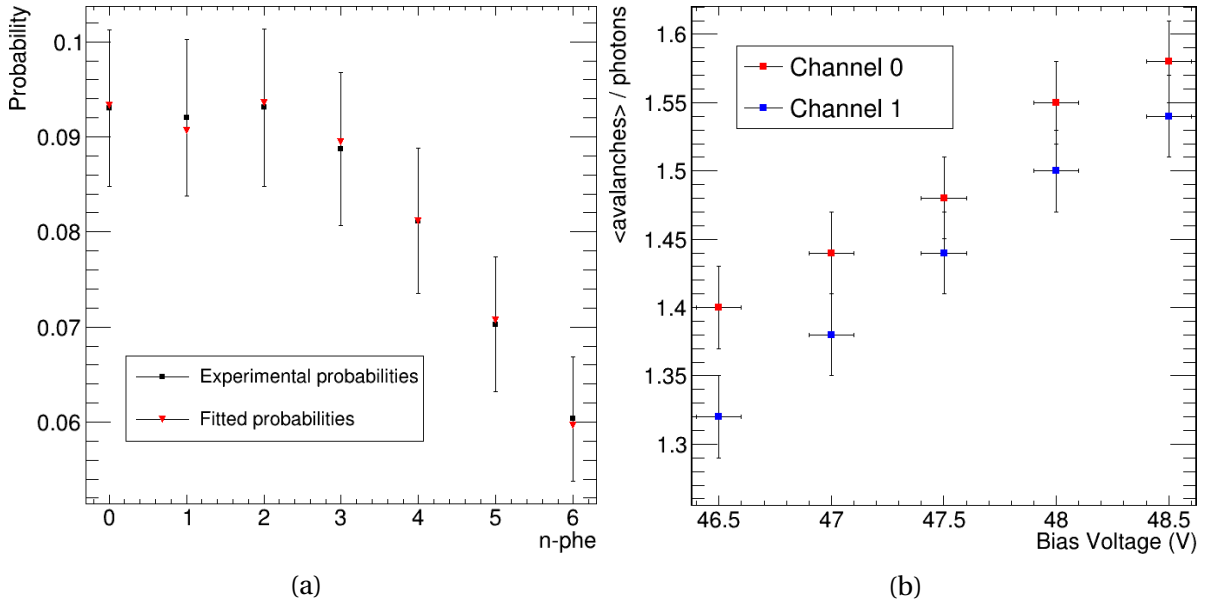


Figure 5.6: **(a)** Probability of detecting  $n$  photo-electrons (black squares). A  $\chi^2$  minimization of the experimental points with equation 5.3 [100] was performed and the result is shown as red triangles. **(b)** Avalanches per photons versus bias voltage for each channel [89].

The cross-talk probability is quite high if compared with the  $\sim 7\%$  reported in the SiPM's datasheet. The reason for that may be explained by the cryogenic temperatures along side with the SiPM pulse resolution. However, during the measurements performed at Milano-Bicocca, dedicated tests were performed in the S13360-6050VE SiPMs and it was noticed

small after-pulses in the single photo-electron pulses that degraded the resolution of the spectrum. In fact, one can see that the spectrum of Fig. 5.4 is very broad and the Gaussian distributions overlap significantly compromising the resolution of single peaks.

The two main sources of uncertainties are the single photo-electron calibration and the cross-talk probability. An uncertainty of 15% due to the s.p.e. was taken based in the quality of the fits of Fig. 5.4. The cross-talk calibration had a maximum variation of  $\sim 10\%$  which was conservatively chosen. The combined uncertainty was taken as 20%.

### Liquid Argon purity

The liquid argon purity was monitored by the triplet time constant (see Sec. 3.1) for all measurements. The information of the triplet time constant is important to validate the tests and correct the total amount of photo-electrons detected. To perform this analysis an average signal was retrieved as shown in Figure 5.7a for  $\alpha$ -particles (red),  $\gamma$ -rays (black) and cosmic muons (blue). The difference in the ratio between singlet and triplet contributions is evident by the plots, where the  $\alpha$ 's have more singlet contribution and electrons and muons have a greater triplet contribution [37, 38, 60]. It was shown that  $N_2$  and  $O_2$  contamination, at a few ppm level, can significantly quench the triplet scintillation emission, thus reducing the total photon yield [59]. In order to correct for this effect, an overall fit of the average scintillation waveforms is performed and the value of the triplet scintillation decay time is extracted. This value is used to extrapolate the number of photo-electrons which would be detected in the case of perfectly pure LAr.

Equation 5.4 is used to fit the waveform as presented in Figure 5.7b, where  $\tau_S$  and  $\tau_T$  are the singlet and triplet components and  $A_S + A_T = 1$  are the relative amplitudes [49]. The third term of the sum is a component related to a possible PTP delayed emission [101], with  $N$  and  $A$  as constants depending on the nature of the scintillator and  $t_a$  is the relaxation time.  $A$  and  $t_a$  were constrained to vary between 0.22 – 0.55 and 20 – 100 ns, respectively. The fit is performed with a  $\chi^2$  minimization of the signal with the light pulses of eq. 5.4, convoluted with a Gaussian, which takes into account the effect of the readout electronics.

$$L(t) = \frac{A_f}{\tau_f} e^{-t/\tau_f} + \frac{A_s}{\tau_s} e^{-t/\tau_s} + \frac{N}{[1 + A \ln(1 + t/t_a)]^2 (1 + t/t_a)} \quad (5.4)$$

The fit was performed with the TMinuit tool from Root Cern [88]. The discrete convolution is performed considering that each point from Eq. 5.4 has a corresponding normalized

Gaussian distribution with a certain fixed standard deviation  $\sigma$ . The convolution of a certain point at  $t = t'$  is performed from left to right, where only points with  $t \leq t'$  are considered. The convoluted point at  $t'$ , that is  $C(t')$ , will be the sum of every point within<sup>5</sup>  $5\sigma$  from  $L(t)$  times the corresponding Gaussian amplitude of that specific point, that is:

$$C(t') = \sum_{t=0}^{t'} \text{Gaus}(t, t', \sigma) \times L(t), \quad (5.5)$$

where,  $\text{Gaus}(t, t', \sigma)$  means a Gaussian with mean value  $t'$ , standard deviation  $\sigma$  evaluated at the point  $t$ . This operation is performed on the waveform at every step of the minimization, therefore, it is very time consuming. The approach done in the X-ARAPUCA double-cell was to deconvolve the waveform as shown in Sec. 5.2.

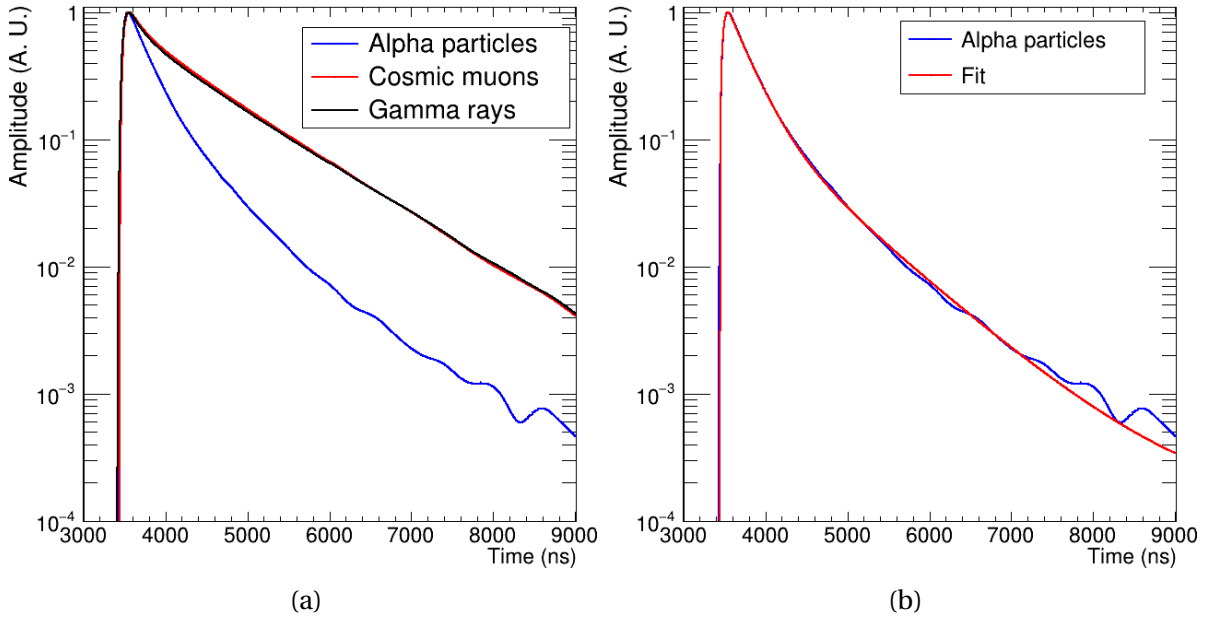


Figure 5.7: **(a)** Average signals for the three different particles. **(b)** Average signal of  $\alpha$ -particles fitted with equation 5.4 [89].

The triplet time constant was found to be  $780 \pm 20$ ,  $1100 \pm 20$  and  $1050 \pm 20$  ns for  $\alpha$ 's,  $\gamma$ 's and muons, respectively.

Comparing the values of the triplet decay times, found with this fitting procedure, with the expected values [59], we determined the correction factors of 1.16, 1.43 and 1.47 for  $\alpha$ -particles,  $\gamma$ -rays and cosmic muons, respectively.

<sup>5</sup>This value is chosen to take only Gaussian that are effectively contributing to the convolution and to minimize the time consumption.

#### 5.1.4. Experimental setup Monte Carlo Simulation

A dedicated GEANT4 Monte Carlo simulation was developed [102] for each type of ionizing radiation to properly estimate the device photon collection efficiency. All the dimensions of the experimental setup were carefully measured and implemented: the stainless-steel cylinder and cryostat, the X-ARAPUCA and  $\alpha$ -source PVC support (Figure 5.1a) and the X-ARAPUCA prototype.

The liquid argon scintillation light yield was set at 51,000 photons per MeV ( $\gamma/\text{MeV}$ ) [37, 60] times the quenching factor, which was set at 0.71 for the  $\alpha$ -particles and at 0.78 for electrons and muons [37, 72, 89, 103].

The emission of the  $\alpha$ -source was set uniformly and isotropically inside the aluminium disc with the energy distribution given in Table 5.1. The  $\alpha$ -particles lose a fraction of their initial energy inside the aluminium disc (which goes undetected) and leave the aluminium alloy with a continuous residual energy distribution [104].

To simulate the detection of  $\gamma$ -rays, the  $^{60}\text{Co}$  source was positioned outside the cryostat. The two emission lines, one at 1.17 MeV and the other at 1.33 MeV [105], were chosen to be isotropic. Figure 5.8 shows an example, with the gamma source placed outside the cryostat and optical photons (green) generated in the LAr reaching the X-ARAPUCA (yellow).

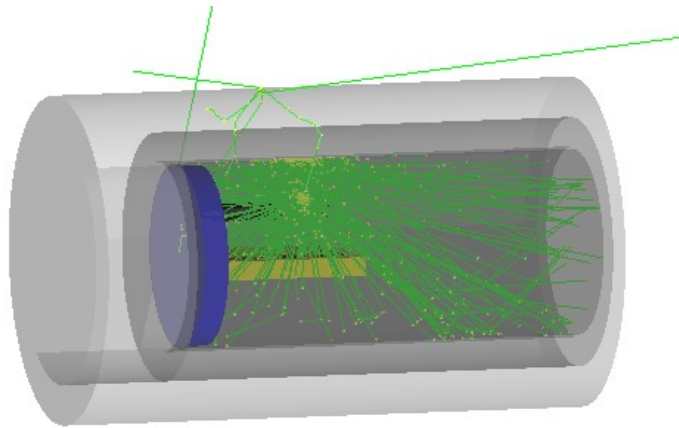


Figure 5.8: Example of the experimental setup with simulated gamma source outside the cryostat and the optical photons (green lines) reaching the X-ARAPUCA [89].

Cosmic muons were generated uniformly in a 4 meters diameter disc positioned 50 cm above the cryostat, with a  $\cos^2 \theta$  angular distribution (where  $\theta$  is the zenith angle), with an uniform azimuth angle distribution and a fixed energy of 4 GeV, which corresponds to the average energy of muons at ground level [12, 13]. The reflectivity of the internal stainless-

steel surfaces was set at 20% for the scintillation photons. The final Monte Carlo output is the number of photons that reaches the X-ARAPUCA acceptance window per particle generated. The simulated spectrum is shown at Figure 5.9.

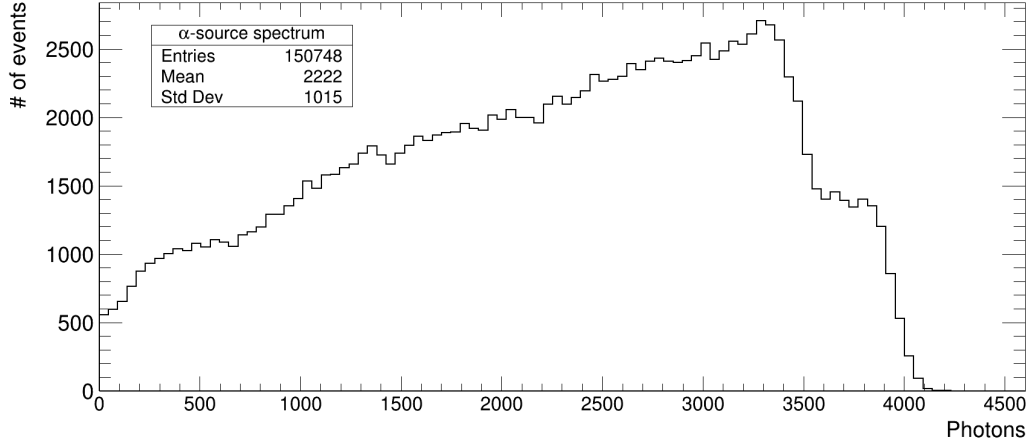


Figure 5.9: Monte Carlo simulation output, the number of expected photons compose the  $\alpha$ -source spectrum.

### 5.1.5. Efficiency analysis

The final light collection efficiency of the X-ARAPUCA single-cell was measured comparing the simulated spectrum with the experimentally measured one. The digitized waveforms were integrated over  $15.3 \mu\text{s}$  starting from 300 ns before the onset. The integral value is first multiplied by the correction factor due to the LAr purity and secondly divided by the gain of the SiPMs times the number of avalanches per photon found. The output is the total amount of photo-electrons detected.

The simulated spectrum must go through a Gaussian smearing, which simulates the electronic response of the detector. The  $\alpha$ -source spectrum can be represented by the convolution of a Gaussian and three exponentials, one for each line of the spectrum [104]:

$$F(E) = \sum_{i=1}^3 \frac{A_i}{2\tau} \exp\left(\frac{E - \mu_i}{\tau} + \frac{\sigma^2}{2\tau^2}\right) \text{erf}\left(\frac{1}{\sqrt{2}} \left(\frac{E - \mu_i}{\sigma} + \frac{\sigma}{\tau}\right)\right), \quad (5.6)$$

where  $\mu_i$  is the peak position for the energy line  $i$ ,  $A_i$  is the relative abundance of each spectral line,  $\sigma$  is the width of the alpha-peaks and  $\tau$  is the slope of the tail on the peak low-energy side. The fit is performed by setting the two lower energy lines of Tab. 5.1 as function of the higher energy one. An example of the fit is shown in Figure 5.10, an exponential decaying term is added to MC spectra to take into account the very low energy background entering the stainless-steel vessel and which is not included in the MC simulation.

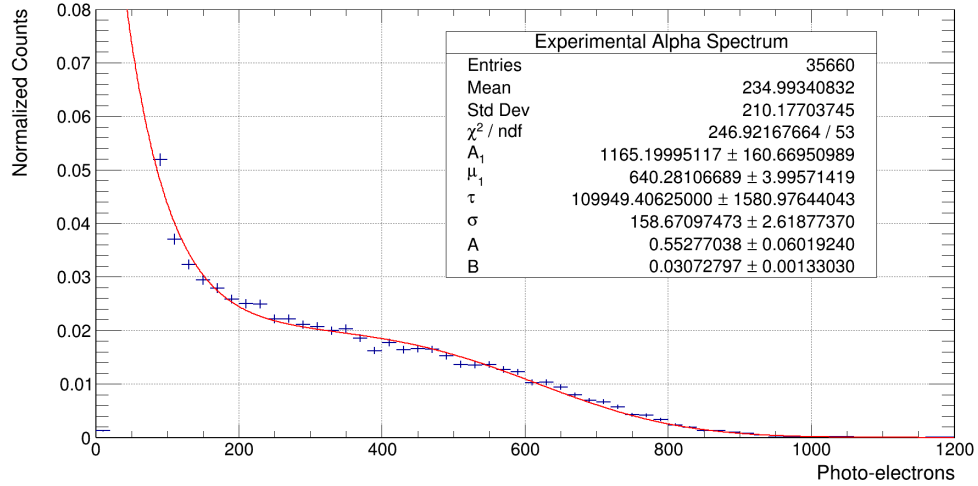
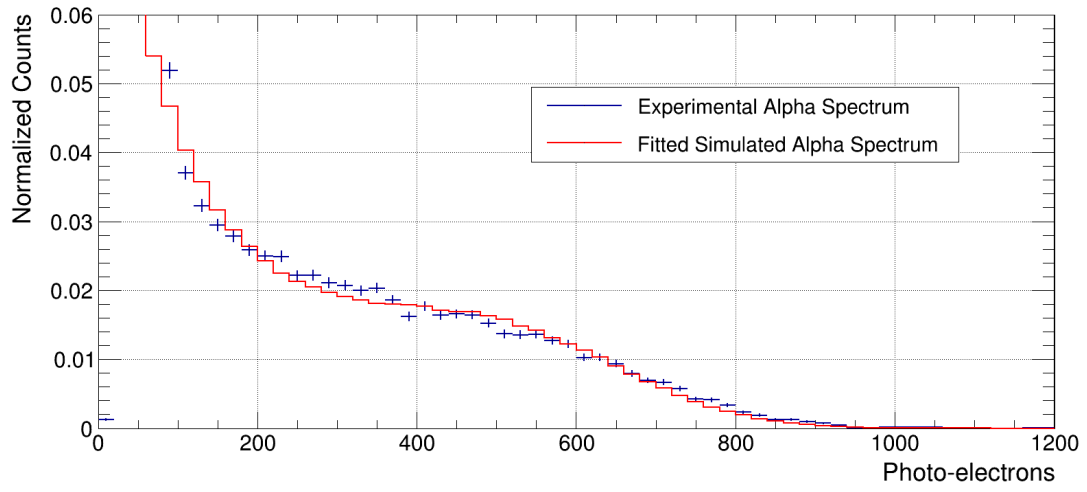


Figure 5.10: Fit of the  $\alpha$ -spectrum following Eq. 5.6 with an exponential noise added.

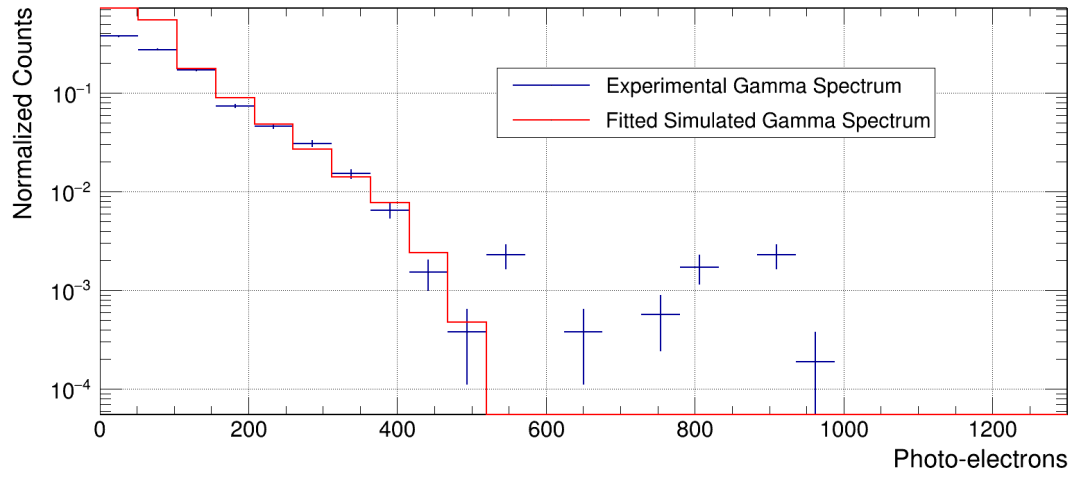
The simulated spectrum of Fig. 5.9 is smeared with the Gaussian's standard deviation  $\sigma$  taken from the fit shown in Fig. 5.10 and the exponential noise is inserted based on the fit parameters. The fitting procedure of the experimental spectrum on top of the MC ones foresees the use of four free parameters: two parameters for the low energy exponential noise, an overall normalization constant and a scale factor, which directly represents the total detection efficiency of the X-ARAPUCA.

There was no need to apply a Gaussian smearing to  $\gamma$ -rays and cosmic muons MC outputs, as data were already well fitted without smearing. The experimental  $\gamma$ -source spectrum is taken by subtracting the histogram done without source from the histogram with the source. Figure 5.11 shows the  $\chi^2$  minimization for all the ionizing radiations for a bias voltage of 48.0 V ( $+ 5.0 \pm 0.2$  O.V.). The  $\alpha$  spectrum in Fig. 5.11a was fitted starting with 75 p.e., the  $\gamma$ -ray spectrum in Fig. 5.11b was fitted between 200 and 500 p.e. and the  $\mu$  spectrum in Fig. 5.11c was fitted starting with 3400 p.e..

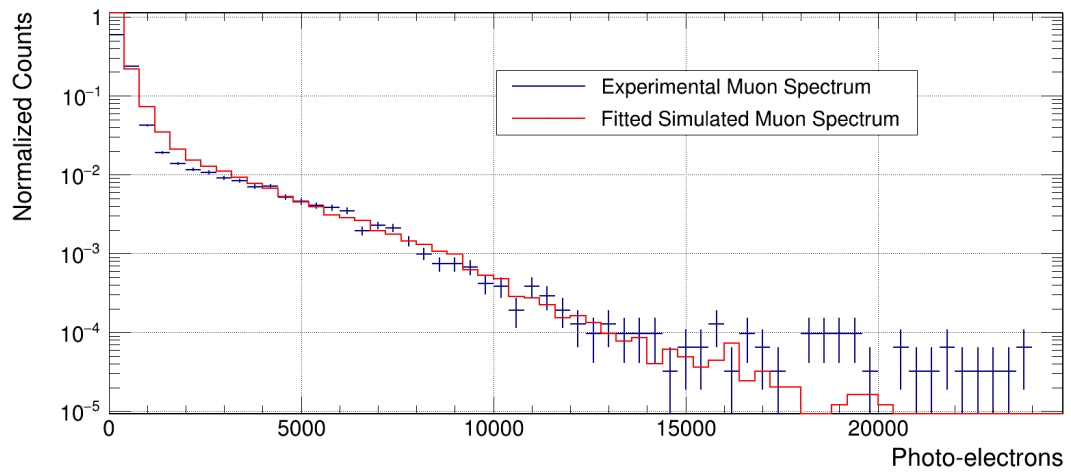
As previously mentioned, the calibration failed for an overvoltage below 5 V in the  $\gamma$ -ray and cosmic muons runs. Figure 5.12b and Fig. 5.12a show the X-ARAPUCA photon collection efficiency, taken with the  $\alpha$ -source, versus the bias voltage without and with cross-talk correction, respectively. In order to compare these results with the ones achieved in Italy [95] (described in Sec. 5.2), the voltage of 48 V, which corresponds to  $5.0 \pm 0.2$  O.V., should be taken. This is due to the fact that the SiPM reaches 50% quantum efficiency at this O.V. [92], the same quantum efficiency at which the SiPMs were operated in Italy. The uncertainties were taken as described in the calibration (Sec. 5.1.3), i.e., 15% without cross-talk correction and 20% with correction.



(a)



(b)



(c)

Figure 5.11: Monte Carlo simulated spectrum (red) fitted to the experimental (blue) spectrum of (a)  $\alpha$ -particles, (b)  $^{60}\text{Co}$   $\gamma$ -rays and (c) cosmic muons [89].

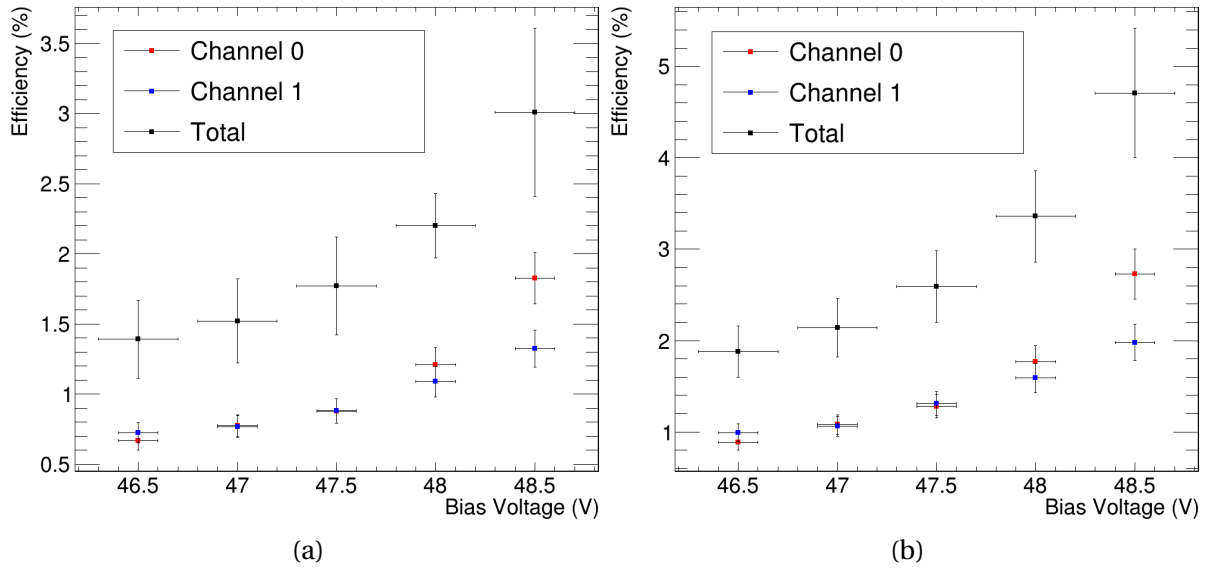


Figure 5.12: Photon collection efficiency versus bias voltage without correcting **(a)** and correcting **(b)** for the cross-talk factor.

Finally, the results for the X-ARAPUCA single-cell efficiency are summarized in table 5.2 comparing between the three ionizing radiations. The cases where the cross-talk is considered or not are both shown. One can notice that the results are compatible considering the uncertainties between  $\alpha$ 's,  $\gamma$ -rays and cosmic muons, which shows that the estimation of the X-ARAPUCA efficiency does not depend on the particle type nor on the topology of the energy deposition.

Table 5.2: Efficiency obtained not considering and considering the cross-talk correction.

	$\mu$ eff. (%)	$\gamma$ eff. (%)	$\alpha$ eff. (%)
Without Cross-talk			
48.0 V	$3.47 \pm 0.52$	$3.43 \pm 0.51$	$3.36 \pm 0.50$
48.5 V	$5.00 \pm 0.75$	$4.20 \pm 0.63$	$4.71 \pm 0.71$
With Cross-talk			
48.0 V	$2.33 \pm 0.47$	$2.32 \pm 0.46$	$2.20 \pm 0.44$
48.5 V	$3.13 \pm 0.63$	$2.65 \pm 0.53$	$3.01 \pm 0.60$

Before these three tests in LAr, other runs with  $\alpha$ -source to evaluate the DUT efficiency were performed with a reasonable agreement [106]. However, a decrease in efficiency was noticed between the first and last tests, which gave efficiencies of  $(3.5 \pm 0.5)\%$  and  $(3.01 \pm 0.60)\%$  respectively. We believe this could be due to the several thermal stresses along these tests. In fact we also noticed micro-cracks formation in the internal WLS slab and in the PTP coating, as shown in Figure 5.13. The cracks formation in PTP can be reduced by avoiding exposure of the X-ARAPUCA to moisture while performing the thermal cycle.

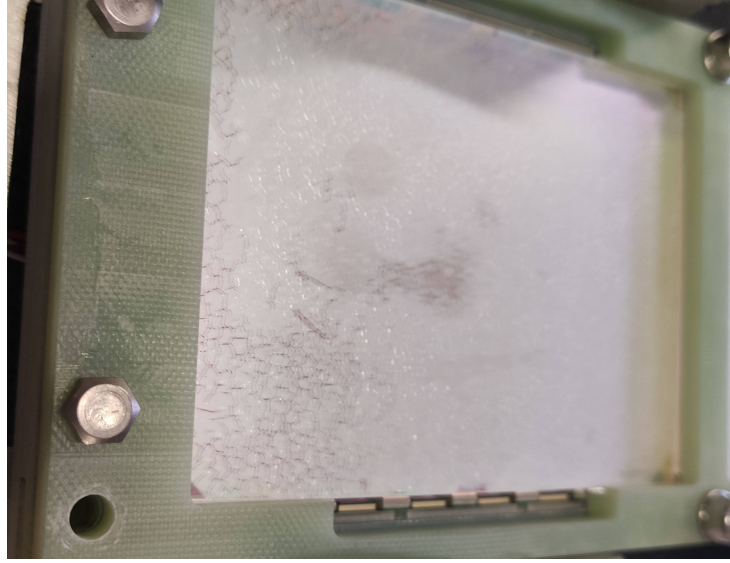


Figure 5.13: Micro-cracks in the PTP deposition after several thermal cycles.

## 5.2. X-ARAPUCA double-cell tests

In Italy, the DUT was the X-ARAPUCA double-cell sizing ( $200 \times 75$ ) mm<sup>2</sup> in Fig. 5.14 [95], the same model that will be deployed in SBND [24]. The two dichroic filters were from the same company (OPTO), but the PTP coating was slightly higher at  $\sim 500 \mu\text{g}/\text{cm}^2$ . The SiPMs were replaced by 4 boards with 4 S14160-6050HS with active area of  $(6 \times 6)$  mm<sup>2</sup> produced by Hamamatsu [92], maintaining the same coverage area of the device. The goal of the experiment was not only to measure the photon detection efficiency of the X-ARAPUCA, but to verify the light collection enhancement due to the WLS developed at Milano-Bicocca (see Sec. 4.4). Therefore, the standard WLS Eljen EJ-286 [73] and the Glass to Power (G2P) [94], denoted FB118, were tested. Besides, the enhancement of the light collection by inserting Vikuiti on the edges of the WLS slab was also tested with the EJ-286 slab. The setup also featured two cold trans-impedance amplifiers, ganging two boards of SiPMs in parallel.

### 5.2.1. Experimental setup and DAQ

The experimental setup, shown in Fig. 5.15, uses the same thermal bath of the X-ARAPUCA single-cell test at Campinas but with a few differences. An exposed 5.49 MeV <sup>241</sup>Am source was used. An alpha source manipulator was installed, which allowed to change the height of the alpha source along the DUT longitudinal axis and eventually to completely remove it. A longer pipe to connect the external warm electronics to the testing

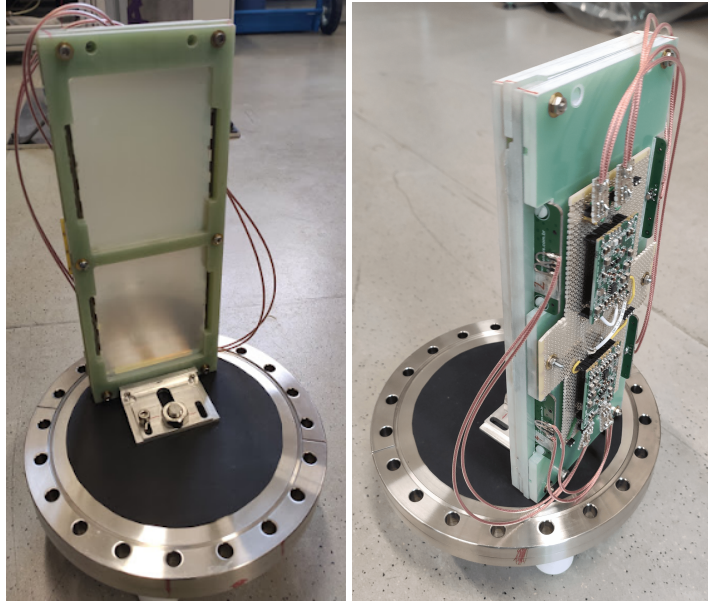


Figure 5.14: Front and back views of the X-ARAPUCA device mounted on the bottom flange of the cryogenic chamber. On the back two readout trans-impedance amplifier circuits are mounted on a service board providing the input/output electrical connections and contacts to the SiPMs. Eight SiPMs are ganged in input to each circuit [95].

chamber minimized the heat transfer, allowing measurements overnight and reduced LAr losses. There was no optical fiber for the s.p.e. calibration.

The method to liquefy the GAr was improved and a better LAr purity was reached. After pumping down the chamber to a pressure of  $\sim 10^{-3}$  mbar, gas argon 6.0 was carefully injected into the system, instead of making the cryogenic pump down as done in the single-cell test. Keeping the GAr at a pressure of  $\sim 1.4$  bar inside the chamber after making the vacuum prevent impurities to get into the stainless steel wall when cooling down.

The  $\alpha$ -source was fixed to the rail at a distance of  $5.5 \pm 0.2$  cm from the dichroic filter and five different positions were tested, as shown in Fig. 5.16, one at the center of the X-ARAPUCA and the other four symmetrically at  $\pm 2.3$  and  $\pm 7.5$  cm away from the center. The source-to-DUT distance was chosen to not saturate the cold amplifiers as the dynamic range was about 500 p.e.. The exposed source was covered with a Teflon mask to reduce the trigger rate.

The readout was performed by a CAEN Digitizer DT5725 with 250 MSamples/s and 14 bits resolution. As the digitizer was similar, the same DAQ presented in Sec. 5.1.2 was used. The ADC readout was done whenever one of the two channels exceeded a fixed threshold of about 10 to 15 p.e.. The threshold was tuned to reach a count rate around 300 Hz and 60 Hz for  $\alpha$  and muon runs, respectively. Triggered events were recorded for

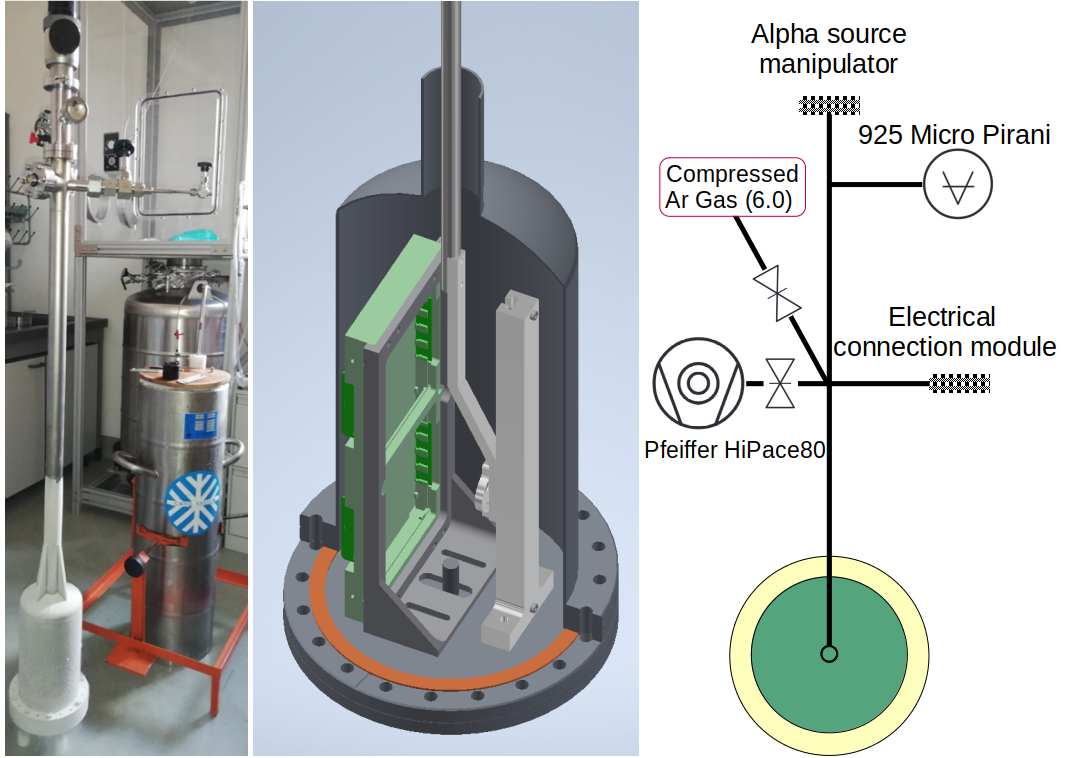


Figure 5.15: The test chamber after removal from the LAr bath (left), 3D drawing of the chamber with the X-Arapuca and the source sliding rail (center) and schematic diagram of the cryogenic setup (right).

$20 \mu\text{s}$  (5,000 points) for each channels with  $5.6 \mu\text{s}$  of pre-trigger.

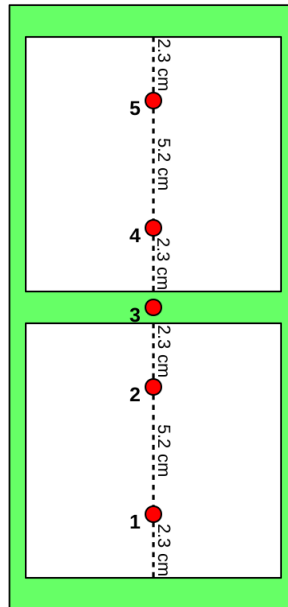


Figure 5.16: The five positions at fixed distance from the X-Arapuca used to characterize the WLS bars [95].

For each position a total of 40,000 events were recorded. The same root files format

adopted in the X-ARAPUCA single-cell test, with the denoise algorithm [98] and the baseline (calculated in the first 5  $\mu\text{s}$  of the pretrigger) applied, was used.

### 5.2.2. Calibration

#### Single photo-electron (s.p.e.) calibration

The s.p.e. calibration had to be performed searching for dark counts in the pre-trigger, as the experimental setup did not featured an optical fiber. The s.p.e. candidates are searched in the first 5  $\mu\text{s}$  of the pre-trigger. All pulses above 3.5 r.m.s of the baseline are integrated for 0.46  $\mu\text{s}$  and their trace stored for  $\sim 1$   $\mu\text{s}$  from the onset. Figure 5.17a shows the obtained spectrum with five well defined peaks, corresponding to the baseline and one to four p.e.. By comparing with the s.p.e. spectra obtained at Unicamp (see Fig. 5.4), one can notice that the spectrum of Fig. 5.17a has a higher resolution. This is a benefit of the use of the cold amplification, that reduces the electrical noise, together with the SiPM model, that has a better shaped s.p.e. compared to the S13360 series.

The fit performed to obtain the gain (G) of the SiPMs is the same as described in Sec. 5.1.3. The recorded traces are displayed at Figure 5.17b, which contains also the averaged waveform (black line) of s.p.e. obtained by selecting waveforms inside plus or minus one sigma interval of the s.p.e. ( $\sigma_1$ ) in Fig. 5.17a.

#### Cross-talk evaluation

The cross-talk calibration was performed offline, by submerging the array of SiPMs in liquid nitrogen and flashing a blue LED through an optical fiber. The same method described in Sec. 5.1.3 was applied on the data and Figure 5.18 shows the result of the fit. The cross-talk probability is evaluated to be  $(18.7 \pm 0.4)\%$ .

A more precise measurement, that was adopted by the community to characterize the SiPMs candidates for DUNE, was performed to calculate the cross-talk probability. In this measurement the SiPM was kept in dark and events triggered above half s.p.e. were recorded. The only assumption in this method is that the dark count should be (basically) composed of s.p.e. and that any signal above one photo-electron is caused by cross-talk. Therefore, the cross-talk probability is defined as the ratio between the number of events above 1 p.e. and the total number of the event registered [99]. By choosing this method, a cross-talk probab-

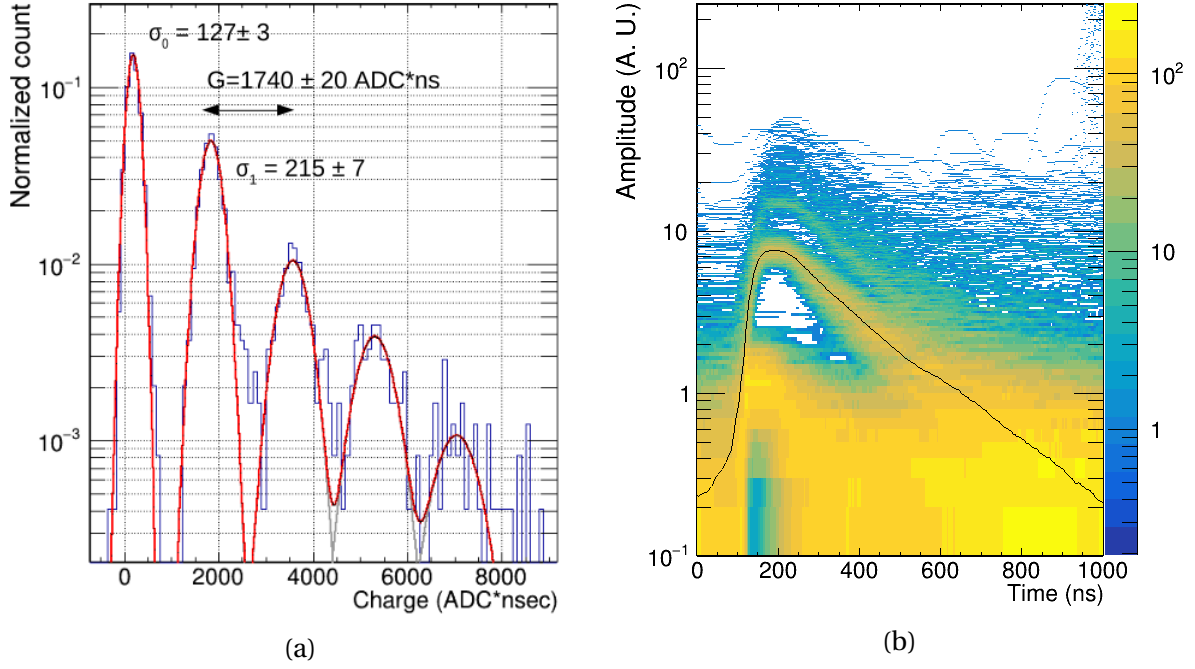


Figure 5.17: **(a)** Charge histogram of the selected peaks, the gain is defined by the distance between the first and second peak. The fit is described in the text. **(b)** Persistence histogram of the selected waveforms together with the average waveform of one single photo-electron [95].

ity ranging from 20 to 24% was measured, corresponding to  $1.22 \pm 0.02$  avalanches/photon. Afterpulses, i.e. the number of secondary pulses within  $10 \mu\text{s}$ , contribute for 11.7% [95].

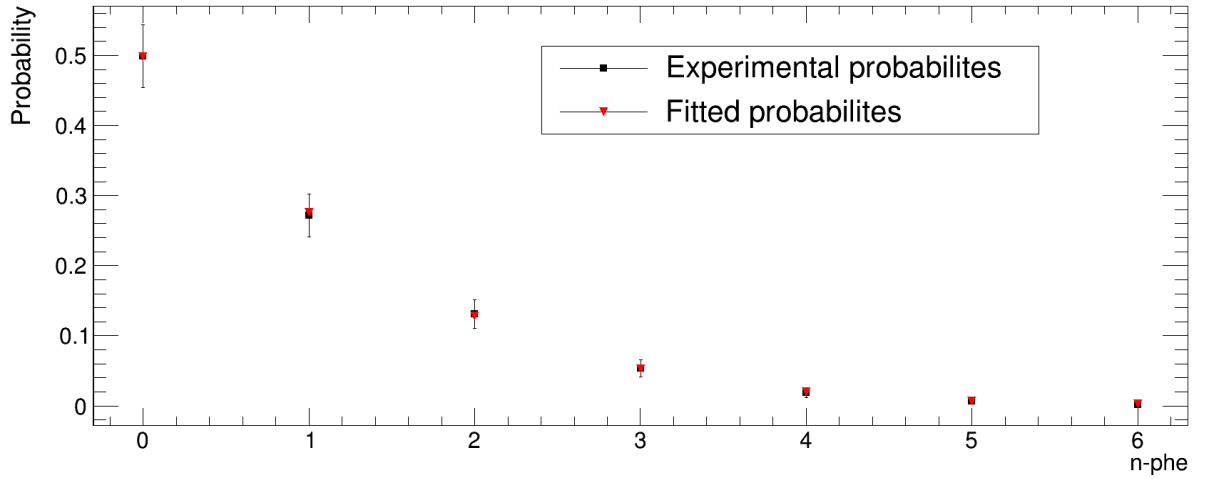


Figure 5.18: Probability of detecting  $n$  photo-electrons (black squares) for the SiPM S14160-6050HS. A  $\chi^2$  minimization of the experimental points with equation 5.3 [100] was performed and the result is shown as red triangles.

## Liquid Argon purity

The purity of the LAr was monitored through the triplet time constant as in the X-ARAPUCA single-cell test (Sec. 5.1.3). In the tests performed at Italy, there was the possibility to make muon runs during the  $\alpha$ -source measurements by rising the source on the top part of the testing chamber. This reduces the amount of light reaching the DUT originated from  $\alpha$ -particles. Rising the threshold will, therefore, increase the number of events from muons. It was not possible to surpass the amplitude of signals from  $\alpha$ -particles due to the saturation of the cold amplifier. The particle identification was performed via  $F_{\text{prompt}}$  classifier, defined as the ratio of the prompt ( $<600$  ns) to the total charge [57, 107, 108] as:

$$F_{\text{prompt}} = \frac{\int_{t_0}^{t_0+0.6 \mu\text{s}} I(t) dt}{\int_{t_0}^{t_0+15.3 \mu\text{s}} I(t) dt}, \quad (5.7)$$

where  $I(t)$  is the waveform,  $t_0$  is the starting point of the integration chosen as 300 ns before the onset and the total charge is evaluated by integrating up to 15.3  $\mu\text{s}$ . Figure 5.19a shows the  $F_{\text{prompt}}$  versus the number of p.e.. As  $\alpha$  particles have a higher contribution of the singlet component and muons will have a higher triplet component (Sec. 3.1), one can choose  $F_{\text{prompt}} > 0.5$  for  $\alpha$  particles and  $F_{\text{prompt}} < 0.5$  for muons. This selection allows to obtain the averaged waveforms for each type of particle in the two different tests, with EJ-286 and FB118. Figure 5.19b presents the waveforms, where one can immediately notice that the LAr purity was the same for the two different tests, as the triplet time constant is basically the same.

The high signal-to-noise resolution noticed in Fig. 5.17b due to the cold amplification allows to deconvolve the s.p.e. response in the averaged waveform. In this scenario, deconvolving was a more precise method than the convolution described in Sec. 5.1.3. The ROOT Cern class TSpectrum [88] was used, with the Gold deconvolution algorithm [109] already implemented. Details about the method are described in Appendix A. The s.p.e. averaged waveform from Fig. 5.17b is deconvolved from the averaged waveforms of Fig. 5.19b.

Figure 5.20 shows the deconvolved waveforms for  $\alpha$  particles (top) and cosmic muons (bottom). A zoom is displayed on the top right corner, so the reader can notice the oscillation on the peak of the waveform which is, most probably, caused by the divergence between the fit and the true s.p.e. waveform (see Fig. A.1). The waveform is fitted by the function  $I(t)$

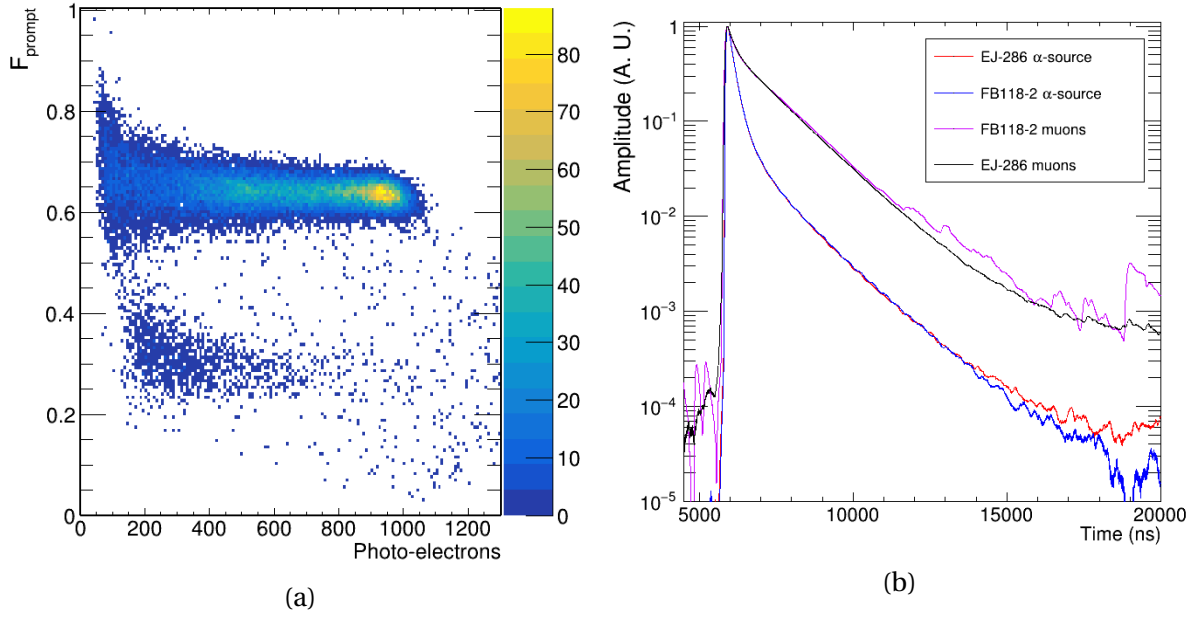


Figure 5.19: **(a)**  $F_{\text{prompt}}$  versus number of p.e.: alphas and muons have  $F_{\text{prompt}} > 0.5$  and  $< 0.5$  respectively. **(b)** The normalized average waveforms of the events, selected on the  $F_{\text{prompt}}$  classifier [95].

(from Sec. 3.1):

$$I(t) = A_S \exp\left(-\frac{t}{\tau_S}\right) + A_T \exp\left(-\frac{t}{\tau_T}\right), \quad (5.8)$$

where  $A_S$  and  $A_T$  are the relative amplitudes and  $\tau_S$  and  $\tau_T$  are the time constants of the singlet and of the triplet dimer states respectively.

The  $\tau_S$  and  $\tau_T$  were computed by the fit of Eq. 5.8.  $A_S$  was taken by integrating the deconvolved waveform of Fig. 5.20 from the rising edge up to 4 times  $\tau_S$  and the  $A_T$  by integrating the triplet component fitted from the rising edge up to 20  $\mu\text{s}$ . Three different measurements were taken: (1) DUT with EJ-286 slab without Vikuiti on the edges, (2) DUT with EJ-286 slab with Vikuiti on the edges and (3) DUT with FB118 slab with Vikuiti. Table 5.3 reports, for each measurement (row), the average values among all the available runs. The uncertainties are the combination of the individual standard deviations with the uncertainty of the average. The ratio  $\langle A_S/A_T \rangle$  was computed from all the runs within each measurement, the ratio weighted average is then computed, properly propagating the uncertainties [95].

Consistent values were found among the three measurements, both for the singlet/triplet decay times and for the relative amplitudes, allowing to evaluate the average. The uncertainties include both the statistical and the systematics which are dominated by the single p.e. calibration. The average triplet time constant of  $1414 \pm 21$  ns and  $1294 \pm 35$  ns for muons and alphas respectively are in agreement with the literature [59, 60, 106] as it is the singlet decay

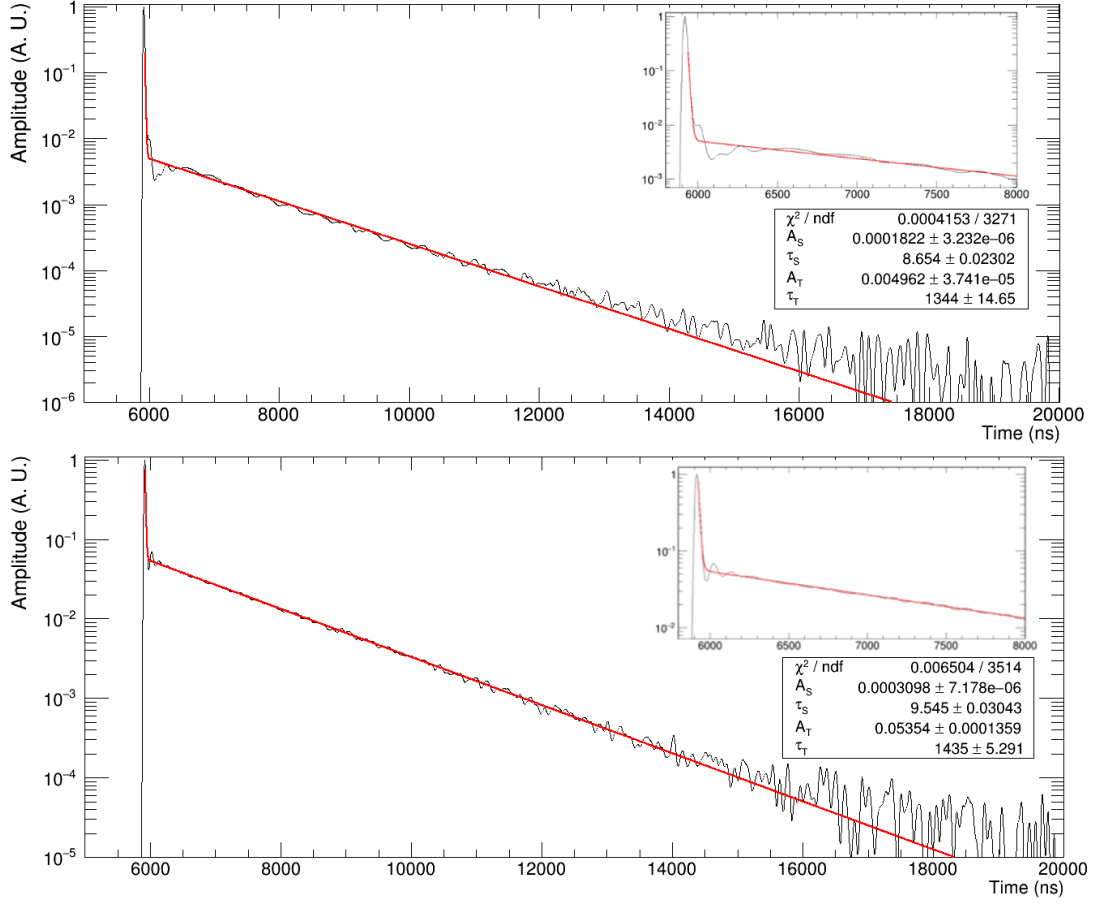


Figure 5.20: The deconvolved averaged waveforms of  $\alpha$ -particles (top) and muons (bottom). A fit of two exponential is made to retrieve the triplet time constant ( $\tau_T$ ). The same fit is displayed with a zoom on the top right corner [95].

time constant. However, one should notice that the fast component is the most difficult to extract due to the poor fitting of the s.p.e. waveform shown in Fig. A.1. The ratio  $\langle A_S/A_T \rangle$  also agrees, even though there are some divergences such as the one found in Ref. [60].

Table 5.3: The singlet and triplet decay time constants ( $\tau_S$  and  $\tau_T$ ) and their relative amplitudes ( $A_S$  and  $A_T$ ) from the waveforms fit for each liquefaction and their averaged values [95].

		$\tau_S$ (ns)	$\tau_T$ (ns)	$A_S$	$A_T$	$A_S/A_T$
$\alpha$	EJ-286 w.o. Vikuiti	$9.3 \pm 0.9$	$1287 \pm 35$	$0.76 \pm 0.06$	$0.24 \pm 0.03$	$3.10 \pm 0.42$
	EJ-286 w. Vikuiti	$11.9 \pm 1.8$	$1286 \pm 37$	$0.77 \pm 0.06$	$0.23 \pm 0.03$	$3.41 \pm 0.51$
	FB118 w. Vikuiti	$7.8 \pm 1.8$	$1331 \pm 22$	$0.79 \pm 0.07$	$0.21 \pm 0.03$	$3.67 \pm 0.58$
	Average	$9.7 \pm 3.0$	$1294 \pm 35$	$0.77 \pm 0.04$	$0.23 \pm 0.02$	$3.35 \pm 0.28$
$\mu$	EJ-286 w.o. Vikuiti	$10.6 \pm 0.5$	$1371 \pm 18$	$0.22 \pm 0.04$	$0.78 \pm 0.10$	$0.28 \pm 0.07$
	EJ-286 w. Vikuiti	$9.6 \pm 0.1$	$1411 \pm 33$	$0.23 \pm 0.05$	$0.77 \pm 0.11$	$0.29 \pm 0.08$
	FB118 w. Vikuiti	$10.6 \pm 4.4$	$1459 \pm 35$	$0.23 \pm 0.05$	$0.77 \pm 0.11$	$0.30 \pm 0.08$
	Average	$10.2 \pm 5.1$	$1414 \pm 21$	$0.18 \pm 0.03$	$0.82 \pm 0.04$	$0.29 \pm 0.03$

The higher triplet time constant of  $1294 \pm 35$  ns in the X-ARAPUCA double-cell test (com-

pared with the  $780 \pm 20$  in Sec. 5.1.3) implied a correction of only +1.4 to 2.6% more light. However, the precise evaluation of the waveforms showed that all the three measurements reached the same LAr purity level. Therefore, it is possible to evaluate the difference in light collection among the three measurements.

### 5.2.3. Monte Carlo “Toy-model”

A Monte Carlo numerical evaluation was performed to estimate the amount of light that would reach the X-ARAPUCA acceptance window. The name “toy-model” comes from the fact that this is not a complete Geant4 simulation of the experimental setup, as the one described at Sec. 5.1.4, but a geometrical estimation using Monte Carlo through the ROOT Cern libraries [88].

The  $\alpha$  particles emission light was considered to be point-like from the center of the disk  $5.5 \pm 0.2$  cm away from the center of the DUT. The point like approach is quite enough, because the open surface of the source was about 6 mm diameter and the maximum range for the  $\alpha$  particles in LAr will be around  $50 \mu\text{m}$  [110]. The light is emitted isotropically, assuming a light yield of  $51,000 \gamma/\text{MeV}$  times the quenching factor of 0.71 [37, 60, 103] (the same values used in Sec. 5.1.4). To speed up the simulation, a factor of 0.01 was applied to the photons production. Reducing the amount of photons by this factor is equivalent to having a collection efficiency of 1%.

The photons are tracked and the amount of photons reaching the DUT dichroic filter is computed. Figure 5.21 shows the expected number of photons for each position of the  $\alpha$  source (as shown in Fig. 5.16). One can notice positions 1 and 5 are indeed symmetric and for the central positions 2, 3 and 4 the output is basically the same. This is quite expected as the solid angle for the central positions is basically the same.

The expected number of photo-electrons is retrieved by fitting the spectra with a Gaussian distribution and the uncertainty set as 2% by taking the deviation due the alpha-to-device distance uncertainty. The results are presented in Tab. 5.4 for the analysis of the X-ARAPUCA efficiency.

### 5.2.4. Efficiency and enhancement analysis

The waveforms were integrated from 5.6 to  $11 \mu\text{s}$  and the s.p.e. calibration applied. Figure 5.22 shows the calibrated  $\alpha$  spectrum, for both the FB118 (left) and EJ-286 (right). As

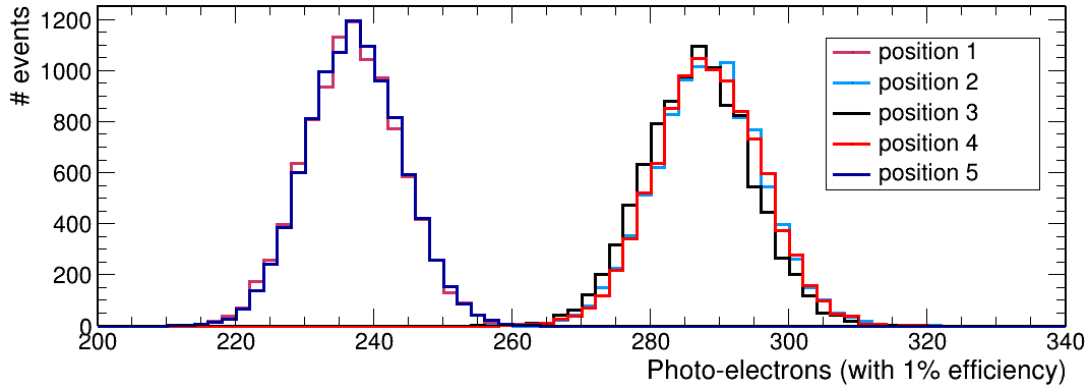


Figure 5.21: Expected photo-electron for each position considering an efficiency of 1%.

expected from the geometry and the “toy-model”, the spectra for position 2, 3 and 4 overlap. However, a significant difference can be noticed between position 1 and 5, which are expected to be identical. This is attributed to the shadowing of the  $\alpha$ -source holder of Fig. 5.15 (central figure), which blocks light on the top part of the DUT when the source is at the bottom. Because of that, the position 1 was not used for the evaluation of the X-ARAPUCA light collection efficiency, but was still used to estimate the enhancement in the light collection

The spectra of Fig. 5.22 are presented with the same range, so it is straightforward to notice the sizable increase of the collected photons when the optical cell is equipped with the FB118 instead of the EJ-286.

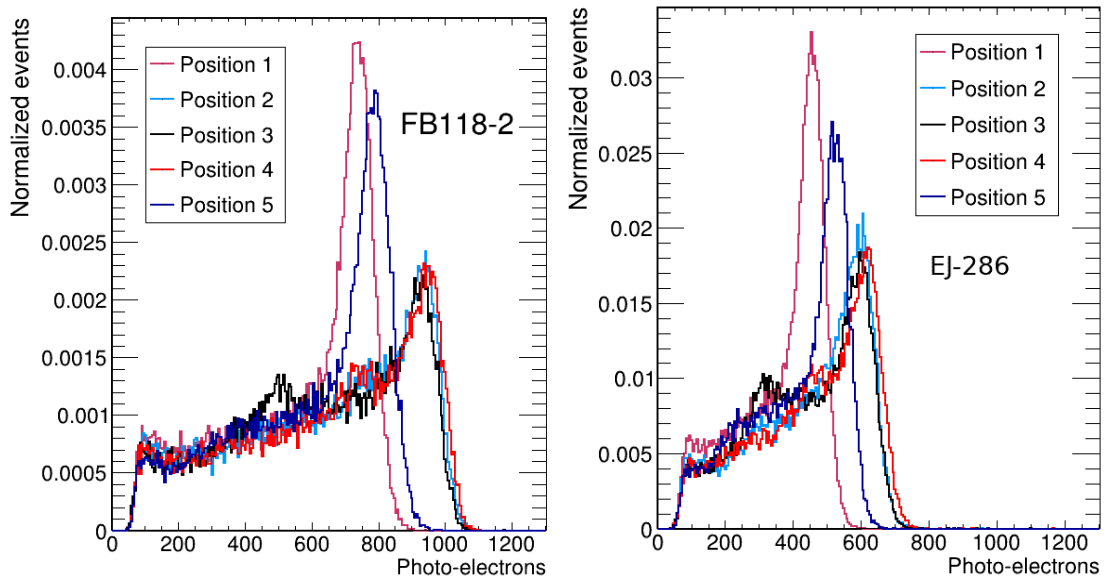


Figure 5.22: The  $\alpha$  spectrum in number of detected photo-electrons for each of the five source positions: the X-Arapuca is equipped with FB118 (Left) and EJ-286 (Right) respectively [95].

To determine the alpha peak position, the same function as in Eq. 5.6 was used, however

with only one emission line, that is [104]:

$$F(E) = \frac{A}{2\tau} \exp\left(\frac{E-\mu}{\tau} + \frac{\sigma^2}{2\tau^2}\right) \operatorname{erf}\left(\frac{1}{\sqrt{2}}\left(\frac{E-\mu}{\sigma} + \frac{\sigma}{\tau}\right)\right), \quad (5.9)$$

where  $\mu$  is the peak position,  $A$  is the area,  $\sigma$  is the spread of the alpha-peak and  $\tau$  is the slope of the tail on the peak low-energy side. Figure 5.23 shows the spectrum when the source is in the central position (#3), and superimposed the fits for both the EJ-286 and FB118.

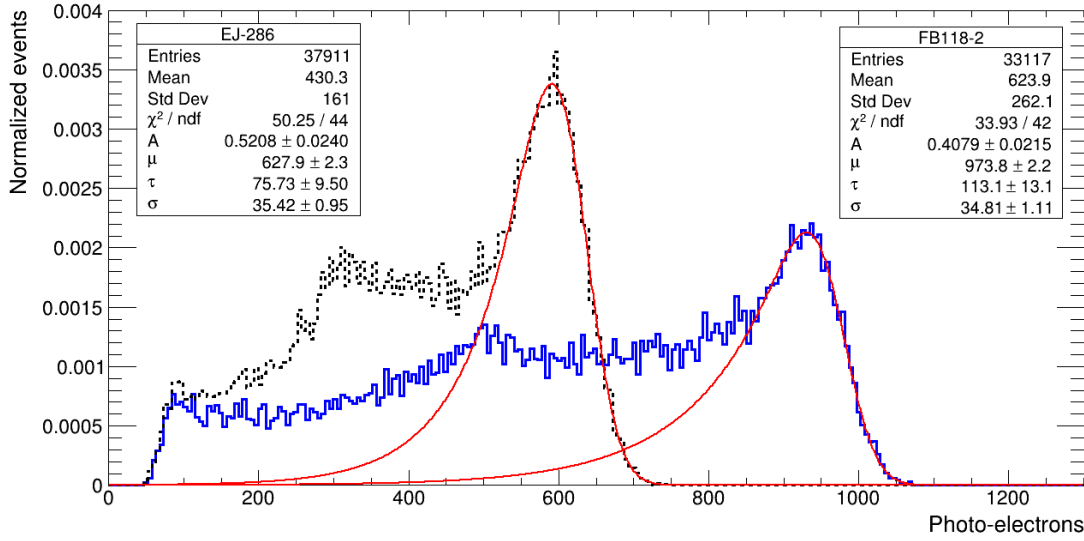


Figure 5.23: The  $\alpha$  spectrum fit with Eq. 5.9 for the source in the central position (#3) for EJ-286 (black, dashed line) and FB118 (blue, solid line) [95].

Table 5.4 shows the expected number of photo-electrons for a 1% efficiency X-ARAPUCA, and the detected ones for the three measurements performed. The uncertainty of the peak was assumed as 2.5% due to the s.p.e. calibration and the average of position 2, 3 and 4 was taken to make a better comparison. These values can be directly compared in order to retrieve the light collection enhancement of the DUT with the FB118 slab or by the application of the Vikuiti. For the efficiency of the device, however, the cross-talk and liquid argon purity must be applied.

Table 5.4: Expected value of photons reaching the X-Arapuca acceptance window given by numerical evaluation described in Sec. 5.2.3 and number of photo-electrons detected in the three different configurations. An average of position 2, 3 and 4 was taken [95].

Positions	Expected (MC) # p.e.	EJ-286 w/o Vikuiti # p.e.	EJ-286 w/ Vikuiti # p.e.	FB118 # p.e.
2,3,4	$288 \pm 6$	$607 \pm 9$	$637 \pm 9$	$986 \pm 14$
5	$236 \pm 5$	$515 \pm 13$	$548 \pm 14$	$825 \pm 20$
1	$236 \pm 5$	$443 \pm 11$	$473 \pm 12$	$770 \pm 18$

From the ratio of the alpha-peak means, for each source position, the photo detection efficiency variation  $G_e$  was computed when the X-ARAPUCA had the FB118 as secondary wavelength shifter instead of the EJ-286, the result is presented at Table 5.5, defining  $G_e$  as:

$$G_e = \left( \frac{\mu_{\text{FB118}}}{\mu_{\text{EJ-286}}} - 1 \right) \times 100 [\%], \quad (5.10)$$

where  $\mu$  is the alpha-peak mean from Eq. 5.9 already presented in Table 5.4.

Table 5.5: The PDE increase ( $G_e$ ) when replacing the EJ-286 in the X-Arapuca with the FB118, for the five source positions as in Table 5.4 [95].

Positions	$G_e$
2,3,4	$55 \pm 5 \%$
5	$50 \pm 5 \%$
1	$63 \pm 6 \%$

Finally, the absolute efficiencies of the X-Arapuca with EJ-286 (with and without Vikuiti) and FB118 with Vikuiti are displayed in Table 5.6. The efficiency uncertainty includes those from LAr purity correction, the single photo-electron calibration and the solid angle [95]. The signal-to-noise ratio is reported and defined as:

$$S/N = \frac{\mu_1}{\sqrt{\sigma_0^2 + \sigma_1^2}}, \quad (5.11)$$

where  $\mu_1$  is the mean charge of a single p.e.,  $\sigma_0$  and  $\sigma_1$  are the standard deviation of the noise and s.p.e., respectively, in Fig. 5.17a. This is an important feature for the trans-impedance amplifier, as one of the DUNE requirements is a signal-to-noise  $> 4$  [5]. It is important to notice that here, however, only eight SiPMs were ganged together and for the supercell module there will be 48 SiPMs ganged. The resolution ( $\sigma/\mu$ ) of the alpha peak ( $\sigma$  and  $\mu$  from the fit function 5.9) is also reported and, as expected, it scales with the number of detected photons.

The application of Vikuiti on the EJ-286 slab edges resulted in an increase from 3 to 11% where positions (1 and 5) show the largest increase as measured at room temperature (see Sec. 4.4). However, the increase in the PDE was lower in LAr than in air/vacuum. We believe this is caused by the critical angle in LAr of about  $55.4^\circ$  and  $51.4^\circ$  for FB118 and EJ-286, respectively, compared with  $41.8^\circ$  and  $39.2^\circ$  in air, therefore less photons are trapped in LAr reducing the effectiveness of applying Vikuiti on the edges.

The enhancement of about 50% with the Glass-to-Power WLS with respect to the Eljen EJ-286 WLS was a very important result: increasing the efficiency of the X-ARAPUCA helps to

Table 5.6: Summary of the relevant facts for the X-Arapuca efficiency measurements by  $^{241}\text{Am}$   $\alpha$  source radiation and the three considered configurations: Energy Resolution of the  $\alpha$  peak, S/N: signal-to-noise,  $\epsilon_{\text{raw}}$ ,  $\epsilon$ ; Efficiency prior (raw) and post corrections respectively [95].

	EJ-286 w/o Vikuiti	EJ-286 w/ Vikuiti	FB118
En. res. ( $\sigma/\mu$ )	$6.3 \pm 0.2 \%$	$6.0 \pm 0.2 \%$	$3.6 \pm 0.1 \%$
S/N	$6.8 \pm 0.3$	$7.3 \pm 0.3$	$7.3 \pm 0.3$
$\epsilon_{\text{raw}}$	$2.1 \pm 0.1 \%$	$2.3 \pm 0.1 \%$	$3.5 \pm 0.1 \%$
$\tau_T$	$1294 \pm 35 \text{ ns}$		
LAr purity correction	$+ (1.4 \text{ to } 2.6) \%$		
Cross-talk correction	$- (18 \pm 1) \%$		
$\epsilon$	$1.8 \pm 0.1\%$	$1.9 \pm 0.1\%$	$2.9 \pm 0.1\%$

approach the DUNE specifications of average light yield of p.e./MeV (see Sec. 2.2.3). The research developed in Milano-Bicocca has set a more direct contact between the DUNE collaboration and the vendor of the WLS. New batches of both WLS were sent for different groups of the collaboration for the tests of the X-ARAPUCA supercell, Eljen Co. has provided EJ-286 slabs with two times and four times more concentration than the commercial batches. In ProtoDUNE run II, both WLS will be deployed which will help the selection for the DUNE first far detector.

The efficiency of  $(1.9 \pm 0.1)\%$  for the X-ARAPUCA double-cell with the EJ-286 slab agrees with the efficiency of  $(2.20 \pm 0.44)\%$  found at Sec. 5.1 for the single-cell, as both SiPMs operated at 50% PDE [92]. This efficiency satisfies the minimum requirement of the DUNE FD for an efficiency  $> 1.3\%$  [5]. The X-ARAPUCA equipped with the FB118 slab, however, presented an efficiency of  $(2.9 \pm 0.1)\%$  which satisfies the average efficiency requirement.

# Chapter 6

## The ProtoDUNE-SP and Xenon Doping

### 6.1. The ProtoDUNE-SP experiment

Even though the LArTPC technology has been quite explored and proved to meet the requirements for excellent neutrino detection and physics, the DUNE experiment gather around many new technologies and techniques with major challenges. The biggest LArTPC built up to now is the ICARUS T600 [38], with a LAr fiducial volume of about 500 t divided into two drift regions, the detector is basically 20 times smaller than one DUNE FD module. Besides, the ICARUS T600 maximum drift distance of 1.5 m requires a high voltage of  $-75$  kV, while the DUNE FD will have a drift distance of 3.5 m and high voltage of  $-180$  kV.

The ProtoDUNE-SP experiment [71] is a prototype built at CERN with 419 t of instrumented LAr mass. The two TPC volumes with  $6.086$  (h)  $\times$   $3.597$  (w)  $\times$   $7.045$  (l)  $\text{m}^3$  are shown in Figure 6.1 with total active volume of  $2 \times 154 \text{ m}^3$ , each with drift distance of 3.572 m and  $-180$  kV high voltage bias in the APA. One of the instrumented TPCs receives a beam that can

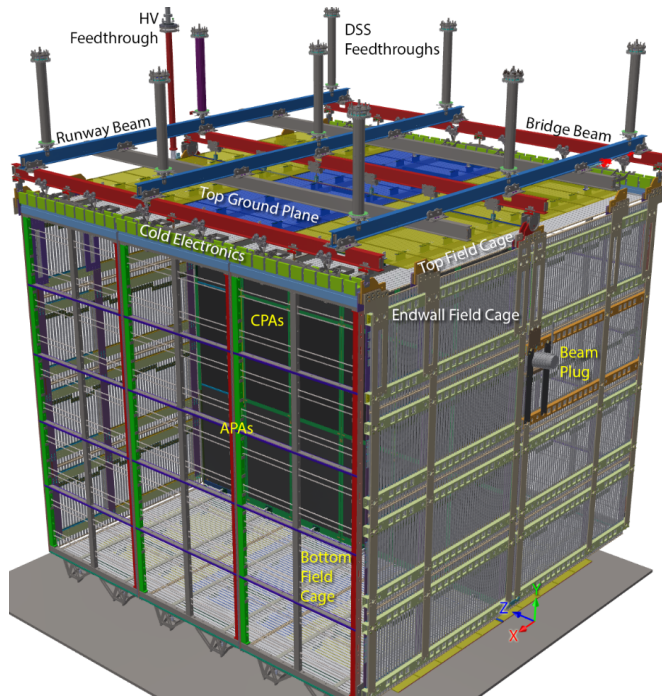


Figure 6.1: View of the ProtoDUNE TPC, the APAs area placed in the side of the detector and the CPA in the middle. The beam arrives in one right-side TPC [39].

deliver pions, kaons, protons, muons and electrons with momenta ranging from 0.3 GeV/c

to 7 GeV/c. The wires pitch, distance and voltage in the APAs have the same construction proposed for DUNE (described at Sec. 2.2.2).

The prototype operated in the first run from September 2018 to January 2020 and had as primary goals to: (1) stress-test the production and quality assurance of the detector components, (2) validate the installation procedures, (3) validate the detector performance with cosmic rays and (4) measure the physics response of the detector with beam data [2].

All the details about the performance of the TPC and the light detectors are very well described in the performance paper [39]. It is worth mentioning the light collection efficiency found for the ARAPUCA devices installed in the prototype.

A total of 60 light collector modules were installed: two of them are based on the S-ARAPUCA concept (see Sec. 3.2) and the other 58 were equally divided into dip-coated and double-shift light guides [39]. The dip-coated light guide consist of  $207.4 \times 8.2 \text{ cm}^2$  wavelength shifter bars with TPB dip-coated to downshift the light to 430 nm. The double-shift light guides have TPB evaporated in a wavelength shifter that downshifts the 430 nm light to 490 nm. Both devices detect the total internal reflected light in the shorter edge of the bar with 12 SiPMs.

One S-ARAPUCA module consisted of 12 cells, eight with optical area of  $9.8 \times 7.9 \text{ cm}^2$  and 4 with  $19.6 \times 7.9 \text{ cm}^2$ . Each cell with its own readout of the 12 Hamamatsu S13360-6050CQ SiPMs. The ratio of photon sensors area to the light collectors surface area was 0.25% for the light-guides and 5.6% and 2.8% for the two S-ARAPUCAs modules with “normal” and double area, respectively.

It was found an efficiency of  $(2.00 \pm 0.25)\%$  and  $(1.06 \pm 0.09)\%$  for the S-ARAPUCA cells with normal and double area, respectively. An efficiency of  $(0.21 \pm 0.03)\%$  and  $(0.08 \pm 0.02)\%$  was found for the double-shift and dip-coated light guides [39]. It is worth mentioning that the LAr tests performed in Brazil (Sec. 5.1) had the same type of SiPM installed in the X-ARAPUCA with an area ratio of 3.6% and an efficiency of  $(2.2 \pm 0.44)\%$  with  $\alpha$ -particles. This shows the improvement of the X-ARAPUCA.

The PDS light yield was evaluated by measuring the average light detected by the ARAPUCA module for different electron energies from the beam, as shown in Figure 6.2a [39]. By comparing the number of detected photons with the expected number of incident photons simulated and by extrapolating to a PDS composed only of ARAPUCAs, a light yield of 1.9 p.e./MeV was found. A value greater than the 0.5 p.e./MeV is required by DUNE [5].

The time resolution of the PDS was taken by measuring the time difference between two LED light signals, as shown in Figure 6.2b. The value of 14 ns fulfills the DUNE requirement of a time resolution lower than 100 ns [5, 39]. Finally, it was reported an electron lifetime greater than 20 ms, while it is required  $e$ -lifetime  $> 3$  ms.

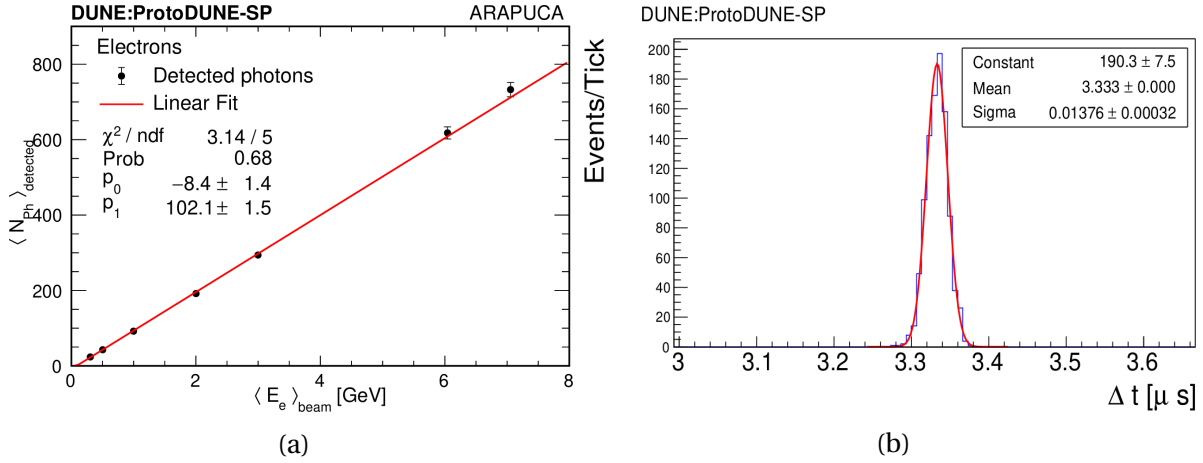


Figure 6.2: **(a)** Average detected photons versus as function of incident electron energy for the ARAPUCA module. **(b)** PDS time resolution (using the time difference between two LED signals) [39].

## 6.2. Xenon Doping tests

At the end of the ProtoDUNE-SP run I there was a failure in the gas re-circulation pump, which resulted in a certain amount of air inside the detector. The LArTPC purification system could remove the  $O_2$ ,  $CO_2$  and  $H_2O$ : however, the system was not able to remove  $N_2$ . It was estimated that about 5 ppm of  $N_2$  were leaked into the detector.

As described in Sec. 3.1.4, nitrogen contaminant decreases the light yield of the detector by quenching the triplet state light emission.

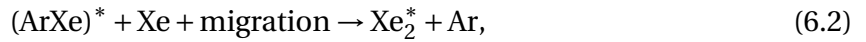
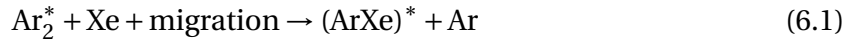
Xenon emits scintillation light at 175 nm [111–113], that can be more efficiently collected, and have a longer Rayleigh scattering length [62, 63], which can improve the uniformity of the light response across a large detector such as DUNE. Besides, the xenon light emission is faster than argon, which can improve the detector time resolution. Because of that, the DUNE Collaboration was already studying the possibility of doping LAr with a few tens of ppm level of xenon (Xe).

The nitrogen contamination event was a great opportunity to test this technology in a large scale experiment. In the case where the TPC works properly and the PDS is restored, Xe

doping may be considered as a solution for the DUNE experiment in a case of contamination leakage such the one just described.

### 6.2.1. Xe doping effect in LAr

Doping LAr with small amounts of xenon (at few ppm levels) causes the transfer of the excitation energy from argon to xenon dimers through the following series of reactions [107, 111]:



where the excimer singlet and triplet states will decay with a characteristic time of 4,2 ns and 22 ns, respectively, by emitting light around 175 nm. As for the quenching effect (see Sec. 3.1.4), the Xe energy transfer will affect mostly the argon triplet state as it is the longest living one. The light production rate can be taken as the sum of the Ar and Xe excimer distributions, that is:

$$r = \lambda_{\text{Ar},1} N_{\text{Ar},1} + \lambda_{\text{Ar},3} N_{\text{Ar},3} + \lambda_{\text{Xe},1} N_{\text{Xe},1} + \lambda_{\text{Xe},3} N_{\text{Xe},3}, \quad (6.3)$$

where  $N$  corresponds to the number of singlet and triplets (depending on the index 1 or 3) of Ar or Xe, and  $\lambda$  is the decay constant of each state.

Defining  $\lambda_m$  as the transition rate to the excimer ArXe,  $\lambda_d$  as the transition rate to the Xe excimer,  $q$  as the fraction of Ar excimer in the singlet state and  $p$  as the fraction of Xe excimer in the singlet state, one can obtain the transition differential equations for different states [111]:

$$\frac{dN_{\text{Ar},1}}{dt} = -\lambda_{\text{Ar},1} N_{\text{Ar},1} - \lambda_m N_{\text{Ar},1} \quad (6.4)$$

$$\frac{dN_{\text{Ar},3}}{dt} = -\lambda_{\text{Ar},3} N_{\text{Ar},3} - \lambda_m N_{\text{Ar},3} \quad (6.5)$$

$$\frac{dN_{\text{ArXe}}}{dt} = +\lambda_m N_{\text{Ar},1} + \lambda_m N_{\text{Ar},3} - \lambda_d N_{\text{ArXe}} \quad (6.6)$$

$$\frac{dN_{\text{Xe},1}}{dt} = +\lambda_d p N_{\text{ArXe}} - \lambda_{\text{Xe},1} N_{\text{Xe},1} \quad (6.7)$$

$$\frac{dN_{\text{Xe},3}}{dt} = +\lambda_d (1 - p) N_{\text{ArXe}} - \lambda_{\text{Xe},3} N_{\text{Xe},3}. \quad (6.8)$$

The argon light output will have the same usual two exponential decays. By defining:

$$\lambda_{1m} \equiv \lambda_{\text{Ar},1} + \lambda_m \quad (6.9)$$

$$\lambda_{3m} \equiv \lambda_{\text{Ar},3} + \lambda_m, \quad (6.10)$$

the solved equation can be simplified by disregarding the exponential terms with  $\lambda_{Xe,1}$  and  $\lambda_{Xe,3}$  as [107]:

$$r = A_1 e^{-\lambda_{1m}t} + A_2 e^{-\lambda_{3m}t} - A_3 e^{-\lambda_d t}, \quad (6.11)$$

where the decay time constants fast, slow and delayed can be defined as:

$$\tau_{\text{fast}} = \frac{1}{\lambda_{1m}} \quad (6.12)$$

$$\tau_{\text{slow}} = \frac{1}{\lambda_{3m}} \quad (6.13)$$

$$\tau_d = \frac{1}{\lambda_d}. \quad (6.14)$$

Equation 6.11 translates the competition between LAr scintillation emission and Xe shifting. The light output becomes faster with the increasing of Xe concentration: as the transfer rates  $\lambda_m$  and  $\lambda_d$  increase, the argon triplet contribution decreases. Therefore, the time constants  $\tau_{\text{slow}}$  and  $\tau_d$  are expected to decrease at higher concentrations. The assumption that a few ppm of  $N_2$  does not affect the singlet or triplet excimer de-excitation is reasonable due to the time scales. Consequently, it is expected that increasing the Xe concentration in the case of  $N_2$  contamination, the Xe shift process happens before the quenching, restoring the light yield.

### 6.2.2. Experimental setup

The xenon doping test consisted of doping the LAr five times, the first had Xe injected so the proportion of 0.8 ppm was achieved. A proportion of 3.3 ppm, 11 ppm, 15 ppm and 20 ppm were achieved in the following Xe injections (dopings).

It was decided to deploy two X-ARAPUCA modules of the SBND type in the cryostat. The X-ARAPUCAs were installed behind the APA, as can be seen in Figure 6.3a. The APA (and the PDS modules) can be seen 22.69 cm away from the X-ARAPUCA on the top. The second X-ARAPUCA is 36 cm below. The double-cell was of the same size and construction as the one described in Sec. 5.2, with EJ-286 WLS slab and PTP coated in the Opto Co. dichroic filter, but with SiPMs Hamamatsu S13360-6050VE, the same used in the single-cell test. The tests performed in the Monochromator (Sec. 4.2.1) showed that fused silica (quartz) has a transparency of 80% to 90% for the 175 nm while completely blocking the 128 nm LAr scintillation light. Therefore, the bottom X-ARAPUCA was deployed with a quartz window in the front, to detect only Xe emitted light.

An external trigger was used with three detectors (denoted *paddles*) of plastic scintillator sizing  $44 \times 15.5 \text{ cm}^2$  coupled to PMTs and vertically aligned, as shown in Figure 6.3b with the paddles over the LArTPC cryostat. The top paddle is 34 cm away from the center one, while the bottom paddle is distanced 29 cm. The triple coincidence of the detectors selects mostly vertical muons and was used as external trigger for the readout of the X-ARAPUCAs. The readout was performed by an ADC of 150 MSamples/s with a total of 2000 “ticks” each with 6.67 nm.

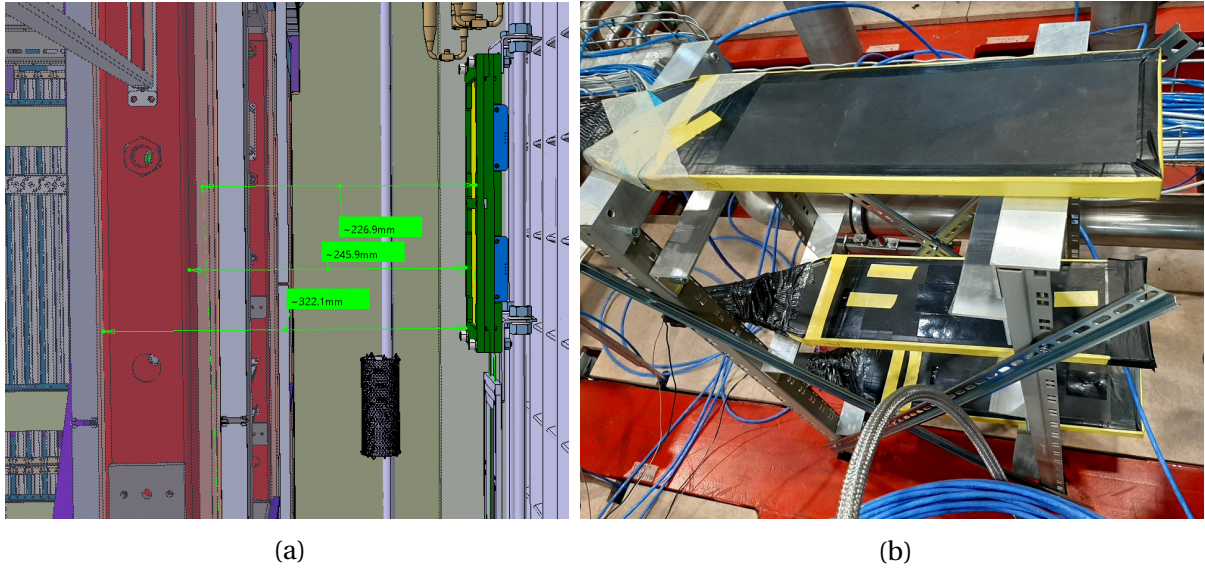


Figure 6.3: **(a)** Schematic assembly of the X-ARAPUCA behind the APA. **(b)** Muon telescope composed with three plastic scintillator detector above the ProtoDUNE-SP cryostat.

### 6.2.3. Waveform analysis

A dedicate team performed the analysis of the data collected with xenon doped LAr. Here is described the waveform analysis performed by the author and Niccoló Gallice (Università degli Studi di Milano). The waveform behavior along the increasing Xe doping concentration was analyzed.

The averaged waveforms for each of the four channels of the X-ARAPUCA was taken. As each channel has four SiPMs ganged passively in parallel, the time response of the detector is not enough to retrieve the shape described by Eq. 6.11. Two different approaches were taken to retrieve the time constants. In the first one, the single photo-electron (s.p.e.) response was deconvolved from the averaged signal so a fit with Eq. 6.11 could be performed, the same approach used for the X-ARAPUCA double-cell (Sec. 5.2). The second approach consisted in

convolving the s.p.e. response with the theoretical signal and performing a  $\chi^2$  minimization of the experimental waveform, a method similar to the one used for the X-ARAPUCA single-cell (Sec. 5.1).

For the deconvolution, the s.p.e. responses were searched and selected in the pretrigger (the first 400 ticks), the s.p.e. spectrum of Figure 6.4a was taken by integrating the pulses for about 200 ticks. The averaged s.p.e. waveform is taken by selecting events with charge inside  $1\sigma$  from the adjusted Gaussian in Figure 6.4a. The resulting waveform, displayed in Figure 6.4b, is then fitted with two exponentials convoluted with a Gaussian response (see Appendix A), represented in red.

Figure 6.5a shows the averaged waveforms of the five Xe concentrations for the X-ARAPUCA without quartz window. The “Gold deconvolution algorithm” implemented in the TSppectrum class of Root Cern [88] was used (see Appendix A) and the results are presented in Figure 6.5b. The fast, slow and delayed components are more evident in the deconvolved waveforms and can be more accurately retrieved. One can verify that the slow component is restored after the first doping (0.8 ppm) and decreases with the increasing concentration while the delayed light increases. Reaching stability after 15 ppm.

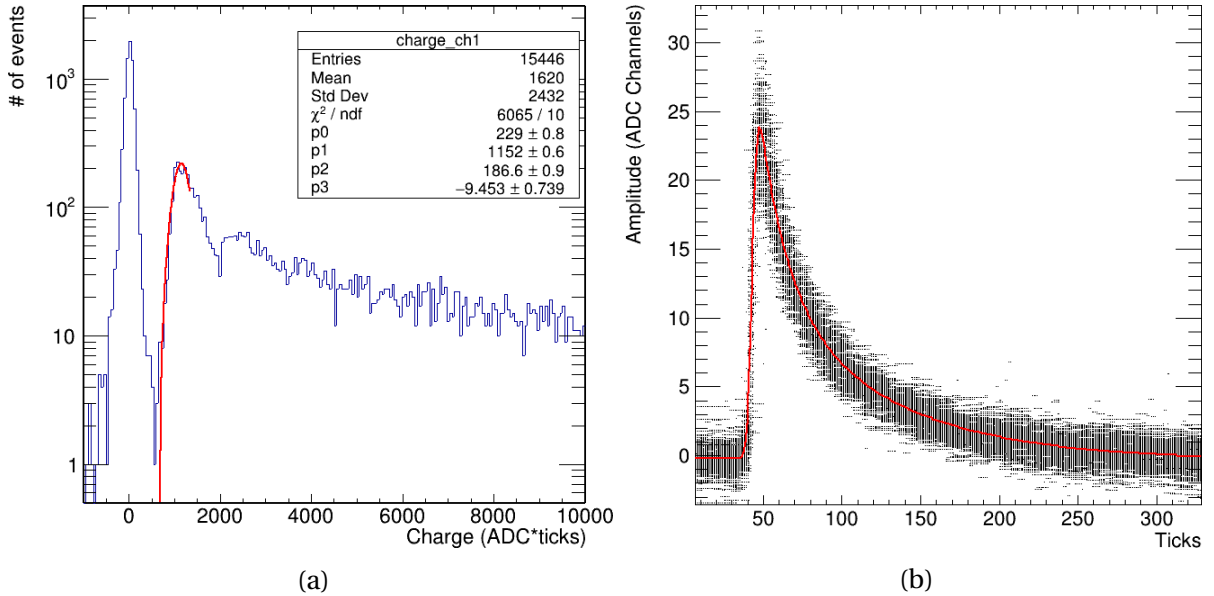


Figure 6.4: **(a)** Single photo-electron spectrum obtained, a Gaussian was adjusted in the data (red) to retrieve the corresponding s.p.e. events. **(b)** Waveforms (black points) selected inside  $1\sigma$  of Gaussian fit and the averaged waveform fit (red line).

Finally, Figure 6.6 shows the fits performed with the two methods, where Fig. 6.6a shows the fit of Eq. 6.11 in the deconvolved waveform for the last doping. On the other hand, Fig.

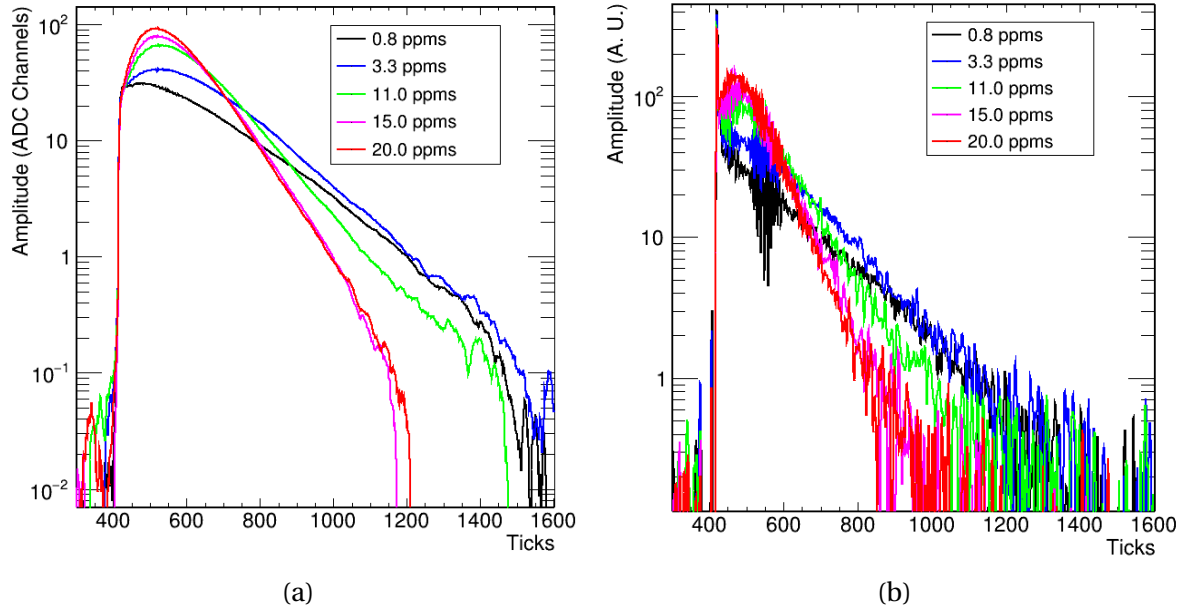


Figure 6.5: **(a)** Averaged waveforms obtained for each xenon doping concentration, each one contain 10 thousand events. **(b)** Resulting waveforms after deconvolving the s.p.e. response.

Figure 6.6b shows the  $\chi^2$  minimization with TMinuit [88] of the averaged waveforms (black) with the exponential terms of Eq. 6.11 convoluted with the s.p.e. response (red).

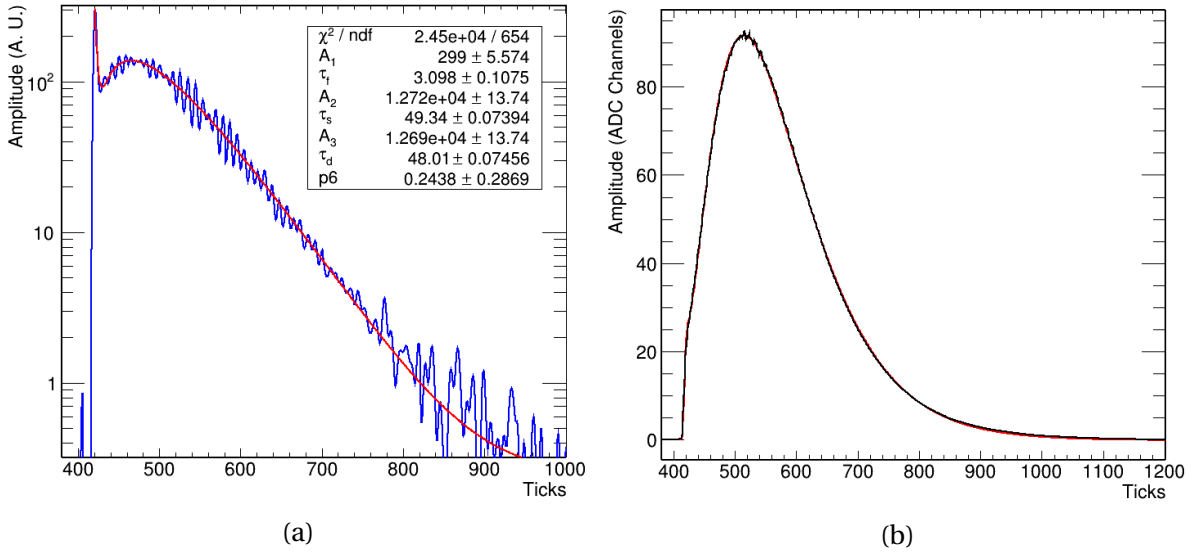


Figure 6.6: **(a)** Deconvolved waveform (blue) adjusted by Eq. 6.11 (red) with the addition of a baseline constant (fitted values are in ticks). **(b)** Averaged waveform (black) fitted by the expected signal Eq. 6.11 convoluted with the s.p.e. response (red).

The data were collected for several days, each day had about four runs with 10 thousand events each. The methods just described were applied for each run. Both X-ARAPUCAs deployed presented problems in one of the channels, so the analysis was done in six channels. Figure 6.7a shows the slow time constant ( $\tau_{\text{slow}}$ ) as function of time, while Figure 6.7b

shows the result for the delayed time constant ( $\tau_d$ ). The doping periods are labeled with a crosshatched area. One can note the decreasing behavior of both time constants, including during doping periods, where the Xe shifting takes place. Inside the plots, the time constants found by Ref. [107] are displayed, in which a good correspondence was found.

The presented values were taken by averaging the response of the six channels, where the uncertainty was calculated with the combination of the fit uncertainty with the average uncertainty calculated with the difference of the extreme values divided by root square of six.

#### 6.2.4. Light yield recovery

To verify the recovery in the light yield, the average number of photo-electrons (p.e.) detected was computed for each run. For each channel, the amount of p.e. was evaluated by dividing the averaged charge by the s.p.e. charge in the respective run. The response of the three channels was summed up, resulting in the average number of photo-electrons of the run, as can be seen in Figure 6.8a. The NQ X-ARAPUCA is the device deployed without the quartz window that collects LAr scintillation light and Xe shifted light. On the other hand, the Q X-ARAPUCA is sensitive only to Xe shifted light (175 nm) as it was deployed with the quartz window. The drops in the average number of p.e. is caused by the electric field applied in the LArTPC (see Sec. 3.1.2).

The increase in light yield is evident in Figure 6.8a, showing the recovery expected by doping with xenon. Another interesting feature is the ratio between p.e. of the Q by the NQ X-ARAPUCA, that can be translated as:

$$\text{Ratio} = \frac{\varepsilon \times \text{Xe light}}{\text{Ar light} + \text{Xe light}}, \quad (6.15)$$

where  $\varepsilon$  is the quartz window transparency to Xe light. Figure 6.8b shows this result, where the ratio seems to stabilize after the fourth doping, that is, at 15 ppm of Xe. Taking into account that the measured transparency of the quartz window was between 80% and 90%, the true ratio between the light can be computed as 0.72 to 0.81, which corresponds to the relative intensity of triplet and singlet for LAr (see Table 3.1). This means that, at this concentration, the argon triplet component is completely eliminated by the Xe.

By analyzing the data from the X-ARAPUCAs deployed and from the S-ARAPUCAs, which compose the ProtoDUNE PDS, it was concluded that 95% of the light lost due to the nitrogen

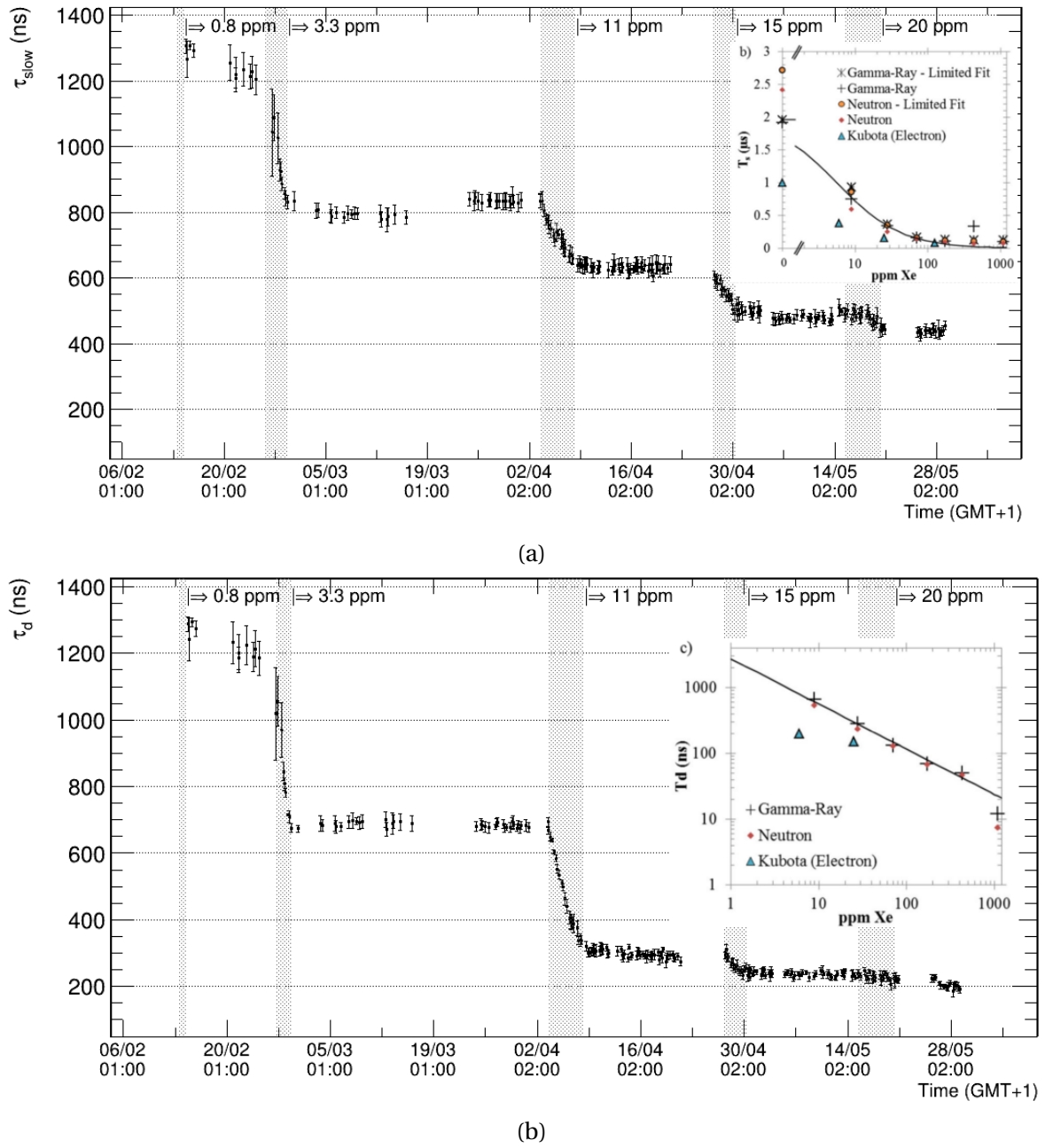


Figure 6.7: **(a)** Slow time constant and **(b)** delayed dimer constant versus time. The internal plots are the results found by Ref. [107] for different Xe concentrations.

contamination was recovered with the xenon doping.

The recovery in the light yield plus the fact that the LArTPC operated normally during the tests leave the xenon doping as an alternative for the DUNE FD module. The results found by the collaboration are yet unpublished and they may significantly help to understand the operation of DUNE if the xenon is used.

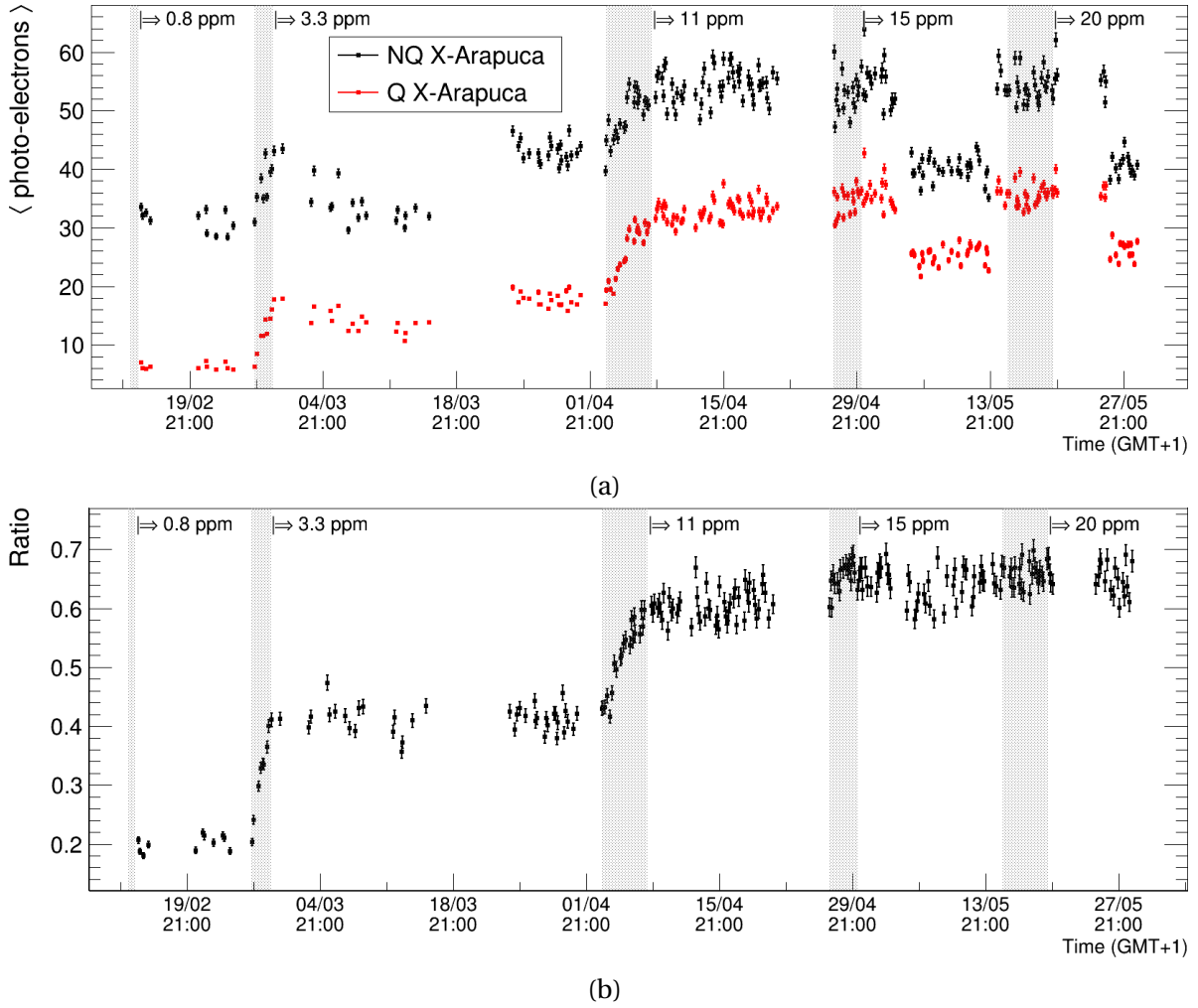


Figure 6.8: **(a)** Average number of photons detected versus times for the X-ARAPUCA without quartz (NQ) and with quartz (Q) window. **(b)** Ratio between Xe light and total light (Xe+Ar) versus time.

### 6.2.5. Toy model Monte Carlo

During the period of analysis, it was not easy to explain the plot of the number of photo-electrons detected by the NQ versus Q X-ARAPUCA for each external trigger as shown in Figure 6.9. The number of p.e. was computed by the sum of the three channels during the third doping. It is noticeable that there are three distinct populated regions (lobes) with different angular coefficients.

In order to investigate this behavior, a “Toy Model” Monte Carlo simulation was developed to verify if it was a geometrical effect of the detector. The simulation was performed using Root Cern [88], and it was made trying to bring plausible and simple approaches to the problem. The geometry of the X-ARAPUCAs was implemented, the  $3.6 \times 6 \times 7 \text{ m}^3$  cryostat and the two structures that could interfere (drastically) with the light collection: the PDS

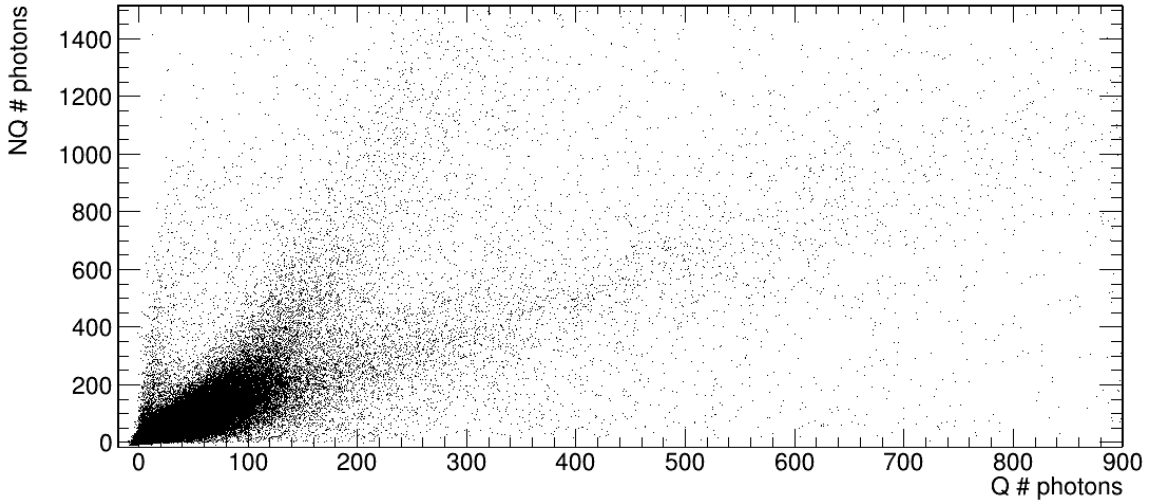


Figure 6.9: Number of p.e. detected by the X-ARAPUCA without quartz window (NQ) versus quartz (Q).

modules and the APA division (in red in Fig. 6.3a).

The muons are generated in the first *paddle* of the muon telescope with uniform distribution along the azimuth angle and  $\cos^2(\theta)$  for the zenith [114]. The energy distribution of the muons was taken from the vertical muon flux at sea level [115]:

$$D_\mu(p, h = 1030 \text{ g/cm}^2, \theta = 0^\circ) = C p^{-(\gamma_0 + \gamma_1 \log p + \gamma_2 \log^2 p + \gamma_3 \log^3 p)}, \quad (6.16)$$

where  $p$  is the momentum,  $h$  is the atmospheric depth adjusted to the sea level,  $\theta$  is the zenith angle, and the parameters  $C, \gamma_0, \gamma_1, \gamma_2, \gamma_3$  are given at Table 6.1.

Table 6.1: Parameters used at Eq. 6.16 [115]

Momentum Range (GeV/c)	$C \text{ (cm}^{-2}\text{s}^{-1}\text{sr}^{-1}\text{GeV}^{-1}\text{)}$	$\gamma_0$	$\gamma_1$	$\gamma_2$	$\gamma_3$
1 - 10	$2.95 \times 10^{-3}$	0.3061	1.2743	-0.2630	0.0252

The external trigger of the experiment was simulated by selecting only muons that cross all the three detectors. A few images can be found in Appendix D. The muon selection can be verified in Fig. D.1. A step of 1 cm was defined for the muon interactions after entering the TPC. In this case, for each 1 cm traveled by the muon, an energy loss is defined by the Bethe-Block curve of Figure 6.10 and converted to 400 photons per MeV emitted isotropically. The number of photons is set by the quenched factor of 0.8 for muons (see Sec. 3.1) divided by 100, for a faster simulation.

To implement statistical fluctuations, the Landau distribution was used in conjunction with the energy loss. The most probable energy loss is given by the Bethe-Block curve and

the full width at half maximum (FWHM) set to  $4\varepsilon$ , defined as [13]:

$$\varepsilon = (K/2)(Z/A)(x/\beta^2) \text{ MeV}, \quad (6.17)$$

where  $K = 4\pi N_A r_e^2 m_e c^2$  ( $N_A$  is the Avogadro constant,  $r_e$  is the classic electron radius and  $m_e c^2 = 0.511 \text{ MeV}$  is the electron mass),  $Z = 18$  and  $A = 40$  are, respectively, the atomic number and mass of the absorber (LAr),  $\beta = v/c$  is the relative velocity of the muon and  $x$  is the thickness of LAr in  $\text{g}/\text{cm}^2$ .

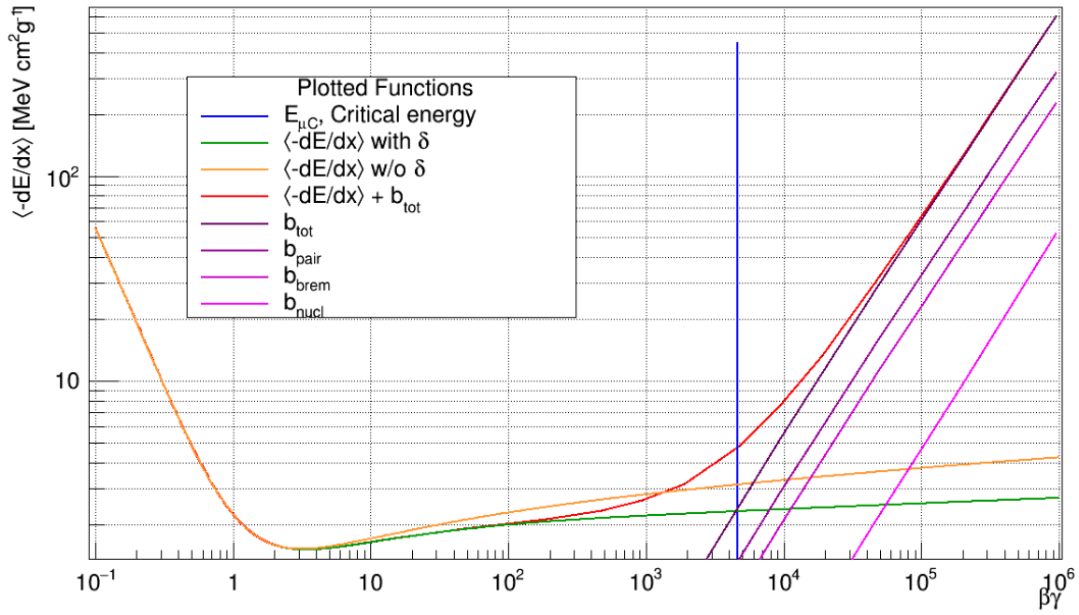


Figure 6.10: Expected muons energy loss in liquid argon [116].

An absorption length of 20 meters was set for the light and Rayleigh scattering length was set to 1 meter [62, 63, 65]. The simulation does not treat photons with the wavelength of LAr scintillation (127 nm) or xenon shifted (175 nm) any differently. To optimize the run time<sup>1</sup>, the “type” of the photons are selected if they are detected by the X-ARAPUCA. A proportion of 30% LAr light and 70% Xe shifted light was set, corresponding to a doping greater than 11 ppm.

The APA wires and the grounding mesh were not simulated. The angle of incidence of the photons arriving in the X-ARAPUCA acceptance window was recorded and, in the post production, a random selection based on the grid transparency (see Sec. 4.3) was performed. A transparency of 80% was used for the quartz window for the Xe light (see Sec. 4.2.1).

The results of the simulation are shown in Figure 6.11, with number of photo-electrons detected by the X-ARAPUCA without quartz window (NQ) versus quartz (Q). An efficiency of

<sup>1</sup>No difference was noticed when changing the selection from the production to the detection.

2.1% was set for the X-ARAPUCAs. Although the simulation does not retrieve the expected results with precision, the goal was reached by reproducing the two main lobes and, eventually, the third one when comparing with Fig. 6.9. The populated regions appeared when the Rayleigh scattering was implemented and accentuated when the TPC column and PDS modules were implemented.

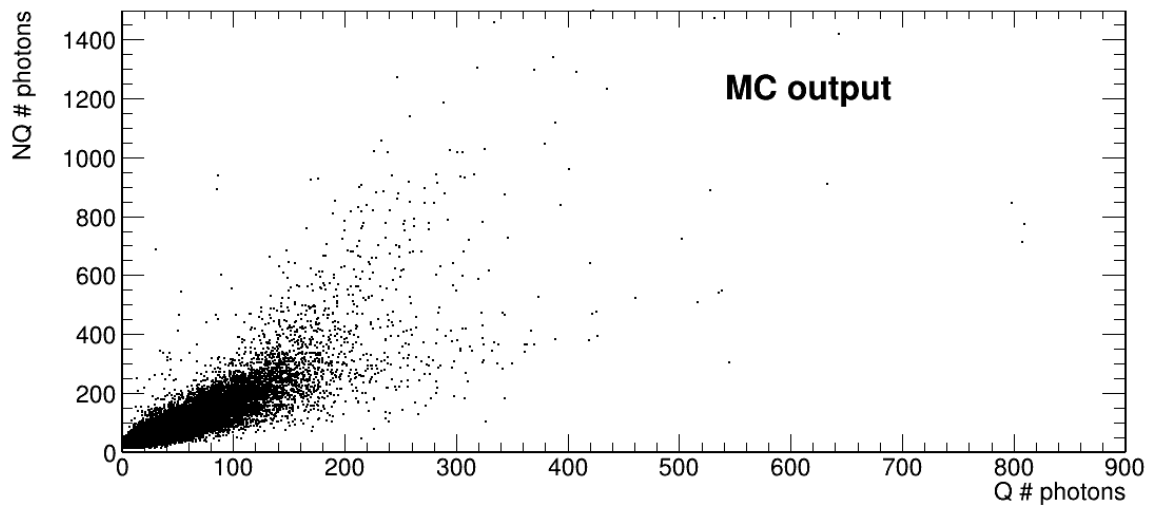


Figure 6.11: Results of the Monte Carlo simulation for the number of photons detected by the X-ARAPUCA without quartz (NQ) versus quartz (Q).

The notable CP-violation measurement proposed by the Deep Underground Neutrino Experiment, together with a rich primary and ancillary science program were discussed in Chapter 1. The DUNE experiment will be an essential tool to advance in the current knowledge and understanding of neutrino physics. In Chapter 2, the experiment was described in details together with the Liquid Argon Time Projection Chamber principle of work. An essential aspect of the experiment is the detection of liquid argon scintillation light. The scintillation light was explored in Chapter 3 with the introduction of the ARAPUCA as the DUNE photon detection system.

The research and development of the S-ARAPUCA and X-ARAPUCA performed in the period of this thesis were presented in Chapter 4. The trapping effect of the device was tested in 2018 in a dark box at room temperature. The Dark Box test aided the search for improvements in the S-ARAPUCA device in a simple experimental setup and its concept was later implemented for the room and cryogenic temperature tests performed in Italy. The tests with the Monochromator have successfully characterized different dichroic filters, substrates and wavelength shifters. Moreover, the transparency measurements of the grounding mesh were used as input for Monte Carlo simulations, helping to model better the light signals in the LArTPC. The experimental setup preparation for these tests have significantly helped to establish the Leptons Laboratory at the University of Campinas as an outstanding research facility.

In Chapter 5, the tests in liquid argon performed with a X-ARAPUCA single-cell and double-cell in Brazil and Italy, respectively, were described. The author of this thesis was responsible for the data analysis of the experiments and the results are published as Refs. [89, 95].

The X-ARAPUCA single-cell was characterized with three different ionizing radiations: alpha particles, gamma rays and cosmic muons. The comparable efficiencies found completely characterize the device, showing that the efficiency does not depend on the particle type nor on the energy deposition topology. The efficiency of  $(2.2 \pm 0.4)\%$  and  $(3.0 \pm 0.6)\%$  were found with the SiPM biased with 5.0 V and 5.5 V overvoltage, respectively. The analysis were performed with a direct comparison between Geant4 Monte Carlo simulation.

The X-ARAPUCA double-cell was characterized with an  $^{241}\text{Am}$  source in five different positions along the device longitudinal axis. Measurements comparing the enhancement

in light collection showed an efficiency increase of about 50% when using the new wavelength shifter developed at Milano- Bicocca. An efficiency of  $(1.9 \pm 0.1)\%$  was found for the X-ARAPUCA, a result in agreement with the efficiency found for the single-cell. Moreover, by deploying the new wavelength shifter, an efficiency of  $(2.9 \pm 0.1)\%$  was found. These results probe the use of the X-ARAPUCA as the standard photon detection system (PDS) of DUNE, fulfilling the requirements of 1.3% and 2.6% efficiency for proton decay search and supernova neutrino burst detection.

The deployment of two X-ARAPUCAs in ProtoDUNE-SP for the xenon doping experiments was explored in Chapter 6. The joint analysis of the X-ARAPUCAs and S-ARAPUCAs (part of the ProtoDUNE PDS), together with data from the TPC, showed a recovery of 95% of the light lost due to nitrogen contamination. The carried out research has established the xenon doping as an alternative for DUNE in the case of a contamination with nitrogen.

The X-ARAPUCA super-cells are going to be tested in dedicated setups in Brazil, Italy and Spain and are going to be deployed in ProtoDUNE for the second run. The validation of the super-cell is crucial for the DUNE collaboration. Currently, different versions of X-ARAPUCA are under study for the vertical drift modules, where there X-ARAPUCA will be placed in the cathode plane and on the field cage of the LArTPC. The first module PDS assembly is foreseen to finish in beginning of 2023 and the first module operation should start in mid 2026, with a lot of work to be done.

1. Reines, F. & Cowan, C. L. The neutrino. *Nature* **178**, 446–449 (1956).
2. Abi, B. *et al.* Deep Underground Neutrino Experiment (DUNE), Far Detector Technical Design Report, Volume I: Introduction to DUNE (2020). [2002.02967](#).
3. Abi, B. *et al.* Deep Underground Neutrino Experiment (DUNE), Far Detector Technical Design Report, Volume II: DUNE Physics (2020). [2002.03005](#).
4. Abi, B. *et al.* Deep Underground Neutrino Experiment (DUNE), Far Detector Technical Design Report, Volume III: DUNE Far Detector Technical Coordination (2020). [2002.03008](#).
5. Abi, B. *et al.* Deep Underground Neutrino Experiment (DUNE), Far Detector Technical Design Report, Volume IV: Far Detector Single-phase Technology (2020). [2002.03010](#).
6. Abud, A. A. *et al.* Deep Underground Neutrino Experiment (DUNE) Near Detector Conceptual Design Report. *Instruments* **5** (2021). <https://www.mdpi.com/2410-390X/5/4/31>.
7. Abi, B. *et al.* The DUNE Far Detector Interim Design Report Volume 1: Physics, Technology and Strategies (2018). [1807.10334](#).
8. Strumia, A. & Vissani, F. Neutrino masses and mixings and... (2006). [hep-ph/0606054](#).
9. Abdurashitov, J. *et al.* Results from SAGE (The Russian-American gallium solar neutrino experiment). *Physics Letters B* **328**, 234–248 (1994). <https://www.sciencedirect.com/science/article/pii/0370269394904545>.
10. Anselmann, P. *et al.* Solar neutrinos observed by GALLEX at Gran Sasso. *Physics Letters B* **285**, 376–389 (1992). <https://www.sciencedirect.com/science/article/pii/037026939291521A>.
11. Bahcall, J. N., Serenelli, A. M. & Basu, S. New Solar Opacities, Abundances, Helioseismology, and Neutrino Fluxes. *The Astrophysical Journal* **621**, L85–L88 (2005). <https://doi.org/10.1086/428929>.
12. Cecchini, S. & Spurio, M. Atmospheric muons: experimental aspects. *Geoscientific Instrumentation, Methods and Data Systems* **1**, 185–196 (2012). <https://gi.copernicus.org/articles/1/185/2012/>.

13. Zyla, P. *et al.* Review of Particle Physics. *PTEP* **2020**, 083C01 (2020).
14. Hirata, K. *et al.* Observation of a small atmospheric  $\nu_\mu/\nu_e$  ratio in Kamiokande. *Physics Letters B* **280**, 146–152 (1992). <https://www.sciencedirect.com/science/article/pii/0370269392907886>.
15. Jelley, J. V. *Cherenkov Radiation and its applications* (United Kingdom Atomic Energy Authority, London, 1958).
16. Fukuda, Y. *et al.* Evidence for Oscillation of Atmospheric Neutrinos. *Phys. Rev. Lett.* **81**, 1562–1567 (1998). <https://link.aps.org/doi/10.1103/PhysRevLett.81.1562>.
17. Aharmim, B. *et al.* Determination of the  $\nu_e$  and total  $^8\text{B}$  solar neutrino fluxes using the Sudbury Neutrino Observatory Phase I data set. *Phys. Rev. C* **75**, 045502 (2007). <https://link.aps.org/doi/10.1103/PhysRevC.75.045502>.
18. Eguchi, K. *et al.* First Results from KamLAND: Evidence for Reactor Antineutrino Disappearance. *Phys. Rev. Lett.* **90**, 021802 (2003). <https://link.aps.org/doi/10.1103/PhysRevLett.90.021802>.
19. Ahn, M. H. *et al.* Measurement of neutrino oscillation by the K2K experiment. *Phys. Rev. D* **74**, 072003 (2006). <https://link.aps.org/doi/10.1103/PhysRevD.74.072003>.
20. Thomson, M. *Modern particle physics* (Cambridge University Press, New York, 2013).
21. Pontecorvo, B. Neutrino Experiments and the Problem of Conservation of Leptonic Charge. *Sov. Phys. JETP* **26**, 984–988 (1968).
22. Ashie, Y. *et al.* Evidence for an Oscillatory Signature in Atmospheric Neutrino Oscillations. *Phys. Rev. Lett.* **93**, 101801 (2004). <https://link.aps.org/doi/10.1103/PhysRevLett.93.101801>.
23. Giunti, C. & Kim, C. W. *Fundamentals of Neutrino Physics and Astrophysics* (2007).
24. Acciarri, R. *et al.* A Proposal for a Three Detector Short-Baseline Neutrino Oscillation Program in the Fermilab Booster Neutrino Beam (2015). [1503.01520](https://arxiv.org/abs/1503.01520).
25. Benetti, P. *et al.* A three-ton liquid argon time projection chamber. *Nuclear Instruments and Methods in Physics Research Section A: Accelerators, Spectrometers, Detectors*

- and Associated Equipment* **332**, 395 – 412 (1993). <http://www.sciencedirect.com/science/article/pii/016890029390297U>.
26. Bahcall, J. N. Solar Neutrinos: Where We Are, Where We Are Going. *The Astrophysical Journal* **467**, 475 (1996). <http://dx.doi.org/10.1086/177624>.
  27. Nunokawa, H., Parke, S. & Valle, J. W. CP violation and neutrino oscillations. *Progress in Particle and Nuclear Physics* **60**, 338 – 402 (2008). <http://www.sciencedirect.com/science/article/pii/S014664100700083X>.
  28. Upadhyay, A. & Batra, M. Phenomenology of Neutrino Mixing in Vacuum and Matter. *ISRN High Energy Physics* **2013**, 1–15 (2013). <http://dx.doi.org/10.1155/2013/206516>.
  29. Bass, M. *et al.* Baseline optimization for the measurement of  $CP$  violation, mass hierarchy, and  $\theta_{23}$  octant in a long-baseline neutrino oscillation experiment. *Phys. Rev. D* **91**, 052015 (2015). <https://link.aps.org/doi/10.1103/PhysRevD.91.052015>.
  30. Abe, K. *et al.* Search for  $CP$  Violation in Neutrino and Antineutrino Oscillations by the T2K Experiment with  $2.2 \times 10^{21}$  Protons on Target. *Phys. Rev. Lett.* **121**, 171802 (2018). <https://link.aps.org/doi/10.1103/PhysRevLett.121.171802>.
  31. Acero, M. A. *et al.* First measurement of neutrino oscillation parameters using neutrinos and antineutrinos by NOvA. *Phys. Rev. Lett.* **123**, 151803 (2019). <https://link.aps.org/doi/10.1103/PhysRevLett.123.151803>.
  32. Esteban, I., Gonzalez-Garcia, M. C., Maltoni, M., Schwetz, T. & Zhou, A. The fate of hints: updated global analysis of three-flavor neutrino oscillations. *Journal of High Energy Physics* **2020**, 178 (2020). [https://doi.org/10.1007/JHEP09\(2020\)178](https://doi.org/10.1007/JHEP09(2020)178).
  33. Minakata, H. & Nunokawa, H. Neutrino flavor conversion in supernova 1987A. *Phys. Rev. D* **38**, 3605–3609 (1988). <https://link.aps.org/doi/10.1103/PhysRevD.38.3605>.
  34. Abi, B. *et al.* Supernova Neutrino Burst Detection with the Deep Underground Neutrino Experiment. *Eur. Phys. J. C* **81**, 423 (2021). [2008.06647](https://doi.org/10.1007/978-94-007-0664-7).

35. Gratieri, D. R., Guzzo, M. M. & Peres, O. L. G. Impact of standard neutrino oscillations and systematics on proton lifetime measurements. *Journal of Physics G: Nuclear and Particle Physics* **46**, 075006 (2019). <https://doi.org/10.1088/1361-6471/ab0b56>.
36. Rubbia, C. The Liquid Argon Time Projection Chamber: A New Concept for Neutrino Detectors (1977).
37. Doke, T. *Fundamental Properties of Liquid Argon, Krypton and Xenon as Radiation Detector Media*, 537–577. [https://www.worldscientific.com/doi/abs/10.1142/9789814355988\\_0010](https://www.worldscientific.com/doi/abs/10.1142/9789814355988_0010).
38. Amerio, S. *et al.* Design, construction and tests of the ICARUS T600 detector. *Nuclear Instruments and Methods in Physics Research Section A: Accelerators, Spectrometers, Detectors and Associated Equipment* **527**, 329–410 (2004). <https://www.sciencedirect.com/science/article/pii/S0168900204004966>.
39. Abi, B. *et al.* First results on ProtoDUNE-SP liquid argon time projection chamber performance from a beam test at the CERN Neutrino Platform. *Journal of Instrumentation* **15**, P12004–P12004 (2020). <https://doi.org/10.1088/1748-0221/15/12/p12004>.
40. Miller, L. S., Howe, S. & Spear, W. E. Charge Transport in Solid and Liquid Ar, Kr, and Xe. *Phys. Rev.* **166**, 871–878 (1968). <https://link.aps.org/doi/10.1103/PhysRev.166.871>.
41. Li, Y. *et al.* Measurement of longitudinal electron diffusion in liquid argon. *Nuclear Instruments and Methods in Physics Research Section A: Accelerators, Spectrometers, Detectors and Associated Equipment* **816**, 160–170 (2016). <https://www.sciencedirect.com/science/article/pii/S0168900216001443>.
42. Aitken, F., Li, Z.-L., Bonifaci, N., Denat, A. & von Haeften, K. Electron mobility in liquid and supercritical helium measured using corona discharges: a new semi-empirical model for cavity formation. *Phys. Chem. Chem. Phys.* **13**, 719–724 (2011). <http://dx.doi.org/10.1039/C0CP00786B>.
43. Soderberg, M. The MicroBooNE Proposal. *MicroBooNE Public Note* (2008). <https://microboone-docdb.fnal.gov/cgi-bin/ShowDocument?docid=70>.

44. Sakai, Y., Schmidt, W. F. & Khrapak, A. High- and low-mobility electrons in liquid neon. *Chemical Physics* **164**, 139–152 (1992). <https://www.sciencedirect.com/science/article/pii/030101049287138Y>.
45. Chepel, V. & Araújo, H. Liquid noble gas detectors for low energy particle physics. *Journal of Instrumentation* **8**, R04001–R04001 (2013). <https://doi.org/10.1088/1748-0221/8/04/r04001>.
46. Miyajima, M. *et al.* Average energy expended per ion pair in liquid argon. *Phys. Rev. A* **9**, 1438–1443 (1974). <https://link.aps.org/doi/10.1103/PhysRevA.9.1438>.
47. Segreto, E. *Analysis and Simulation of events with scintillation light emission from the ICARUS T600 LAr detector*. Ph.D. thesis, Università degli Studi di L'Aquila (2006).
48. Doke, T. *et al.* Absolute Scintillation Yields in Liquid Argon and Xenon for Various Particles. *Japanese Journal of Applied Physics* **41**, 1538–1545 (2002). <https://doi.org/10.1143/jjap.41.1538>.
49. Segreto, E. Properties of liquid argon scintillation light emission. *Phys. Rev. D* **103**, 043001 (2021). <https://link.aps.org/doi/10.1103/PhysRevD.103.043001>.
50. Dang, H. *Particle induced strand breakage in plasmid DNA*. Ph.D. thesis, University of Groningen (2010). Relation: <http://www.rug.nl/> Rights: University of Groningen.
51. Kubota, S. *et al.* Recombination luminescence in liquid argon and in liquid xenon. *Phys. Rev. B* **17**, 2762–2765 (1978). <https://link.aps.org/doi/10.1103/PhysRevB.17.2762>.
52. Amoruso, S. *et al.* Study of electron recombination in liquid argon with the ICARUS TPC. *Nuclear Instruments and Methods in Physics Research Section A: Accelerators, Spectrometers, Detectors and Associated Equipment* **523**, 275–286 (2004). <https://www.sciencedirect.com/science/article/pii/S0168900204000506>.
53. Liquid Argon Properties (Tables and Calculators). <https://lar.bnl.gov/properties/>. Accessed: 2021-08-01.
54. Thomas, J. & Imel, D. A. Recombination of electron-ion pairs in liquid argon and liquid xenon. *Phys. Rev. A* **36**, 614–616 (1987). <https://link.aps.org/doi/10.1103/PhysRevA.36.614>.

55. Scalettar, R. T., Doe, P. J., Mahler, H. J. & Chen, H. H. Critical test of geminate recombination in liquid argon. *Phys. Rev. A* **25**, 2419–2422 (1982). <https://link.aps.org/doi/10.1103/PhysRevA.25.2419>.
56. Aprile, E., Ku, W. H.-M., Park, J. & Schwartz, H. Energy resolution studies of liquid argon ionization detectors. *Nuclear Instruments and Methods in Physics Research Section A: Accelerators, Spectrometers, Detectors and Associated Equipment* **261**, 519–526 (1987). <https://www.sciencedirect.com/science/article/pii/0168900287903627>.
57. Segreto, E. *et al.* Liquid argon test of the ARAPUCA device. *Journal of Instrumentation* **13**, P08021 (2018). <http://stacks.iop.org/1748-0221/13/i=08/a=P08021>.
58. Heindl, T. *et al.* The scintillation of liquid argon. *EPL (Europhysics Letters)* **91**, 62002 (2010). <https://doi.org/10.1209/0295-5075/91/62002>.
59. Acciarri, R. *et al.* Effects of Nitrogen contamination in liquid Argon. *Journal of Instrumentation* **5**, P06003 (2010). <http://stacks.iop.org/1748-0221/5/i=06/a=P06003>.
60. Hitachi, A. *et al.* Effect of ionization density on the time dependence of luminescence from liquid argon and xenon. *Phys. Rev. B* **27**, 5279–5285 (1983). <https://link.aps.org/doi/10.1103/PhysRevB.27.5279>.
61. Ishida, N. *et al.* Attenuation length measurements of scintillation light in liquid rare gases and their mixtures using an improved reflection suppresser. *Nuclear Instruments and Methods in Physics Research Section A: Accelerators, Spectrometers, Detectors and Associated Equipment* **384**, 380–386 (1997). <https://www.sciencedirect.com/science/article/pii/S0168900296007401>.
62. Seidel, G., Lanou, R. & Yao, W. Rayleigh scattering in rare-gas liquids. *Nuclear Instruments and Methods in Physics Research Section A: Accelerators, Spectrometers, Detectors and Associated Equipment* **489**, 189–194 (2002). <https://www.sciencedirect.com/science/article/pii/S0168900202008902>.
63. Grace, E., Butcher, A., Monroe, J. & Nikkel, J. A. Index of refraction, Rayleigh scattering length, and Sellmeier coefficients in solid and liquid argon and xenon. *Nuclear Instruments and Methods in Physics Research Section A: Accelerators, Spectrometers, Detectors*

- and Associated Equipment* **867**, 204–208 (2017). <https://www.sciencedirect.com/science/article/pii/S0168900217306848>.
64. Babicz, M. *et al.* A measurement of the group velocity of scintillation light in liquid argon. *Journal of Instrumentation* **15**, P09009–P09009 (2020). <https://doi.org/10.1088/1748-0221/15/09/p09009>.
  65. Jones, B. J. P. *et al.* A measurement of the absorption of liquid argon scintillation light by dissolved nitrogen at the part-per-million level. *Journal of Instrumentation* **8**, P07011–P07011 (2013). <http://dx.doi.org/10.1088/1748-0221/8/07/P07011>.
  66. Machado, A. & Segreto, E. ARAPUCA a new device for liquid argon scintillation light detection. *Journal of Instrumentation* **11**, C02004 (2016). <http://stacks.iop.org/1748-0221/11/i=02/a=C02004>.
  67. DeVol, T., Wehe, D. & Knoll, G. Evaluation of p-terphenyl and 2,2" dimethyl-p-terphenyl as wavelength shifters for barium fluoride. *Nuclear Instruments and Methods in Physics Research Section A: Accelerators, Spectrometers, Detectors and Associated Equipment* **327**, 354 – 362 (1993). <http://www.sciencedirect.com/science/article/pii/0168900293907011>.
  68. Francini, R. *et al.* Tetraphenyl-butadiene films: VUV-Vis optical characterization from room to liquid argon temperature. *Journal of Instrumentation* **8**, C09010 (2013). <http://stacks.iop.org/1748-0221/8/i=09/a=C09010>.
  69. Vikuiti<sup>TM</sup> Enhanced Specular Reflector (ESR). <https://www.3m.com/>. Accessed: 2021-08-01.
  70. Acciarri, R. *et al.* The Liquid Argon In A Testbeam (LArIAT) experiment. *Journal of Instrumentation* **15**, P04026–P04026 (2020). <https://doi.org/10.1088/1748-0221/15/04/p04026>.
  71. Abi, B. *et al.* The Single-Phase ProtoDUNE Technical Design Report (2017). [1706.07081](https://arxiv.org/abs/1706.07081).
  72. Machado, A. *et al.* The X-ARAPUCA: an improvement of the ARAPUCA device. *J. Instrum.* **13**, C04026–C04026 (2018). <https://doi.org/10.1088/1748-0221/13/04/C04026>.

73. ELJEN. <https://eljentechnology.com>. Accessed: 2021-08-01.
74. Paulucci, L., Marinho, F., Machado, A. & Segreto, E. A complete simulation of the X-ARAPUCA device for detection of scintillation photons. *Journal of Instrumentation* **15**, C01047–C01047 (2020). <https://doi.org/10.1088/1748-0221/15/01/c01047>.
75. Bass, M. The Short Baseline Neutrino Oscillation Program at Fermilab. *PoSICHEP2016*, 481 (2016). [1702.00990](https://arxiv.org/abs/1702.00990).
76. Acciarri, R. *et al.* Construction of precision wire readout planes for the Short-Baseline Near Detector (SBND) (2020). [2002.08424](https://arxiv.org/abs/2002.08424).
77. Fleming, B. The MicroBooNE Technical Design Report (2012). <https://www.osti.gov/biblio/1333130>.
78. for the SBND Collaboration, D. G.-G. Light Detection System simulations for SBND. *Journal of Physics: Conference Series* **888**, 012094 (2017). <https://doi.org/10.1088/1742-6596/888/1/012094>.
79. Ghassemi, A., Kobayashi, K. & Sato, K. A technical guide to silicon photomultipliers (MPPC) - Overview (2018).
80. An Introduction to the Silicon Photomultiplier. SensL, technical note.
81. Leo, W. R. *Techniques for nuclear and particle physics experiments: a how-to approach* (Springer Science & Business Media, 2012).
82. PTP absorption and emission spectra taken from OMLC. <https://omlc.org/>. Accessed: 2021-08-01.
83. Med Phys 4r06/6r03 Radioisotopes and Radiation Methodology 2-1 Chapter 2 General Properties of Radiation Detectors 2.1. Operation Modes.
84. Edmund optics. <http://www.edmundoptics.com>. Accessed: 2021-08-01.
85. Opto Electronica S.A. <https://www.opto.com.br/>. Accessed: 2021-08-01.
86. Ashai Spectra Co. <https://www.asahi-spectra.com/>. Accessed: 2021-08-01.
87. Omega Optical Inc. <http://www.omegafilters.com/>. Accessed: 2021-08-01.

88. Brun, R. & Rademakers, F. ROOT: An object oriented data analysis framework. *Nucl. Instrum. Meth. A* **389**, 81–86 (1997).
89. Souza, H. *et al.* Liquid argon characterization of the X-ARAPUCA with alpha particles, gamma rays and cosmic muons **16**, P11002 (2021). <https://doi.org/10.1088/1748-0221/16/11/p11002>.
90. Horiba. <https://www.horiba.com>. Accessed: 2021-08-01.
91. Ogawa, M. Absorption Cross Sections of O<sub>2</sub> and CO<sub>2</sub> Continua in the Schumann and Far-uv Regions. *The Journal of Chemical Physics* **54**, 2550–2556 (1971). <https://doi.org/10.1063/1.1675211>. <https://doi.org/10.1063/1.1675211>.
92. Hamamatsu MPPCs. <https://www.hamamatsu.com/>. Accessed: 2021-08-01.
93. Fused Silica transmission taken from Newport Corporation. <https://www.newport.com/n/optical-materials>. Accessed: 2021-08-01.
94. Glass to Power - Luminescent Solar Concentrators. <https://www.glasstopower.com/>. Accessed: 2021-08-01.
95. Brizzolari, C. *et al.* Enhancement of the X-Arapuca photon detection device for the DUNE experiment **16**, P09027 (2021). <https://doi.org/10.1088/1748-0221/16/09/p09027>.
96. Bertrand, G. H. V., Hamel, M. & Sguerra, F. Current Status on Plastic Scintillators Modifications. *Chemistry European Journal* **20**, 15660–15685 (2014). <https://chemistry-europe.onlinelibrary.wiley.com/doi/abs/10.1002/chem.201404093>. <https://chemistry-europe.onlinelibrary.wiley.com/doi/pdf/10.1002/chem.201404093>.
97. <https://www-nds.iaea.org/>.
98. Condat, L. A Direct Algorithm for 1-D Total Variation Denoising. *IEEE Signal Processing Letters* **20**, 1054–1057 (2013).
99. Eckert, P., Schultz-Coulon, H.-C., Shen, W., Stamen, R. & Tadday, A. Characterisation studies of silicon photomultipliers. *Nuclear Instruments and Methods in Physics Re-*

- search Section A: Accelerators, Spectrometers, Detectors and Associated Equipment* **620**, 217–226 (2010). <http://dx.doi.org/10.1016/j.nima.2010.03.169>.
100. Vinogradov, S., Vinogradova, T., Shubin, V., Shushakov, D. & Sitarsky, K. Probability distribution and noise factor of solid state photomultiplier signals with cross-talk and afterpulsing. In *2009 IEEE Nuclear Science Symposium Conference Record (NSS/MIC)*, 1496–1500 (2009).
  101. Segreto, E. Evidence of delayed light emission of tetraphenyl-butadiene excited by liquid-argon scintillation light. *Phys. Rev. C* **91**, 035503 (2015). <https://link.aps.org/doi/10.1103/PhysRevC.91.035503>.
  102. Sarmiento, R. *et al.* Test of X-ARAPUCA through Monte Carlo simulation in Brazil. *Revista dos Trabalhos de Iniciação Científica da UNICAMP* 1–1 (2019). <https://econtents.bc.unicamp.br/eventos/index.php/pibic/article/view/2106>.
  103. Mei, D. M., Yin, Z. B., Stonehill, L. & Hime, A. A model of nuclear recoil scintillation efficiency in noble liquids. *Astroparticle Physics* **30**, 12–17 (2008). <http://dx.doi.org/10.1016/j.astropartphys.2008.06.001>.
  104. Pommé, S. & Marroyo, B. C. Improved peak shape fitting in alpha spectra. *Applied Radiation and Isotopes* **96**, 148 – 153 (2015). <http://www.sciencedirect.com/science/article/pii/S0969804314004175>.
  105. Bé, M.-M. *et al.* *Table of Radionuclides*, vol. 3 of *Monographie BIPM-5* (Bureau International des Poids et Mesures, Pavillon de Breteuil, F-92310 Sèvres, France, 2006). [http://www.bipm.org/utils/common/pdf/monographieRI/Monographie\\_BIPM-5\\_Tables\\_Vol3.pdf](http://www.bipm.org/utils/common/pdf/monographieRI/Monographie_BIPM-5_Tables_Vol3.pdf).
  106. Segreto, E. *et al.* First liquid argon test of the X-ARAPUCA. *Journal of Instrumentation* **15**, C05045–C05045 (2020). <https://doi.org/10.1088/1748-0221/15/05/C05045>.
  107. Peiffer, P., Pollmann, T., Schönert, S., Smolnikov, A. & Vasiliev, S. Pulse shape analysis of scintillation signals from pure and xenon-doped liquid argon for radioactive background identification. *Journal of Instrumentation* **3**, P08007 (2008). <http://stacks.iop.org/1748-0221/3/i=08/a=P08007>.

108. Lippincott, W. H. *et al.* Scintillation time dependence and pulse shape discrimination in liquid argon. *Phys. Rev. C* **78**, 035801 (2008). <https://link.aps.org/doi/10.1103/PhysRevC.78.035801>.
109. Morháč, M., Kliman, J., Matoušek, V., Veselský, M. & Turzo, I. Efficient one- and two-dimensional gold deconvolution and its application to  $\gamma$ -ray spectra decomposition. *Nuclear Instruments and Methods in Physics Research Section A: Accelerators, Spectrometers, Detectors and Associated Equipment* **401**, 385–408 (1997). <https://www.sciencedirect.com/science/article/pii/S0168900297010589>.
110. Berger, M., Coursey, J., Zucker, M. & Chang, J. Stopping-Power & Range Tables for Electrons, Protons, and Helium Ions. <https://physics.nist.gov/PhysRefData/Star/Text/ASTAR.html>. Accessed: 2021-08-01.
111. Wahl, C. G. *et al.* Pulse-shape discrimination and energy resolution of a liquid-argon scintillator with xenon doping. *Journal of Instrumentation* **9**, P06013–P06013 (2014). <http://dx.doi.org/10.1088/1748-0221/9/06/P06013>.
112. Akimov, D. *et al.* Fast component re-emission in Xe-doped liquid argon. *Journal of Instrumentation* **14**, P09022–P09022 (2019). <http://dx.doi.org/10.1088/1748-0221/14/09/P09022>.
113. Kubota, S., Hishida, M., Himi, S., Suzuki, J. & Ruan, J. The suppression of the slow component in xenon-doped liquid argon scintillation. *Nuclear Instruments and Methods in Physics Research Section A: Accelerators, Spectrometers, Detectors and Associated Equipment* **327**, 71 – 74 (1993). <http://www.sciencedirect.com/science/article/pii/S016890029391413H>.
114. Cecchini, S. & Spurio, M. Atmospheric muons: experimental aspects (2012). [1208.1171](#).
115. Bugaev, E. V. *et al.* Atmospheric muon flux at sea level, underground, and underwater. *Phys. Rev. D* **58**, 054001 (1998). <https://link.aps.org/doi/10.1103/PhysRevD.58.054001>.
116. MUON ENERGY LOSS IN LIQUID ARGON. [https://indico.fnal.gov/event/14933/contributions/28526/attachments/17961/22583/Final\\_SIST\\_Paper.pdf](https://indico.fnal.gov/event/14933/contributions/28526/attachments/17961/22583/Final_SIST_Paper.pdf). Accessed: 2021-08-01.

117. Resnick, R. *Introduction to special relativity* (New York, 1971).

# Appendix A

## Deconvolution method

The ROOT Cern class TSpectrum [88] has the Gold deconvolution [109] algorithm already implemented. The one dimensional deconvolution wants to find the original discrete impulse response  $x(i)$  from the convoluted waveform  $y(i)$  in the form:

$$y(i) = \sum_{k=0}^{N-1} h(i-k)x(k), \quad i = 0, 1, 2, \dots, N-1, \quad (\text{A.1})$$

where, in the case of this analysis,  $y(i)$  is the output averaged waveform from  $\alpha$ 's or muons,  $h(i)$  is the input average waveform of a single photo-electron and  $x(i)$  is the original LAr light response. In matrix form we have<sup>1</sup>:

$$\begin{bmatrix} y(0) \\ y(1) \\ \dots \\ y(2N-2) \\ y(2N-1) \end{bmatrix} = \begin{bmatrix} h(0) & 0 & 0 & \dots & 0 \\ h(1) & h(0) & 0 & \dots & 0 \\ h(2) & h(1) & h(0) & \dots & \dots \\ \dots & \dots & h(1) & \dots & \dots \\ \dots & \dots & \dots & \dots & \dots \\ h(N-1) & h(N-2) & \dots & \dots & 0 \\ 0 & h(N-1) & h(N-2) & \dots & h(0) \\ 0 & 0 & h(N-1) & \dots & h(1) \\ \dots & \dots & \dots & \dots & \dots \\ 0 & 0 & 0 & \dots & h(N-1) \end{bmatrix} \begin{bmatrix} x(0) \\ x(1) \\ \dots \\ x(N-2) \\ x(N-1) \end{bmatrix}. \quad (\text{A.2})$$

The proposed solution utilizes the transposed matrix  $H$  to find a solution to  $x$  as:

$$\begin{aligned} y &= Hx \\ H^T y &= H^T Hx \\ y' &= H'x, \end{aligned} \quad (\text{A.3})$$

and the Gold deconvolution algorithm solution is:

$$x^{k+1}(i) = \frac{y'(i)}{\sum_{m=0}^{N-1} H'_{im} x^k(m)} \cdot x^k(i), \quad (\text{A.4})$$

where  $k$  is the number of iterations and  $x^0 = [1, 1, \dots, 1]^T$  is the initial guess [88, 109].

<sup>1</sup>Here, to match the dimensions, we are using the indexes in loop. That is, the  $N-1$  vector  $y$  on the left hand is composed as  $y(0) = y(0) + y(N)$ ,  $y(1) = y(1) + y(N+1)$ , ...,  $y(N-1) = y(N-1) + y(2N-1)$

The algorithm has a drawback here, it is suitable to process positive definite data, such as histograms. Therefore, an offset needs to be applied in the waveforms to avoid negative values. Moreover, the s.p.e. average waveform of Fig. 5.17b is still too noisy to extract a decent output from the deconvolution, specially because of the small oscillation present at 600 ns.

Because of that, a fit to retrieve  $h(t)$  is performed with three exponential and a Heaviside step function convoluted with a Gaussian as:

$$h(t) = \frac{1}{\sqrt{2\pi\sigma^2}} \int_{-\infty}^{\infty} \exp\left(-\frac{(t-x)^2}{2\sigma^2}\right) H(x) \sum_{i=1}^3 \exp\left(-\frac{x}{\tau_i}\right) dx, \quad (\text{A.5})$$

where  $H(x)$  is the Heaviside step function and the Gaussian was set as common for all the exponential. Solving this equation is quite simple, one can notice that the equation:

$$\exp\left(-\frac{(t-x)^2}{2\sigma^2}\right) \exp\left(-\frac{x}{\tau}\right) = \exp\left(-\frac{\left(x - \left(t + \frac{\sigma^2}{\tau}\right)\right)^2}{2\sigma^2}\right) \exp\left(-\frac{t}{\tau}\right) \exp\left(-\frac{2\sigma^2}{\tau}\right)$$

can be split in the integral. Because of the Heaviside step function, only the positive area will contribute to the integral. Therefore, we need to solve:

$$I(t) = \frac{1}{\sqrt{2\pi\sigma^2}} \exp\left(-\frac{t}{\tau}\right) \exp\left(-\frac{\sigma^2}{2\tau}\right) \int_0^{\infty} \exp\left(-\left[\frac{x - \left(t + \frac{\sigma^2}{\tau}\right)}{\sqrt{2}\sigma}\right]^2\right) dx. \quad (\text{A.6})$$

Taking the variable substitution:

$$u = \frac{x - \left(t + \frac{\sigma^2}{\tau}\right)}{\sqrt{2}\sigma} \longrightarrow dx = \sqrt{2}\sigma du$$

the integral becomes:

$$I(t) = \frac{1}{\sqrt{\pi}} \exp\left(-\frac{t}{\tau}\right) \exp\left(-\frac{\sigma^2}{2\tau}\right) \int_{-\frac{t}{\sqrt{2}\sigma} + \frac{\sigma}{\sqrt{2}\tau}}^{\infty} e^{-u^2} du, \quad (\text{A.7})$$

which is solved by using the definition of the erf(x) function:

$$I(t) = \frac{1}{\sqrt{\pi}} \exp\left(-\frac{t}{\tau}\right) \exp\left(-\frac{\sigma^2}{2\tau}\right) \left[ \frac{\sqrt{\pi}}{2} \text{erf}(x) \right]_{-\frac{t}{\sqrt{2}\sigma} + \frac{\sigma}{\sqrt{2}\tau}}^{\infty}.$$

Finally, using the fact that  $\text{erfc}(x) = 1 - \text{erf}(x)$ , the solution is given by:

$$I(t) = \frac{1}{2} \exp\left(-\frac{t}{\tau}\right) \exp\left(-\frac{\sigma^2}{2\tau}\right) \text{erfc}\left(-\frac{t}{\sqrt{2}\sigma} + \frac{\sigma}{\sqrt{2}\tau}\right). \quad (\text{A.8})$$

Using the result of Eq. A.8 into Eq. A.5, adding a phase  $\phi$  for the onset of the waveform and a amplitude  $A_i$  for each exponential, the final fit function is:

$$h(t) = \sum_{i=1}^3 A_i \exp\left(-\frac{t-\phi}{\tau_i}\right) \exp\left(-\frac{\sigma^2}{2\tau_i}\right) \text{erfc}\left(\frac{\phi-t}{\sqrt{2}\sigma} + \frac{\sigma}{\sqrt{2}\tau_i}\right), \quad (\text{A.9})$$

with eight free parameters. The method described above is the best estimation we could find to avoid the oscillation, the result is shown in Fig. A.1 where one can notice the peak of the waveform is not well fitted. Unfortunately, this could not be solved in the fit and the consequence is a not well deconvolved peak.

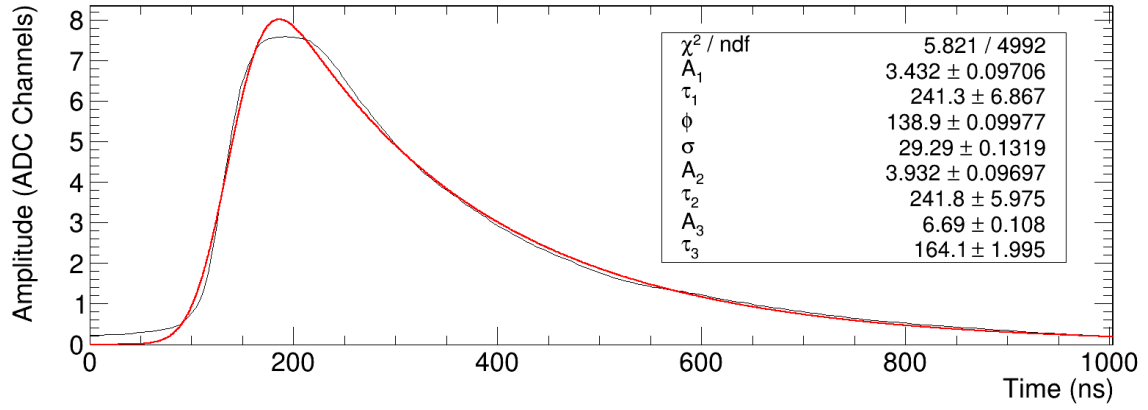


Figure A.1: Single photo-electron averaged waveform from Fig. 5.17b fitted with Eq. A.9.

## Total internal reflection

Total internal reflection happens when an incident light crosses the interface of two different index of refraction mediums ( $n_{\text{in}} > n_{\text{out}}$ ) with a high enough oblique angle. The *Snell's law* relates the angle of incidence the incident light  $\theta_{\text{in}}$  with the refracted light  $\theta_{\text{out}}$  as:

$$n_{\text{out}} \cdot \sin \theta_{\text{out}} = n_{\text{in}} \cdot \sin \theta_{\text{in}}, \quad (\text{B.1})$$

that can be extended to the total internal reflection considering that  $\theta_{\text{out}} = 90^\circ$ . In this case, the critical angle ( $\theta_C$ ) in which the effect starts can be calculated by:

$$\theta_C = \sin^{-1} \left( \frac{n_{\text{out}}}{n_{\text{in}}} \right), \quad (\text{B.2})$$

with solution only if  $n_{\text{in}} > n_{\text{out}}$ . In the specific case of the X-ARAPUCA, the outer medium can be liquid argon or vacuum/air, and the inner medium is the wavelength shifter slab. For instance, the EJ-286 slab has an index of refraction  $n_{\text{EJ-286}} = 1.58$ , this means that in vacuum the critical angle would be  $\theta_C \sim 39.2^\circ$  and in LAr ( $n_{\text{LAr}}(\lambda = 430 \text{ nm}) = 1.2344$ )  $\theta_C \sim 51.4^\circ$ .

To evaluate the amount of photons trapped by total internal reflection, one can take solid angle of emission of the photons as illustrated in Figure B.1. The fraction of light exiting the WLS ( $F_E$ ) is related to the solid angle as:

$$F_E = \frac{2\Omega}{4\pi} = \frac{1}{2\pi} \int_0^{\theta_C} \int_0^{2\pi} d\phi \sin \theta d\theta = 1 - \cos \theta_C = 1 - \sqrt{1 - \sin^2(\theta_C)} \quad (\text{B.3})$$

Using Eq. B.3 together with Eq. B.2, one can take the fraction of light trapped in the slab due to total internal reflection:

$$F_T = 1 - F_E = \sqrt{1 - \left( \frac{n_{\text{out}}}{n_{\text{in}}} \right)^2}. \quad (\text{B.4})$$

About 77.4% and 62.4% of the light is trapped in vacuum and LAr, respectively.



Figure B.1: Solid angle of the photons emitted in the critical angle  $\theta_C$ , illustration based on the image found in the MUONCA manual by Prof. Anderson Campos Fauth.

## Photomultiplier tube (PMT)

A Photomultiplier tube (PMT) works through the photoelectric effect, in which photons colliding with a metallic material may eject electrons from it. The electron has the energy of the photon subtracting the energy necessary for the ejection [117]:

$$K = h\nu - \phi, \quad (\text{C.1})$$

where  $K$  is the kinetic energy of the electron,  $h\nu$  is the photon energy and  $\phi$  is the material work function, that is, the energy necessary to eject the bounded electron. The electrons, called photo-electrons, are ejected according to the quantum efficiency of the photocathode. A high voltage accelerate the photo-electrons towards dynodes stages that releases more electrons up collision. The multiplied electrons are than collected by the anode. The process is illustrated in Figure C.1.

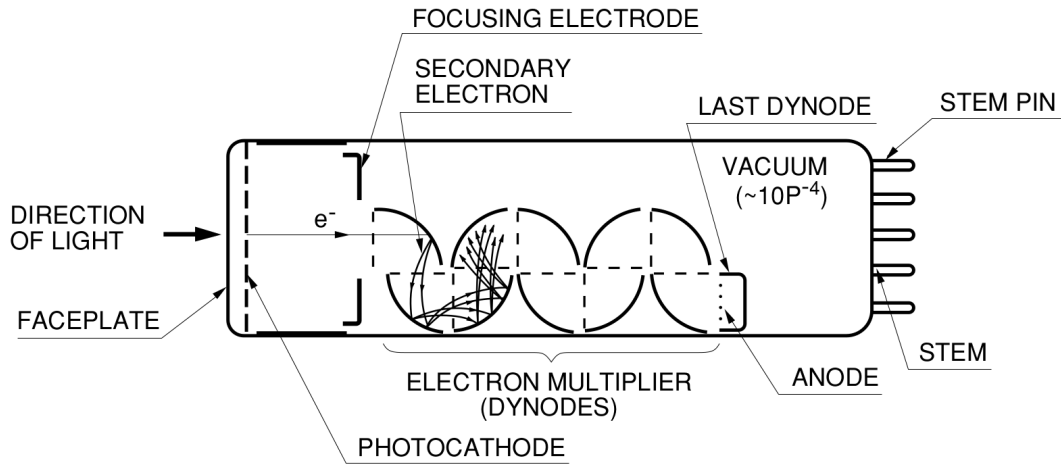


Figure C.1: Schematic operation of a photomultiplier tube. Image from Hamamatsu [92].

The gain of the PMT depends on the number of dynodes stages and high voltage applied between the anode and photo-cathode, but its typically of  $10^6$  up to  $10^8$ . A negative or positive high voltage power supply of 1 kV up to 2 kV is required.

## Toy Model images

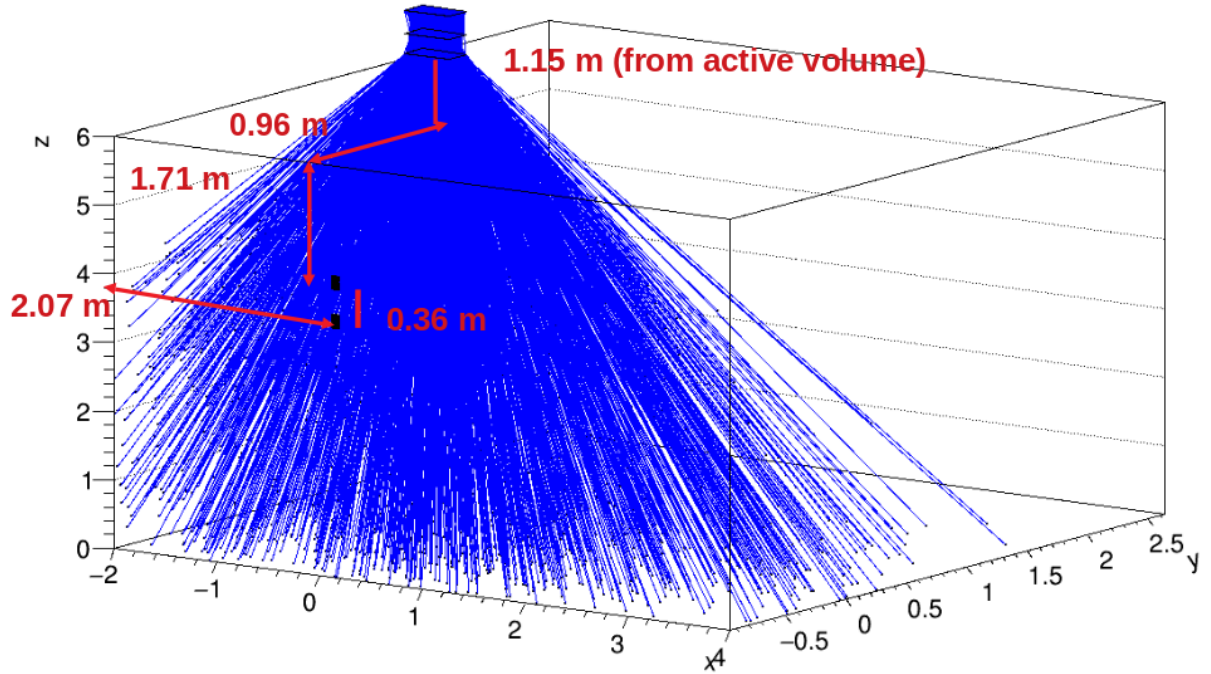


Figure D.1: Selected muons (blue lines) by the telescope composed by three detectors of plastic scintillator above the LArTPC. The two X-ARAPUCAs can be seen in the plane  $y = -1$  m as black boxes.

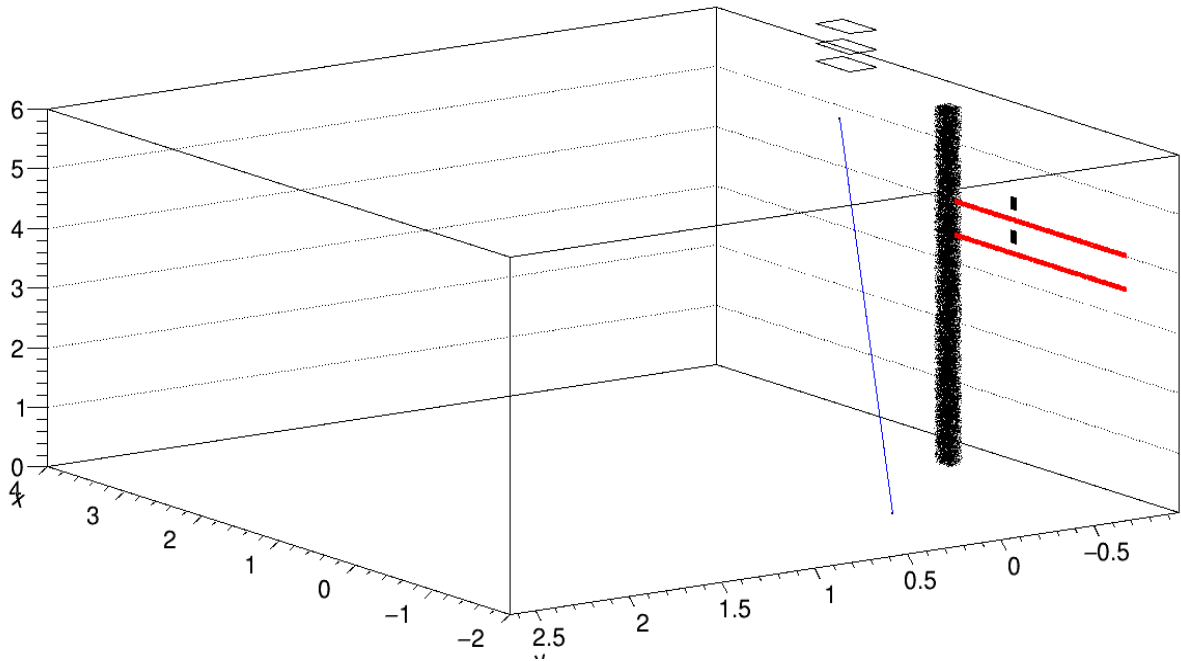


Figure D.2: A muon (blue line) crossing the LArTPC will emit light only after 1 m inside the TPC. The APA column and the two X-ARAPUCAs are illustrated in black. The PDS modules are being show in red.

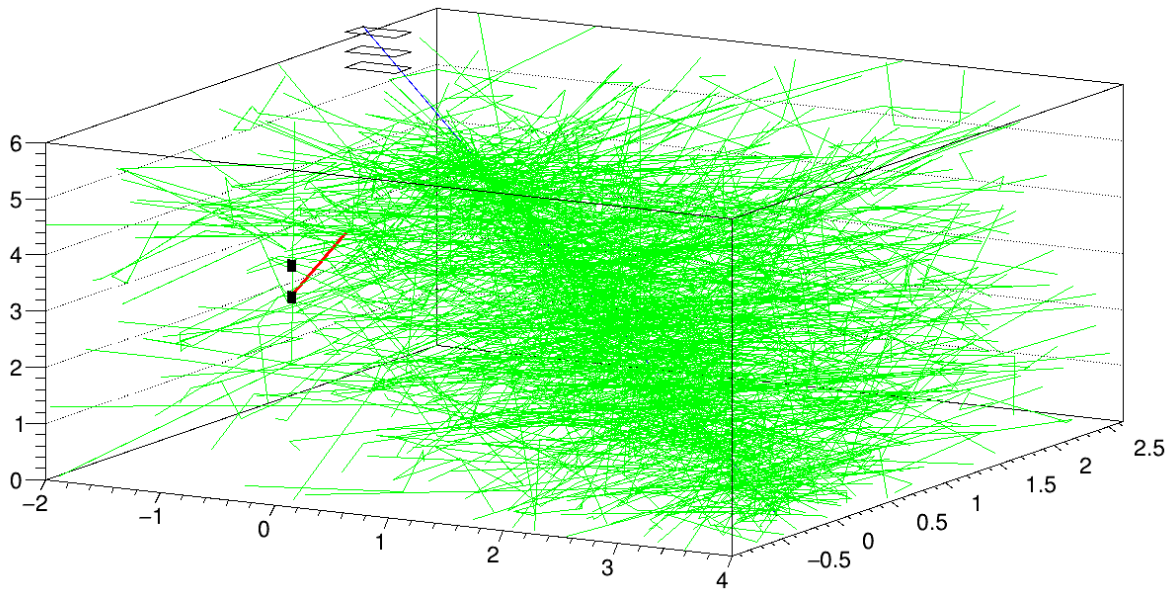


Figure D.3: Example of a muon (blue line) crossing the LAr and emitting scintillation photons (green lines) isotropically. The red line represents a photon that was successfully collected after begin Rayleigh scattered. The light yield was significantly reduced to produce the image.